



Vrije Universiteit Brussel
Applied Sciences and Engineering
Brussels, Belgium



Royal Military Academy
Polytechnic Faculty
Brussels, Belgium

COMPRESSED SENSING AS A TOOL FOR DEFENSE APPLICATIONS IN THE GHZ FREQUENCY BAND

Edison Cristofani Caldero

Supervisors: Prof. Marijke Vandewal,
Prof. Johan Stiens and Prof. Nikolaos Deligiannis

Thesis submitted in fulfillment of the requirements for the degree of Doctor in
Engineering Sciences (RMA) and Doctor in Engineering Sciences (VUB)

November 13th 2018

Abstract

Perfect signal recovery from discretized continuous signals has been studied under the name of the Nyquist-Shannon sampling theorem. If a signal is sufficiently sparse in a given representation domain, only a fraction of the original measurement samples can be randomly kept: This sparse vector recovery problem can be solved using compressed sensing (CS), which first appeared in mid-2000 and has grown in interest, reaching countless fields and creating new development paths for future applications. In this PhD dissertation we investigate CS within defense in the GHz frequency band. This work will generalize the results of CS in terms of performance and implementation. CS is here used as bridge between a mathematical reconstruction problem and an applied, computationally affordable solution for numerous applications. Three applications are studied in this PhD: Non-destructive testing (NDT) for defect detection, ground penetrating radars (GPR) for landmine detection, and passive coherent location (PCL) using passive opportunistic radars for airspace surveillance. This research has found that for NDT of certain materials using step-by-step frequency sweeps, the number of collected frequencies can be reduced down to only 20% of the original measurement volume achieving simplified and immediate reconstructions thanks to the CS algorithm known as orthogonal matching pursuit and dictionary modeling. This implies reduced acquisition times, hence increasing the efficiency of testing or maintenance tasks. An extension to a second (or potentially a third) measurement dimension is also possible as it is the case of GPR, whose sensor moves linearly on a platform. Additionally to reducing the frequency steps to be kept, CS can also discard complete measurements in the platform's path and be able to reconstruct the scene satisfactorily. For large targets, we have found that the frequency subsampling can be reduced to only 5% of the original data or 10% of the scanning positions. For smaller targets, these figures change to 15% and 20%, respectively, in combination with a modeling that reduces the effects of all intrinsic antenna-ground reverberations. Finally, we have found that applying CS on DVB-T echoes coming back from moving targets reduces the typically huge data volumes collected, simplifies the reconstructed scene, enables using more channels or possibly using multiple receivers scattered around the surveyed area for a more precise target location. The obtained results show that CS reduces data collection down to just 0.1% of the originally required data.

Acknowledgments

First and foremost, I would like to show my gratitude to my promoters Prof. Johan Stiens and Prof. Nikolaos Deligiannis for believing in me in the early stages of this study and paving the way of what would later become a doctoral dissertation. My most emphatic gratitude must be to Prof. Marijke Vandewal, my mentor for many years and direct supervisor during this work. Her help was paramount in every sense: the countless hours of discussions, guidance and support were worth every single moment spent.

I must also thank all my colleagues from the CISS Department and also those who made the effort of helping me collect data like Dr. Gokarna Pandey (ETRO-VUB) and Prof. Sébastien Lambot (ELIE-UCLouvain). A very special mention must go to Dr. Osama Mahfoudia (EMP, Algeria), whose support and friendship during and after his stay at the RMA are invaluable to me.

Finally, I want to express my admiration to my parents, my family and, especially, to Alicia and Sofia for supporting me unconditionally and sharing with me all these years.

Members of the Jury

Prof. Dr. Ir. GALLANT, Johan (President)
Royal Military Academy, ABAL Department, BE

Prof. Dr. Ir. PINTELON, Rik (Vice president)
Vrije Universiteit Brussel, ELEC Department, BE

Prof. Dr. Ir. LAUWENS, Ben (Secretary)
Royal Military Academy, MWMW Department, BE

Prof. Dr. Ir. VANDEWAL, Marijke (Promoter)
Royal Military Academy, CISS Department, BE

Prof. Dr. Ir. DELIGIANNIS, Nikolaos (Promoter)
Vrije Universiteit Brussel, ETRO Department, BE

Prof. Dr. Ir. STIENS, Johan (Promoter)
Vrije Universiteit Brussel, ETRO Department, BE

Prof. Dr. MARTORELLA, Marco
University of Pisa, Department of Information Engineering, IT

Prof. Dr. Ir. MOEYAERT, Véronique
Université de Mons, Faculté Polytechnique, BE

Ir. BOURDOUX, André
IMEC, BE

Contents

List of Figures	xii
List of Tables	xxiii
List of Abbreviations	xxv
List of Symbols	xxix
1 Introduction	1
1.1 Motivation	1
1.2 Objectives of the work	3
1.3 Thesis organization	3
2 Radar sensors	5
2.1 Introduction and applications	6
2.2 Radar fundamentals	8
2.3 Other types of radars	12
2.3.1 Continuous-wave radars	12
2.3.2 Frequency-Modulated Continuous-Wave radars	15
2.3.3 Stepped-frequency radars	19
2.3.4 The vector network analyzer as a SFCW radar	21
2.4 Brief introduction to detection theory	23
2.4.1 Basic detection problem example	23
2.4.2 The detector	25
2.4.3 The matched filter and pulse compression	31
2.4.4 The CFAR detector as a detection metric	33
2.4.5 Radar ambiguity function	38
2.5 Synthetic aperture radars	40
2.5.1 Introduction	40
2.5.2 Processing SAR data	42
2.6 Bistatic radars	44
2.6.1 Introduction	44
2.6.2 Scene description	45
2.6.3 Target location	48
2.6.4 Multistatic radars	49

2.7	Conclusions	52
3	Fundamentals of Signal Sampling and Compressed Sensing	55
3.1	Signal sampling and historic approach	55
3.2	New solutions to new needs: Compressed Sensing	59
3.3	Problem description and formulation	61
3.4	Greedy algorithms for solving the CS problem	66
3.5	Sparsity enhancement	67
3.5.1	Sparsity enhancement using data transformations	69
3.5.1.1	The (inverse) Fourier transform	70
3.5.1.2	PCA as data-dependent sparsifying basis	70
3.5.2	Sparsity enhancement using data-based dictionaries	70
3.5.3	Sparsity enhancement using the re-weighted ℓ_1 minimization	71
3.6	Side information	72
3.7	Conclusions	73
4	UWB Radars for Non-Destructive Testing	75
4.1	Introduction and applications	75
4.2	Typical structures, materials and failure modes	77
4.2.1	Composite structures and materials	77
4.2.2	Typical composite failure modes	78
4.3	Focused NDT sensors	80
4.3.1	Set-up using focusing mirrors	80
4.3.2	The beam-waist effect	81
4.3.3	Interactions between waves and multilayered materials	83
4.3.3.1	Snell's law	83
4.3.3.2	Media interfaces and interactions with waves	85
4.4	Description of measurements	87
4.4.1	Sensor specifications	87
4.4.2	Data simulation	90
4.4.3	Adapting NDT sensors to CS sampling	92
4.4.4	Populating the dictionaries	94
4.5	Experimental results and CS reconstructions	94
4.5.1	CS reconstructions possibilities	94
4.5.2	General simulation parameters	95
4.5.3	Reconstruction metrics	95
4.5.4	Results: the signal reconstruction approach	97
4.5.5	Results: the reflectivity function reconstruction approach	99
4.5.6	Examples of the effects of subsampling and noise	101
4.6	Conclusions and discussion	107
5	Ground Penetrating Radar	109
5.1	Introduction and applications	109
5.2	Types of landmines	111
5.3	Interactions with the ground	112

5.4	Adapting common theory from NDT	114
5.5	Intrinsic antenna modeling	115
5.6	Adapting GPR sensors to CS sampling	119
5.6.1	Subsampling strategies	121
5.6.1.1	Frequency subsampling	122
5.6.1.2	Spatial subsampling	123
5.6.1.3	Combining subsampling strategies	124
5.7	Measurement campaign description and sensor specifications	125
5.8	CS reconstruction results and discussion	127
5.8.1	Example of CS reconstruction of a GPR scene	128
5.8.2	The AT landmine	129
5.8.3	The AP landmines	135
5.9	Conclusions	142
6	Passive Coherent Location	145
6.1	Illuminators of opportunity	145
6.2	OFDM fundamentals	146
6.3	Structure and generation of DVB-T transmissions	147
6.4	OFDM signal generation	148
6.5	The Doppler effect	151
6.6	Target detection using range-Doppler	153
6.7	Adapting a PCL setup to CS	157
6.7.1	Signal subsampling and reference signal recovery	157
6.7.2	Sensor specifications and description of measurements	160
6.7.3	PCL data transformation	162
6.8	Performance analysis	162
6.9	The sparsifying effect of using the re-weighted ℓ_1 minimization	165
6.10	Side information: a-priori knowledge of the scene clutter	170
6.11	Conclusions	171
7	Conclusions and future work	173
7.1	Summary of results for NDT	173
7.2	Summary of results for GPR	174
7.3	Summary of results for PCL	175
7.4	Closing remarks	176

List of Publications

All the publications produced during this dissertation are listed next:

Book chapters

- E. Cristofani, F. Friederich, M. Vandewal, and J. Jonuscheit. Non destructive testing of aeronautics composite structures using UWB radars. In James D Taylor, editor, *Advanced Ultrawideband Radar. High Resolution Materials, Sensor Systems, and Practical Applications*, chapter 6, pages 237–270. Taylor & Francis Group, 6000 Broken Sound Parkway NW, Suite 300, Boca Raton, FL 33487-2742 CRC Press 2016, 2016

Peer-reviewed journal articles

- E. Cristofani, M. Becquaert, S. Lambot, M. Vandewal, J. H. Stiens, and N. Deligiannis. Random subsampling and data preconditioning for ground penetrating radars. *IEEE Access*, 6:26866–26880, 2018
- M. Becquaert, E. Cristofani, H. Van Luong, M. Vandewal, J. Stiens, and N. Deligiannis. Compressed sensing mm-wave sar for non-destructive testing applications using multiple weighted side information. *Sensors*, 18(6):1761, May 2018

Journal articles under production or pre-press

- M. Becquaert, E. Cristofani, B. Lauwens, M. Vandewal, J. Stiens, and N. Deligiannis. Online Sequential Compressed Sensing with Multiple Information for Through-the-Wall Radar Imaging. *Submitted to: IEEE Sensors*, 2018
- Journal paper on Compressed sensing and NDT, IEEE Access. To be submitted.
- Journal paper on Compressed sensing and DVB-T-based PCL, IEEE Access. To be submitted.

Peer-reviewed conference papers

- E. Cristofani, O. Mahfoudia, M. Becquaert, X. Neyt, F. Horlin, N. Deligiannis, J. Stiens, and M. Vandewal. Exploring side information for DVB-T-based passive radars. In *URSI Benelux Forum 2018*, pages 1–1. URSI, 1 2018
- M. Becquaert, E. Cristofani, M. Vandewal, J. Stiens, and N. Deligiannis. Online sequential compressed sensing with weighted multiple side information for through the wall imaging. In *URSI Benelux Forum 2018*, pages 1–5. URSI, 1 2018
- E. Cristofani, O. Mahfoudia, M. Becquaert, X. Neyt, F. Horlin, N. Deligiannis, J. Stiens, and M. Vandewal. Compressive Sensing and DVB-T-Based Passive Coherent Location. In *26th URSI Benelux Forum*, Brussels, Belgium, 2017. URSI
- M. Becquaert, E. Cristofani, J. Stiens, M. Vandewal, and N. Deligiannis. Compressed Sensing SAR Through-the-Wall Imaging with Side Information. In *26th URSI Benelux Forum*, Brussels, Belgium, 2017. URSI
- M. Becquaert, E. Cristofani, G. Pandey, M. Vandewal, J. Stiens, and N. Deligiannis. Compressed sensing mm-wave SAR for non-destructive testing applications using side information. In *2016 IEEE Radar Conference (RadarConf)*, number 2, pages 1–5. IEEE, may 2016
- E. Cristofani, M. Becquaert, G. Pandey, M. Vandewal, N. Deligiannis, and J. Stiens. Compressed Sensing And Defect-Based Dictionaries For Characteristics Extraction In Mm-Wave Non-Destructive Testing. In *Infrared, Millimeter, and Terahertz Waves (IRMMW-THz), 2016 41st International Conference on*, Copenhagen, Denmark, 2016

Vulgarization articles

- E. Cristofani. Une nouvelle façon d’acquérir les signaux. *Belgisch Militair Tijdschrift - Revue Militaire Belge Nr. 14*, pages 121–127, june 2017

List of Figures

1.1	The radio-electric spectrum. The applications explored in this work are shown in their corresponding frequency band.	2
2.1	Classic classification of radars based on their configuration and the transmitter type.	7
2.2	Schematic of a typical radar configuration. A transmitted wave is reflected by a target located at range R in the scene. The echoes $x(t)$ are processed and the range of the target is extracted.	8
2.3	Schematic of a typical radar configuration. A transmitted wave is reflected by a target located at range R in the scene. The echoes are processed and the range of the target is extracted.	9
2.4	Angles θ and ϕ describe the radiation direction of an antenna.	11
2.5	Schematic of a typical radar configuration. A transmitted wave is reflected by two targets located at ranges R_1 and R_2 in the scene. The echoes are processed and the ranges of the targets are extracted.	12
2.6	Simplified conceptual schematic of a CW radar.	13
2.7	Simplified conceptual schematic of a FMCW radar.	15
2.8	A sawtooth FMCW signal: Top, frequency evolution in time of a transmitted FMCW signal (solid line) and a received replica delayed τ_r (dashed line); bottom, frequency evolution in time of the beat frequency $f_b(t)$	16
2.9	A linearly frequency modulated continuous wave waveform, known as chirp, linearly increases its frequency to sweep its bandwidth in one period.	17
2.10	Generation of an SFCW signal. Top, sequence of individual frequencies or tones generated and covering a given bandwidth B . Bottom, the time evolution of the generated signal frequency. Each tone is transmitted for a fixed time interval T_f , completing the total duration T_p of the frequency sweeping.	19
2.11	Time evolution of the generated SFCW signal. A sequence of tones at increasing frequencies is radiated, closely emulating the FMCW waveform.	20
2.12	Interactions of the traveling waves $a_{1,2}$ and $b_{1,2}$ for a generic two-port as well as the resulting S -parameters and their physical influence.	21
2.13	Radar measurement of a target using a VNA which sweeps a bandwidth B of discrete frequencies from f_0 to f_{max} in frequency steps of Δf . For reflection measurements (S_{11} parameters) only one port is necessary.	23
2.14	The echoes from two targets overlap in time. Left, the noise-free received signal; right, the received signal corrupted by noise (SNR = 8 dB). The two targets are difficult to identify.	24

2.15	The echoes from four targets overlap in time. Left, the noise-free received signal; right, the received signal corrupted by noise ($SNR = 8$ dB). It is not possible to identify any of the targets but just a rough approximation of the beginning and end of the received echoes.	24
2.16	Block diagram of a generic detector and a binary comparator with two hypotheses, \mathcal{H}_0 and \mathcal{H}_1	25
2.17	The two curves show the probability distribution functions of two Gaussian distributed processes with equal variances but different means ($\mu_1 > \mu_0 = 0$). A threshold γ is used to set the boundary between deciding whether \mathcal{H}_0 or \mathcal{H}_1 is true.	26
2.18	An experiment with low SNR conditions: $SNR = 6.02$ dB with undesirably high P_{fa}	28
2.19	An experiment with high SNR conditions: $SNR = 23.52$ dB with negligible P_{fa} and virtually perfect detection $P_d = 1$	29
2.20	Semi-log graph representing the P_d curves for varying SNR values and for different chosen P_{fa} . For every value of P_{fa} there is a variation in SNR and P_d that must be considered when assessing the performance of the detector.	30
2.21	Block diagram of the matched-filter along with the input and output signals. . .	31
2.22	A MF is applied to the generic radar scenario where two targets are illuminated and their echoes are received without a clear indication of the targets positions. The output of the MF compacts the received energy from the targets as indicated by the ambiguity function of the radar, revealing the correct respective ranges as well as reflectivities.	33
2.23	Schematic of a CA-CFAR detector using an envelope detector or a matched filter on the input signal $x(t)$	34
2.24	A typical subdivision in cells of a reconstructed 2-D scene. CA-CFAR detectors compute the threshold from the training cells (gray) to decide if a target is present in the cell under test (black). Guard cells (white) are used to avoid wrong threshold estimations.	34
2.25	A CA-CFAR detector is applied to a received signal $x(t)$ with $SNR = 20$ dB after an envelope detector containing three echoes at time delays 2 ms, 3.5 ms and 6 ms. The dashed line corresponds to the CA-CFAR adaptive threshold which varies depending on the sensed noise levels. For a $P_{fa} = 10^{-5}$ all three targets are detected.	36
2.26	P_d vs. SNR curves describe the same results obtained using an envelope detector and the CA-CFAR detector and several imposed P_{fa}	36
2.27	A CA-CFAR detector is used similarly to the results shown in Figure 2.25, although pulse compression is used instead of the envelope detector. The resulting SNR after pulse compression is increased, as expected, which leads to a potential performance improvement. For a $P_{fa} = 10^{-5}$ all three targets are detected. . . .	37
2.28	P_d vs. SNR curves describe the same results obtained using pulse compression and the CA-CFAR detector and several imposed P_{fa}	37
2.29	Schematic of a typical radar configuration. A transmitted wave is reflected by a target located at range R in the scene. The echoes are processed and the range of the target is extracted.	39

2.30	Schematic of a typical radar configuration. A transmitted wave is reflected by a target located at range R in the scene. The echoes are processed and the range of the target is extracted.	39
2.31	Schematic of a wide-beam antenna with dimension D illuminating a point-target at range R	40
2.32	Schematic of a SAR measurement using a wide-beam antenna with an opening angle θ_{phys} . The point-target is illuminated by the radar from different measurement positions along its motion path.	41
2.33	Conventional processing steps for generating SAR imagery.	42
2.34	Two approaches to create SAR imagery are possible: the conventional SAR processing based on range and cross-range compression, and the CS approach for which no SAR processing is necessary.	43
2.35	Three-dimensional representation of a SAR measurement. The energy collected along the hyperbola $r(t)$ follows the antenna radiation diagram of the radar. . . .	44
2.36	General bistatic setup: A moving target at height h and speed v_t is illuminated by a transmitter. The receiver, which is not collocated with transmitter and sufficiently far by a baseline L , receives the echoes from the target as well as from the static clutter in the scene.	45
2.37	Bistatic configurations: Left, forward-scattering with a bistatic angle $\beta > 90^\circ$; right, backward-scattering with $\beta < 90^\circ$	46
2.38	Ellipse obtained by intersecting the ellipsoid with iso-range R_B generated by the foci Tx and Rx with the vertical plane including the Tx, Rx and target. The two unknown distances R_R and R_T satisfy the condition $R_B = R_R + R_T$. Other two candidate targets selected arbitrarily and with identical R_B are displayed in with grey dashed lines.	47
2.39	A 3-D representation of a bistatic scene with one transmitter and one receiver. The ellipsoid above the ground plane indicates all possible target loci when ideal isotropic antennas are used.	48
2.40	Two directive antennas are used in Tx and Rx. In contrast to the generic case assuming isotropic antennas, the iso-range is limited to the volume created by the intersection of both main lobes.	49
2.41	A 3-D representation of a multistatic scene with one transmitter and two receivers. All possible target loci are reduced to the intersection of the two ellipsoids, highlighted as a grey curve.	50
2.42	A 2-D view corresponding to the intersection of an arbitrary plane and the two ellipsoids as presented in Figure 2.41. For this view, two target loci are considered.	50
2.43	A 3-D representation of a multistatic scene with one transmitter and three receivers, all isotropic. The intersection of the ellipsoids shows the position of the target.	51
2.44	A 2-D view of the intersection of an arbitrary plane and the three ellipsoids as shown in Figure 2.43. Only one target locus is decided with no ghost targets. . . .	51
3.1	Top, a signal $x(t)$, continuous in time, is sampled at nT intervals, generating discrete voltage values.	56
3.2	Different definitions of the maximum frequency of a signal depending on its definition: tone, baseband or bandpass.	57

3.3	Effects of sampling a continuous signal with different sampling rates: a) continuous signal, b) $f_s = f_{max}/3$; c) $f_s = 2f_{max}$, d) shifted signal by 90° and $f_s = 2f_{max}$, e) shifted signal by 90° and $k_{os} = 1.2$, f) $k_{os} = 2$, and g) $k_{os} = 6$. . .	58
3.4	Time line of the evolution of CS from its initial mathematical conception to the current situation with countless applications and methods being explored.	60
3.5	Two representations of the same function: Left, a sinusoidal wave in time domain; right, its frequency representation. Examples of non-sparse and sparse signals, respectively.	61
3.6	After sampling a continuous signal, the discrete elements can be transformed into several representation domains providing different sparsity levels.	68
3.7	Normalized, sorted amplitudes of an original time-domain data set and its transformed coefficients using PCA. The decay on the PCA-transformed data is steeper, indicating sparser data.	68
4.1	Schematics of typical composite materials: a) a solid or monolithic laminate, b) a multi-layered composite, c) an A-sandwich, d) a B-sandwich.	77
4.2	Failure mode: a delamination between two layers (1) and a delamination at the edge of the sample (2).	78
4.3	Failure mode: different cracks affect differently the structure with (1) an initial crack with low impact on the material integrity, (2) a crack that may produce a delamination between layers, and (3) a progressive crack affecting all the layers of the material and, thus, critically compromising its integrity.	79
4.4	Failure mode: a foreign inclusion, which creates an integrity problem due to poor gluing between layers.	79
4.5	An additional failure mode: Buckling is produced after axial compression forces are applied to the structure, deforming it. If, during the decompression process, the material does not recover its original shape totally or partially, a delamination-like defect is created.	80
4.6	Schematic of a typical beam focusing set-up in NDT measurements. The concave mirrors are used to focus into a focal point the initially diverging wavefront radiated by the sensor.	81
4.7	Schematic representation of the beam waist effect using a focusing lens. At the beam waist the beam spot size is of minimum size and, therefore, obtaining the finest system resolution possible.	81
4.8	General case of reflection and refraction effects in an interface between two media ($n_1 > n_0$) for a wavefront impinging at $\theta_i > 0^\circ$	83
4.9	Particular case of reflection and refraction angles for an air-medium-air interface ($n_1 = n_3 = 1$ and $n_2 = 2$) and an incident angle of 0°	84
4.10	Particular case of reflection and refraction angles for an air-medium-air interface ($n_1 = n_3 = 1$ and $n_2 = 2$) and an incident angle of 10°	85
4.11	Equivalent circuit based on transmission lines theory for representing a multi-layered material and the interactions between interfaces and incident wavefronts.	86
4.12	NDT measurement set-up in which two ABS blocks (foreground) replicate a delamination artifact. A set of reflectors and conic antenna (background) is used to collimate the beam into a focal point.	88
4.13	VNA model MVNA-8-350 by AB Millimetre with a visualization and data storage unit on the left side. Image obtained from [12].	89

4.14	Conical horn antenna model AB Millimetre SH-V-FB-10. Image obtained from [13].	89
4.15	Top-down view of the measurement set-up. The antenna, two reflectors and D.U.T. follow the same arrangement as displayed in Figure 4.6.	90
4.16	Close perspective view of the antenna, parabolic mirrors and the DUT.	90
4.17	Schematic of the NDT set-up simulating an air gap between two delaminated layers of a composite polymer. Two identical ABS blocks (M_1 and M_2) with a width of $l = 20$ mm are used, whereas the air gap thickness g is manually adjustable.	91
4.18	Generation of NDT measurements using a VNA could be governed by virtual instrumentation. The VNA needs to only interrogate those frequencies randomly selected as specified by f	93
4.19	Image reconstruction possibilities: 1) the solid line shows the path using sparse signal reconstruction and farther conventional imagery; 2) the dashed line uses a measurement-based or synthetic dictionary to reconstruct the reflectivity function.	95
4.20	Schematic of the Metric A applied to signal reconstruction using CS. The amplitude and interface positioning differences are considered to compute a global reconstruction score.	96
4.21	Schematic of the Metric B for which results are separated into classes and their respective likelihoods from which a final score is obtained for the winner class candidate. In the example, only 6 classes are considered.	97
4.22	Reconstruction score vs. SNR using an IFFT transformation basis as sparsifying basis, OMP and 500 Monte-Carlo realizations.	98
4.23	Matching scores for CS measurement reconstructions using an IFFT basis and OMP. A total of 500 Monte-Carlo simulations were run for each combination of subsampling rate (k_f) and SNR value.	99
4.24	Reconstruction scores vs. SNR using real S_{11} measurements as sparsifying basis, OMP and 500 Monte-Carlo realizations.	99
4.25	Matching scores for real-data dictionary and OMP. 500 Monte-Carlo simulations were run for each combination of subsampling rate (k_f) and SNR value.	100
4.26	Reconstruction scores vs. SNR using synthetic S_{11} measurements as sparsifying basis, OMP and 500 Monte-Carlo realizations.	100
4.27	Matching scores for a synthetic-data dictionary and OMP. 500 Monte-Carlo simulations were run for each combination of subsampling rate (k_f) and SNR value.	101
4.28	CS reconstruction of real NDT measurements using the signal reconstruction approach and OMP: a) $k_f = 0.50$ and SNR = 16 dB, b) $k_f = 0.50$ and SNR = 0 dB.	102
4.29	CS reconstruction of real NDT measurements using the signal reconstruction approach and OMP: a) $k_f = 0.05$ and SNR = 16 dB, b) $k_f = 0.05$ and SNR = 0 dB.	102
4.30	Decisions for an 11-mm air gap, SNR = 16 dB, and $k_f = 0.5$: Top, decided thickness atoms; bottom, decided thickness class. A dictionary built up using real measurements is used, along with OMP.	103
4.31	Decisions for an 11-mm air gap, SNR = 0 dB, and $k_f = 0.5$: Top, decided thickness atoms; bottom, decided thickness class. A dictionary built up using real measurements is used, along with OMP.	104

4.32	Decisions for an 11-mm air gap, SNR = 16 dB, and $k_f = 0.05$: Top, decided thickness atoms; bottom, decided thickness class. A dictionary built up using real measurements is used, along with OMP.	105
4.33	Decisions for an 11-mm air gap, SNR = 0 dB, and $k_f = 0.05$: Top, decided thickness atoms; bottom, decided thickness class. A dictionary built up using real measurements is used, along with OMP.	105
4.34	Gap class decisions for an 11-mm air gap, $k_f = 0.5$, and: a) SNR = 16 dB; b) SNR = 0 dB. A dictionary built up using simulated measurements is used, along with OMP.	106
4.35	Gap class decisions for an 11-mm air gap, $k_f = 0.05$, and: a) SNR = 16 dB; b) SNR = 0 dB. A dictionary built up using simulated measurements is used, along with OMP.	106
5.1	Example of a GPR measurement. A moving platform (e.g. remote rover or pushed cart) mounts a VNA used for signal generation, transmission and detection, while a wide-beam antenna illuminates an object buried deep into the ground.	110
5.2	Schematic diagram of an anti-tank landmine.	111
5.3	Commonly used AP landmines: Left, the PMN2; right, the M14. Both are mostly made of plastics and difficult to detect using standard mine detection techniques.	112
5.4	Example of a GPR measurement. A moving platform (e.g. remote rover or pushed cart) mounts a VNA used for signal generation, transmission and detection, while a wide-beam antenna illuminates an object buried deep into the ground.	114
5.5	Block diagram describing the internal reverberations within the antenna aperture as well as the antenna-ground reflections.	116
5.6	Echoes from a GPR range-compressed measurement not applying (top) and applying (bottom) the antenna-ground interaction modeling. The two AP mines are visible after modeling is applied and depths (time-of-flight) for all targets are corrected.	117
5.7	The depth profile after the Fourier correlator is shown for the AT landmines. The thin solid curve indicates raw, unfiltered data. The thicker curve shows the filtered profiles including a landmine, while the dashed curve does not include any target.	118
5.8	The depth profile after the Fourier correlator is shown for the PMN2 landmines. The thin solid curve indicates raw, unfiltered data. The thicker curve shows the filtered profiles including a landmine, while the dashed curve does not include any target.	118
5.9	The depth profile after the Fourier correlator is shown for the M14 landmines. The thin solid curve indicates raw, unfiltered data. The thicker curve shows the filtered profiles including a landmine, while the dashed curve does not include any target.	119
5.10	Conventional data acquisition in a SAR measurement. For every cross-range measurement position, N reflection responses are collected, each corresponding to a discrete frequency in the swept bandwidth.	119
5.11	Conventional (range- and cross-range compression-based) and CS processing steps for generating SAR imagery.	120
5.12	Frequency subsampling scheme in GPR. The VNA interrogates random frequencies following a subsampling rate k_f	122

5.13	Cross-range positions subsampling scheme in GPR. The VNA only performs measurements collecting all Shannon-Nyquist frequencies at certain cross-range positions following a subsampling rate k_{xr}	123
5.14	If the maximum interspacing between cross-range random measurements is too large, objects in the scene may be missed. The cross-range interspacing will depend on the antenna aperture and the depth of the object.	124
5.15	Frequency and cross-range positions are randomly subsampled in a GPR measurement. The VNA collects random frequencies at random cross-range positions following the subsampling rates k_f and k_{xr} , respectively.	125
5.16	A sandbox hosted at TNO was used to obtain the presented GPR measurements. The scanner carries a portable VNA and horn antenna placed at a standoff distance of 200 mm from the ground.	125
5.17	Three mines (AT, PMN2 and M14) were buried on a sandbox at different depths and separated by 75 cm of each other. The SFCW radar ran over a scanning path 2.5 m long at a distance of 20 cm from the ground.	126
5.18	The three buried mines are correctly located with a dictionary-based CS recovery of a GPR scene and applying the antenna-ground modeling. Only 50% of the frequencies and scanning positions were used and no noise was added.	128
5.19	Robustness analysis of the CS reconstructions of the AT landmine using BPDN and raw data. The P_d vs. SNR curves are plotted for multiple k_f values. The solid line indicates intrinsic filtering is applied, whereas the dashed line indicates otherwise.	129
5.20	Robustness analysis of the CS reconstructions of the AT landmine using BPDN and PCA as data preconditioner. The P_d vs. SNR curves are plotted for multiple k_f values. The solid line indicates intrinsic filtering is applied, whereas the dashed line indicates otherwise.	130
5.21	Robustness analysis of the CS reconstructions of the AT landmine using BPDN and raw data. The P_d vs. SNR curves are plotted for multiple k_{xr} values. The solid line indicates intrinsic filtering is applied, whereas the dashed line indicates otherwise.	131
5.22	Robustness analysis of the CS reconstructions of the AT landmine using BPDN and PCA as data preconditioner. The P_d vs. SNR curves are plotted for multiple k_{xr} values. The solid line indicates intrinsic filtering is applied, whereas the dashed line indicates otherwise.	131
5.23	P_d vs. SNR for several subsampling rates $k_{xr} = 0.10, 0.3$ and 0.5 and $k_f = 0.05 - 0.25$ for the AT landmine and original non-transformed data. A probability of false alarm of 10^{-2} was chosen and 500 Monte-Carlo trials were run. A CA-CFAR detector was used to extract the P_d values.	132
5.24	P_d vs. SNR for several subsampling rates $k_{xr} = 0.10, 0.3$ and 0.5 and $k_f = 0.05 - 0.25$ for the AT landmine and PCA-transformed data. A probability of false alarm of 10^{-2} was chosen and 500 Monte-Carlo trials were run. A CA-CFAR detector was used to extract the P_d values.	133
5.25	Robustness analysis of the CS reconstructions of the PMN2 AP landmine using BPDN and raw data. The P_d vs. SNR curves are plotted for multiple a) k_f and b) k_{xr} values. The solid line indicates intrinsic filtering is applied, whereas the dashed line indicates otherwise.	135

5.26	Robustness analysis of the CS reconstructions of the PMN2 AP landmine using BPDN and PCA data preconditioning. The P_d vs. SNR curves are plotted for multiple a) k_f and b) k_{xr} values. The solid line indicates intrinsic filtering is applied, whereas the dashed line indicates otherwise.	136
5.27	Robustness analysis of the CS reconstructions of the M14 AP landmine using BPDN and raw data. The P_d vs. SNR curves are plotted for multiple a) k_f and b) k_{xr} values. The solid line indicates intrinsic filtering is applied, whereas the dashed line indicates otherwise.	137
5.28	Robustness analysis of the CS reconstructions of the M14 AP landmine using BPDN and PCA-transformed data. The P_d vs. SNR curves are plotted for multiple a) k_f and b) k_{xr} values. The solid line indicates intrinsic filtering is applied, whereas the dashed line indicates otherwise.	138
5.29	P_d vs. SNR for several subsampling rates $k_{xr} = 0.1 - 0.5$ and $k_f = 0.05 - 0.25$ for PCA-transformed data for the PMN2 landmine. A probability of false alarm of 1×10^{-2} was chosen and 500 Monte-Carlo trials were run. A CA-CFAR detector was used to extract the P_d values.	139
5.30	P_d vs. SNR for several subsampling rates $k_{xr} = 0.1 - 0.5$ and $k_f = 0.05 - 0.25$ for PCA-transformed data for the M14 landmine. A probability of false alarm of 1×10^{-2} was chosen and 500 Monte-Carlo trials were run. A CA-CFAR detector was used to extract the P_d values.	140
6.1	Seven orthogonal sub-channels cover the bandwidth of an OFDM signal.	146
6.2	A CP of duration Δ_{GI} is added to the OFDM symbol to prevent ASI.	147
6.3	Subcarrier structure of a 8k DVB-T frame, which expands over 68 DVB-T symbols. The subcarriers are categorized as: continual or scattered pilots, TPS and data.	147
6.4	Block diagram of generic OFDM transmission and reception chains.	149
6.5	Time- (top) and frequency-domain (bottom) representations of a DVB-T signal.	150
6.6	Histograms showing the noise-like distribution of DVB-T signals: Left, real values; right, imaginary values.	150
6.7	Description of possible Doppler shift situations: Left, the source moves at a constant speed towards the observer radially; right, the source moves at constant speed but its path will not intersect the observer's position.	152
6.8	Schematic representation of a simplified PCL scenario: A passive Rx uses the broadcasts of a TV station to locate a target overflying the surveyed airspace. The Rx measures both the reflected $x(t)$ and LOS signals $x_{ref}(t)$. Finally, a DSP unit produces a rD image.	153
6.9	Conceptual block diagram of a r-D processor. The $x_{ref}(t)$ signal is delayed up to $N - 1$ time units and mixed with $x(t)$. The range-Doppler data are obtained after FFT of all the mixed signals.	154
6.10	A, arbitrary range-Doppler diagram identifying the typical target appearances in this type of imagery.	154
6.11	2-D ambiguity function of a DVB-T signal. By inspecting range or frequency cuts of the the peak centered at $\tau = 0$ and $\nu = 0$, the PCL radar's Doppler frequency and range resolutions can be extracted, respectively.	155
6.12	Two cuts of the DVB-T ambiguity function: Left) a zero-Doppler frequency cut $\gamma_{rD}(\tau, 0)$; right, a zero-range cut $\gamma_{rD}(0, \nu)$	155

6.13	An extended zero-frequency cut of a DVB-T signal reveals two bright target ambiguities due to the signal's structure: one at $298.6 \mu\text{s}$ (or a bistatic range of 44.79 km), and a second one at exactly twice that distance (89.58 km).	156
6.14	Example of a rD diagram obtained from simulated DVB-T data of a target located at a bistatic range of 2.6 km and $f_D = 35 \text{ Hz}$ (moving away at 22 km/h).	156
6.15	Two possible configurations for a passive radar to receive the reference and surveillance signals: Top, two physically separated receiving channels; bottom, one single reception chain is used for which signal separation of the two signals happens in software.	157
6.16	Two signals are received: The reference signal in direct LOS from the Tx and the surveillance signal from scene. Random subsampling (in black) in time domain is applied simultaneously in both signals.	158
6.17	Obtaining a range-Doppler image using CS with a synthetically reconstructed reference signal from a subsampled, incomplete measurement.	159
6.18	Obtaining a range-Doppler image using CS and full Nyquist sampling of the reference signal.	160
6.19	Photograph of the measurement setup used for PCL, located at the rooftop of the Royal Military Academy of Belgium.	161
6.20	Map of Brussels (BE) and its NE suburbs showing the Tx, Rx, and a typical climb path of airplanes taking off from BRU airport.	161
6.21	Normalized, sorted amplitudes of a DVB-T acquisition in the original time domain (solid line) and the frequency-domain transformed data (dashed line).	162
6.22	P_d vs. SNR curves for a 50-symbol DVB-T measurement and different DS rates. The dictionary matrix Ψ was populated using: a) measured reference signal; b) synthetically reconstructed reference signal. Left column, $P_{fa} = 10^{-4}$; right column, $P_{fa} = 10^{-2}$.	163
6.23	P_d vs. SNR curves for a 100-symbol DVB-T measurement and different DS rates. The dictionary matrix Ψ was populated using: a) measured reference signal; b) synthetically reconstructed reference signal. Left column, $P_{fa} = 10^{-4}$; right column, $P_{fa} = 10^{-2}$.	164
6.24	Initial (top left), intermediate (top right) and final (bottom) scene reconstructions using the re-weighted ℓ_1 minimization. A low-noise assumption ($\text{SNR} = 24 \text{ dB}$) was used for this experiment, subsampling 0.01 and 100 DVB-T symbols.	166
6.25	Initial (top left), intermediate (top right) and final (bottom) scene reconstructions using the re-weighted ℓ_1 minimization. A low-noise assumption ($\text{SNR} = 0 \text{ dB}$) was used for this experiment, subsampling 0.01 and 100 DVB-T symbols.	167
6.26	P_d vs. SNR results for the re-weighted ℓ_1 minimization: a) Number of symbols 50; b) number symbols 100.	168
6.27	Schematic of the proposed method to integrate scene clutter SI into the CS reconstruction of PCL imagery.	170

List of Tables

2.1	The four possible combinations given the two hypotheses and the binary outcome of the comparator.	26
2.2	Definition of the conditional probabilities for every considered case in Table 2.1.	26
4.1	Evaluation of different NDT techniques for inspecting dielectric composites based on multiple criteria.	76
4.2	Main VNA and antenna parameters involved in the NDT measurement campaign discussed in this chapter.	93
4.3	Conclusions table providing concise guidelines on the exploitability of the three presented CS reconstruction approaches applied to NDT. The evaluations are given for three frequency subsampling rates: conservative (0.5), moderate (0.25) and extreme (0.05).	108
5.1	Metal content, diameter, height and depth of the tested landmines.	112
5.2	Configuration parameters used during the measurement campaign.	127
5.3	Reconstruction position deviation: Percentage of the reconstructions (using PCA and 500 trials) at the correct depth bin, or one or two depth bins away from the ground truth (GT). Several values for k_{xr} , k_f and SNR levels are used for each landmine type. The probabilities of detection for each case are also displayed.	134
5.5	Reconstruction position deviation: Percentage of the reconstructions (using PCA and 500 trials) at the correct depth bin, or one or two depth bins away from the ground truth (GT). Several values for k_{xr} , k_f and SNR levels are used for each landmine type. The probabilities of detection for each case are also displayed.	141
5.6	Reconstruction position deviation: Percentage of the reconstructions (using PCA and 500 trials) at the correct depth bin, or one or two depth bins away from the ground truth (GT). Several values for k_{xr} , k_f and SNR levels are used for each landmine type. The probabilities of detection for each case are also displayed.	142
5.9	Conclusions table providing concise guidelines on the exploitability of GPR and CS on the three types of landmines.	143
6.1	Main parameters of 8-MHz DVB-T channels for the transmissions modes 8K and 2K.	148

List of Abbreviations

ABS	Acrylonitrile Butadiene Styrene
ADC	Analog-to-Digital Converter
AM	Amplitude Modulation
AP	Anti-Personnel
ASI	Adjacent Symbol Interference
AT	Anti-Tank
BP	Basis Pursuit
BPDN	Basis Pursuit Denoising
DS	Direct Subsampling
CA-CFAR	Cell-Averaging Constant False Alarm Rate
CAD	Computer-Aided Design
CAF	Cross Ambiguity Function
CFAR	Constant False Alarm Rate
CNR	Clutter-to-Noise Ratio
CoSAMP	Compressive Sampling Matched Pursuit
CP	Cyclic Prefix
CS	Compressed/Compressive Sensing
CUT	Cell Under Test
CW	Continuous Wave
DAB-T	Digital Audio Broadcast-Terrestrial
DOA	Direction Of Arrival
DUT	Device Under Test
DVB-T	Digital Video Broadcast-Terrestrial
EHF	Extremely High Frequency
ETSI	European Telecommunications Standards Institute
FDM	Frequency-Division Multiplex
FFT	Fast Fourier Transform
FIR	Fast Impulse Response
FM	Frequency Modulation
FMCW	Frequency Modulated Continuous Wave
GO-CFAR	Greatest-Of Constant False Alarm Rate
GPR	Ground Penetrating Radars
GPS	Global Positioning System

GSM	Global System for Mobile communication
HF	High frequency
HPBW	Half-Power Beam Width
IATA	International Air Transport Association
ICI	Intercarrier Interference
IF	Intermediate Frequency
IOP	Illuminator of Opportunity
IR	Inter Channel Interference
LASSO	Least Absolute Shrinkage and Selection Operator
LF	Low Frequency
LFM	Linear Frequency Modulation
LOS	Line-Of-Sight
LTE	Long Term Evolution
MF	Matched Filter
MRI	Magnetic Resonance Imaging
NDT	Non-Destructive Testing
OFDM	Orthogonal Frequency Division Multiplexing
OMP	Orthogonal Matching Pursuit
OS-CFAR	Ordered Statistic Constant False Alarm Rate
PCA	Principal Component Analysis
PCL	Passive Coherent Location
PRI	Pulse Repetition Interval
QAM	Quadrature Amplitude Modulation
QPSK	Quadrature Phase Shift Keying
RCS	Radar Cross-Section
RF	Radio Frequency
RIP	Restricted Isometry Property
ROMP	Regularized Orthogonal Matching Pursuit
Rx	Receiver
SAR	Synthetic Aperture Radar
SDR	Software Defined Radio
SFCW	Stepped Frequency Continuous Wave
SHF	Super High Frequency
SI	Side Information
SNR	Signal-to-Noise Ratio
SO-CFAR	Smallest Of Constant False Alarm Rate
SOMP	Simultaneous Orthogonal Matching Pursuit
StOMP	Stagewise Orthogonal Matching Pursuit
TDOA	Time Different Of Arrival
TEM	Transverse Electric and Magnetic
TM-CFAR	Trimmed Mean Constant False Alarm Rate
TWI	Through-the-Wall Imaging
Tx	Transmitter
UHF	Ultra High Frequency

USRP	Universal Software Radio Peripheral
UWB	Ultra Wideband
VCO	Voltage-Controlled Oscillator
VHF	Very High Frequency
VLB	Very Low Frequency
VNA	Vector Network Analyzer
WiFi	Wireless Fidelity

List of Symbols

c	speed of light
c_0	speed of light in vacuum or air
f	frequency
f_s	sampling frequency
f_{max}	maximum frequency
f_c	carrier or center frequency
f_n	vector of tone frequencies
f_0	tone or center frequency
k_{os}	Oversampling factor
$h(t)$	impulse response
$n(t)$	thermal noise contribution to the signal
n_{RC}	number of reference cells
$r(k)$	range-compressed signal
$r_n(k)$	range-compressed contribution of $n(t)$
$r_s(k)$	range-compressed contribution of $s(t)$
$s(t)$	generic signal in the time domain
$s_b(t)$	beat signal or demodulated signal
\hat{x}	reconstructed approximation of x
x	vectorized observation of $x(t)$
$x(t)$	received signal
$s(t)$	transmitted signal
t	time domain
v_c	velocity of the clutter
v_t	velocity of the target
v_R	velocity of the receiver
v_T	velocity of the transmitter
y	incomplete observation of x
B	bandwidth
K	atoms in the dictionary matrix Ψ
G_r	gain of the receiving antenna
G_t	gain of the transmitting antenna
L	baseline length

L_p	propagation loss
N	length of x
M	length of the subsampled measurement y
P_{fa}	probability of false alarm
P_n	average noise power
P_r	received power
P_t	transmitted power
$P1$	port 1 of a VNA
$P2$	port 2 of a VNA
R	range of one target
R_{max}	maximum range
R_B	bistatic range
R_C	clutter-to-receiver range
R_D	direct path range
R_T	transmitter-to-target range
R_R	target-to-receiver range
S	non-zero coefficients, level of sparsity
S_{11}	S-parameters, reflection coefficients
T_h	threshold
T_p	pulse duration
T_C	amplitude of the cell under test
α	amplitude of a detected signal
α_n	amplitude of the n -th detected signal
β	bistatic angle
δr	range resolution
$\gamma_s(\eta)$	ambiguity function
μ	frequency slope
λ	wavelength
λ_t	trade-off parameter in BPDN
λ_0	wavelength in vacuum
ϕ	phase
Φ	observation or sensing matrix
ϕ_0	initial phase
τ	time delay
τ_n	round-trip time delay of the n -th target
τ_R	round-trip time delay for a target at range R
σ	scene reflectivity function
σ_c	clutter reflectivity
σ_m	conductivity of a material
σ_t	target reflectivity
Δf	frequency step size
Δ_r	range bin size
Δ_{xr}	cross-range bin size
\mathcal{H}_0	null hypothesis

\mathcal{H}_1	alternative hypothesis
ℓ_0	pseudo norm
ℓ_1	ℓ_1 norm
ℓ_2	ℓ_2 norm
\mathcal{D}	generic representation domain
\mathcal{H}_0	null hypothesis
\mathcal{H}_1	alternative hypothesis

Chapter 1

Introduction

1.1 Motivation

Radar target ranging, positioning or imagery have been widely studied for which countless applications and variations are available for exploitation. Although, the general perception in the civilian and military worlds is that radar is a mature technique with formidable results, a new way of understanding data sensing has exploded, especially since the last decade after the initial skepticism and reluctance showed by conventional sensors developers and firms. The concept of randomly sampling a signal on purpose for farther reconstruction, as described by compressed sensing (CS) [14], has attracted the research community since it defies the hitherto strictly respected Shannon-Nyquist sampling criterion [15]. Although countless research groups have joined the path to making CS as fast, efficient and accurate as possible, whether it is by adding or modifying large-scale concepts to very specific details, there seems to be a lack of connection between concrete applications and what CS can do for them. New research on CS concepts can be easily found every other month with ground-breaking algorithms outperforming the previous ones. This work is based on the believe that consumers of CS from the civilian and military environments need to have access to a straightforward performance analysis and implementation possibilities for an application of their interest. Beyond providing performance figures, some of the main questions that arise when a new sampling paradigm as CS appears are:

- How can CS be implemented in an existing sensor that uses conventional sampling?
- What would the economic motivation be for developing new sensors operating according to random sampling?
- Are CS reconstructions ‘good’ enough to compete against conventional high-resolution imagery?

- And, similarly, are there trade-offs between conventional and CS-based sensors?
- And if the answer is positive, can CS be applied equally to civilian as well as to military applications despite such trade-offs?

Being able to answer to those questions should be possible before implementing a CS receiver in hardware. Although this dissertation does not aim to directly and systematically address such questions, answers and guidelines will be derived from the proposed sampling schemes and performance analyses.

Regarding the implementation of CS in real sensors, it is easy to imagine that reducing the amount of data collected is an interesting option in every frequency band although it becomes of special interest for those sensors using large bandwidths or continuous data acquisition requiring costly processing power. Such large bandwidths must be accommodated in the higher bands of the radio-electric spectrum for spectrum availability and technical restrictions and, therefore, that is as well where the sensors presented in this work will be operating.

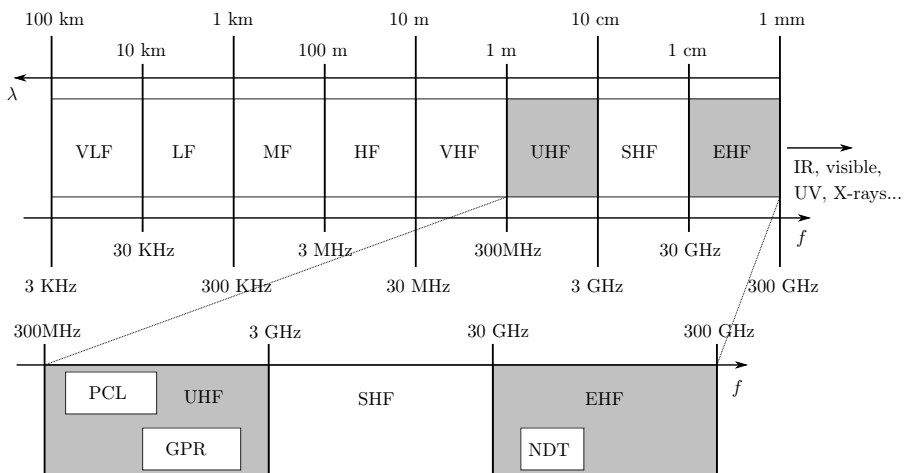


Figure 1.1: The radio-electric spectrum. The applications explored in this work are shown in their corresponding frequency band.

Figure 1.1 shows the radio-electric spectrum from 3 kHz to 300 GHz, which includes the three applications discussed in this dissertation: Non-destructive testing (NDT), ground penetrating radars (GPR), and passive coherent location (PCL). All three are already developed applications (with diverse levels of maturity and establishment) both for civilian and military uses.

1.2 Objectives of the work

The main objectives pursued in this thesis are related to the possibility that CS is offering in order to obtain comparable performances for conventional sensors used in a variety of applications. The objectives can be detailed as:

- Propose different-enough applications that may be adapted to CS operation.
- Propose subsampling schemes to reduce the amount of data collected or acquisition times to a minimum.
- Model CS-based sensors in software and perform thorough performance analyses for each sensor.
- Aim at obtaining simplified imagery for better interpretation by a trained operator, avoiding distractions by non-interesting features and without diminishing the imagery quality.
- Find subsampling limits to suggest potential hardware simplification since data sampling requirements may be greatly relaxed.

1.3 Thesis organization

This thesis is organized in six farther chapters:

- Chapter 2 will explain the fundamentals radar concepts required to understand the application chapters in which radar-based sensors are used. The signal models of pulsed on-off keying and continuous wave radars are also provided. Moreover, stepped-frequency radars and radars based on a vector network analyzer to perform frequency sweeping are described. Finally, more complex radar concepts are described such as synthetic aperture radar, which increases the radar's cross-range resolution by exploiting the motion of the sensor; and bistatic or multistatic radars, which enable target imagery without requiring direct access to a radar transmitter.
- Chapter 3 will introduce the concept of conventional signal sampling and the new sampling paradigm, compressed sensing, which will provide a general overview of the mathematical aspects supporting it, what the problem statement is from a mathematical approach and the most usual methods for finding a solution to the problem, such as the ℓ_0 or ℓ_1 minimization, basis pursuit denoising, or the greedy algorithm orthogonal matching pursuit. Additionally, reaching a solution to a CS minimization problem requires satisfying some conditions such as presenting sparsity in a given domain and validating the restricted isometry property. Finally, several sparsity enhancement methods are proposed based on data transformations, using training dictionaries or an iterative ℓ_1 -based minimization. Adding side information or a-priori information describing partly the scene or data to be recovered can help in reaching a sparser solution.

- In Chapter 4 the first application is proposed: non-destructive testing. After a short state-of-the-art review, some of the typical composite materials and structures are introduced as well as common failure modes found in the industry. Sensors using focusing mirrors are described along with its limitations and how the wavefronts they generate interact with the different media during measurements. Finally, suggestions on how to implement CS on this type of sensors are proposed, as well as providing a detailed analysis of the obtained performances.
- Chapter 5 deals with ground penetrating radar as a prospective CS application. A state-of-the-art revision is followed by a description of the most typical targets (landmines) in this application and how the waves interact with the ground. An intrinsic antenna modeling is described to remove the effects of the air-to-soil reflections and reverberations inside the antennas. How to adapt the sensor to the CS sampling needs is also discussed in the chapter which, finally, reproduces the results of the performed tests in terms of probabilities of detection.
- As for Chapter 6, the common illuminators of opportunity employed in passive coherent location are described in a state-of-the-art review. Then, the fundamental ideas behind digital video broadcast-terrestrial transmissions and their signal modeling are presented. Aspects related to imagery are described such as the Doppler effect. Finally, the proposed sensor is adapted to CS which leads to a performance analysis of the direct application of CS but also to more advanced ideas such as the iterative re-weighted ℓ_1 minimization or side information.
- Finally, Chapter 7 summarizes all the results in displayed in Chapters 4 to 6, and draws conclusions and concise and generic guidelines for applying CS on new applications, both civilian- and military-oriented.

Chapter 2

Radar sensors

In this chapter we will explain fundamental radar concepts such as range and cross-range resolutions, pulse compression, the matched filter and the ambiguity function, target detection theory or the constant false alarm rate detector. All these concepts are required to completely understand the following three application chapters in which radar concepts and radar-like sensors are used in different manners. The signal model of the typical radar waveforms and their respective performances are evaluated thanks to the ambiguity function and briefly discussed, starting by a simple pulsed on-off keying radar to the more recent continuous wave radars. Two continuous wave radars presenting very simple, cost-effective implementation are also introduced: One based on transmitting stepped-frequency signals in the form of a train of discrete tones to emulate a signal linearly modulated in frequency; or a second one using a vector network analyzer to perform an identical operation via a frequency sweeping. The last part of the chapter briefly introduces two concepts derived from radar theory: synthetic aperture radars and bistatic or multistatic radars. In the former, creating a synthetic aperture allows increasing the theoretical cross-range or spatial resolution defined by the antenna by coherently integrating the received echoes from a same target and for different radar positions. Thanks to this echo integration, synthetically improved spatial resolution are obtained, enabling high-resolution imagery with a relatively low complexity and no added hardware cost. The latter concept considers that the transmitting and receiving chains of a radar do not need to be collocated in order to locate targets. In this work, the bistatic radars are based on the exploitation of illuminators of opportunity (IOP) by passive radars. Using IOP creates diversity in exploiting open-access signals and reduces significantly operation and deployment costs since a powerful transmitter is no longer required, although signal synchronization becomes a delicate problem to be solved for producing usable imagery.

2.1 Introduction and applications

Radars (acronym derived from radio detection and ranging) have been intensively used since the 1940's in multiple areas and were, as reported by US Lt. Col. John H. DeWitt Jr. [16], once defined as:

"The art of detecting by means of radio echoes the presence of objects, determining their direction and range, recognizing their character, and employing the data thus obtained in the performance of military action."

The idea behind radars is substantiated on the now obvious fact that objects can reflect electromagnetic waves, discovered by Hertz around 1888 [17, 18] and supported on the previous works by Maxwell and his omnipresent, game-changing equations defining electromagnetic radiation [19].

Among other object characteristics, radars are used to extract the distance (or range) of an object by calculating the time difference of arrival (TDOA) a known electromagnetic signal takes to go to that object and back to the radar, just as echolocation [20] is used in nature [21]. The very simple concept behind radars, although the hardware and operation may be difficult to understand, makes these systems a technology widely known to most of the society. Initially conceived for military purposes, the radar then became also of interest for civilian applications as the same DeWitt said in 1946, not long after the World War II finished:

"Now that war has ended its great potentialities will undoubtedly be directed with equal effectiveness to many peacetime tasks."

Although it is still mostly identified as a military technology by the general public, it has provided outstanding results in every area it has been used in and its benefits are perceived as being multiple and remarkable. The relative ease of implementation of radars thanks to their wireless operation limiting deployment costs, the possibility of long- or short-distance operation in all kinds of weathers and inside many materials, and the vast experience gained since their invention, make radars an attractive and solid option for current and prospective technology developments.

Over the years, several types of radars have been developed to suit the needs of the growing list of applications. Figure 2.1 gives a very unadorned categorization of a radar which can be monostatic or bistatic, and the generalization of the latter, the multistatic radar. If transmitter and receiver are collocated, that is, they roughly share the same location —although in practice there is some room for concessions— the radar is said to be monostatic. In any other case, we should be referring to bistatic radars if transmitter and receiver are physically far from each other or multistatic radar if several receivers or several transmitters are used or both. Non-collocated transmitters, in turn, can be cooperative if the receiver has direct, exact and unrestricted access

to the original signal used in transmissions, or opportunistic if the receiver must gain access to it or estimate it by its own means.

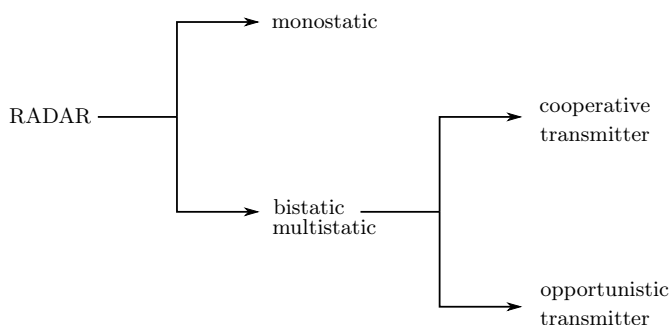


Figure 2.1: Classic classification of radars based on their configuration and the transmitter type.

Some of the current applications that are being exploited and are in a mature stage can be subdivided into the following suggested categories.

- **Air surveillance:** Aircraft and missile airspace surveillance were possibly the two applications that led to conceiving and developing radars as we know them [22]. Air navigation [23] also has several applications such as ground avoidance, altimeters, or weather radars [24] (also used for ships) based on Rayleigh scattering.
- **Maritime surveillance [25]:** radars are principally used in navigation for shore and vessel location.
- **Ground surveillance:** Law enforcement uses radars for controlling the velocity of cars which produce a Doppler shift in the received signal [26]. Radars in the automotive world have recently exploded with applications that include proximity and anti-collision sensors, or autonomous cruise control systems [27]. Simpler radars are also used for sensing and tracking human activities at home or common spaces [28].
- **Space- and air-borne:** a vast variety of applications are available such as wind scatterometers [29], remote sensing for accurate mapping the ground [30], ice regions [31], or soil moisture [32] applications.
- **Medicine:** cardiac, body [33] and sleep monitoring [34].
- **Other derived technologies:** NDT [35], GPR in geological sites [36], depth measurement [37], TWI [38] and detection and rescue of victims [39].

These applications are just a glimpse of what radars can offer and, as it often happens when technologies become mature, more and more applications are being developed for very specific goals.

The remaining of this chapter is devoted to describing the basic radar concepts as well as more advanced aspects worth considering.

2.2 Radar fundamentals

Radars perform target range determination —or simply ranging— by transmitting a known signal $s(t)$ at a given time instant used as a time reference and extracting the time delay until any echo received from a target in the scene is detected at the receiver [40], known as received signal $x(t)$. Radars can also estimate the reflectivity of the detected targets by measuring the power of the received echo, making possible target size approximation. If the radar has a range resolution several times smaller than the size of a target, i.e., several echoes are scattered back from different parts of a target, the shape and size of the target can be inferred. For a moving target, the received echoes will present a Doppler shift, a variation in the frequency proportional to the target velocity. In Figure 2.2 a generic radar, comprising a transmitting (Tx) and a receiving (Rx) block connected to an antenna by means of a duplexer, illuminates a given target with reflectivity σ_t located at distance R . Considering an ideal situation, any backscattered energy from the target will be detected by the radar receiver for farther information extraction.

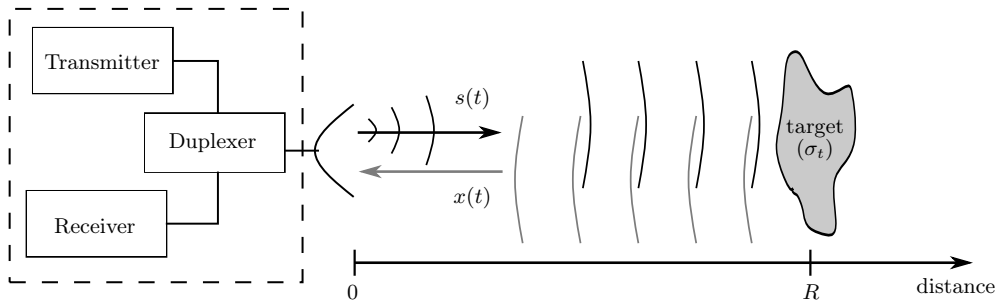


Figure 2.2: Schematic of a typical radar configuration. A transmitted wave is reflected by a target located at range R in the scene. The echoes $x(t)$ are processed and the range of the target is extracted.

A time mark must be generally employed to create a time reference for extracting the distance to a target. This is usually done by including a modulation in the transmitted signal which can be unequivocally identified or by using pulsed signals with listening periods. Regardless of the method chosen, any echo from a target detected by the receiver will be a time-delayed version of the transmitted signal by the round-trip time τ_R , that is, the time the transmitted signal takes to fulfill the radar-target-radar or $2R$ path as in:

$$x(t) = \alpha s(t - \tau_R) + n(t), \quad (2.1)$$

with α the amplitude of the detected signal which depends on the transmitted power, the target's reflectivity, propagation losses and weather conditions (e.g., clouds or fog); and $n(t)$ the thermal

noise and clutter at the receiver. Assuming that the signals are propagating through air or free space, τ_R is directly computed as:

$$\tau_R = \frac{2R}{c_0}, \quad (2.2)$$

with c_0 the speed of light in vacuum.

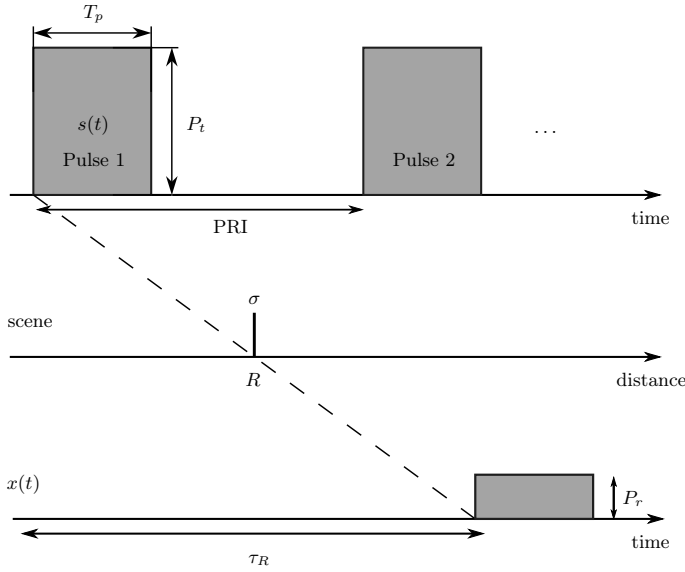


Figure 2.3: Schematic of a typical radar configuration. A transmitted wave is reflected by a target located at range R in the scene. The echoes are processed and the range of the target is extracted.

In Figure 2.3, a pulse of duration T_p with arbitrary modulation is radiated by a radar with power P_t . The signal is transmitted periodically following a given pulse repetition interval (PRI). A target at a distance R intercepts the transmitted signal and reflects it back to the radar. It is common jargon to say that the target has been interrogated by the radar. Finally, the radar receiver detects $x(t)$ which includes the echo of the target with received power P_r and a certain time delay τ_R with respect to the time when $s(t)$ was transmitted.

The distance up to which a pulsed radar can determine a target position unambiguously is closely related to the PRI. Let us define the maximum range or non-ambiguous range as:

$$R_{max} = \frac{c_0 PRI}{2}, \quad (2.3)$$

which, recalling (2.2), can be interpreted as the range for a target located at a round-trip time $\tau_R = PRI$. Any target located farther than R_{max} is detected as if it was interrogated by the

next pulse, creating an ambiguous result or ghost target. Several techniques exist successfully facing this problem although they will not be discussed in this work.

The ability of a radar to accurately locate and discern between two targets is known as range resolution, which is defined as:

$$\Delta R = \frac{c_0 T_P}{2} \approx \frac{c_0}{2B}, \quad (2.4)$$

indicating that the shorter the pulse is, the finer the range resolution becomes. These two definitions are valid for pulsed, not intra-pulse modulated radars, since only in this case the approximation for the bandwidth $B \approx 1/T_P$ holds. For any other type of radar, we will define range resolution as:

$$\Delta R = \frac{c_0}{2B}. \quad (2.5)$$

In pulsed radars, a minimum detectable range must also be considered since during transmission the receiver is isolated from the antenna by the duplexer and, therefore, no detection can be performed. This blind time will be equal to the time during which the pulse is being transmitted T_p and the switching reaction time of the duplexer t_S :

$$R_{min} = \frac{c_0 (T_P + t_S)}{2}, \quad (2.6)$$

The power of the received signal P_r is defined by the characteristics of the radar, the propagation losses during the round-trip path, the media transitions, as well as the reflectivity of the target σ_t or the radar cross section (RCS). P_r is commonly written following what is known as the radar equation [23], or:

$$P_r = \frac{P_t G_t G_r \lambda_0^2}{(4\pi)^3 R^4} \sigma_t = \frac{P_t G^2 \lambda_0^2}{(4\pi)^3 R^4} \sigma_t, \quad (2.7)$$

where P_t is the transmitted power by the radar, G_t and G_r are the transmitting and receiving antenna gains, respectively, G the product of both gains, and $\lambda_0 = c_0/f$ is the signal's wavelength in free space. From the radar equation we can also extract the propagation losses in free space:

$$L_p = \left(\frac{\lambda_0}{4\pi R} \right)^2. \quad (2.8)$$

Every antenna is defined by its radiation pattern or diagram which gives information about the radiation level for every direction departing from the antenna phase center. Consequently, the gain G cannot be assumed to be of constant value and, therefore, a gain varying with the angle

must be redefined as $G(\theta, \phi)$, with θ and ϕ the angles with respect to the horizontal and vertical axes, respectively (see Figure 2.4).

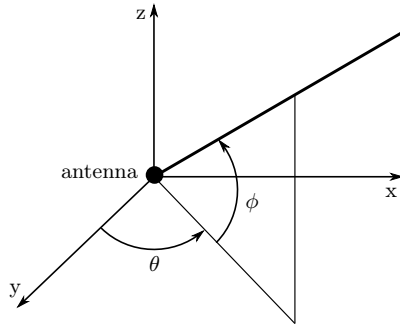


Figure 2.4: Angles θ and ϕ describe the radiation direction of an antenna.

Similarly, the RCS also responds differently to waves depending on their incident direction into the target and, therefore, the use of $\sigma_t(\theta, \phi)$ is preferred. The radar equation in (2.7) must be rewritten as:

$$P_r(\theta, \phi) = \frac{P_t G^2(\theta, \phi) \lambda_0^2}{(4\pi)^3 R^4} \sigma_t(\theta, \phi). \quad (2.9)$$

In more complex scenes it is very likely that an arbitrary number of targets N_T may be illuminated by the radar, thus modifying (2.1) accordingly to:

$$x(t) = \sum_n^{N_T} \alpha_n s(t - \tau_{R,n}) + n(t), \quad (2.10)$$

where α_n represents the amplitude of the received signal corresponding to the n -th target.

A variation of Figure 2.3 is shown in Figure 2.5 in which a radar illuminates two targets with reflectivities $\sigma_{t,1}$ and $\sigma_{t,2}$, located at distances R_1 and R_2 from the radar generating time-delays of $\tau_{R,1}$ and $\tau_{R,2}$, respectively.

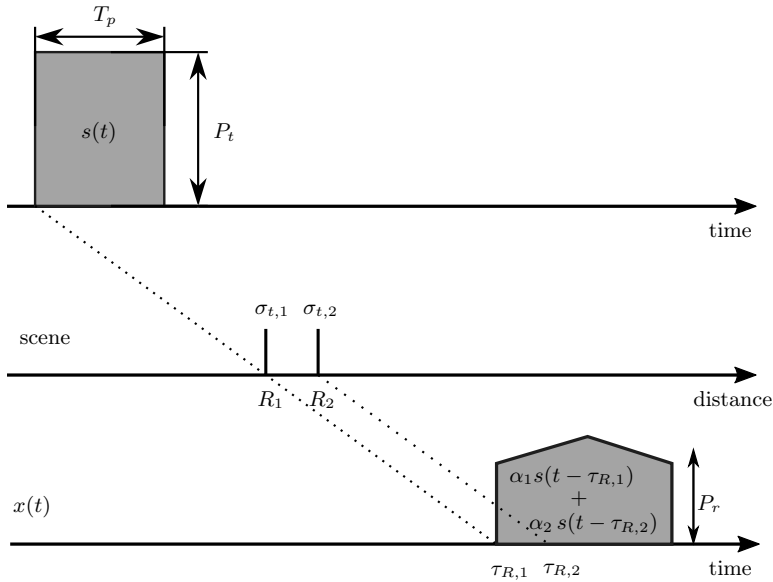


Figure 2.5: Schematic of a typical radar configuration. A transmitted wave is reflected by two targets located at ranges R_1 and R_2 in the scene. The echoes are processed and the ranges of the targets are extracted.

The received signal is described as:

$$x(t) = \alpha_1 s(t - \tau_{R,1}) + \alpha_2 s(t - \tau_{R,2}) + n(t), \quad (2.11)$$

Although two echoes are received, their exact location may not be easily derived automatically or even by a trained operator simply from direct exploration of $x(t)$ if their signals overlap in time or SNR levels are low. In combination with adequate hardware requirements, the very well-known detection theory optimally solves the problem of target detection and separation.

2.3 Other types of radars

In addition to the pulsed radar, which has already been introduced in the previous section, other types of radars can be found in nowadays applications. Some of them will be reviewed in this section, although the presented list of existing radar types is far from being exhaustive.

2.3.1 Continuous-wave radars

A continuous-wave (CW) radar (see Figure 2.6) is a radar that transmits a single, non-modulated frequency f_0 in an uninterrupted way. This type of radars has a very poor range resolution

capability, which is limited by the minimum observable phase variation $\Delta\phi_{min}$ —closely related to the sampling frequency—, and is typically used only for moving targets by exploiting the Doppler-frequency shift it introduces in the reflected echoes, hence its alternative name: the Doppler radar.

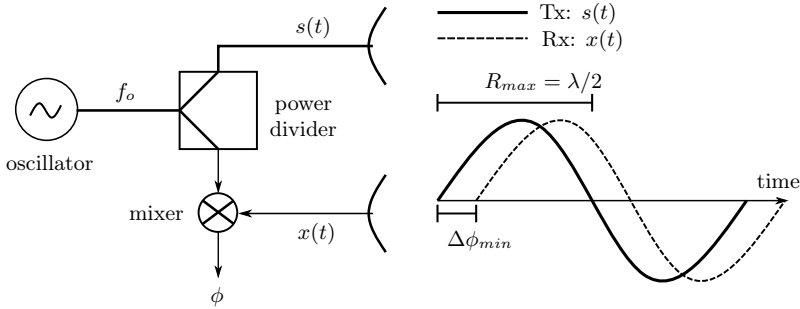


Figure 2.6: Simplified conceptual schematic of a CW radar.

For any CW radar, the transmitted signal $s(t)$, without considering the transmitted amplitude, can be defined as:

$$s(t) = \exp(j2\pi f_0 t), \quad (2.12)$$

whereas the received signal in a noiseless situation is a version of $s(t)$ delayed by the round-trip time to the target τ_R and proportional to the propagation losses and the amount of backscattered energy:

$$x(t) \propto s(t - \tau_R) = \exp(j2\pi f_0 (t - \tau_R)). \quad (2.13)$$

For simplicity, the signal amplitude in reception is also disregarded. The previous expression can be redefined as:

$$x(t) \propto \exp(j2\pi f_0 t - j\phi(\tau_R)), \quad (2.14)$$

if we consider that the time-delay due to τ_R is a phase contribution, or $\phi(\tau_R) = 2\pi f_0 \tau_R$. The homodyne detection or demodulation of the received signal allows extracting phase information in $x(t)$, namely the phase delay introduced by the round-trip time to a target at range R . The demodulation is performed as:

$$s_b(t) = s(t) \cdot x^*(t), \quad (2.15)$$

which, for the CW case, can be reformulated as follows:

$$s_b(t) = \exp(j2\pi f_0 t) \cdot \exp(-j2\pi f_0 t + j\phi(\tau_R)) = \exp(j\phi(\tau_R)). \quad (2.16)$$

The phase of $s_b(t)$ only depends on τ_R and is expressed as:

$$\phi(\tau_R) = 2\pi f_0 \tau_R, \quad (2.17)$$

or using the definition of $\tau_R = 2R/c_0$, ϕ can be rewritten in function of the range R :

$$\phi(R) = \frac{2\pi f_0 2R}{c_0} = \frac{4\pi R}{\lambda_0}. \quad (2.18)$$

The range of a target given the phase shift detected in s_b can be easily computed as:

$$R = \phi \frac{\lambda_0}{4\pi}, \quad (2.19)$$

which is maximum when $\phi = 2\pi$:

$$R_{max} = 2\pi \frac{\lambda_0}{4\pi} = \frac{\lambda_0}{2}, \quad (2.20)$$

and is known to be the maximum distance that the CW radar can detect a target non-ambiguously and includes negative ranges. Hence, the maximum distance is limited by $\lambda_0/4$. Due to the periodic nature of the waveform used in CW radars and the lack of modulation, any phase shift produced by $R > R_{max}$, would result in ambiguous results or $R = \text{mod}(R, R_{max})$, which derives from $\phi = \text{mod}(\phi, \pi)$.

The range resolution ΔR in CW radars is driven by the oversampling factor k_{osf} applied to the sampling frequency f_s , as expressed in:

$$\Delta R = \frac{c_0}{2f_s} = \frac{c_0}{2k_{osf}f_0}. \quad (2.21)$$

According to (2.20) and (2.21), a CW radar transmitting a 10-MHz tone with an oversampling factor of 8 would be able to perform ranging on a target at maximum of 7.5 m and with a range resolution of 1.88 m. These radar characteristics are insufficient for performing target detection and ranging at medium distance.

Finally, assuming that the CW radar is static for the sake of simplicity, the radial velocity of a target can be derived directly from the phase information:

$$\frac{d}{dt}\phi(R) = -\frac{4\pi}{\lambda_0} \frac{d}{dt}R = -\frac{4\pi V_r}{\lambda_0}, \quad (2.22)$$

with V_r the radial velocity, yielding the Doppler frequency of the target:

$$|f_D| = \frac{1}{2\pi} \frac{d}{dt} \phi(R) = \frac{2V_r}{\lambda_0}. \quad (2.23)$$

2.3.2 Frequency-Modulated Continuous-Wave radars

In contrast to CW radars, frequency-modulated continuous-wave (FMCW) radars transmit signals known as chirps which are typically linearly modulated in frequency, that is, their frequency varies (increasing for up-chirps, decreasing for down-chirps) at a constant frequency variation rate, sweeping its operational bandwidth for a limited pulse duration.

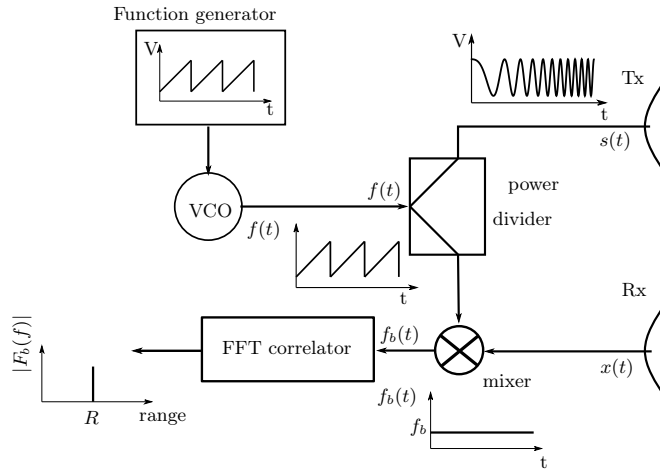


Figure 2.7: Simplified conceptual schematic of a FMCW radar.

The generation of FMCW signals is schematically displayed in Figure 2.7. A function generator creates a sawtooth waveform with a given T_p and chirp rate μ which drives a local voltage-controlled oscillator (VCO). The output of the VCO is a signal following a linear frequency modulation (LFM) which is radiated by the transmitting antenna. Other intermediate stages such as power or low-noise amplification, filtering, and signal upconversion from intermediate to radio frequencies —or downconversion in reception— are avoided for simplicity.

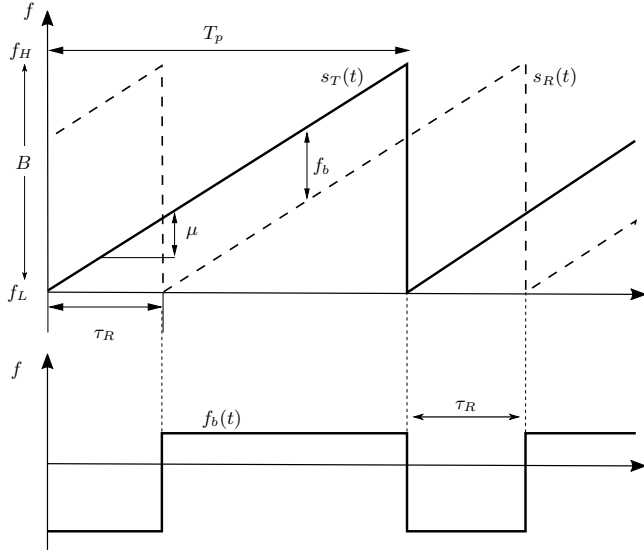


Figure 2.8: A sawtooth FMCW signal: Top, frequency evolution in time of a transmitted FMCW signal (solid line) and a received replica delayed τ_r (dashed line); bottom, frequency evolution in time of the beat frequency $f_b(t)$.

In Figure 2.8, a sawtooth-like function describes the frequency evolution in time of an FMCW radar in an up-chirp configuration. The frequency output generated by the VCO covers the whole bandwidth B from f_L to f_H following the frequency sweeping rate, which is defined as $\mu = B/T_P$. The frequency evolution of a signal with a LFM with respect to time for $0 \leq t \leq T_p$ is:

$$f_{LFM}(t) = f_L + \mu t, \quad (2.24)$$

which is, indeed, a linear frequency variation with f_L as the lowest frequency of B . The phase of an LFM waveform is commonly defined as:

$$\phi_{LFM}(t) = 2\pi \int_0^t f_{LFM}(t) dt = 2\pi(\phi_0 + f_L t + \frac{\mu}{2} t^2), \quad (2.25)$$

with ϕ_0 is the initial phase of the oscillator which is canceled out in the demodulation stage. Therefore, the transmitted signal with amplitude A_0 will present a quadratic phase evolution:

$$s(t) = A_0 \exp(j\phi_{LFM}(t)) = \exp(j2\pi[\phi_0 + f_L t + \frac{\mu}{2} t^2]), \quad (2.26)$$

for which, to simplify the notation, A_0 is assumed to be equal to the unity. Due to the nature of these continuous chirped signals, less power-demanding hardware can be used to generate a

significantly wide bandwidth, thus increasing range resolution which, exactly like in the pulsed case, is defined as in (2.5), as well as the unambiguous range in (2.6). Figure 2.9 displays one period of a typical up-chirp LFM signal with $\phi_0 = 0$ rad as mathematically displayed in (2.26), which is typically used for single target or static scenes.

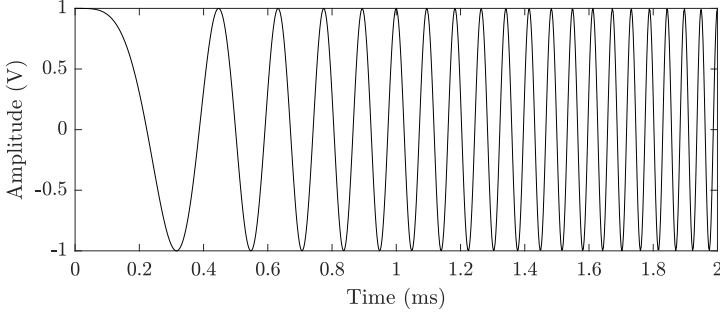


Figure 2.9: A linearly frequency modulated continuous wave waveform, known as chirp, linearly increases its frequency to sweep its bandwidth in one period.

The detection of the received signals is performed by homodyne detection in FMCW systems, as defined in (2.15). The received signal $x(t)$ for one target at range R is as follows:

$$x(t) \propto s(t - \tau_R) = \exp(j2\pi[\phi_0 + f_L(t - \tau_R) + \frac{\mu}{2}(t - \tau_R)^2]), \quad (2.27)$$

and, after detection by mixing $x(t)$ with $s(t)$, the beat signal is comprised by three terms:

$$s_b(t) \propto \exp(j2\pi [f_L\tau_R + \mu\tau_R t - \frac{\mu}{2}\tau_R^2]), \quad (2.28)$$

and defining the beat frequency $f_b = \mu\tau_R$, the expression becomes:

$$s_b(t) \propto \exp\left(-j\frac{4\pi R}{\lambda_0}\right) \cdot \exp(j2\pi f_b t) \cdot \exp(-j\pi f_b \tau_R). \quad (2.29)$$

The first term in (2.29) is a constant phase difference produced by the time delay between the reference signal and the received echo from the target at range R , the second one is a sinusoidal proportional to the range of the target and the third one is the residual video phase.

The baseband or intermediate frequency waveform $s_b(t)$ presents a much lower bandwidth $B_{bb} \ll B$ than the original FMCW signal and is limited by the highest tone possible f_b^{max} corresponding to the maximum range expected, including negative ranges:

$$B_{bb} = f_b^{max} = \mu \tau_r^{max} = \mu \frac{2R_{max}}{c_0}. \quad (2.30)$$

As a simple illustrative case study, let us suppose that a FMCW radar with a desired $\Delta R = 1.5$ m would require $B = 100$ MHz in RF. If the maximum range at which targets are expected is $R_{max} = 6$ km and the IF sampling frequency is limited to $f_s = 1$ MS/s by design, the maximum beat frequency expected is $f_b^{max} \leq f_s/2 = 500$ kHz. The required period duration to satisfy these design conditions is $T_p = 8$ ms. Under this configuration, the bandwidth from RF to IF is reduced by a factor 200.

A FMCW radar presents several benefits such as:

- Its continuous operation enables the possibility of low transmitted energy at the expense of longer integration times. A low transmitted energy implies that the maximum range for a same sensor sensitivity will be much more limited than in pulsed radars but it also minimizes the risk of being detected by a foe [41].
- Moreover, not requiring high peaks of transmitted power simplifies the hardware since there is no risk of damaging the receiver with strong power leakages from the transmitter. Simple circulators may be enough to protect the receiving stage. Simultaneous signal transmission and reception is possible using one single antenna, farther reducing the physical dimension and cost of the radar.
- Simultaneous operation eliminates the restriction of minimum observable distance since no guard periods are required. This, as well as the low emitted power levels, is why FMCW are widely used for very short-distance radar measurements involving objects (NDT applications) but also humans since radiation within healthy limits still produce exploitable results.
- The waveform generation is simple and it allows extremely wide bandwidths, providing very good range resolutions.
- The FMCW waveform presents a sinus-cardinal-like ambiguity function (see Section 2.4.5 for farther details) with relatively low secondary lobes which can be farther reduced in reception by applying windowing.
- Very easy target detection can be performed using a Fourier transform correlator to transform beat frequencies into target providing range and reflectivity information at once.
- FMCW can also determine the speed of a target by using a triangular function to generate $f_{LFM}(t)$ and extracting the Doppler frequency shift produced by the difference in speed between the target and the radar [42]. To do so, two beat frequencies are extract: one in the up-chirp and a second one in the down-chirp part of the period.

Some disadvantages are also to be expected:

- The lower transmitted energy than in pulsed radars yields much shorter ranges, according to the radar equation in (2.7).

- A very wide bandwidth presents higher risk of suffering from external interfering transmissions in the bandwidth of operation, whether these transmissions are unintentional interferences or directly jammers.
- During a transmission, the already weak FMCW signals reflected from a target may be masked by power leakage from the transmitter into the receiver.

2.3.3 Stepped-frequency radars

An FMCW waveform can be synthetically generated by means of a stepped-frequency continuous-wave radar (SFCW) which generates a sequence of N_f pulses of unmodulated CW at discrete frequencies f_n for a pulse duration T_p . The frequency in each pulse varies with a step size Δf in order to cover the system bandwidth $B = (N_f - 1)\Delta f$. The expression of f_n is:

$$f_n = f_1 + (n - 1)\Delta f, \quad (2.31)$$

with n the n -th discrete frequency in the bandwidth. In Figure 2.10, the SFCW signal generation in frequency and time is described.

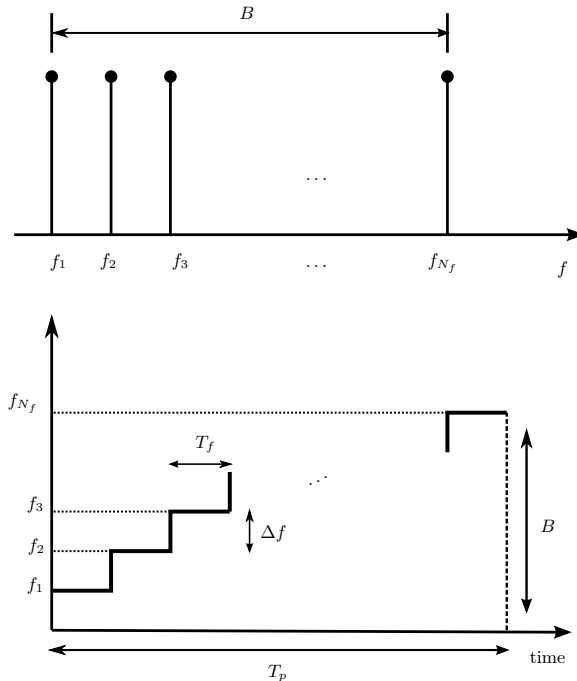


Figure 2.10: Generation of an SFCW signal. Top, sequence of individual frequencies or tones generated and covering a given bandwidth B . Bottom, the time evolution of the generated signal frequency. Each tone is transmitted for a fixed time interval T_f , completing the total duration T_p of the frequency sweeping.

This generation method is simple to implement with tunable digital synthesizers or vector network analyzers (VNA), thus enabling affordable high-resolution, ultra-wideband (UWB) radar systems. A general expression for a transmitted baseband signal using SFCW is:

$$s(t) = \sum_{n=1}^{N_f} \text{rect}\left(\frac{t - (n-1)T_f}{T_f}\right) \exp(j2\pi f_n t), \quad (2.32)$$

with $\text{rect}(\cdot)$ the rectangle function and n indicates the n -th discrete frequency tone. The plot in Figure 2.11 shows the time-domain evolution of an SFCW signal with an initial frequency $f_1 = 2$ Hz and a frequency step size $\Delta f = 2$ Hz.

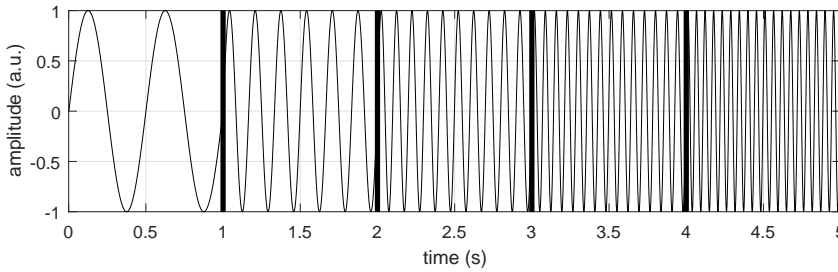


Figure 2.11: Time evolution of the generated SFCW signal. A sequence of tones at increasing frequencies is radiated, closely emulating the FMCW waveform.

The resolution in distance of SFCW radars can be derived from (2.5) as:

$$\Delta R = \frac{c_0}{2B} = \frac{c_0}{2(N-1)\Delta f}, \quad (2.33)$$

whereas the maximum unambiguous range is, including positive and negative ranges:

$$R_{max} = \frac{c_0}{2\Delta f}. \quad (2.34)$$

The detection of SFCW signals is performed with homodyne detection, in the same manner as the FMCW radar.

Some of the advantages of using SFCW signal synthesis are:

- Very easy implementation due to the discrete frequency generation approach.
- Bandwidth limitation is a less of a limiting factor than in FMCW and especially pulsed radars. In practice, modern UWB systems are implemented using SFCW.

- The bandwidth is highly tunable thanks to digital synthesizers, this enables the possibility of creating gaps in the bandwidth to avoid interfering signals or jammers.
- The output power for every discrete frequency in the form of a CW can be controlled, hence, having more control on the generated waveform.
- As in FMCW, a Fourier transform correlator can be used for detection.

The disadvantages of using SFCW signal synthesis are:

- SFCW signals can be generated using VNA's without any modification to the hardware. This option may be much slower compared to FMCW radars and a stop-and-go measurement scheme may have to be adopted, significantly increasing the total measurement time.
- Phase transitions between discrete frequencies must be considered to affecting the ambiguity function and, therefore, reducing the SFCW radar performance.
- If Doppler frequency measurements must be performed using SFCW, a very poor Doppler ambiguity function can be expected due to the typically short duration of SFCW pulses and, therefore, insufficient integration times for Doppler frequency extraction.

2.3.4 The vector network analyzer as a SFCW radar

A vector network analyzer is a measurement instrument that characterizes the frequency response both in amplitude and phase of a circuit or device under test (DUT) to a stimulus signal. VNAs may have one, two or more ports depending on the characteristics of the DUT, although two ports are the most common. Two-port VNA's allow to perform reflection and transmission characterization for one single frequency or a whole bandwidth of discrete frequencies, in a conceptually similar way to SFCW radars. The extracted parameters are called S -parameters or scattering parameters and are a concise and useful way of defining the frequency response of a device.

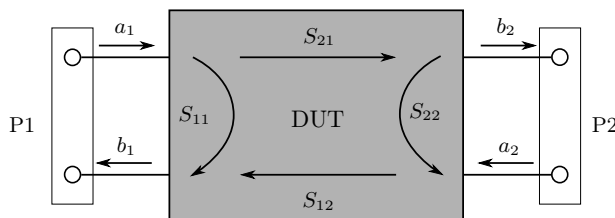


Figure 2.12: Interactions of the traveling waves $a_{1,2}$ and $b_{1,2}$ for a generic two-port as well as the resulting S -parameters and their physical influence.

Figure 2.12 shows the physical link between ports P1 and P2 and the S -parameters for a two-port VNA. The arrows coming in and out the ports in the figure, labeled as a_i and b_i , are known

as the incident or incoming and reflected or outgoing traveling waves for the i -th port, that is, the incident waves are the stimuli generated by the VNA and injected in the DUT whereas the reflected waves are the waves coming back from it. The S -parameters can be rearranged in a matrix known as the $[\mathbf{S}]$ matrix. For an N -port VNA, matrix $\mathbf{S} \in \mathbb{C}^{N \times N}$ is populated as:

$$[\mathbf{S}] = \begin{bmatrix} S_{11} & S_{12} & \dots & S_{1N} \\ S_{21} & S_{22} & \dots & S_{2N} \\ \vdots & \vdots & \ddots & \vdots \\ S_{N1} & S_{N2} & \dots & S_{NN} \end{bmatrix}. \quad (2.35)$$

The relation between the traveling waves and the S -parameters is defined by the linear system $b = \mathbf{S}a$, which for a two-port VNA is:

$$\begin{pmatrix} b_1 \\ b_2 \end{pmatrix} = \begin{pmatrix} S_{11} & S_{12} \\ S_{21} & S_{22} \end{pmatrix} \cdot \begin{pmatrix} a_1 \\ a_2 \end{pmatrix} \quad (2.36)$$

Expanding (2.36) we obtain the following equations:

$$b_1 = S_{11}a_1 + S_{12}a_2, \quad b_2 = S_{21}a_1 + S_{22}a_2. \quad (2.37)$$

In order to isolate the S -parameters from (2.37) the traveling waves a_1 and a_2 must be forced to zero. From the point of view of a VNA measurement, zeroing a_i implies getting no stimulus from the i -th port, which is done by attaching to that port a matched load equal to the reference load of the VNA. Zeroing a_1 yields:

$$b_1 = S_{12}a_2, \quad b_2 = S_{22}a_2, \quad (2.38)$$

whereas zeroing a_2 results in:

$$b_1 = S_{11}a_1, \quad b_2 = S_{21}a_1. \quad (2.39)$$

From (2.38) and (2.39) it is directly derived that the S -parameters are defined as:

$$\begin{aligned} S_{11} &= \left. \frac{b_1}{a_1} \right|_{a_2=0} & S_{12} &= \left. \frac{b_1}{a_2} \right|_{a_1=0} \\ S_{21} &= \left. \frac{b_2}{a_1} \right|_{a_2=0} & S_{22} &= \left. \frac{b_2}{a_2} \right|_{a_1=0} \end{aligned} \quad (2.40)$$

The S -parameters S_{11} and S_{22} can be assimilated to the reflection coefficients measured at ports P1 and P2, respectively, whereas S_{21} and S_{12} are the transmission coefficients from ports P2 to P1 and vice versa, respectively.

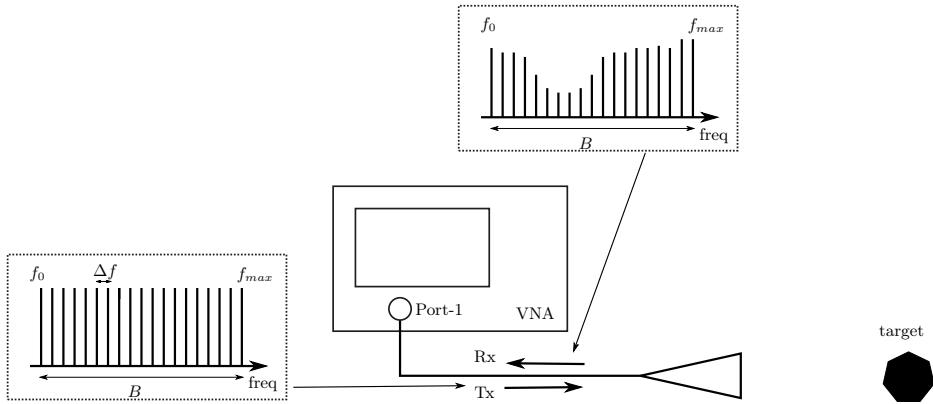


Figure 2.13: Radar measurement of a target using a VNA which sweeps a bandwidth B of discrete frequencies from f_0 to f_{max} in frequency steps of Δf . For reflection measurements (S_{11} parameters) only one port is necessary.

In a typical radar measurement, only reflection measurements are performed since the main objective is detecting reflecting targets in the scene. In order to use a VNA as a radar transceiver, an antenna must be attached to one port and the appropriate bandwidth must be specified in the VNA, as shown in Figure 2.13. In fact, simpler 1-port VNAs are an affordable solution for this type of measurements. Thanks to the circulators already built in the VNA port module, one single set of antenna and wiring can be used for emitting and receiving, helping reducing costs, hardware elements in use and volume.

2.4 Brief introduction to detection theory

The main problem that detection theory tries to address is whether a signal $s(t)$ other than noise is present in the acquired signal $x(t)$. This is a very simple conceptual reduction of the classical detection problem statement which calls for a detector making a binary decision: There is or there is not a signal. Correct target detection is, unsurprisingly, of utmost importance in radars since false positives must be avoided as much as possible to prevent a performance loss.

2.4.1 Basic detection problem example

An illustrative example of a real-life case is presented in Figure 2.14, based on Figure 2.5, to help understand the need of a signal detector for correct radar operation. In the left figure, the echoes from two targets overlapping in time are received by the radar under ideal reception

conditions (noise-free). The figure on the right shows a contaminated version of the 1-D received radar signal with a simulated $\text{SNR} = 8 \text{ dB}$. The scene is designed so the first and second echoes slightly overlap and no time separation can be distinguished by the naked eye. The transmitted signal $s(t)$ has a duration of 0.2 ms and the two targets are located at 30 and 45 km from the radar. Even for the ideal case, the two targets are difficult to identify and their presence is noticeable enough in the noisy case but this could not be no longer true if the SNR is slightly worsened.

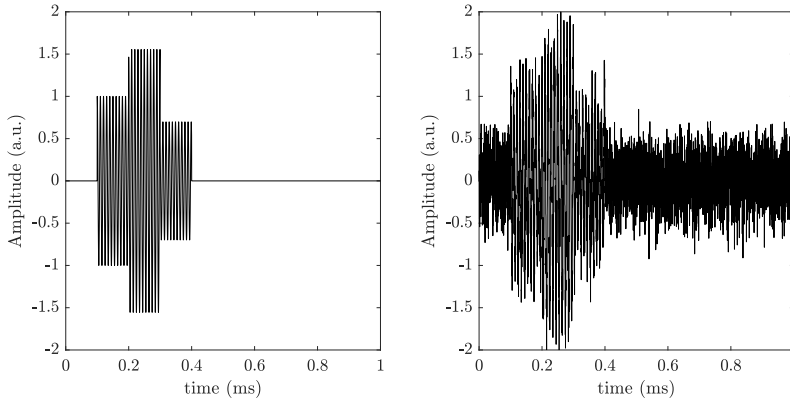


Figure 2.14: The echoes from two targets overlap in time. Left, the noise-free received signal; right, the received signal corrupted by noise ($\text{SNR} = 8 \text{ dB}$). The two targets are difficult to identify.

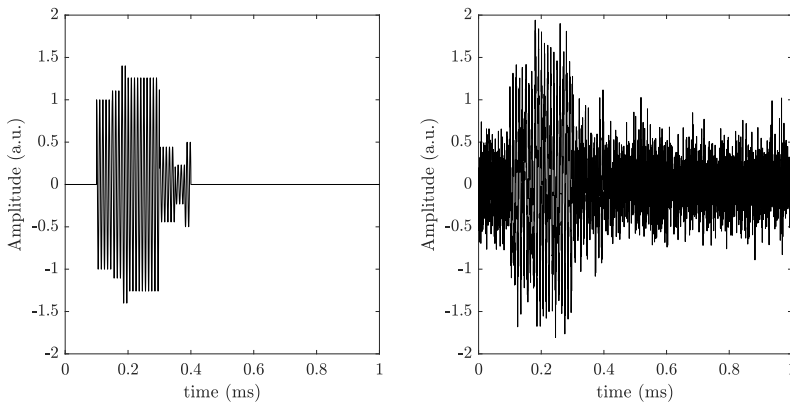


Figure 2.15: The echoes from four targets overlap in time. Left, the noise-free received signal; right, the received signal corrupted by noise ($\text{SNR} = 8 \text{ dB}$). It is not possible to identify any of the targets but just a rough approximation of the beginning and end of the received echoes.

The simulation in Figure 2.15 now accounts for four targets overlapping so that the beginning and end of the time window receiving echoes is the same as in Figure 2.14. In this case the four

targets are located at 30, 37, 42 and 45 km from the radar. Although four targets are present, neither the noisy nor the ideal noiseless received signals are enough to distinguish them and only a rough, approximate conclusion about the scene can be extracted which announces a lack of resolution in range.

A radar such as the one simulated would be unexploitable. Reducing the duration of the transmitted pulse to minimize the overlap and locating the echoes from the targets is an obvious solution as actually do air surveillance radars such as the ASR-9, presenting a pulse duration of $1\mu\text{s}$ [43]. In practice, reducing the pulse duration requires an increase in the hardware complexity as well as its associated economic costs. Therefore, it is desirable to have a method such as a detector that could allow target discrimination even from overlapping radar responses.

2.4.2 The detector

In a generic detector as the one depicted in Figure 2.16, two hypotheses are considered following the aforementioned problem statement: the so-called null hypothesis \mathcal{H}_0 , which only assumes noise is present; and the alternative hypothesis \mathcal{H}_1 , which assumes a signal of interest with constant voltage A and noise are received.

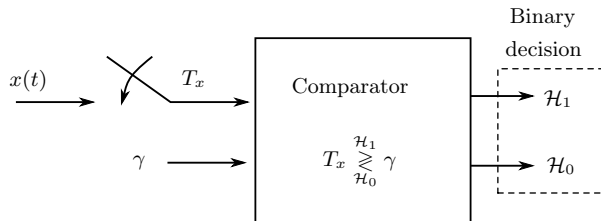


Figure 2.16: Block diagram of a generic detector and a binary comparator with two hypotheses, \mathcal{H}_0 and \mathcal{H}_1 .

The hypotheses can be formulated in a straightforward way as follows [44]:

$$\begin{aligned} \mathcal{H}_0: x(t) &= n(t), \\ \mathcal{H}_1: x(t) &= s(t) + n(t). \end{aligned}$$

On the one hand, if the null hypothesis \mathcal{H}_0 is true the signal $x(t)$ only contains a noise waveform $n(t) \sim \mathcal{N}(\mu_0, \sigma_n^2)$ which behaves like a random variable following a zero-mean ($\mu_0 = 0$) Gaussian distribution with variance σ_n^2 . On the other hand, if the alternative hypothesis \mathcal{H}_1 is true, $x(t)$ contains a constant voltage signal and a noise waveform with the same parameters as in \mathcal{H}_0 , yielding a random variable with Gaussian distribution —although \mathcal{H}_1 may not always be Gaussian in real situations— with a mean shifted to $\mu_1 = A$, that is, $x(t) \sim \mathcal{N}(A, \sigma_n^2)$.

Based on these hypotheses, the chosen threshold γ and the value of test variable T_x , the possible outcomes of the tests performed by the detector include two correct decisions and types of two

errors [45]. In Table 2.1, the false alarm and miss errors are known as Type I and II errors, respectively.

True hypothesis / decision	\mathcal{H}_1 is decided	\mathcal{H}_0 is decided
\mathcal{H}_1 is true	Detection	Miss
\mathcal{H}_0 is true	False alarm	No signal

Table 2.1: The four possible combinations given the two hypotheses and the binary outcome of the comparator.

All the possible cases in Table 2.1 can be mathematically expressed following the conditional probability nomenclature as $P(C|\Omega)$, that is, the probability of satisfying a certain condition C provided that the event Ω is true. The mathematical definition of the probabilities based on the type of decision are listed in Table 2.2. Although all four probabilities are given recognizable names in statistics, only the probability of detection (P_d) and probability of false alarm (P_{fa}) are considered in this work.

True hypothesis / decision	\mathcal{H}_1 is decided	\mathcal{H}_0 is decided
\mathcal{H}_1 is true	$P(T_x > \gamma H_1) = P_d$	$P(T_x < \gamma H_1)$
\mathcal{H}_0 is true	$P(T_x > \gamma H_0) = P_{fa}$	$P(T_x < \gamma H_0)$

Table 2.2: Definition of the conditional probabilities for every considered case in Table 2.1.

Figure 2.17 shows the probability density function of the test variable T_x under the two hypotheses \mathcal{H}_0 and \mathcal{H}_1 , a chosen threshold γ and a constant voltage A .

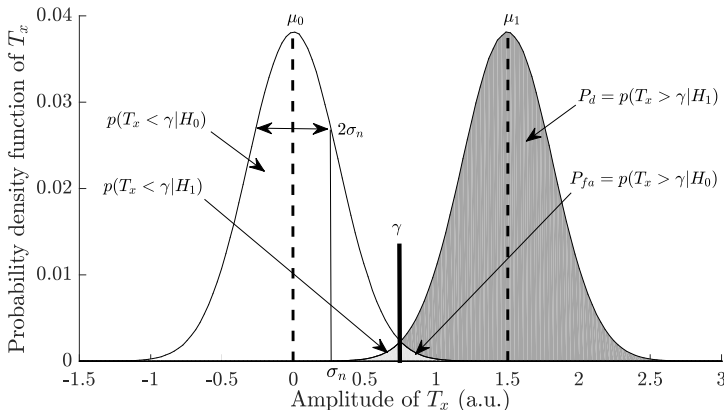


Figure 2.17: The two curves show the probability distribution functions of two Gaussian distributed processes with equal variances but different means ($\mu_1 > \mu_0 = 0$). A threshold γ is used to set the boundary between deciding whether \mathcal{H}_0 or \mathcal{H}_1 is true.

The white bell describes the distribution of the variable $x(t)$ under \mathcal{H}_0 , whereas the gray bell is the analog case for \mathcal{H}_1 . The areas where the two bells overlap, split in two by the threshold γ , create uncertainty in the decision process (Type I and II errors, right and left of γ , respectively).

The probabilities P_d and P_{fa} for the simple detector hereby discussed are obtained using the following expressions:

$$P_{fa} = Q\left(\frac{\gamma - \mu_0}{\sigma_n}\right), \quad (2.41)$$

and

$$P_d = Q\left(\frac{\gamma - A}{\sigma_n}\right). \quad (2.42)$$

The threshold γ can be selected in function of a given P_{fa} based on receiver design criteria following Neyman-Pearson's tests [46] for which the two considered hypotheses are not equiprobable:

$$\gamma = \sigma_n Q^{-1}(P_{fa}), \quad (2.43)$$

or Bayes' fixed solution assuming \mathcal{H}_0 and \mathcal{H}_1 are equiprobable:

$$\gamma = \frac{A}{2}. \quad (2.44)$$

The expressions for P_d , P_{fa} and γ in Neyman-Pearson's approach are conveniently defined and simplified thanks to the use of the Q -function [47], which is calculated for any z value as:

$$Q(z) = \frac{1}{\sqrt{2\pi}} \int_z^\infty \exp\left(-\frac{u^2}{2}\right) du = \frac{1}{2} \operatorname{erfc}\left(\frac{z}{\sqrt{2}}\right), \quad (2.45)$$

with $\operatorname{erfc}(z)$ the complementary error function of z :

$$\operatorname{erfc}(z) = 1 - \operatorname{erf}(z) = \frac{2}{\sqrt{\pi}} \int_z^\infty e^{-t^2} dt, \quad (2.46)$$

and $\operatorname{erf}(z)$ the error function of z . After adequate mathematical manipulation of (2.41) and (2.44), the P_d can be expressed as a function of the P_{fa} , as well as the SNR at the input of the detector, or SNR_i :

$$P_d = Q\left(Q^{-1}(P_{fa}) - \sqrt{A^2/\sigma^2}\right) = Q\left(Q^{-1}(P_{fa}) - \sqrt{SNR_i}\right), \quad (2.47)$$

and, after rewriting (2.47), the minimum SNR required for a $P_d - P_{fa}$ combination of choice can be calculated as:

$$SNR_{min} = (Q^{-1}(P_{fa}) - Q^{-1}(P_d))^2. \quad (2.48)$$

For the scenario described in Figure 2.17 and a threshold $\gamma = A/2 = 0.75$, the probability of detection is $P_d = 0.9912$ whereas the probability of false alarm is $P_{fa} = 8.83e-3$, which implies an $SNR = 13.52$ dB.

A general and desirable objective that will constrain the design of a detector is that these areas become as reduced as possible to maximize the P_d and minimize P_{fa} . Reducing the noise power, increasing the power of the signal of interest or a combination of both would draw the two bells apart. Doing the opposite would make the two bells overlap, worsening the performance of the detector. To illustrate these effects, two experiments for the same detector are depicted in Figure 2.18, a noisy signal with $\sigma_n = 0.5$, $A = 1$ ($SNR = 6.02$ dB) and $\gamma = 0.5$, yielding $P_d = 0.8413$ and $P_{fa} = 0.1587$; and Figure 2.19, an experiment with $\sigma_n = 0.2$, $A = 3$ ($SNR = 23.52$ dB) and $\gamma = 1.5$, producing $P_d = 1$ and $P_{fa} \approx 0$.

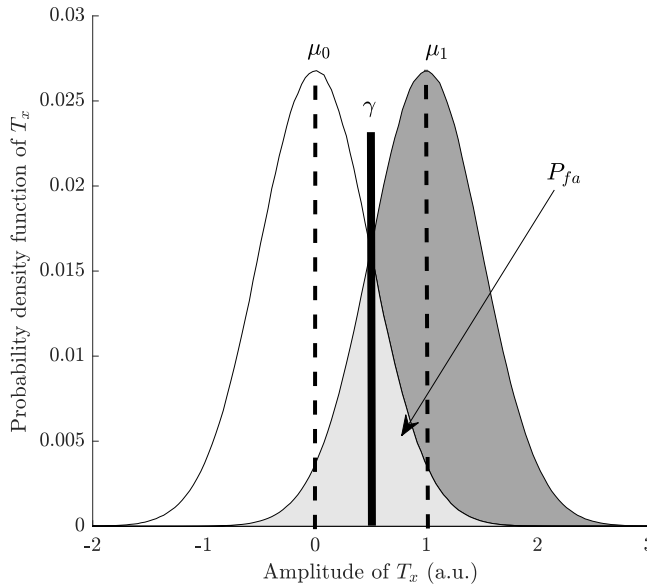


Figure 2.18: An experiment with low SNR conditions: $SNR = 6.02$ dB with undesirably high P_{fa} .

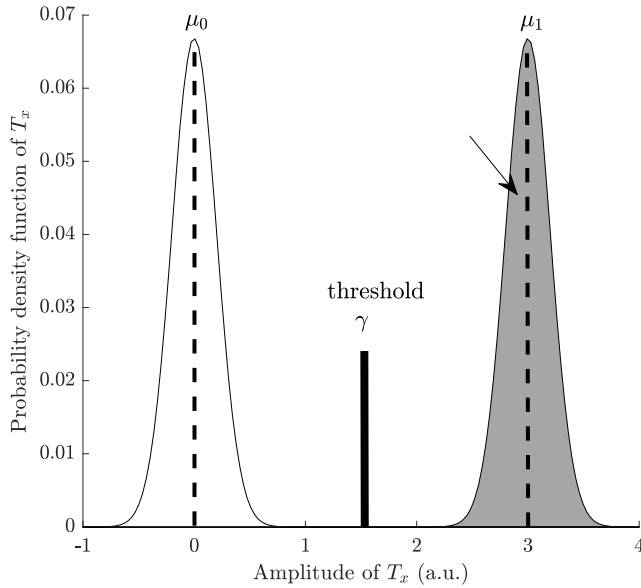


Figure 2.19: An experiment with high SNR conditions: $SNR = 23.52$ dB with negligible P_{fa} and virtually perfect detection $P_d = 1$.

Finally, it is imperative to highlight that these definitions are only valid for a detector with a decision by simple thresholding as the one shown in Figure 2.17 and the assumption that Gaussian signals are expected. Any modification to the detector architecture or statistical distribution of $s(t)$ or $n(t)$ must be considered in the formulation to statistically model the correct expressions for P_d and P_{fa} .

Thanks to having access to the probabilities of detection and false alarm, an automatic and unbiased metric is available for assessing and comparing the performance of a detector or several detectors: the ‘ P_d vs. SNR’ metric and overlapping curves for different P_{fa} values.

The ‘ P_d vs. SNR’ metric corrupts on purpose the input signal $x(t)$ with $n(t)$ for increasing noise levels or, in other words, multiple scenarios are considered with varying SNR. The P_d for each SNR scenario is computed, which gives an idea of the robustness of the detector against noise or how well can it discern between the null and alternative hypotheses. The P_d can be directly computed using the expression (2.47) which only requires the SNR at the input and the P_{fa} set for the detector. Finally, the results are typically displayed as in Figure 2.20, a semi-log graph with the SNR in dB in the x axis and the P_d in the y axis. Overlapping ‘ P_d vs. SNR’ curves representing several fixed P_{fa} provides farther insight on how the detector will perform under different operation constraints. As it was expected, higher SNR levels provide an increase in P_d for every case, and vice versa. It can be noticed that for a relatively high probability of false alarm, let us consider $P_{fa} = 10^{-1}$ for this case, the detector is providing an almost perfect probability of detection ($P_d \geq 0.99$ for $SNR = 11$ dB), the lowest of all cases considered, which

indicates a rather permissive detector. Alternatively, this kind of detector modeling can also help indicate how permissive a detector must be for a given expected SNR.

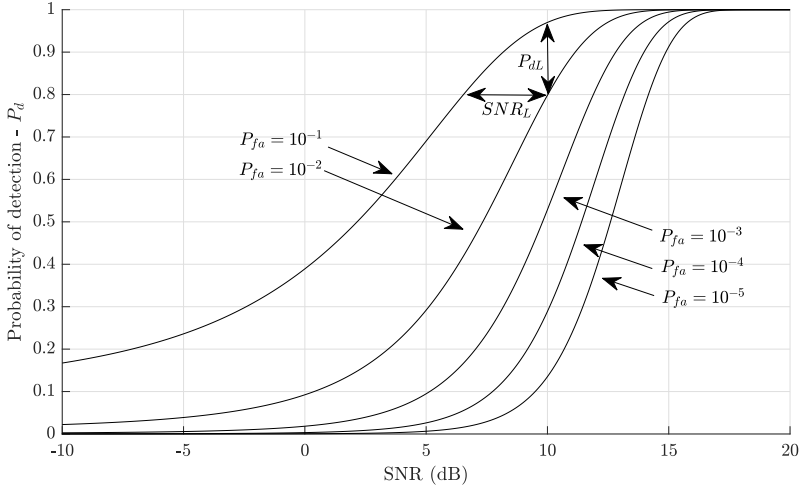


Figure 2.20: Semi-log graph representing the P_d curves for varying SNR values and for different chosen P_{fa} . For every value of P_{fa} there is a variation in SNR and P_d that must be considered when assessing the performance of the detector.

The graph provides useful information about what would be the SNR loss if the P_{fa} were to be decreased from $P_{fa} = 10^{-1}$ to $P_{fa} = 10^{-2}$. From these two losses we can extract an indication of what are the costs of increasing the strictness of a detector by setting a lower P_{fa} . As an example, for a given target $P_d = 0.8$, the SNR loss would be:

$$\begin{aligned} SNR_L &= SNR(P_{fa} = 10^{-1}, P_d = 0.8) - \\ &SNR(P_{fa} = 10^{-2}, P_d = 0.8) = 10 - 6.5 = 3.5 \text{ dB}, \end{aligned} \quad (2.49)$$

and the P_d loss for a fixed SNR = 10 dB:

$$\begin{aligned} P_{dL} &= P_d(P_{fa} = 10^{-1}, SNR = 10 \text{ dB}) - \\ &P_d(P_{fa} = 10^{-2}, SNR = 10 \text{ dB}) = 0.97 - 0.8 = 0.13. \end{aligned} \quad (2.50)$$

The P_d vs. SNR tool for evaluating the performance of a detector will be used in the GPR and PCL chapters of this thesis. The results obtained for those applications are many and thorough, which require simple yet highly informative ways of displaying the different combinations of findings and make a comparison between the studied approaches. It is common to find in the literature goal P_d figures of 0.8 [48, 49] or 0.9 [50], which are considered to be sufficiently safe

for the concerned applications. In this work, we selected the stricter $P_d = 0.9$ as a performance goal for all the presented performance comparisons.

2.4.3 The matched filter and pulse compression

At reception, the reflected echo from an illuminated target may present power levels comparable or lower than thermal noise levels, hindering the ability of the detector to decide whether a target is present or not. Concentrating the scarce available energy along time is therefore desirable, which is equivalent to maximizing the amount of received energy in few compressed coefficients, regardless of what their representation domain may be.

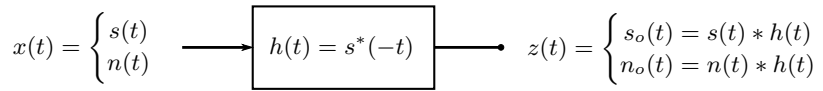


Figure 2.21: Block diagram of the matched-filter along with the input and output signals.

Figure 2.21 represents a generic matched filter (MF), denoted by its impulse response $h(t)$, as well as the output after matched-filtering $x(t)$. It is a well-known fact in detection theory that the SNR at the output of the detector is maximized when a matched filter is used, and this solution is proven to be the optimum solution when Gaussian noise is present [44]. The output SNR is defined by the following expression:

$$(SNR)_o = \frac{P_{s,o}}{\sigma_n^2} = \frac{|h^H s|^2}{\mathbf{E}[|h^H n|^2]}, \quad (2.51)$$

with $P_{s,o}$ the power of the output signal $s_o(t)$:

$$P_{s,o} = |h^* s|^2, \quad (2.52)$$

and with $h^H s$ the convolution of the input signal with the MF or $s_o(t) = s(t) * h(t)$. Additionally, the noise at the output of the MF is $n_o(t) = n(t) * h(t)$. The Cauchy-Schwarz inequality [51] tells us that:

$$|h^H s|^2 \leq |h^H h| |s^H s|, \quad (2.53)$$

and that the equality only holds if, for any given constant κ :

$$h = \kappa s, \quad (2.54)$$

which is the definition of the matched filter. In its turn, the power of noise σ_n^2 is expanded as follows:

$$\sigma_n^2 = E[|h^H n|^2] = \mathbf{E}[h^H n n^H h] = h^H \mathbf{R}_{nn} h = \frac{N_0}{2} h^H h, \quad (2.55)$$

since the autocorrelation of Gaussian noise, \mathbf{R}_{nn} , is defined by the identity matrix \mathbf{I} with $N_0/2$ in its diagonal and zero elsewhere:

$$\mathbf{R}_{nn} = \mathbf{E}[n n^H] = \frac{N_0}{2} \mathbf{I} \quad (2.56)$$

Finally, substituting (2.52) and (2.56) into (2.51), taking into account the Cauchy-Schwarz condition for the equality (2.54) and defining the energy of the signal $s(t)$ as $E = |s^H s|$ the expression for the output SNR of the optimum detector is reached:

$$(SNR)_o = \frac{|s^H s|}{\frac{N_0}{2}} = \frac{2E}{N_0} \quad (2.57)$$

The idea behind the MF is simple: A finite impulse response (FIR) system $h(t)$ providing the best matching for a given expected signal $s(t)$ will present an impulse response equal to the time-reversed, complex conjugate version of $s(t)$, as displayed in Figure 2.21. That is, the system $h(t)$ is designed ad-hoc for the signal $s(t)$ and acts as a autocorrelator in the noiseless case $x(t) = s(t - \tau)$.

The more than interesting option of maximizing the SNR opens the application in radars of using the MF as a correlator of the expected reference signal and the received signal, corrupted with Gaussian measurement noise. When a MF is applied to $x(t)$ the received radar signal is reduced to the characteristic response of the autocorrelation of $s(t)$, also known as the radar ambiguity function of $s(t)$ or χ_s . Therefore, it is desirable that this ambiguity function be designed to be as short and prominent as possible, compacting the total energy of the signal into few elements.

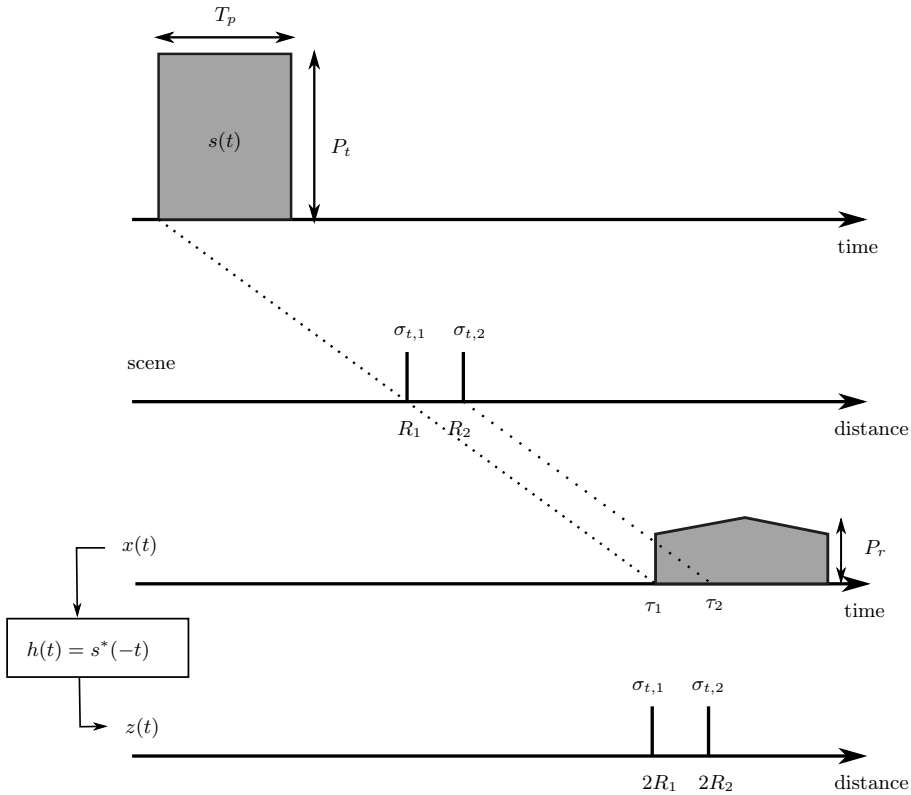


Figure 2.22: A MF is applied to the generic radar scenario where two targets are illuminated and their echoes are received without a clear indication of the targets positions. The output of the MF compacts the received energy from the targets as indicated by the ambiguity function of the radar, revealing the correct respective ranges as well as reflectivities.

Figure 2.22 gives an approximate general idea of what can be expected when a MF is used for pulse compression in a radar measurement. The energy of the echo returns in $x(t)$, which is spread along the time measurement axis, is compacted according to the ambiguity function of $s(t)$ after applying matched filtering. Two peaks at the right location and with amplitudes proportional to their respective reflectivities $\sigma_{t,1}$ and $\sigma_{t,2}$ are now identifiable.

2.4.4 The CFAR detector as a detection metric

The performance of a radar system can be assessed automatically by using an adaptive threshold detector known as constant-false alarm rate (CFAR). Let us consider a sliding measurement vector Z_t which may contain or not a target. Finding the optimum threshold may not be straight-forward since the distributions of the possible processes are not sufficiently known or the environment producing the measurement is too rapidly changing in time.

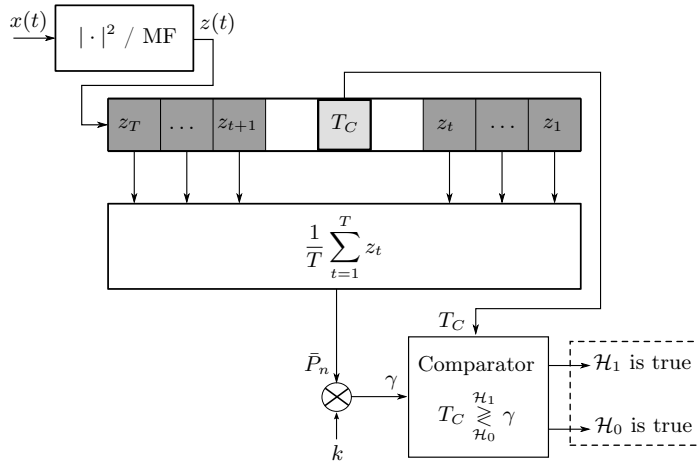


Figure 2.23: Schematic of a CA-CFAR detector using an envelope detector or a matched filter on the input signal $x(t)$.

As depicted in Figure 2.23, cell-averaging CFAR (CA-CFAR) feeds the sliding measurement vector Z_t with the input vector $z(t)$ which results from applying an envelope detector or a MF correlator to the received signal $x(t)$. Each element of the vector is known as cell. One test cell T_C , or cell under test (CUT), is located at the central element of the vector whereas T training or reference cells for computing the average noise power \bar{P}_n are fixed symmetrically on both ends of the vector. Guard cells around T_C prevent high power levels from a target from leaking into the training cells, which would generate unrealistically high \bar{P}_n estimations and hinder the detector performance.

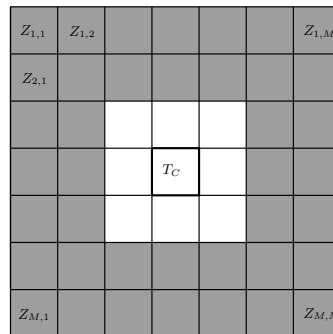


Figure 2.24: A typical subdivision in cells of a reconstructed 2-D scene. CA-CFAR detectors compute the threshold from the training cells (gray) to decide if a target is present in the cell under test (black). Guard cells (white) are used to avoid wrong threshold estimations.

The same reasoning can be applied for 2D CFAR detectors used in, for instance, target detection in slow-time and fast-time measurements like in synthetic aperture radars (SAR). Figure 2.24 visually describes the same principle as the 1D case in Figure 2.23.

The following hypothesis model is used by the CA-CFAR detector to determine whether a target is located within the CUT:

$$\begin{aligned}\mathcal{H}_0: & \text{ only noise is present in the CUT,} \\ \mathcal{H}_1: & \text{ a target and noise are present in the CUT,}\end{aligned}$$

which are the null and alternative hypotheses, respectively. The decision is made by the CA-CFAR detector after comparing the test variable T_C (the power of the CUT) against the threshold γ :

$$T_C \underset{\mathcal{H}_0}{\overset{\mathcal{H}_1}{\geq}} \gamma. \quad (2.58)$$

The threshold γ is not derived from a probabilistic analysis of the hypotheses as in Subsection 2.4 but it automatically adapts its value depending on the noise level in the tested signal. Numerous threshold definitions exist for CFAR [52, 53, 54]. The one used for CA-CFAR is defined as:

$$\gamma = k \cdot \bar{P}_n, \quad (2.59)$$

where \bar{P}_n is the average noise power level of the training cells, and

$$k = T \cdot (P_{fa}^{-1/T} - 1) \quad (2.60)$$

is a multiplying factor with P_{fa} a selected probability of false alarm and T the number of reference or training cells available. The value of γ will be modified according to the sensed noise power and will assure a P_{fa} in the detector outcome.

Although its conservative approach with respect to clutter and noise reduces the P_d and the resolution of the radar [23] because it may mask targets close to each other or simply determine there is no target present due to a poor selection of operation parameters for the CFAR detector.

To illustrate how CA-CFAR operates, a simple simulation with the echoes of three targets is generated. The transmitted signal is a chirp and in reception the SNR = 8 dB. A $P_{fa} = 10^{-5}$ was selected to minimize false positives. Following diagram in Figure 2.23, a signal envelope detector and a matched filter correlator were tested individually at the input of the CA-CFAR detector.

Figure 2.25 shows a logarithmic plot of the power of the noisy waveform including the three targets after the envelope detector. The presence of the targets is clearly visible thanks to the significant and sharp power increase where targets are supposed to be. The CA-CFAR detector adapts the threshold γ accordingly to the evolution of the noise level and raises it abruptly whenever the sliding training mask encounters a target. This sudden increase in γ can be

dangerous if P_{fa} is set to even lower values, since it could prevent the detector from deciding that a target is present.

For the same example, Figure 2.26-left displays the P_d vs. SNR plot for different P_{fa} . The results for $P_{fa} = 1$ yielding $P_d = 1$ for any SNR tested are obviously arbitrary since such a P_{fa} would have no interest for a radar system. The rest of the curves for lower P_{fa} values give a better understanding on how the CA-CFAR detector performs using an envelope detector. From these results we can extract the fairly high SNR levels are required to achieve exploitable P_d and P_{fa} .

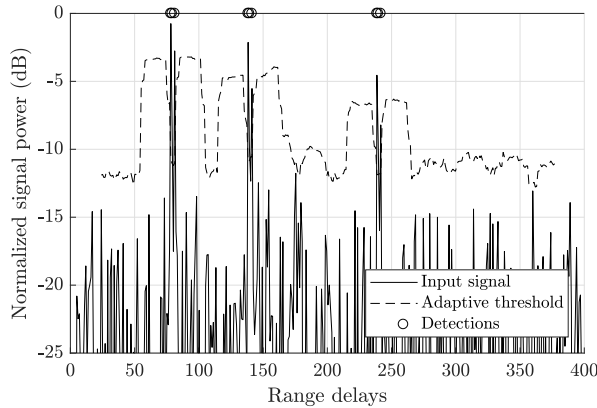


Figure 2.25: A CA-CFAR detector is applied to a received signal $x(t)$ with SNR = 20 dB after an envelope detector containing three echoes at time delays 2 ms, 3.5 ms and 6 ms. The dashed line corresponds to the CA-CFAR adaptive threshold which varies depending on the sensed noise levels. For a $P_{fa} = 10^{-5}$ all three targets are detected.

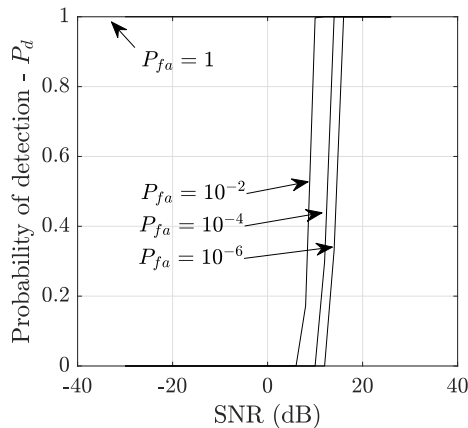


Figure 2.26: P_d vs. SNR curves describe the same results obtained using an envelope detector and the CA-CFAR detector and several imposed P_{fa} .

The same exercise as for the envelope detector is performed for the matched filter correlator or pulse compression case. Figure 2.27 show that the clearance of the target peak with respect to the noise ground level is higher for the matched filter correlator than the signal envelope detector, as expected. CA-CFAR is able to safely detect all three targets while adapting the threshold γ as required by the imposed P_{fa} .

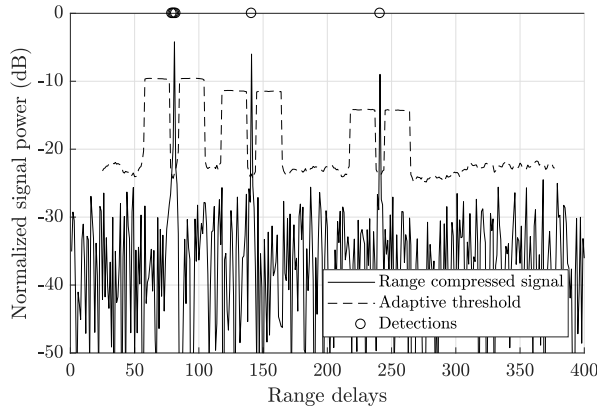


Figure 2.27: A CA-CFAR detector is used similarly to the results shown in Figure 2.25, although pulse compression is used instead of the envelope detector. The resulting SNR after pulse compression is increased, as expected, which leads to a potential performance improvement. For a $P_{fa} = 10^{-5}$ all three targets are detected.

The plots in Figure 2.28 describe the CA-CFAR detector when using pulse compression. Again, the the $P_{fa} = 1$ in the left figure yields arbitrary results irrespective of the applied SNR, whereas lower P_{fa} values reflect the true performance of CA-CFAR in combination with pulse compression.

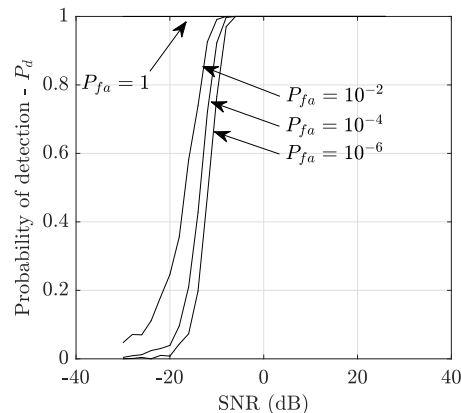


Figure 2.28: P_d vs. SNR curves describe the same results obtained using pulse compression and the CA-CFAR detector and several imposed P_{fa} .

It is worth noticing that for $P_{fa} \leq 10^{-2}$, the $P_d = 1$ goal is reached by the pulsed compressed data with SNR levels roughly 30 dB lower than in the envelope detector case, highlighting the formidable superiority of the former detector.

Depending on the type of signals or the nature of the noise, other variations of CFAR could be used. Some of the best-known alternatives are:

- Order Statistics (OS-CFAR) [55, 56]: The elements of the measurement vector Z_t are ordered by decreasing magnitude and the q -th element of the sorted vector, the q -th largest value in fact, is chosen for determining the decision threshold. Tests must be performed to evaluate the right value of q , which can also be computed in an adaptive way.
- Greatest of (GO-CFAR) [55, 57]: Its principle is similar to that of CA-CFAR, the training cells are split in two (before and after the test cell), so their respective average noise power levels can be estimated independently under the assumption that both noise contributions may not be identical due to clutter present in the measurement or any other phenomenon with a non-symmetrical behavior in both sets of training cells. The greatest of the two average noise power levels is chosen to compute the threshold. This type of detector is preferred in heterogeneous scenes with high clutter presence.
- Smallest of (SO-CFAR) [56, 58]: The same principle as in GO-CFAR is used although the smallest of all average noise power levels is selected. This is a common choice to gain robustness when possible interfering signals or targets are present in the training cells.
- Trimmed mean (TM-CFAR) [56, 59]: Similarly to OS-CFAR, this method sorts the cells by magnitude and then trims or cuts off the first T_1 and the last T_2 cells of Z_t . Then, the average noise power of the kept cells is used for obtaining γ . Performances may be better than for OS-CFAR, although this is highly dependent on the T_1/T_2 selection and the distribution of the noise.

2.4.5 Radar ambiguity function

The evaluation of the intrinsic characteristics of a radar waveform can be done in a objective way computing its ambiguity function, which is based on the matched filter of the transmitted signal $s(t)$, considered to be the reference signal, with its complex conjugate time-reversed version as in:

$$\gamma_s(\tau, \nu) = \int_{-\infty}^{\infty} s(t)s^*(t - \tau)e^{j2\pi\nu t} dt, \quad (2.61)$$

for any given delay τ . The obtained function γ_s describes what the radar response will be to an ideal infinitesimal target, given a certain time delay and frequency shift (or Doppler shift). An ideal waveform would have an ideal response of a Dirac delta in each dimension, range and Doppler frequency:

$$\gamma_s(\tau, \nu) = \delta(\tau) \cdot \delta(\nu). \quad (2.62)$$

Figure 2.29 shows a 3-D graph of the ambiguity function in (2.62) for which delay vs. Doppler shift are plotted. A peak is located at $\gamma_s(0, 0)$, whereas the ambiguity function is zero elsewhere as expected by the Dirac delta function. This indicates ideal infinitesimal resolutions for both range and Doppler frequency, which is an unreachable result.

During the design of or choosing a radar waveform, it is common to assess the response, resolution, or energy leakage through the secondary lobes of the waveform by showing cuts of the ambiguity function crossing the zero delay or zero Doppler frequency points. The plot $\gamma_s(\tau, 0)$ is used for assessing the response in range, whereas $\gamma_s(0, \nu)$ is used in Doppler frequency.

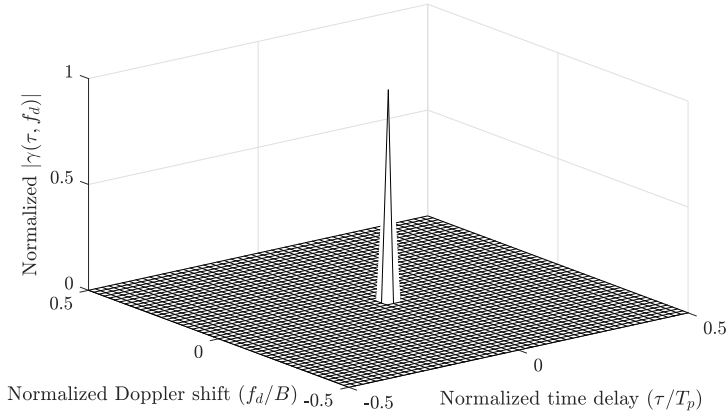


Figure 2.29: Schematic of a typical radar configuration. A transmitted wave is reflected by a target located at range R in the scene. The echoes are processed and the range of the target is extracted.

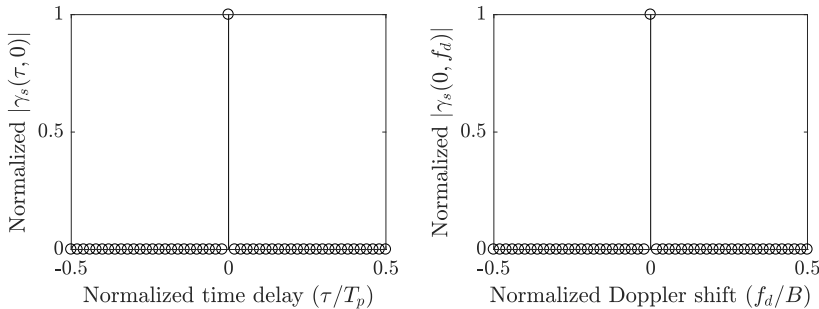


Figure 2.30: Schematic of a typical radar configuration. A transmitted wave is reflected by a target located at range R in the scene. The echoes are processed and the range of the target is extracted.

2.5 Synthetic aperture radars

2.5.1 Introduction

The spatial or cross-range resolution of a radar system describes the minimum separation distance in the cross-range direction that two targets must present for the radar to detect them individually. As depicted in Figure 2.31, let us assume that a radar with an antenna is illuminating a target at range R .

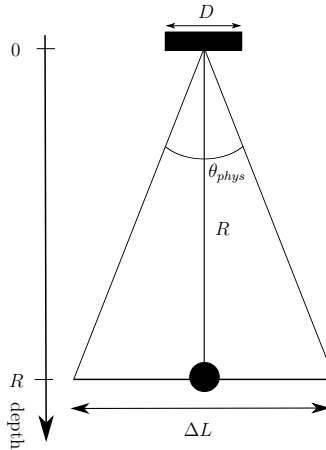


Figure 2.31: Schematic of a wide-beam antenna with dimension D illuminating a point-target at range R .

The size of the antenna aperture in the dimension perpendicular to its orientation is D , which is also known as the physical or real aperture. The half-power beam width (HPBW) of the antenna radiation pattern, which is used as a common ground to characterize antennas, is calculated as:

$$\theta_{phys} \approx \frac{\lambda_0}{D}. \quad (2.63)$$

It is worth noticing that the shape and width of the antenna radiation pattern is dependent on the frequency. From θ_{phys} we can directly derive that the diameter of the beam footprint ΔL onto a flat surface at range R , normal to the orientation of the antenna, is:

$$\Delta_L \approx R\theta_{phys} = \frac{R\lambda_0}{D}. \quad (2.64)$$

If two or more targets are placed in the beam of the antenna the receiver will not be able to discern between them. Therefore, any other target will have to be outside of the HPBW of the antenna, that is, a clearance of $\pm\Delta L/2$. As a conclusion, the spatial resolution of the real aperture is $\Delta_{xr} = \Delta L$. As an example, for a system with $D = 245$ mm and $\lambda_0 \approx 0.3$ m, the

spatial resolution at $R = 0.5$ m would be $\Delta_{xr} = 0.61$ m, which may be insufficient for performing detection of smaller objects such as wiring or landmines.

Assuming that R and possibly λ_0 are fixed by design to the above-mentioned figures, the only solution to improve the spatial resolution is using a wider antenna (larger D). As a self-explanatory example, and recalling (2.64), a spatial resolution of 10 mm would require an antenna of 15 m wide which would be completely impractical.

An alternative to real aperture radars is building a synthetically large antenna by moving the radar along a linear measurement path while collecting measurements in a coherent way, that is, considering the collected phase information. This is depicted in Figure 2.32. An equivalent narrower beam is synthesized, thus obtaining a much finer spatial resolution.

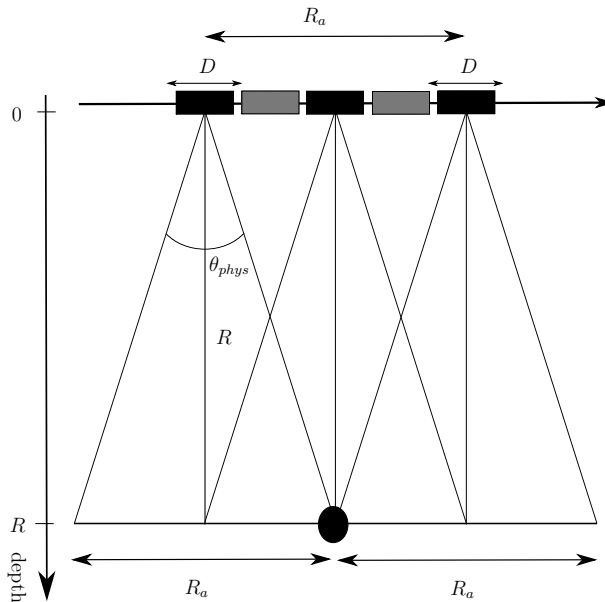


Figure 2.32: Schematic of a SAR measurement using a wide-beam antenna with an opening angle θ_{phys} . The point-target is illuminated by the radar from different measurement positions along its motion path.

The spatial resolution for SAR is calculated similarly to the case of the real aperture:

$$\Delta_{xr} = R\theta_{synth}, \quad (2.65)$$

with $\theta_{synth} = \lambda_0/2R_a$. In the SAR configuration, we must consider the two-way path effect on the beam width and hence the $2R_a$ in the denominator of (2.65): Let us assume that a target is located at a certain angle from the orientation axis of the antenna and that the radiation pattern for that angle is $1/\sqrt{2}$. Once the echo is reflected back to the antenna with the same impinging angle, the received energy will be affected by a factor $(1/\sqrt{2})^2 = 1/2$. It is common practice in the literature [23] to assume that the beam width is reduced to half the real aperture

case due to this two-way path the waves follow. Therefore, a factor of 2 must be added to the denominator in (2.65), which is rewritten as:

$$\Delta_{xr} = R\theta_{synth} = \frac{R\lambda_0}{2R_a}, \quad (2.66)$$

and knowing that $R_a = R\lambda_0/D$, we obtain:

$$\Delta_{xr} = \frac{R\lambda_0}{2R\lambda_0/D} = \frac{D}{2}. \quad (2.67)$$

An alternative definition of the spatial resolution is dependent on the 3-dB opening angle [60]:

$$\Delta_{xr} = \frac{c_0}{2f_c \sin \theta_{phys}}. \quad (2.68)$$

We can immediately deduce that (2.67) and (2.68) indicate that the spatial resolution in SAR is not range-dependent and that if we want to obtain finer spatial resolutions, D should ideally be as small as possible and, therefore, minimally directive and wide beam. Obviously, D will be limited by design depending on the type of antenna and used frequency and will not be a trivial nor easily modifiable parameter. Even if a very small antenna is realizable, its wide beam will spread the radiated energy in mainly uninteresting directions other than the target's, yielding low power levels reflected into the receiver and, thus, degrading the SNR at reception. Therefore, it is advisable to find a compromise between spatial resolution and signal degradation.

2.5.2 Processing SAR data

Coherent combination of these SAR measurements is performed in post-processing using SAR focusing algorithms (see Figure 2.33 for a conceptual scheme of a generic SAR processing) which use matched filtering in time or the equivalent and more affordable processing, whether it is totally or partially, in the frequency domain.

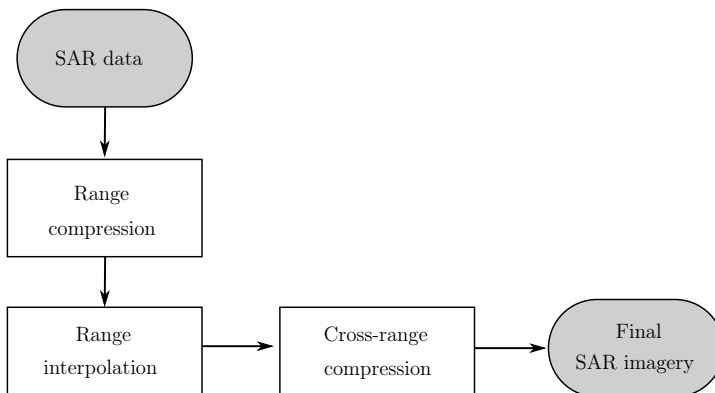


Figure 2.33: Conventional processing steps for generating SAR imagery.

These algorithms exploit the very-well known fact that a target illuminated by a radar following a linear path will generate a range or phase history evolution following a hyperbolic function. This is a direct effect of computing the Euclidean distance or range $r(t) = \|g - p(t)\|_2$ from the radar to the target for all measurements points, where $g = \{g_x, g_y\}$ are the $x - y$ coordinates of the static target and $p(t) = \{p_x(t), p_y(t)\}$ those of the moving platform. The expression of $r(t)$ is obtained as:

$$r(t) = \|g - p(t)\|_2 = \sqrt{(g_x - p_x(t))^2 + (g_y - p_y(t))^2}. \quad (2.69)$$

Figure 2.34 shows, on the left, a schematic scene where a radar following a linear path is illuminating an object. The platform positions shown are those which illuminate the target given an antenna radiation pattern with arbitrary aperture angle θ_{phys} . In other words, the leftmost and rightmost positions of the platform are those for which the object starts and stops being ‘seen’ by the directive antenna. The extremes present the longest radar-target distance R_{max} possible, whereas the middle position corresponds to the distance of closest approach R_0 .

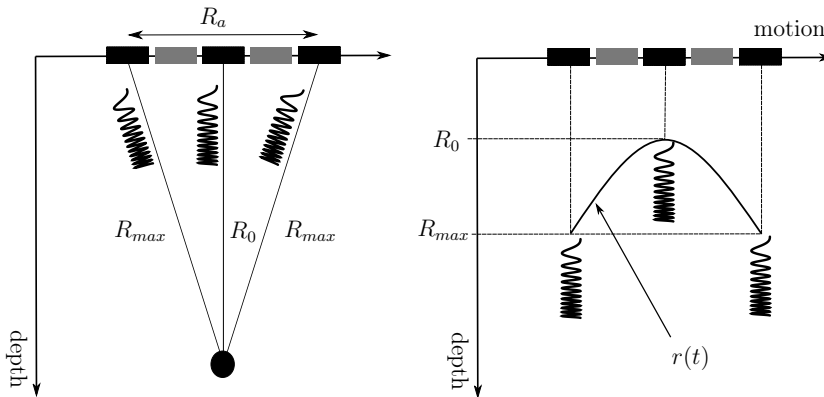


Figure 2.34: Two approaches to create SAR imagery are possible: the conventional SAR processing based on range and cross-range compression, and the CS approach for which no SAR processing is necessary.

If a 3-D scene is used, the expression of the expression of Euclidean distance must be adapted accordingly to compute $r(t)$ from (x, y, z) coordinates.

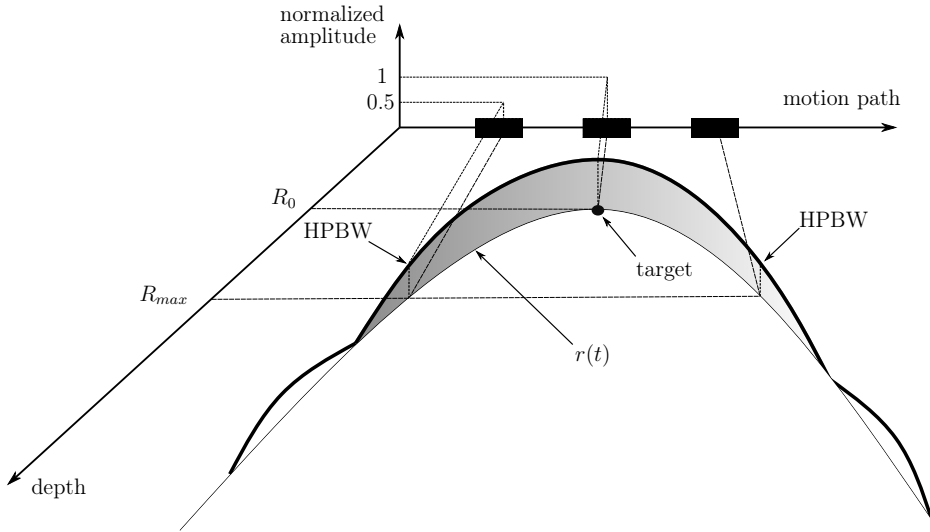


Figure 2.35: Three-dimensional representation of a SAR measurement. The energy collected along the hyperbola $r(t)$ follows the antenna radiation diagram of the radar.

It is well-known that $r(t)$ is a hyperbolic function (or hyperboloid in the 3-D case) and SAR geometries will produce hyperbolic range histories, fact that is depicted on the right schematic of Figure 2.34. In Figure 2.35 we can observe that the amplitude of the collected energy along the hyperbola will be proportional to the two-way radiation pattern of the antenna. In reality, this effect is not only limited within the HPBW but it transcends beyond it following the antenna diagram, yet the received energy from those angles are usually negligible.

2.6 Bistatic radars

2.6.1 Introduction

In contrast to monostatic radars, bistatic radars do not need to share the same location for the transmitter and receiver stages, that is, the transmitter and receiver do not need to be collocated and are physically separated from each other.

The transmitter may be cooperative or non-cooperative depending whether the receiver has direct access to the reference signal or not, which is required to process the received echoes from static or moving targets in the scene. If the transmitter happens to be non-cooperative or opportunistic, the scenario is considered a passive radar case. Bistatic radars are a case of multisatic radars, which consider one transmitter and several scattered receivers.

2.6.2 Scene description

In Figure 2.36 a general bistatic scene is described where a transmitter (Tx) illuminates a moving target flying at a certain altitude h with reflectivity σ_t and velocity v_t , as well as static clutter which presents reflectivity σ_c and null velocity v_c . The echoes from the target and clutter contributions are received by the receiver (Rx). For this specific case, Tx and Rx are stationary with $v_T = v_R = 0$ m/s.

Due to the geometry of the scene, three types of signals reach the receiver:

- Target echoes: replicas of the original signal $s(t)$ reflected by the target and time-delayed by the total propagation path $R_B = R_{T1} + R_R$, or bistatic range, with R_{T1} the transmitter-target and R_R the target-receiver ranges, respectively.
- Static clutter: all echoes generated by the reflections of $s(t)$ on the surrounding buildings, geological formations and structures, time-delayed proportionally to the bistatic range $R_C = R_{T2} + R_c$, with R_{T2} the transmitter-clutter and R_c the clutter-receiver ranges, respectively.
- Direct path: the original transmitted signal has line-of-sight propagation to the receiver without obstacles and is time-delayed proportionally to R_D or the transmitter-receiver range.

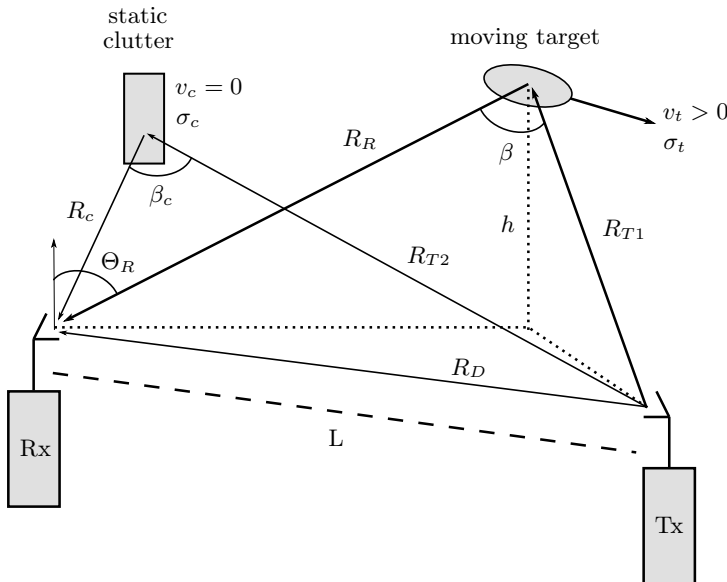


Figure 2.36: General bistatic setup: A moving target at height h and speed v_t is illuminated by a transmitter. The receiver, which is not collocated with transmitter and sufficiently far by a baseline L , receives the echoes from the target as well as from the static clutter in the scene.

An imaginary line L , known as baseline, describes and quantifies the separation between Tx and Rx. It is a common assumption that the measured bistatic range must be safely larger than the baseline L . The bistatic range is extracted from the time delay between the original signal and the received echoes, similarly as in the monostatic case, but does not provide straight-forward range determination as monostatic configurations do. This leads that some authors directly define the bistatic range as the expression $R_{T1} + R_R - L$.

If the direction of arrival (DOA) of the echoes (the angle θ_R) in Figure 2.37 is known at the receiver—using an array of antennas or a very directive antenna—the target-receiver range R_R can be estimated by the following expression:

$$R_R = \frac{(R_T + R_R)^2 - L^2}{2(R_T + R_R + L \sin \theta_R)}, \quad (2.70)$$

which can be greatly simplified since we can identify $R_T + R_R = R_B$ as the bistatic range. R_B can be indirectly calculated as $R_B = c\Delta t_B$, with Δt_B the time delay between the transmitted signal and the received echo.

Figure 2.37 represents two different radar geometries known as forward-scattering (left) and backward-scattering (right), which depend on the bistatic angle β , derived from the positions of the target, Tx and Rx. It is widely assumed that backward-scattering happens if $20^\circ < \beta < 90^\circ$ and forward-scattering for $90^\circ < \beta < 145^\circ$. In the cases where $\beta < 20^\circ$ or $145^\circ < \beta < 180^\circ$, monostatic and fence scattering cases are assumed, respectively.

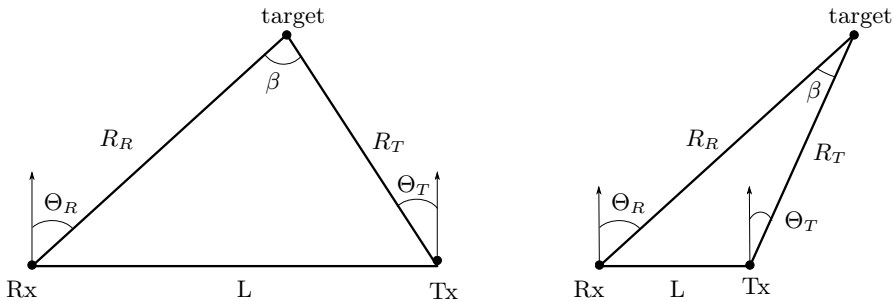


Figure 2.37: Bistatic configurations: Left, forward-scattering with a bistatic angle $\beta > 90^\circ$; right, backward-scattering with $\beta < 90^\circ$.

Fence scattering radars were first used for air surveillance of vast areas. If a transmitter-receiver pair is installed with direct line of sight or baseline, transmitting a continuous-wave signals, any target passing through the baseline would create amplitude disturbances in the received wavefronts due to the signal blocking by the target, and assuming the target is comparable or larger than the signal wavelength, highlighting the presence of a target. In order to cover large territories, several of those pairs must be installed, hence the naming fence scattering, giving a very rough approximation of the target positioning, direction and speed.

Both cases in Figure 2.37 may present the exact same bistatic range although the position of the target varies significantly. This is related to the definition of the bistatic range $R_B = R_{T1} + R_R$ which does not fix any of the two terms in the addition due to the non-collocated nature of bistatic radars. Knowing the bistatic range R_B and the exact locations of Tx and Rx creates infinite positions of the target as plausible solutions, all lying on an ellipsoid of constant range or iso-range R_B with two fixed foci, that is, the positions of Tx and Rx: $(-L/2, 0)$ and $(L/2, 0)$, respectively, with their heights set to 0 for the sake of simplicity. In Figure 2.38, the intersection between the iso-range ellipsoid and the transmitter-receiver-target plane is shown.

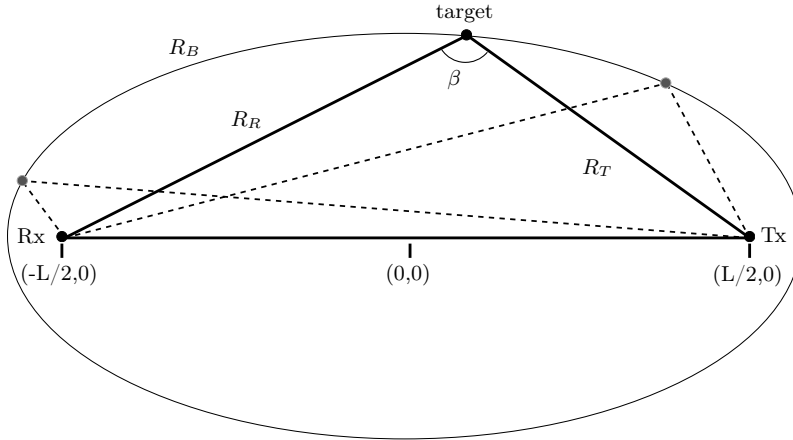


Figure 2.38: Ellipse obtained by intersecting the ellipsoid with iso-range R_B generated by the foci Tx and Rx with the vertical plane including the Tx, Rx and target. The two unknown distances R_R and R_T satisfy the condition $R_B = R_R + R_T$. Other two candidate targets selected arbitrarily and with identical R_B are displayed in with grey dashed lines.

The expression for the received power in (2.7) is modified in bistatic radars according to the definition of the bistatic range. The propagation loss for monostatic radars following $1/R^4$ is substituted by the split distance $1/(R_T^2 R_R)^2$, hence yielding:

$$P_r = \frac{P_t G_t G_r \lambda_0^2}{(4\pi)^3 R_T^2 R_R^2} \sigma_t. \quad (2.71)$$

For equal $R_B = 2R$, the bistatic configuration is more beneficial due to the quadratic decay of the propagation loss L_p except if $R_T = R_R = R$, in which case L_p is the same. As an example, the propagation loss in (2.71) is defined in dB as:

$$L_p = \left(\frac{\lambda_0}{4\pi R_T R_R} \right)^2, \quad (2.72)$$

which for a radar using a center frequency $f_c = 500$ MHz, that is $\lambda_0 = 0.6$ m, a bistatic range of 10 km, with arbitrary $R_T = 8.5$ km and $R_R = 1.5$ km, yields $L_p = -168.53$ dB, whereas

for the monostatic case (single-trip distance of 5 km) $L_p = -174.38$ dB is obtained, or a 5.85-dB difference in favor of the bistatic geometry. However, it must be highlighted that target reflectivity is typically lower in bistatic configurations, hence the benefits of the split propagation path may be compensated or even negatively exceeded by the low reflectivity levels.

2.6.3 Target location

The ellipse shown in Figure 2.38 is the vertical cut or intersection between the ellipsoid of bistatic iso-range R_B with foci at Tx and Rx as depicted in Figure 2.39, and the plane normal to the ground plane and containing Tx and Rx. The trivial solutions to the bistatic range below the ground level are not included in the three-dimensional representations of the iso-range ellipsoid.

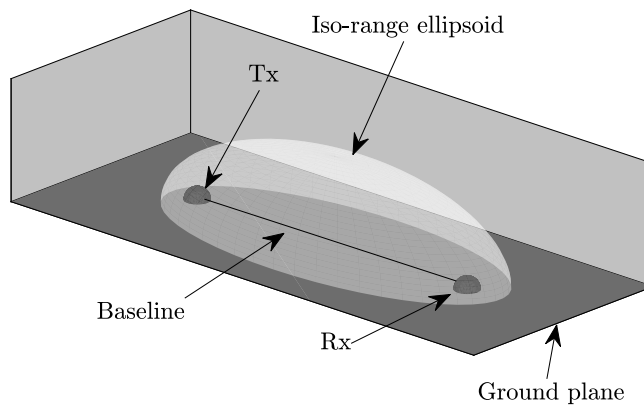


Figure 2.39: A 3-D representation of a bistatic scene with one transmitter and one receiver. The ellipsoid above the ground plane indicates all possible target loci when ideal isotropic antennas are used.

The bistatic ranges seen in Figures 2.38 or 2.39 would only be possible if both transmitting and receiving antennas would be isotropic, that is, an ideal and unfeasible antenna that radiates or receives energy equally for all directions. In practice, antennas present various radiation patterns defining in which particular direction most of the energy is confined (main lobe or main beam) and which directions present very low or almost zero radiation levels (secondary lobes and nulls). By using directive antennas, all the possible positions of a target in the bistatic range are limited to those inside the volume illuminated by the antenna and the equivalent volume for the receiving antenna.

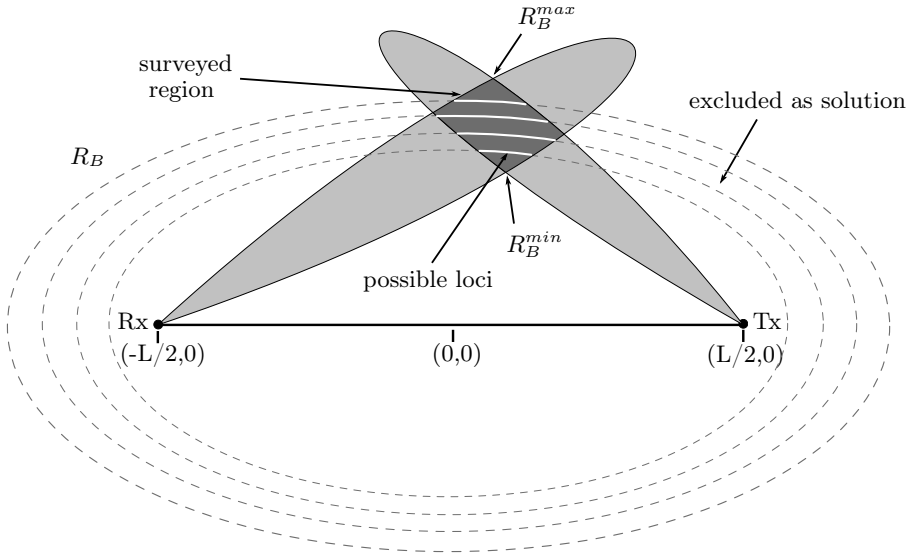


Figure 2.40: Two directive antennas are used in Tx and Rx. In contrast to the generic case assuming isotropic antennas, the iso-range is limited to the volume created by the intersection of both main lobes.

As shown in Figure 2.40, the intersection of the main lobes of the Tx and Rx antennas creates a surveillance volume (dark grey parallelogram) from which target echoes can be received. Any target outside this volume may still be detectable at Rx if it is illuminated by a secondary lobe of the Tx antenna or received also through a secondary lobe of the Rx antenna, or both cases at the same time. The white curves inside the surveyed volume indicate possible loci for the detected target depending on its bistatic range which, due to the directivity of both antennas, is limited by the minimum and maximum bistatic ranges R_B^{min} and R_B^{max} , respectively.

2.6.4 Multistatic radars

The bistatic geometry can be extended to multiple receivers or transmitters into a multistatic configuration benefiting from the fact that an object will reflect echoes from all directions at different intensities. Just as in the bistatic case, if a target is present in the scene, conceivably, each of the N_x Tx-Rx pairs will be able to extract a bistatic range R_{Bn} which, by themselves, create multiple ellipsoids. Having such angular or spatial diversity maximizes the probabilities of target positioning and compensates the fact that certain Tx-Rx pairs may be disabled for several reasons such as objects blocking the bistatic path or losing access to opportunistic transmitters for uncontrolled reasons. Figure 2.41 shows the geometry of a multistatic radar configuration with one Tx, two Rx—all with isotropic antennas—and one target that is detected by Rx1 and Rx2 with different bistatic ranges. The two bistatic ellipsoids created by the bistatic ranges $R_{B,1}$ and $R_{B,2}$ provide a null direction resolution if considered individually but, when combined, their surfaces intersect creating a curve with all possible target loci.

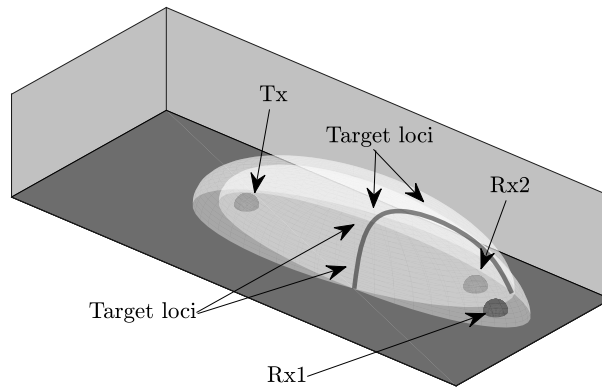


Figure 2.41: A 3-D representation of a multistatic scene with one transmitter and two receivers. All possible target loci are reduced to the intersection of the two ellipsoids, highlighted as a grey curve.

The multistatic map exposed in Figure 2.42 is a horizontal cut at an arbitrary height (an arbitrary plane parallel to the ground plane intersecting the ellipsoid) of the previous multistatic configuration with two intersecting ellipsoids. For that plane the two ellipses intersect in two points which become candidate positions for the detected target (one is the correct position and the other is the ambiguity or ghost target).

All possible planes intersecting the two ellipsoids will present two intersection points, except for the last plane tangent to the highest intersection point, which will have only one. These intersection points create a curve where the target can be located or its loci, as shown in Figure 2.42. The approximate position of the target and maybe its orientation with respect to the receivers can be narrowed down although it is completely dependent to the chosen multistatic geometry.

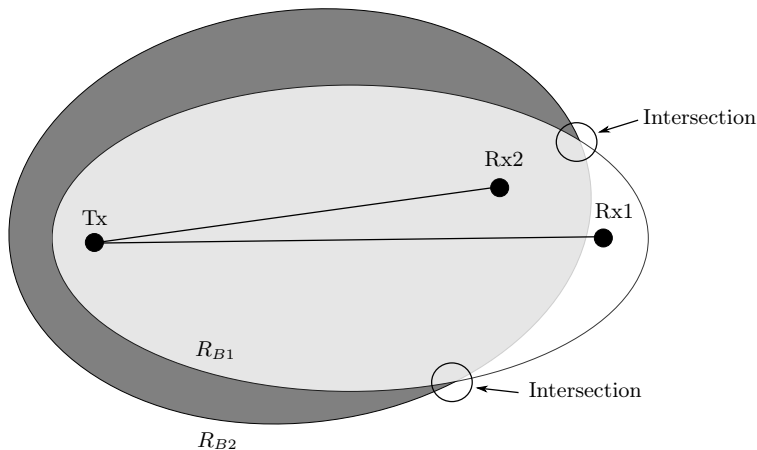


Figure 2.42: A 2-D view corresponding to the intersection of an arbitrary plane and the two ellipsoids as presented in Figure 2.41. For this view, two target loci are considered.

If an extra pair of Tx-Rx is added to the multistatic geometry, the information provided by the additional bistatic range creating a new ellipsoid can be integrated to find a solution confined in a single point, provided that all three ellipsoids intersect. In Figure 2.43, a third receiver Rx3 is used along with Rx1 and Rx2, whose ellipsoid indeed intersects with the two preceding ones. Of course, the position of the target is not exact since we must consider the bistatic range resolutions for every Tx-Rx pair which present limited bandwidths. The target will be within the volume created by the intersection of the three respective range bins, although giving sufficiently good approximation of the target position.

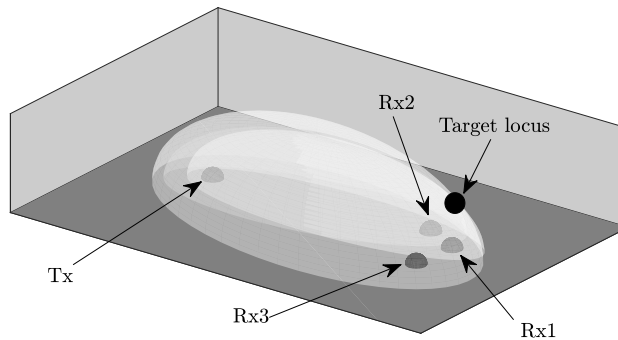


Figure 2.43: A 3-D representation of a multistatic scene with one transmitter and three receivers, all isotropic. The intersection of the ellipsoids shows the position of the target.

The ghost target that had been located at the inferior part of Figure 2.42 can already be ruled out since only two ellipsoids intersect there. The intersection of the three ellipsoids with the arbitrary plane as shown in Figure 2.44 clarifies the ambiguity that existed previously.

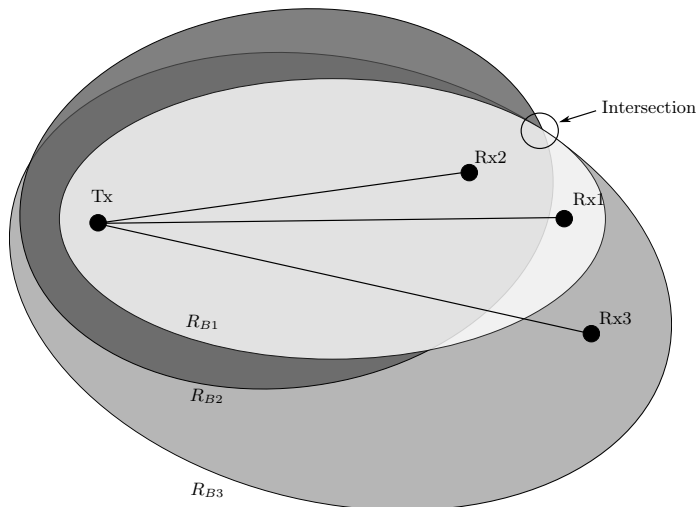


Figure 2.44: A 2-D view of the intersection of an arbitrary plane and the three ellipsoids as shown in Figure 2.43. Only one target locus is decided with no ghost targets.

The time evolution of a moving target in terms of distance and velocity is possible and it is typically calculated by extracting its range and Doppler frequency shift information. This is achieved by computing the cross-ambiguity function (CAF) of the received signal and the reference signal. This technique is basically a reinterpretation of the ambiguity function and will be discussed in Chapter 6.

2.7 Conclusions

In this chapter we have briefly presented the most known radars based on their modulation and type of energy emission. Pulsed radars have been historically present since the invention of the radar and their initial and most popular application was airspace surveillance, requiring detection and ranging capabilities going beyond dozens of kilometers. These radars are also known as ‘on-off’ keying and present some disadvantages but also some restrictions —such as high transmitter power levels or blind distances— that disqualify them as a technology of choice for applications such as speed determination or short-range imagery. CW or FMCW radars are preferred for those short- or mid-range applications and make a better use of transmitted power and reduce the hardware complexity. In the case of UWB FMCW, these radars also can outperform pulsed radars in terms of range resolution thanks to their broader bandwidths. An approximation of the FMCW waveform can be easily generated with affordable VNA’s thanks to the SFCW waveform. Due to the good results, commercial readiness and ease of implementation, we will focus on using SFCW radars with VNA’s for the imagery-related applications discussed in Chapters 4 and 5.

Regardless of the fact that radars can radiate pulsed or CW waveforms, the transmitted signals can be modified in frequency, phase, or coding, to increase the ability of the detector to discern between targets. For that matter, the ambiguity function is the ideal tool for evaluating the waveform performance in terms of range or Doppler resolution, as well as the level of undesired secondary lobes. Approximating the ambiguity function to an ideal Dirac delta (maximum at $\gamma_s(0, 0)$ and zero elsewhere) is a goal that radar engineers have pursued, with coded radars [61, 62] and noise radars [63, 64] possibly yielding the most promising solution nowadays. In radar, signal detection is an essential field and many approaches are available. The matched filter is known to yield the optimum results although less computationally complex alternatives can be sufficiently. The FFT correlator is a powerful and easy to implement tool for target extraction and farther detection and will be used in Chapter 4 for computing the ground truth of NDT measurements, as well as in Chapter 6 for extracting range and Doppler information of the received signals. Moreover, a tools known as the ‘ P_d vs. SNR’ has been introduced in this Chapter which will be vastly used for assessing the reconstruction results obtained after CS reconstructions for several subsampling rates, and how these affect the radar performance with respect to the established approach for every application.

Increasing the cross-range resolution of any radar by simply moving the radar during data acquisition as it is done in SAR is a very powerful tool than leads to 2-D or 3-D imagery. As described in this chapter, the cross-range resolution is constant, that is, it does not degrade

with range. Thanks to this, SAR imagery has become a standard in many fields and especially in air- and space-borne imagery covering huge areas for which wide-beam, out-of-focus radar measurements greatly simplify the acquisition process.

In air space surveillance, bistatic and multistatic radars add a new insight with respect to monostatic radars. The particular geometry of non-monostatic radars makes them interesting for situations in which monostatic radars fail to perform. Multiple transmitters or receivers distributed accordingly to the application needs may maximize the possibility of detecting the target and its surveillance, hence increasing the global detection performance to the maximum, while having radar diversity. This can be achieved by deploying transmitters and receivers on the scene but also by using the transmissions of external services such as TV or radio broadcasts, mobile communications signals, etc. These illuminators of opportunity are not designed for radar-related purposes but assure fast and extremely simple deployment of passive radar receivers.

All the concepts discussed in this chapter will form the sufficient basis for the following three application chapters.

Chapter 3

Fundamentals of Signal Sampling and Compressed Sensing

This chapter introduces the concept of conventional signal sampling and a new sampling paradigm, known as compressed sensing, for which a general overview of its mathematical problem statement and other related aspects will be provided. Solving a minimization problem requires satisfying certain strict conditions such as the restricted isometry property (RIP) of the so-called sensing matrix, or presenting sparsity in any given representation domain. However, when solutions are required for practical applications, these conditions can be relaxed and still achieve valid solutions. The most usual methods for finding a solution to the problem are also introduced, such as the basis pursuit minimization problem using the theoretical ℓ_0 -norm or the more exploitable ℓ_1 -norm. A variation of the problem statement that accepts noisy measurements in the minimization is also presented, namely the basis pursuit denoising algorithm, also known in statistics as the least absolute shrinkage and selection operator. Among the many existing greedy algorithms exploited in compressed sensing, the orthogonal matching pursuit is presented as an alternative to linear programming algorithms and measurements involving large data sets.

3.1 Signal sampling and historic approach

The exploitation of electromagnetic signals requires ad-hoc sensors to receive and transform the signals into the form of voltage variations —continuous in time— into discrete voltage values, as it is schematically displayed in Figure 3.1. These voltages can then be directly processed or stored for farther processing. Signal sampling is unavoidably used in countless applications in every domain requiring data acquisition and discretization, whether the propagation medium is wired or wireless.

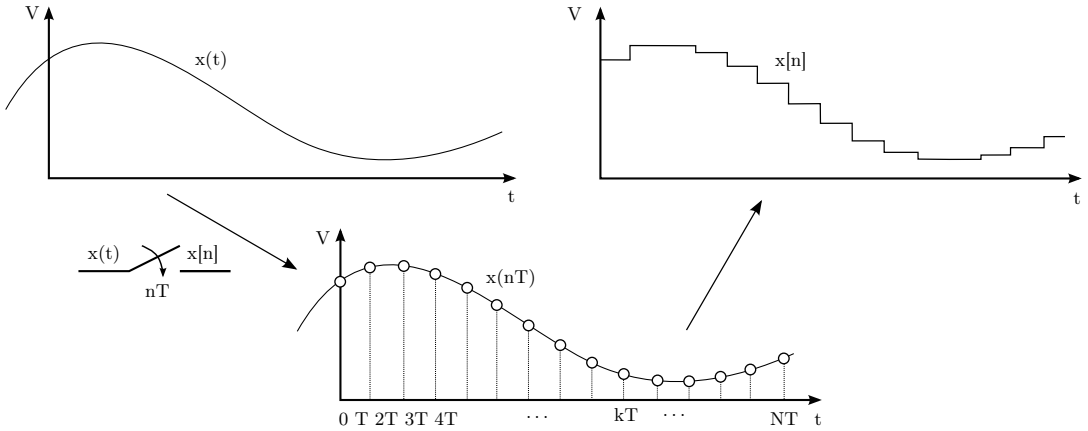


Figure 3.1: Top, a signal $x(t)$, continuous in time, is sampled at nT intervals, generating discrete voltage values.

The applications requiring signal sampling range from early days rudimentary sound or telegraphic systems [2] to recent advanced communications [3] or UWB systems. In every case, a sensor must be designed or chosen in accordance with the characteristics of the signal of interest, which can be defined by a number of parameters such as its operation frequency, bandwidth, polarization, or modulation. The way the signal sampling is performed influences the quality of the signal reconstruction from a discrete set of samples. Ideally, it is desirable that the reconstruction of a discrete signal be performed using the minimum number of samples yet achieving a flawless reconstruction. This is theoretically guaranteed if a criterion is met: The Shannon-Nyquist-Whittaker sampling theorem [15], or the Nyquist sampling theorem for shorter. This theorem, described around 1948, states that any signal can be reconstructed if a sampling frequency f_s of at least twice the maximum frequency describing the signal to discretize is used, that is:

$$f_s \geq 2f_{max}. \quad (3.1)$$

The maximum frequency of a signal can be interpreted thanks to Figure 3.2 as follows:

- For a signal or tone described by one single frequency f_0 and zero bandwidth ($B = 0$ Hz), the maximum frequency is set to $f_{max} = f_0$.
- For a bandpass signal with bandwidth $B > 0$ and a center or carrier frequency f_c , the maximum frequency is half the signal bandwidth above the carrier frequency, or $f_{max} = f_c + B/2$.
- For the case of a baseband signal whose bandwidth ranges from 0 to B Hz, f_{max} is directly B , or $f_{max} = B$.

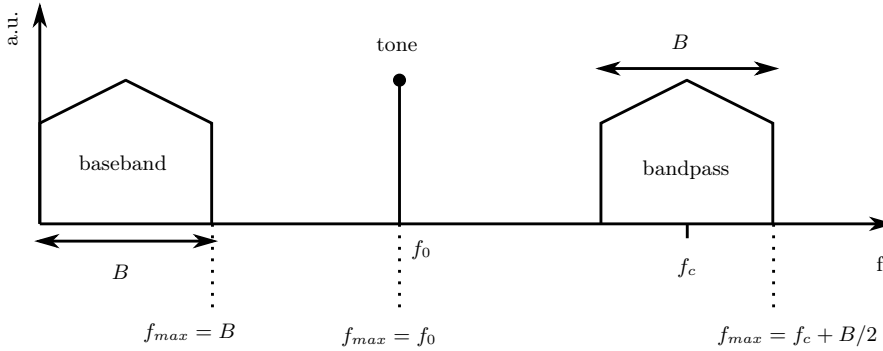


Figure 3.2: Different definitions of the maximum frequency of a signal depending on its definition: tone, baseband or bandpass.

If the sampling criterion is not met, the maximum frequency the sensor can acquire is reduced and, therefore, the complete bandwidth of a sensed signal may not be fully acquired, which does not guarantee perfect signal reconstruction. An additional issue may happen if a given signal is sampled so that its discrete representation corresponds to a lower frequency, or an aliased frequency. Although the Nyquist rate provides sufficient but marginal results, an oversampling factor k_{os} is usually added to the Nyquist rate in order to avoid aliasing or incomplete bandwidth acquisition. In both cases, the oversampling factor alters the sampling frequency as follows:

$$f_s = 2k_{os}f_{max} = 2k_{os}B, \quad (3.2)$$

with $k_{os} > 1$. In Figure 3.3 the effects of using several the sampling frequency for a 3-kHz continuous signal (Figure 3.3-a) in accordance or not to the Nyquist rate are visually explained. Figure 3.3-b) shows the reconstructed signal using a sampling rate of 1 KHz, which is one sixth the Nyquist rate. The reconstructed signal (shown as a dashed line with solid markers) presents a period of 1 ms, hence replicating an aliased signal of 1 kHz instead of the original 3-kHz signal. In contrast, Figure 3.3-c) uses as sampling rate with the exact Nyquist rate, that is, 2 kHz. The reconstructed signal has a period of 3.33 ms matching the 3 kHz original signal, confirming that the Nyquist rate is theoretically sufficient as sampling frequency. However, Figure 3.3-d) shows a particular case where sampling the original waveform shifted in phase by 90° only yields null voltages, which implies no signal is sensed in practice. Figure 3.3-e) shows that using a small oversampling factor of $k_{os} = 1.2$ might be sufficient to approximate the original signal, although better results are obtained if $k_{os} = 2$ is selected, as seen in Figure 3.3-f). Finer approximations to the original continuous signal are produced if higher oversampling factors are used, like in Figure 3.3-g) with $k_{os} = 6$.

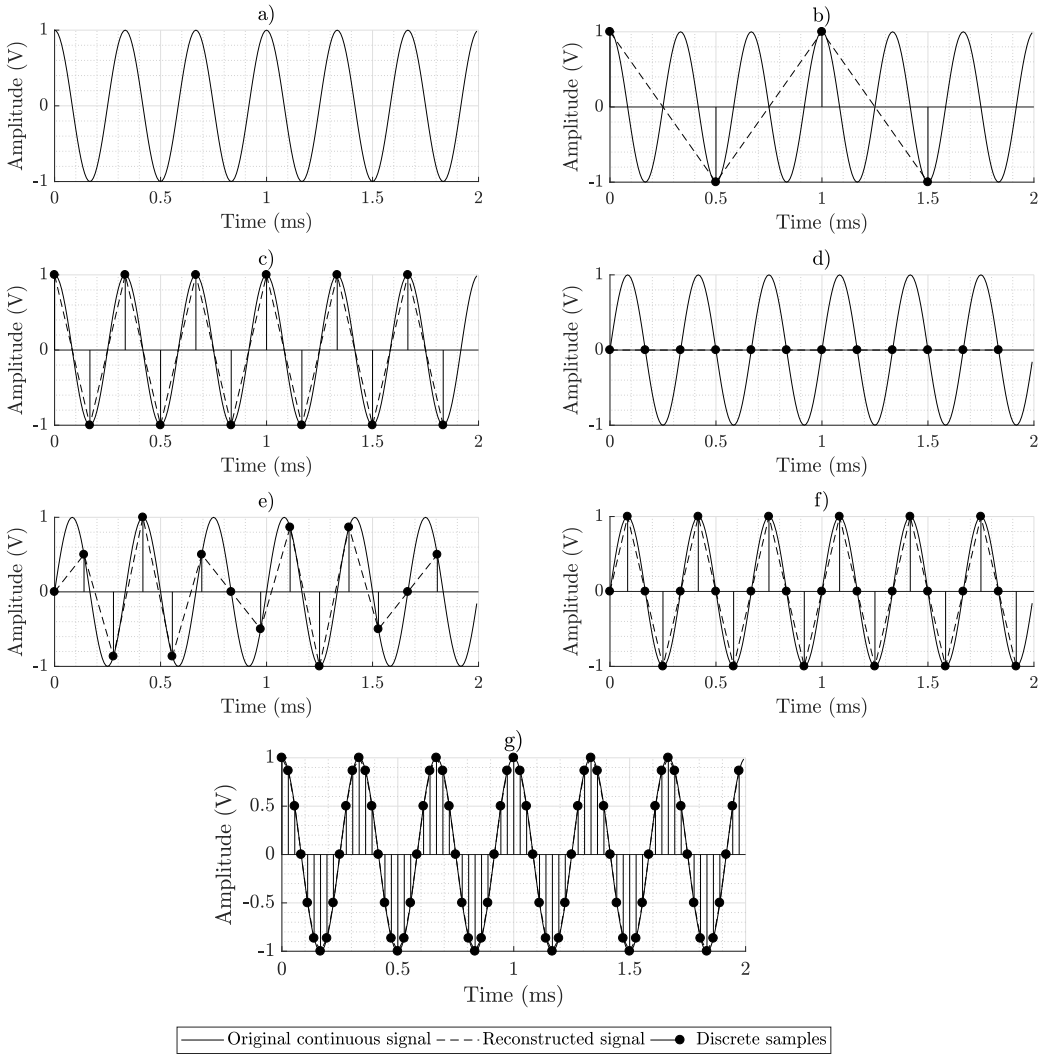


Figure 3.3: Effects of sampling a continuous signal with different sampling rates: a) continuous signal, b) $f_s = f_{max}/3$; c) $f_s = 2f_{max}$, d) shifted signal by 90° and $f_s = 2f_{max}$, e) shifted signal by 90° and $k_{os} = 1.2$, f) $k_{os} = 2$, and g) $k_{os} = 6$.

There are other reasons to increase sampling rates like the need for certain applications to oversample. Beyond what has been already explained in the previous section regarding oversampling and conventional signal sampling, two other simple reasons why this is done are:

- As it is the case in radars, received signals are expected to present low power levels, often difficult to discern from measurement noise, oversampling allows increasing the integrated samples and, thus, the amount of energy related to the signal. This increases the ability to decorrelate the signal of interest from noise.

- In occasions, low ADC resolutions are compensated by oversampling the signal in order to minimize the quantization error [65].

Despite other signal processing-related benefits, oversampling can be a remarkable burden for certain systems, where challenging amounts of data are needed when long measurement times are required or large areas must be measured, high bandwidth is needed, or a combination of both. Handling, storing or transmitting large amounts of data are onerous tasks, and imaging systems may be affected.

3.2 New solutions to new needs: Compressed Sensing

In recent times, technology advances and the maturity reached at an application level in fields like, for instance, radar imagery have led to new and more specific performance requirements. These example applications are just two out of a list that never ceases to increase as research continues. These new sensors with more demanding requirements often involve very fine resolutions and extremely high sampling rates or faster measurements while keeping the obtained resolutions unaffected. Of course, increasing resolution invariantly implies increasing data acquisition, transfer, storage and processing capabilities. In all these cases, more resources and more advanced equipment are necessary. It may be possible that, due to limitations in the available technology, too demanding performances may be unachievable opening the path to alternative solutions.

In medicine, a field a priori far from radars, magnetic resonance imaging (MRI) is a relatively recent although already established technique used to generate fine resolution diagnostic images. This type of imagery is obtained in rather long acquisition times and a substantial reduction would be a clear advantage in exploiting such expensive MRI equipment. Reducing the amount of data or scans to collect would indeed produce faster measurements.

Fortunately, it has been found in [66] that the obtained images can be considered as sparse at the final image or pixel level in some representation space. Different random subsampling approaches showed that MRI measurements could be completed five times faster, while enhancing image contrast and resolution. This is possible thanks to the use of random data subsampling and solving linear minimization problems to achieve equal or similar quality data reconstructions, which is fundamentally the concept behind compressive sensing, compressed sensing or compressed sampling (shortened as CS in all cases) and that will be explained in more details in the following pages. Of course, the use of CS is not limited to MRI or the field of medicine but it is applicable to any other imagery or signal acquisition system.

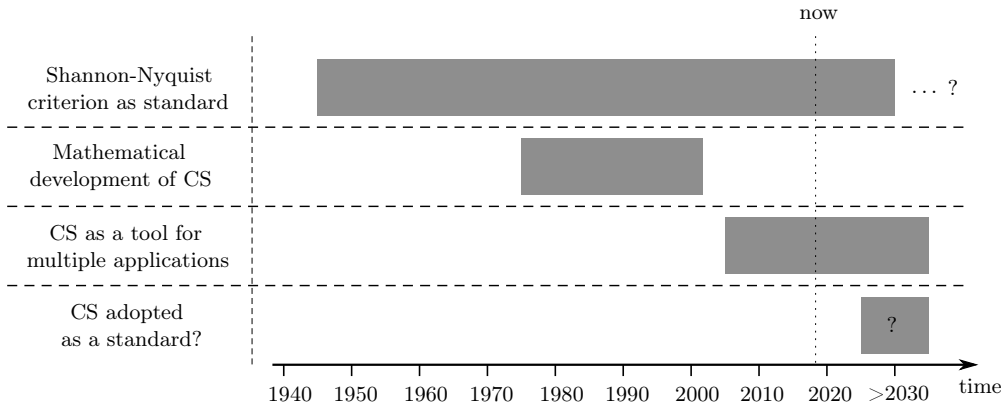


Figure 3.4: Time line of the evolution of CS from its initial mathematical conception to the current situation with countless applications and methods being explored.

In Figure 3.4, the evolution of CS is shown in a simplified time line. Starting from the Shannon-Nyquist sampling theorem in 1948 [15], which is nowadays vastly used in all devices requiring sampling data, to the first mathematical development of CS starting by an application in the seismics and geophysics field [67] in 1973, where the so-called robust modeling method —based on the well-known data regression— was the first approach to the concept of on purpose ‘missing’ data or measurements knowing full well that the original data can be recovered using a minimization method. This path was slowly explored in the subsequent years by other authors [68] although it was not until the mid-2000’s when the idea of CS was mathematically introduced and formulated by Candès and Donoho [69, 70, 71] and the need for sparsity was documented by Daubechies in [72]. From that point on, the concept of CS became a new paradigm and more and more applications found in it a new way to achieve what seemed clearly contravene the —until then— only and valid signal sampling conventions: Randomly discarding data from measurements and, under certain conditions, being able to reconstruct the same signal with high probability and high fidelity. Or, as seen from an even more chimeric point: using signal acquisition systems with much narrower bandwidths at varying sampling rates, yet producing almost perfectly reconstructed, Nyquist-like sampled signals.

The evolution of CS in the engineering world, which has proven to be sound beyond the initial euphoria and despite appeasing some naive promises, clearly has shown to have a bright future. The military as well as the civilian worlds should consider CS in their new prospects for new applications and technologies. There are, nonetheless, advances in the military world that can immediately redound positively in the civilian interests.

Among those, this thesis has identified and explores three radar-based applications that may benefit from CS in achieving faster, lighter measurements and preserved or possibly still high performances within usual exploitation requirements. These applications are non-destructive testing of transparent materials in the sub-terahertz band, ground penetrating radars for concealed landmine location, and passive coherent location for airspace surveillance based on extremely low-cost, undetectable and immediate deployment passive radars.

The following sections of this chapter will introduce the basic notions about CS which are required to understand the results and discussions included in the application chapters.

3.3 Problem description and formulation

Let us imagine that a radar with arbitrary specifications receives a complex signal x of length N which contains the backscattered energy from possible targets in a given scene. The vector x is exactly defined as $x \in \mathbb{C}^{N \times 1}$. Let us also assume that this signal is fully sampled according to the Shannon-Nyquist criterion, as described back in Section 3.1, and that all the N elements in the vector are required to perfectly reconstruct the signal in a conventional way. This signal is said to be compressible or S -sparse if it can be unequivocally represented with just S non-zero coefficients ($S \ll N$). The validity of this statement is extended to any given representation domain of x defined as $\mathcal{D}(x)$, for which the following generalized condition must be satisfied:

$$\|\mathcal{D}(x)\|_0 \leq S, \quad (3.3)$$

with $\|x\|_0$ the l_0 pseudo-norm —also known as the support of x —, which counts the number of non-zero elements in x , or mathematically:

$$\|x\|_0 = \text{supp}(x) = \{\#n : x_n \neq 0\}. \quad (3.4)$$

If the condition stated in (3.3) holds, vector x is categorized as S -sparse and compressible in \mathcal{D} .

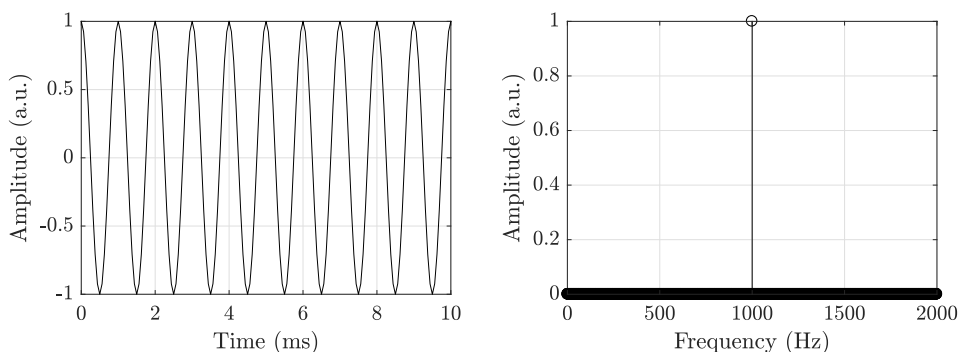


Figure 3.5: Two representations of the same function: Left, a sinusoidal wave in time domain; right, its frequency representation. Examples of non-sparse and sparse signals, respectively.

In Figure 3.5-left a 1-kHz sinusoidal signal in the time domain cannot be considered as sparse since most of its elements are non-zero. Its degree of sparsity S is close to the length of the signal which indicates virtually no sparsity. In contrast, Figure 3.5-right shows the frequency

representation of the same signal after a Fourier transformation —our representation domain of choice is $\mathcal{D}(x) = \mathcal{FT}(x)$ — in which we can see that only one frequency component at 1 kHz is non-zero and all other frequency components are null. This result represents the perfect exemplification of total sparsity with $S = 1$ and ideal sparsification since no other result could be sparser, regardless of the chosen representation domain \mathcal{D} . Of course, intermediate sparsity levels can be achieved if sub-optimal domains \mathcal{D} are tried.

Let us now define a linear system which describes $y \in \mathbb{C}^{N \times 1}$ as a conventional observation of vector x :

$$y = \Phi x, \quad (3.5)$$

where $\Phi \in \mathbb{R}^{N \times N}$ is the observation or sensing matrix relating both vectors x and y , a square matrix of size $(N \times N)$ built following the identity matrix \mathbf{I}_N definition, with all the elements in its diagonal set to one and zeros elsewhere:

$$\mathbf{I}_N = \begin{bmatrix} 1 & 0 & 0 & \dots & 0 \\ 0 & 1 & 0 & \dots & 0 \\ 0 & 0 & 1 & \dots & 0 \\ \vdots & \vdots & \vdots & \ddots & \vdots \\ 0 & 0 & 0 & \dots & 1 \end{bmatrix}. \quad (3.6)$$

This type of observation corresponds to a typical sampling scheme used in any radar or similar system: all the elements in x which guarantee a perfect signal reconstruction, provided that the Shannon-Nyquist criterion is met, must be sampled by a radar receiver to make vector y , our observation, reconstructible as well.

Now, let us assume that the observation defined by the linear system in (3.5) is modified so that the observation vector is $y \in \mathbb{C}^{M \times 1}$, with $M < N$. That implies that the resulting observation no longer meets the Shannon-Nyquist criterion and is now $\Phi \in \mathbb{C}^{N \times M}$. From fundamental linear algebra we know that if $M < N$ is true, the recovery of x from y yields infinite solutions since such system is said to be underdetermined or ill-posed. Hence, the recovery of the original vector x is only feasible if this problem is treated as a minimization problem. A solution can be obtained solving:

$$\hat{x} = \arg \min_x \|x\|_0 \quad \text{subject to } y = \Phi x, \quad (3.7)$$

where \hat{x} is the sparsest solution for x and is achieved by forcing the maximization of the number of zeros. The minimum length of y , M , required to successfully recover a S -sparse signal by solving (3.7) is bounded by [73]:

$$M \geq \mathcal{O}(S \log(N/S)). \quad (3.8)$$

The implementation of the l_0 pseudo-norm in this context is problematic and reconstructing x becomes a non-convex, NP-hard problem to solve [74]. Hence, a relaxation on the minimization problem is commonly proposed by using the l_1 norm instead:

$$\hat{x} = \arg \min_x \|x\|_1 \quad \text{subject to } y = \Phi x. \quad (3.9)$$

with the l_p norm generally defined as:

$$\|x\|_p = \left(\sum_{i=1}^n |x_i|^p \right)^{1/p}. \quad (3.10)$$

The optimization problem formulated in (3.9) is known as basis pursuit (BP) [75, 76] and can be theoretically solved with high probability if the matrix Φ presents a low coherence:

$$\mu = \max_{i < j} |\langle \phi_i, \phi_j \rangle| \quad (3.11)$$

where ϕ_i is the i -th atom in matrix Φ and $0 < \mu < 1$ is the maximum coherence between all the atoms. Another condition to achieve a valid solution is that the RIP [14, 73] of full order M be satisfied. This is done by checking that the matrix Φ and all possible $\binom{N}{M}$ submatrices Φ_m must comply with the following expression for any given $\delta_m \in (0, 1)$:

$$(1 - \delta_m) \|x\|_2^2 \leq \|\Phi_m x\|_2^2 \leq (1 + \delta_m) \|x\|_2^2. \quad (3.12)$$

For fairly large sensing matrices, testing the RIP condition for all submatrices Φ_m becomes unfeasible. This may still be true even if a low order RIP is accepted. In order to circumvent the RIP condition, it is common to use a matrix populated following a random distribution, e.g., Gaussian, $\phi_{n,m} \sim \mathcal{N}(0, 1)$, however this solution cannot be implemented for radar sensors since they follow a sampling scheme based on the identity matrix as the one presented in (3.6). Therefore, the observation matrix Φ must be built up by selecting only those rows as defined in a random vector V containing the indices of the elements in x that will be measured and stored. We can express this as:

$$\Phi = \text{row}_V \mathbf{I}_N. \quad (3.13)$$

As an example, let us assume that $N = 10$, hence \mathbf{I}_{10} is a (10×10) identity matrix and x is 10 elements long. Let us now assume that we choose $M = 3$ with random indices populating vector V being 1, 3 and 8, or $V = [1, 3, 8]$. The measurement matrix would be a fat matrix defined as a submatrix of rows 1, 3 and 8 of \mathbf{I}_{10} , expressed as:

$$\Phi = \text{row}_V \mathbf{I}_{10} = \begin{bmatrix} 1 & 0 & 0 & 0 & 0 & 0 & 0 & 0 & 0 & 0 \\ 0 & 0 & 1 & 0 & 0 & 0 & 0 & 0 & 0 & 0 \\ 0 & 0 & 0 & 0 & 0 & 0 & 0 & 1 & 0 & 0 \end{bmatrix}. \quad (3.14)$$

The resulting observation vector y would be created by only keeping the elements 1, 3 and 8 of x as visually explained next:

$$y = \Phi x = \text{row}_{v_p} \mathbf{I}_N = \begin{bmatrix} \mathbf{1} & 0 & 0 & 0 & 0 & 0 & 0 & 0 & 0 & 0 \\ 0 & 0 & \mathbf{1} & 0 & 0 & 0 & 0 & 0 & 0 & 0 \\ 0 & 0 & 0 & 0 & 0 & 0 & 0 & \mathbf{1} & 0 & 0 \end{bmatrix} \begin{bmatrix} \mathbf{x}_1 \\ x_2 \\ \mathbf{x}_3 \\ x_4 \\ x_5 \\ x_6 \\ x_7 \\ \mathbf{x}_8 \\ x_9 \\ x_{10} \end{bmatrix} = \begin{bmatrix} x_1 \\ x_3 \\ x_8 \end{bmatrix}. \quad (3.15)$$

The previous formulation assumes that a number of atoms in matrix Φ can be selected and perfectly represent y . In real-world situations, noise or undesired effects will corrupt the observation vector y and, therefore, an error tolerance threshold factor $\epsilon > 0$ allowing a certain flexibility for taking into consideration mismatches between the observation vector and Φx must be introduced in the BP problem formulation in (3.10). This modification to BP is known as basis pursuit denoising (BPDN) [75] or its equivalent in statistics, the least absolute shrinkage and selection operator (Lasso) [77], and allows reconstructing noisy measurements within the imposed tolerance ϵ :

$$\hat{x} = \arg \min_x \|x\|_1 \quad \text{subject to} \quad \|\Phi x - y\|_2^2 \leq \epsilon, \quad (3.16)$$

which can also be formulated as:

$$\hat{x} = \arg \min_x \frac{1}{2} \|\Phi x - y\|_2^2 + \lambda_t \|x\|_1, \quad (3.17)$$

with λ_t a trade-off parameter which indicates preference to sparser results in the minimization problem when $\lambda_t \rightarrow \infty$ or to best reconstruction fit otherwise. It is worth pointing out that if $\lambda_t \rightarrow 0$ (or equivalently $\epsilon = 0$), then BPDN becomes a noiseless BP problem.

The Lasso formulation is slightly different from BPDN:

$$\hat{x} = \arg \min_x \|x\|_1 \text{ subject to } \|y - \Phi x\|_2^2 \leq \epsilon, \quad (3.18)$$

although they become equivalent depending on the choice of the parameters ϵ and λ_t . This explains why it is a common practice to exchange the Lasso and BPDN algorithms indistinctly.

It is possible that the observation vector x may not be by itself sparse but it may be described sparsely by a set of coefficients $\sigma \in \mathbb{C}^K$ if a sparsifying representation matrix $\Psi \in \mathbb{C}^{N \times K}$ is available, therefore decomposing vector x as:

$$x = \Psi \sigma. \quad (3.19)$$

The matrix Ψ can be interpreted as a dictionary and includes all possible Ψ_k describing the measurement x . Substituting (3.19) in (3.9), one can obtain:

$$\hat{\sigma} = \arg \min_{\sigma} \|\sigma\|_1 \text{ subject to } y = \Phi \Psi \sigma. \quad (3.20)$$

A new matrix $\Theta = \Phi \Psi$, with $\Theta \in \mathbb{C}^{M \times K}$, is defined as a subsampled dictionary of K atoms, or a dictionary in which only M samples per atom have been randomly kept. Finally, using the compound matrix Θ , the problem statement becomes:

$$\hat{\sigma} = \arg \min_{\sigma} \|\sigma\|_1 \text{ subject to } y = \Theta \sigma. \quad (3.21)$$

Nowadays available algorithms and computing power allow for using BPDN or any other linear programming implementation while offering higher performance rates [78, 79, 80]. However, if data sets become too large the computational burden may hamper or greatly limit the use of CS, whether it is in longer processing times, increased computational requirements, or subdividing the problem into smaller data sets. Greedy algorithms, like orthogonal matching pursuit (OMP) [81, 82], offer a solution in these cases.

3.4 Greedy algorithms for solving the CS problem

Greedy algorithms perform step-by-step approximations towards the optimal solution, testing all candidate solutions and choosing the best fitted in every iteration in order to, eventually, find a global optimum solution, hence the name greedy. Although greedy algorithms may seem inefficient and a computational splurge, they are simple to understand and to implement and help bypassing the very costly and limiting step of matrix inversions, which are often required in linear programming solvers. Moreover, greedy algorithms can be easily parallelized and usually yield significantly shorter times to reach a valid reconstruction from sparse data. Many variations of the OMP algorithm can be found in the literature, each addressing a particular aspect of the minimization process. Some of the most well-known variations are: regularized OMP (ROMP) [83, 84], simultaneous OMP (SOMP) [85], compressive sampling matched pursuit (CoSAMP) [86], or stagewise OMP (StOMP) [84]. In this thesis, the selected greedy algorithm is OMP due to its well-known use in the CS field and ease of implementation yet performing sufficiently fast.

The OMP algorithm tries to find a solution to sparse data recovery and originates from the matching pursuit (MP) algorithm [87, 88]. The heuristic nature of OMP implies that approximations are assumed to reach, at some point, a global minimum in the problem-solving process. In each iteration of during the OMP algorithm, a new approximation to the sparse signal is found based on the information available at that point. As it is described in Algorithm 1, the contribution of the reconstructed signal projected into the measurement matrix Φ_t at that stage is subtracted from the original incomplete measured signal. This obtained residual information is orthogonal to the atoms of Φ_t —hence the orthogonal in OMP—is used in the next iteration as new information, hoping to find another atom in Φ_t that contributes in a more limited way in describing and decomposing the sparse signal \hat{x} . After each iteration, the residual is supposed to tend to 0 if y was a noise-free incomplete observation of x [89]. Otherwise, if measurement noise is expected, a stopping criterion to limit the number of iterations and computational burden could be substantiated on choosing a certain residual tolerance $\|r_t\|_2 \leq \epsilon$, or ℓ_2 -bounded noise [89], in accordance to the noise level. This stopping criterion is not always easy to compute and, therefore, there exist other stopping criteria such as the number of sufficiently prominent atoms found and the expected sparsity of the signal. For instance, a signal with expected sparsity of $S = 4$ would stop after finding the fourth atom, assuming that the following iterations would only add useless reconstruction noise to the approximation of x .

INPUTS:

-
- Sensing or measurement matrix: Φ , $(N \times M)$
 - Incomplete measurement of x : y , $(M \times 1)$
 - Maximum number of iterations: q_{max}

OUTPUTS:

-
- Sparse reconstruction of x : \hat{x}

INITIALIZE:

-
1. Set residual: $R_0 = y$. Clear selection of atoms: $\Lambda_0 = \emptyset$. Set counter: $q = 1$.

COMPUTE:

-
1. $\lambda_q = \arg \max_{j=1\dots d} |\langle r_{q-1}, \phi_j \rangle|$, $\Lambda_q = \Lambda_{q-1} \cup \{\lambda_q\}$
 2. $\Phi_q = [\Phi_{q-1} \quad \phi_j]$, $x_q = \arg \min_x \|y - \Phi_q x\|_2$
 3. $\hat{x}_q = \Phi_q x_q$, $r_q = y - \hat{x}_q$
 4. If $q < q_{max}$, increment counter q and go to 1; else, return $\hat{x} = \hat{x}_q$ and stop.
-

Algorithm 1: The OMP algorithm.

3.5 Sparsity enhancement

Often, data in the acquisition domain is not sparse enough or simply not sparse at all and, therefore, an adequate data preconditioning thanks to data transformations or projection bases must be found and incorporated in the CS recovery problem. Figure 3.6 shows the signal sampling process similarly to Figure 3.1 although including the final transformation step.

A received signal $x(t)$ is sampled every T seconds in a uniform fashion if Nyquist sampling is applied, that is, every nT seconds. The full set of discrete values of $y = x[nT]$ shown in this example is far from being sparse, although a number of transforms denoted as $T_n(\cdot)$ can be applied onto those discrete data to achieve sparse or near-sparse representations. It is the designer's decision to choose which of the N_T transforms provides a better sparsity level or to create a set of rules to automatically determine the winning transform among all candidates. In the proposed example, transforms T_1 and T_2 would yield sparse results presenting only one significant transformed coefficient although the former would show null energy in the other coefficients (all zeros) whereas the latter would present low energy coefficients evenly spread.

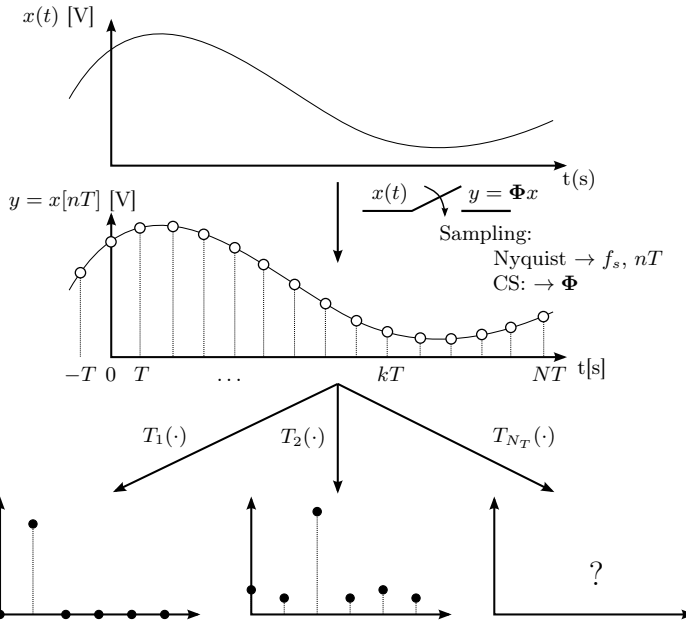


Figure 3.6: After sampling a continuous signal, the discrete elements can be transformed into several representation domains providing different sparsity levels.

Measuring sparsity is not straightforward and many methods can be found in the literature. The simplest and direct idea is sorting the amplitudes of the elements of x in a decreasing order and stored them in \hat{x} , satisfying $\hat{x}_n \geq \hat{x}_{n+1}$. The data in x are said to be sparse or compressible if \hat{x} presents an abrupt decay following a power law $|\hat{x}_n| \leq C \cdot n^{-1/p}$, with $p \leq 1$ and C any given constant.

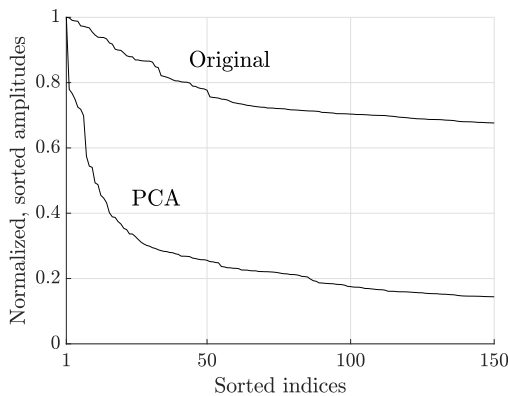


Figure 3.7: Normalized, sorted amplitudes of an original time-domain data set and its transformed coefficients using PCA. The decay on the PCA-transformed data is steeper, indicating sparser data.

As an example, the curves in Figure 3.7 show the normalized, sorted amplitudes of a GPR measurement in both the original time-domain and transformed representation using PCA for preconditioning the minimization problem. When comparing the sorted amplitudes of the two data representations, the decay is significantly sharper in the case of PCA which leads to the conclusion that it provides better energy compaction and, in principle, enhances the chances of finding a sparser scene reconstruction. Tests have shown that data sets showing similar power-law behaviors perform similarly, and those showing sharper decays outperform the other transforms. Despite this checked fact, there is no exact or even approximate way to quantify by how much is the performance improved by comparing curves like those in Figure 3.7 and, therefore, they should only be used as an indication of the data sparsity level and whether to use a given transform or not.

Transforms are not the only way to achieve sparser solutions found in the literature. The following subsections will introduce the concepts of data-based dictionaries which theoretically represent perfectly the scene and maximize sparsity—although inaccuracies, measurement noise and other undesired effects in real-data-based dictionaries produce results far from simulations—as well as including weighting matrices in the BPDN problem statement which are reevaluated iteratively—reweighted—and help bearing with the effort of finding the sparsest solution possible.

3.5.1 Sparsity enhancement using data transformations

A transform is a mathematical tool commonly used in countless applications. It is any mathematical function f that translates a set of elements into itself:

$$f : X \in \mathbb{R}^P \rightarrow X \in \mathbb{C}^P \quad (3.22)$$

or a different set Y , which is the case of interest for CS:

$$f : X \in \mathbb{R}^P \rightarrow Y \in \mathbb{C}^Q \quad (3.23)$$

with $P = Q$ or $P \neq Q$. As a generalization, a transformation matrix $\mathbf{T} \in \mathbb{C}^{N \times N}$ can be defined based on f . Recalling the expression for BPDN in (3.16), data transformations can be applied to the optimization problem by transforming both the dictionary $\tilde{\Theta} = \mathbf{T}_{\Phi}^* \Theta$ and the subsampled measurements $\tilde{y} = \mathbf{T}_{\Phi}^* y$, resulting in:

$$\hat{\sigma} = \arg \min_{\hat{\sigma}} \|\hat{\sigma}\|_1 \quad \text{subject to} \quad \left\| \tilde{y} - \tilde{\Theta} \hat{\sigma} \right\|_2^2 \leq \epsilon, \quad (3.24)$$

where $\mathbf{T}_{\Phi} \in \mathbb{C}^{M \times M}$ is a subsampled version of a given transformation matrix \mathbf{T} following the random subsampling sequence as dictated by Φ .

Data transformations are also known as preconditioners since transforms pre-condition the data in order to find an easier way towards a solution to a problem. For the application herein presented, the two following sparsifying bases or preconditioners have been selected:

3.5.1.1 The (inverse) Fourier transform

The fast Fourier transform (FFT) or its inverse version (IFFT) is a data-independent transform since matrix $\mathbf{T} \in \mathbb{C}^{N \times N}$, a square matrix with orthogonal columns and rows, is based on the generic expression:

$$\mathbf{T}_{mn} = \exp\left(\frac{-j2\pi mn}{N}\right), \quad (3.25)$$

with $m, n = 0, 1, \dots, N - 1$. This transform is of great interest due to its simplicity and efficient implementation, especially when training datasets become too large and other data-dependent transforms fail to produce results within affordable computational costs.

3.5.1.2 PCA as data-dependent sparsifying basis

PCA is a completely unsupervised machine-learning method used mainly for extracting features from data [90]. It relies on the availability of a training dataset which must be large and representative enough. Given the matrix Θ which includes the training dataset of the expected returns in its columns, its autocorrelation matrix is calculated as $\mathbf{R} = \Theta^* \Theta / (N - 1)$, being \mathbf{R} a square matrix of rank M . Previously, the mean of each atom in Θ has been subtracted. The matrix \mathbf{R} is then decomposed as $\mathbf{R} = \mathbf{T} \mathbf{\Sigma} \mathbf{T}^*$, where two new matrices are defined as $\mathbf{T} \in \mathbb{C}^{M \times M}$ or the eigenvectors matrix, $\mathbf{\Sigma} \in \mathbb{C}^{M \times M}$ with the eigenvalues in its diagonal. PCA allows data dimensionality reduction since most of the vector's energy after PCA transformation is reduced to few coefficients, hence discarding the negligible noise subspace since it is of no interest during the minimization problem.

3.5.2 Sparsity enhancement using data-based dictionaries

The matrix Ψ included in the compound matrix Θ is seen as a dictionary since in its columns are described all the expected signal occurrences in a measurement. Such descriptive signals must be accurate enough to guarantee high matching scores between the dictionary Ψ and the randomly measured signal y . From the imagery point-of-view, the goodness of the dictionary will also reflect in the sparsity of the result since, ideally, only one solution in the form of a bright peak in σ and nulls anywhere else indicates perfect sparsity. Of course, dictionary mismatches, even if small, are to be expected as well as measurement noise.

3.5.3 Sparsity enhancement using the re-weighted ℓ_1 minimization

Transformation- or dictionary-based sparsity enhancement may not be sufficient to guarantee the sparsest solution to a minimization problem that is *a priori* known to be sparse. Dictionary mismatch or measurement deviations may alter the reconstruction negatively. Adding an extra degree of freedom in the minimization in the form of weighting coefficients [91] is an interesting solution which may compensate those mismatches and eventually find a sparser solution if the right coefficients are selected.

The already relaxed weighted ℓ_1 minimization, as introduced in [92] by Candès and adapted to CS, is expressed as:

$$\hat{\sigma} = \arg \min_{\sigma} \|\mathbf{W}\Theta\sigma\|_1 \quad \text{subject to } y = \Theta\sigma, \quad (3.26)$$

where $\mathbf{W} \in \mathbb{R}^{K \times K}$ is a diagonal matrix containing K weighting factors w_k as in:

$$\mathbf{W} = \text{diag}(w_1, \dots, w_k). \quad (3.27)$$

Each weighting factor affects the k -th element in the compound dictionary Θ and has a clear impact on its respective k -th element in σ . Unless specific conditions contradict this assumption, the values of the weights in \mathbf{W} are unknown and, therefore, an iterative approximation to the sparsest solution arises a straightforward solution. However, the initial selection of weights and how to update them become two paramount steps in the minimization problem. In [92] the authors propose an algorithm that, after being adapted adequately to the case hereby proposed, initially minimizes the ℓ_1 problem and finds an intermediate solution $\sigma^{(0)}$ given an initial set of weighting coefficients $w_k^{(0)} = 1, k = 1 \dots K$. Since $\mathbf{W} = \mathbf{I}_K$, this first iteration is simply the ℓ_1 minimization proposed in Equation (3.21) which is used to update the weighting coefficients for the next iteration and recompute a new estimate of σ . There exist several rules in the literature to update the weighting coefficients but it has been found that the following definition, which includes a tolerance value ϵ , is one that guarantees avoiding the trivial solution of selecting σ to be zero in order to minimize sparsity and error:

$$w_k^{(q+1)} = \frac{1}{|\sigma_k^{(q)}| + \epsilon}. \quad (3.28)$$

With this update rule the weights in iteration $(q+1)$ depend to the inverse of vector σ found in the previous iteration. Indeed, in case of selecting a null ϵ , any element in σ presenting a value of zero would directly imply having its corresponding weight set to infinity, leading the solver to reach the above-mentioned trivial solution.

The minimize-reweight process can be performed iteratively until a given condition is met. This algorithm can be described in a generalized way as follows:

1. Initial conditions: set iteration $q \leftarrow 0$ and $w^{(0)} = [1, 1, \dots, 1]^T$.
2. Solve Equation (3.26) and find $\sigma^{(q)}$.
3. Update weighting coefficients $w_{(k)}^{(q+1)}$ using $\sigma^{(q)}$ and the selected ϵ according to Equation (3.28).
4. Assess the selected stop criterion (sparsity, convergence, maximum iteration reached, or similar). If not satisfied, increase iteration $q \leftarrow q + 1$, and go to point 2.

Since the literature is vague regarding speed of convergence and how vulnerable this algorithm may be in getting stuck in local minima, it is recommended to use a stopping criterion based on the obtained sparsity when reconstructing σ . In the application presented in Chapter 6 of this work, the maximum value of the reconstructed pixels is used as a reference to set a threshold. In that particular case, those pixel values above 10 % of that threshold will be considered as targets and, thus, will be accounted in terms of sparsity. If S pixels in σ are above the threshold, the sparsity of the image is S . Obviously, the lower the S is, the sparser the image is.

If the expected sparsity of the scene is known, selecting a target sparsity equal or above the expected sparsity would restrict the number of iterations required, making the reweighting process flexible with respect to a desired reconstruction fidelity. For instance, if a maximum of 3 bright targets are known to be present in a measurement, a safe stopping condition would imply setting the expected sparsity slightly above 3. Selecting exactly 3 may lead to a very conservative approach and higher iteration counts.

This method, in general, increases sparsity and reduces the background reconstruction noise although for longer processing times are to be expected since several iterations will be typically required to achieve sparser reconstructions.

3.6 Side information

Under certain conditions, having access to previous data describing the scene of interest may help reaching a solution in a minimization problem since any additional support information may reduce the reconstruction uncertainty and lead the algorithm to focus on fewer targets. This very reasonable and direct idea is mathematically introduced in [93], where the authors describe this support information as side information (SI). Although this is not a sparsity enhancement method by itself, when conditions that will be later discussed are met, using SI leads to sparser solutions.

The support or SI is fed to the generic BPDN minimization problem according to the following expression:

$$\hat{\sigma} = \arg \min_{\sigma} \|\sigma\|_1 + \beta g(\sigma - w) \text{ subject to } \|y - \Theta\sigma\|_2^2 \leq \epsilon, \quad (3.29)$$

where $\beta > 0$ and typically $\beta = 0$, vector w contains the SI, is of equal size as σ and is fundamentally similar to σ , contents-wise. Function $g(\cdot)$ is any function satisfying $\mathbb{R}^N \rightarrow \mathbb{R}$ and providing a similarity metric between σ and w . The minimization problem described in (3.29) is usually known as ℓ_1 - ℓ_1 or ℓ_1 - ℓ_2 if metrics $g(\cdot) = \|\cdot\|_1$ or $g(\cdot) = 1/2 \|\cdot\|_2^2$ are chosen, respectively. The ℓ_1 - ℓ_1 formulation is as follows:

$$\hat{\sigma} = \arg \min_{\sigma} \|\sigma\|_1 + \beta \|\sigma - w\|_1 \text{ subject to } \|y - \Theta\sigma\|_2^2 \leq \epsilon, \quad (3.30)$$

whereas the ℓ_1 - ℓ_2 case is:

$$\hat{\sigma} = \arg \min_{\sigma} \|\sigma\|_1 + \frac{\beta}{2} \|\sigma - w\|_2^2 \text{ subject to } \|y - \Theta\sigma\|_2^2 \leq \epsilon. \quad (3.31)$$

Empirical observations with simulated data lead to a first set of conclusions when testing both minimization approaches:

- ℓ_1 - ℓ_1 : sparsity is encouraged leading to low-contribution background and bright target. In very noisy simulated scenes, this approach provides the most remarkable results.
- ℓ_1 - ℓ_2 : Results respect fidelity to the measurement, which implies more noticeable background noises but still bright targets. The CVX [94] implementation of this approach is several times faster, and varies depending on the complexity of the scene.

In this work, we will use the ℓ_1 - ℓ_1 approach given better performance in increasing sparsity as documented, despite its higher computational load which can be easily overcome by parallel computing.

3.7 Conclusions

This chapter has introduced a limited list of concepts required to understand what the mathematical foundations behind CS are, how some of the most usual tools solve minimization problems, and how applications can benefit from some of the existing sparsity enhancement methods.

The idea describing the conventional signal sampling theorem and the conditions to apply it in real-world applications have been explained with visual examples, as well as mathematically.

In terms of solving minimization problems, the generalized problem statement has been introduced and all the more specific methods used in the following chapters such as the BPDN or the re-weighted ℓ_1 minimization problem. Additionally, the concept of side information is also introduced and aims at reducing the amount of required data to achieve sparse reconstructions.

Chapter 4

UWB Radars for Non-Destructive Testing

This chapter will give a short introduction to NDT, an extremely wide field with numerous frequency bands and endless technologies and materials, which will be immediately limited to the application treated in this manuscript. Some of the typical composite materials found in the industry as well as the most common defects that motivate having NDT techniques are also discussed. A quasi-optical radar used for NDT comprising a VNA and a set of focusing mirrors is used to acquire real measurements of recreations of delaminated ABS composites. The physical interactions and restrictions in this type of measurements are also discussed with illustrative examples. Finally, the benefits of CS for NDT are demonstrated for three differentiated reconstruction approaches: 1) direct raw signal reconstruction using IFFT as a preconditioning basis, 2) reflectivity function reconstruction using a dictionary which is built up using real observations or 3) synthetic data.

4.1 Introduction and applications

Multi-layered or composite materials have become a standard in industrial applications requiring strong resilience against structural and mechanic stress that may occur in a continuous fashion during their lifespan or in isolated, high mechanical stress episodes. Thanks to the combination of several layers of different materials (and potentially cores), each contributing to the whole with their own mechanic characteristics, composite structures outperform those made of typically just one single material. These materials are present in various proportions in an increasing number of strategic resources or components, and present special interest both for civilian and military applications. Windmill blades, aircrafts, submarines, small passenger ships [95] or large strategic infrastructures such as oil or gas pipelines are just some of the many examples where NDT is

currently used. Integrity inspection of those materials in a fast and reliable way becomes necessary and current NDT techniques allow minimally or non-invasive inspections partially satisfying those requirements. These techniques range from simple visual or manual inspection (hearing the sound changes while tapping the material [96] or microscope magnification [97]) to a variety of sensor-based inspection techniques in different frequency bands such as ultrasound [98, 99], microwave or UWB sub-THz radars [1, 100], thermography, time-domain spectroscopy (pulsed THz) [101] or X-ray.

Technique	Penetrability	Portable	Cost	Maturity	Overall score
MW/Sub-THz	++	+	+	+	++
Pulsed THz	+	+	-	-	+
Manual	--	++	+	++	-
X-ray	-	+	--	++	-
Ultrasound	++	-	-	++	+
Thermogr.	++	+	-	++	++

Table 4.1: Evaluation of different NDT techniques for inspecting dielectric composites based on multiple criteria.

Table 4.1 shows an evaluation of the cited NDT techniques based on the following criteria: Penetrability is related to the ability of the waves to propagate through dielectric composite materials (60 % of the total score); portable shows the possibility of transporting the the NDT equipment (10 %); cost implies any economic investment (purchase, operation and maintenance) related to the technique (20 %); maturity indicates how established a technique is in the NDT field (10 %). For all criteria, '++' means better while '--' means worst.

To summarize the evaluation in Table 4.1, manual inspection is limited to superficial inspection and has no penetration or see-through capability other than guessing defects by tapping, whereas X-rays present a very high penetration for polymers although ranging is not possible. Moreover, X-ray equipment requires a considerable economic investment, it is generally non-portable — although portable X-ray systems can be found [102, 103]— and uses ionizing radiation that may pose health risks to the operator [104] while, on the contrary, all the other techniques are considered safe. Microwaves, sub-THz waves and thermography obtain the highest global scores although the latter is the only technique that can provide defect depth information if an adequate bandwidth is used. Finally, the still not deeply explored pulsed THz inspection technique lacks penetrability although it provides very fine spatial resolutions.

This chapter will focus on UWB radars for NDT using VNAs given their ease of implementation, the good penetration of waves in the low EHF band (between 40 and 75 GHz) in dielectric composites and the ranging capability they provide.

4.2 Typical structures, materials and failure modes

4.2.1 Composite structures and materials

Composite structures, also known as smart material, usually consist of several layers of different materials whose specific properties provide higher performances than those of typical monolithic materials. By combining thin skin layers and porous or low-density cores, these structures are typically lightweight but robust against mechanical stress. Some of the most popular cores are the artificial honeycomb [105, 106] and the organic balsa wood [105, 107] (great strength and lightweightness in both cases) or foams (great tolerance to mechanical compression as well as lightweight). Due to the multiple layers these structures have, they receive the name sandwiches, and there exist several definitions which can be found in the literature depending on the number of layers or the layout pattern they follow. In [23, 108], composites are categorized as single layer or monolithic —Figure 4.1-a)—, multi-layer —Figure 4.1-b)—, two skin layers and one core —Figure 4.1-c), known as A-sandwich—, or two skin layers, two cores and one inner layer —Figure 4.1-d), known as C-sandwich.

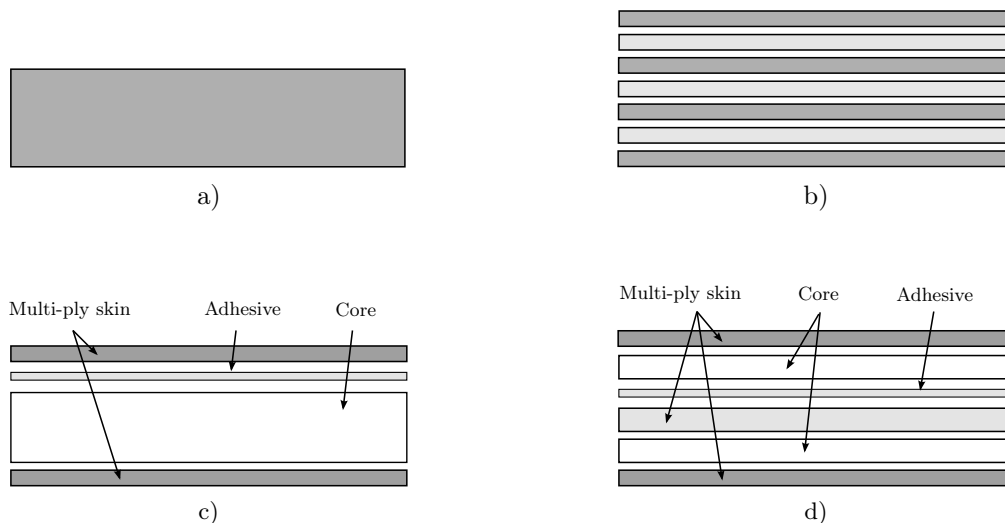


Figure 4.1: Schematics of typical composite materials: a) a solid or monolithic laminate, b) a multi-layered composite, c) an A-sandwich, d) a B-sandwich.

The skin layers can be made of, among others, carbon fiber, aramids (Kevlar) or fiberglass reinforced polymers, although only the non-conductive options allow see-through NDT, practically discarding carbon fiber as a candidate material since only superficial inspection is possible.

In this chapter, we will only focus on a two-layer ABS (acrylonitrile butadiene styrene) polymer to keep sample modeling complexity low.

4.2.2 Typical composite failure modes

Composites are made of several layers of different materials and possible defects or material failure may happen during the manufacturing process or due to structural wear caused by high levels of mechanical stress repeatedly inflicted during its lifespan. These failures endanger the mechanical integrity of the material and may cause a greater structure to fail. Some of the most common composite failure modes are:

Delamination: Separation of one or more layers in a composite forming unglued spaces inside the structure (1) or at the edges (2), as seen in Figure 4.2. An important mechanical property loss is expected after such failure. Since the created delaminations may be millimeter thick they may not be seen during visual inspection, hence the need for high-resolution inspections.

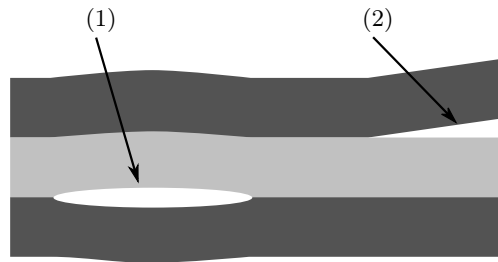


Figure 4.2: Failure mode: a delamination between two layers (1) and a delamination at the edge of the sample (2).

Cracks: These failures, if isolated, are the early sign of a future critical composite failure [109]. Cracks indicate that the composite is subject to a fatigue level sufficiently high to produce damage but still not affecting the integrity of the composite. Figure 4.3 shows possible cracks which will affect the composite in different ways. Point (1) is a superficial crack, whereas (2) happened in an inner layer, producing a small debond in the interface between layers, therefore, the layers adhesion is locally lost. Point (3) shows a transversal or progressive crack [109, 110] caused after advancing from the initial stage (1) which affects the top layer and continues through the other two layers.

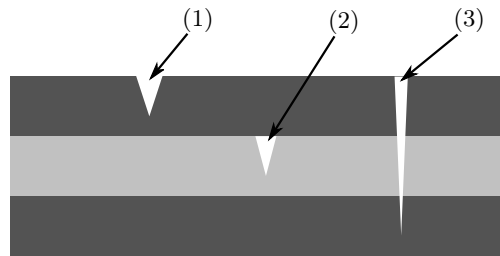


Figure 4.3: Failure mode: different cracks affect differently the structure with (1) an initial crack with low impact on the material integrity, (2) a crack that may produce a delamination between layers, and (3) a progressive crack affecting all the layers of the material and, thus, critically compromising its integrity.

Foreign inclusions: Figure 4.4 shows a foreign inclusion which can occur during the production of the composite material. Water vapor in the form of drops on the layer or pieces of protective sheet may remain partially glued to one layer, weakening the gluing process of the composite and limiting its mechanical strength.

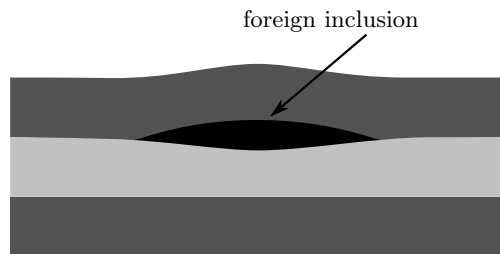


Figure 4.4: Failure mode: a foreign inclusion, which creates an integrity problem due to poor gluing between layers.

Buckling: Material buckling happens when a longitudinal axial tension compresses the composite beyond the nominal limits, bending the totality of the layers (Fig. 4.5). After ceasing compression, the material comes back to its original shape although one or more layers may have disbonded. The composite can no longer guarantee its mechanical resilience to compression.

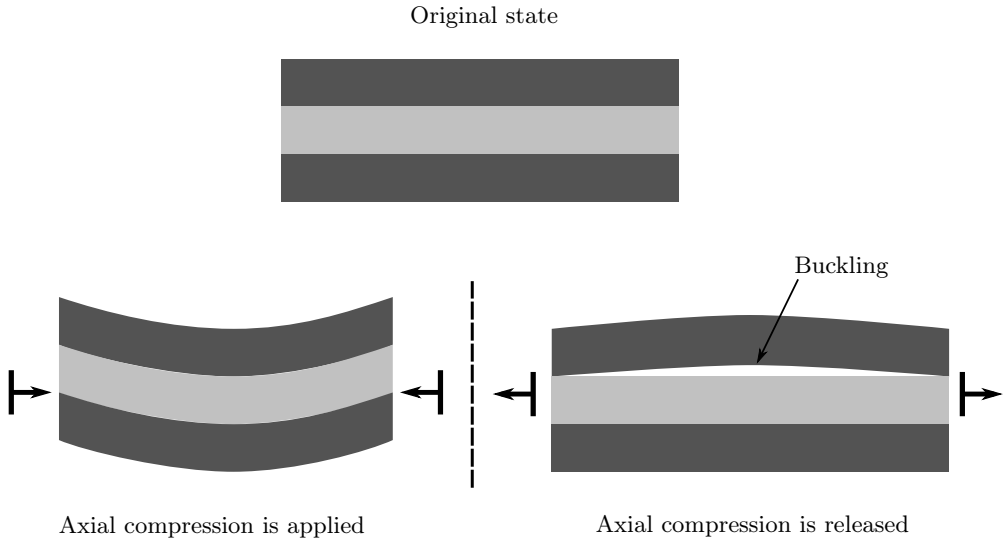


Figure 4.5: An additional failure mode: Buckling is produced after axial compression forces are applied to the structure, deforming it. If, during the decompression process, the material does not recover its original shape totally or partially, a delamination-like defect is created.

This chapter will only explore delamination-like defects which may happen in a two-layer material which, supposedly, has suffered from mechanical stress or gluing failure during production.

4.3 Focused NDT sensors

4.3.1 Set-up using focusing mirrors

The usual focusing set-up when a conical horn aperture is used is shown in Figure 4.6. The transmitted beam, generated by the VNA, originates at the antenna phase center and approximates to a spherical-shaped, diverging wavefront once in far field. A first concave mirror transforms the spherical wavefronts into planar wavefronts with parallel beams of diameter D , physically correcting the phase error or center-edge phase difference produced by the horn aperture. A second concave mirror transforms the beam into converging spherical wavefronts, finally collimating the beam into a focal point. The material to be tested, or DUT, is preferably placed in the focal point, where the beam spot is at its narrowest although imagery is still possible within the Rayleigh region, marked as b . Before every measurement campaign, a routine calibration is performed using full-reflection/no-reflection for making sure the focal point corresponds to the zero range and to compensate for any non-linearity in the measurement or circuit mismatches [111].

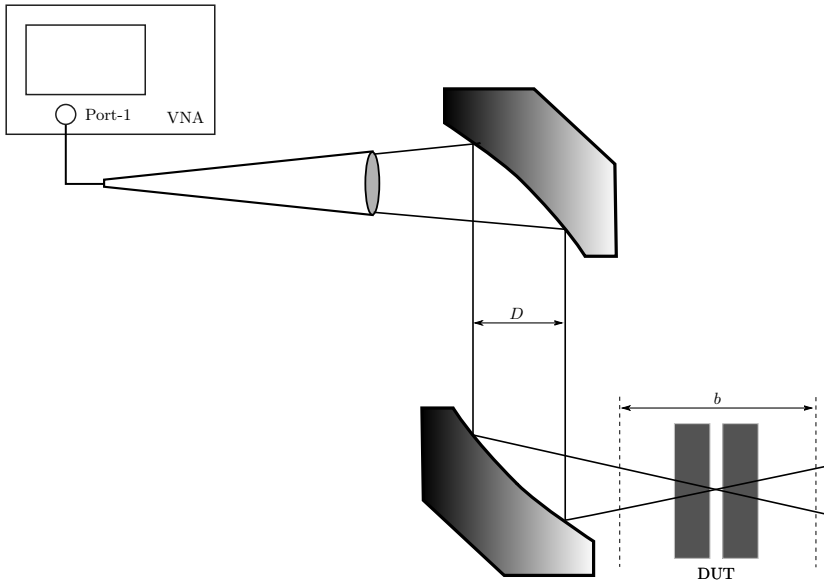


Figure 4.6: Schematic of a typical beam focusing set-up in NDT measurements. The concave mirrors are used to focus into a focal point the initially diverging wavefront radiated by the sensor.

4.3.2 The beam-waist effect

A very restrictive downfall of focused NDT systems is the so-called beam-waist effect, which restricts the thickness of the material to be inspected. In these systems, the parallel beams forming a wavefront are collimated by a convex lens onto a focal point or focus, as shown in Figure 4.7.

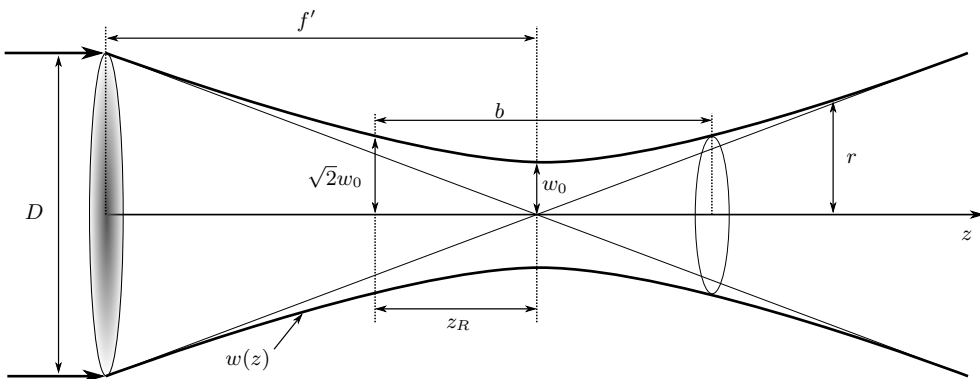


Figure 4.7: Schematic representation of the beam waist effect using a focusing lens. At the beam waist the beam spot size is of minimum size and, therefore, obtaining the finest system resolution possible.

The irradiance or the intensity of the Gaussian beam —generated by the TEM₀₀ fundamental mode— at a radial distance r from the central axis of the beam is defined as:

$$I(r) \propto \exp\left(\frac{-2r^2}{w_0^2}\right), \quad (4.1)$$

where w_0 is the beam waist or the smallest beam spot radius at the focal point f' :

$$w_0 = \sqrt{\frac{\lambda_0 z_R}{n\pi}} = \sqrt{\frac{\lambda_n z_R}{\pi}}, \quad (4.2)$$

with $\lambda_n = \lambda_0/n$ the wavelength inside a material with refractive index n and:

$$z_R = \frac{\pi w_0^2}{\lambda_n}, \quad (4.3)$$

the Rayleigh length or range. The Gaussian spot size along the z axis is expressed as:

$$w(z) = w_0 \sqrt{1 + \left(\frac{z}{z_R}\right)^2}, \quad (4.4)$$

which, for the particular case of $z = z_R$, yields:

$$w(z_R) = \sqrt{2}w_0, \quad (4.5)$$

known as the maximum spot size within the limits of the Rayleigh length. The lengths within a Rayleigh distance from the focal point f' , expressed as $z \in [f' - z_R, f' + z_R]$, are commonly considered to be collimated and of maximum resolution. Outside that interval, imagery should be avoided since the spatial resolution is rapidly worsened and unfocused returns are obtained, in addition to a loss of reflected energy. A direct consequence of the beam-waist effect is that the sample thickness is limited to roughly the confocal parameter:

$$b = 2z_R = 2\frac{\pi w_0^2}{\lambda_n}. \quad (4.6)$$

If thicker samples must be inspected, the sample must be placed at different distances from the focal point in order to cover the totality of the sample thickness or use a focusing lens with a smaller diameter D , worsening the system resolution w_0 . In focusing configurations with two concave mirrors instead of lenses, the diameter parameter D corresponds to the diameter of the parallel beam between the mirrors.

4.3.3 Interactions between waves and multilayered materials

Any multilayered material reached by electromagnetic waves will interact and alter those waves according to two well-known phenomena: Snell's law governing the refraction and reflection effects, and the response to medium interfaces. Their respective mathematical descriptions are discussed next.

4.3.3.1 Snell's law

In NDT measurements, the incidence angle of the impinging planar waves may be decisive in the final imagery quality. Snell's law explains that planar waves propagating between two or more media with different refractive indices will reflect at the interfaces with equal angle ($\theta_i = \theta_r$) but also a portion of the waves will propagate through the next medium due to diffraction, as depicted in Figure 4.8.

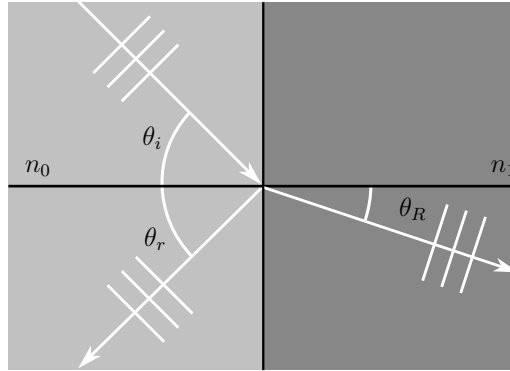


Figure 4.8: General case of reflection and refraction effects in an interface between two media ($n_1 > n_0$) for a wavefront impinging at $\theta_i > 0^\circ$.

The angles of refraction — i.e. transmission — θ_R with respect to the normal axis of the transmitted wave will vary following the expression of the Snell's law:

$$n_0 \sin \theta_i = n_1 \sin \theta_R, \quad (4.7)$$

which, after isolating θ_R , becomes:

$$\theta_R = \sin^{-1} \left(\frac{n_0}{n_1} \sin \theta_i \right). \quad (4.8)$$

From the previous equation we can extract the critical angle of incidence for which no transmission is possible and the wave is completely reflected by forcing $\theta_R = 90^\circ$ or $\sin \theta_R = 1$, which yields:

$$\theta_c = \sin^{-1} \left(\frac{n_1}{n_0} \right). \quad (4.9)$$

The expression in (4.8) and (4.9) are clear in highlighting that the propagation of waves in NDT may be highly conditioned to the alignment of the focusing set-up and the sample. For maximizing see-through capabilities using a monostatic-like configuration, incidence angles $\theta_i \approx 0^\circ$ must be imposed unless a bistatic configuration is foreseen. Figure 4.9 shows a simplified case of an air-material-air configuration with $n_2 = 2$ and an incident angle in the first interface between media 1 and 2 of $\theta_i^{1,2} = 0^\circ$, where the superscripts $m, m+1$ and $m, m-1$ indicate the interface between medium m towards medium $m+1$ and vice versa, respectively. According to Snell's law, both the reflected and refracted angles ($\theta_r^{2,1}$ and $\theta_R^{1,2}$, respectively) will be 0° . In an identical manner, the interface between media 2 and 3 will yield the same results with $\theta_i^{2,3} = \theta_r^{3,2} = 0^\circ$, which is an ideal result for the NDT case treated in this chapter. The wavefront impinging in the interface between media 2 to 1 has an angle $\theta_i^{2,1} = \theta_r^{3,2} = 0^\circ$. Finally, the wavefront from the reflection in the second interface is received in the first medium with $\theta_R^{2,1} = 0^\circ$. Both reflections from the first and second interfaces are indeed received back at the NDT sensor directly into the focusing set-up.

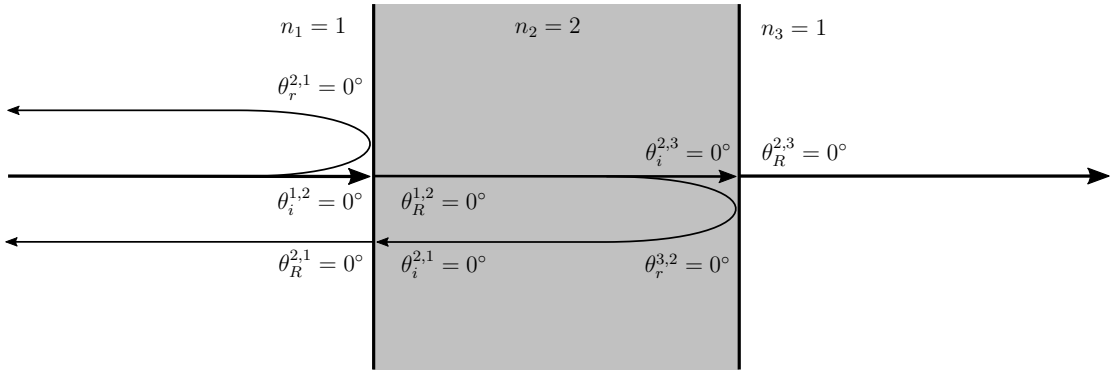


Figure 4.9: Particular case of reflection and refraction angles for an air-medium-air interface ($n_1 = n_3 = 1$ and $n_2 = 2$) and an incident angle of 0° .

For a multi-layered scene, the expression (4.8) for a forward-propagation case can be generalized as:

$$\theta_R^{i,i+1} = \sin^{-1} \left(\frac{n_i}{n_{i+1}} \sin \theta_i^{i,i+1} \right), \quad (4.10)$$

or, in backward-propagation case:

$$\theta_R^{i,i-1} = \sin^{-1} \left(\frac{n_i}{n_{i-1}} \sin \theta_i^{i,i-1} \right). \quad (4.11)$$

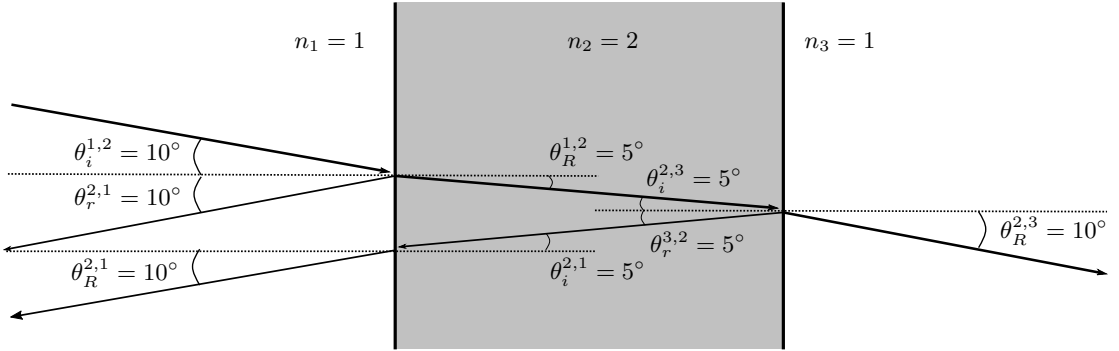


Figure 4.10: Particular case of reflection and refraction angles for an air-medium-air interface ($n_1 = n_3 = 1$ and $n_2 = 2$) and an incident angle of 10° .

If, for the same configuration, an incidence angle greater than 0° is used, let us assume $\theta_i^{1,2} = 10^\circ$, the planar waves will interact with the media transitions as displayed in Figure 4.10. The resulting returns from the first and second interfaces ($\theta_r^{2,1}$ and $\theta_R^{2,1}$, respectively) will no longer be aligned to the normal of the measurement and may end up not being received by the focusing system.

4.3.3.2 Media interfaces and interactions with waves

According to Maxwell's equations, the quotient of the electric and magnetic fields of a complex wave (\mathbf{E} and \mathbf{H} , respectively) yields the impedance the wave is subject to [112]. In the case of propagation in free space, the wave impedance is defined as:

$$Z_0 = \frac{|\mathbf{E}|}{|\mathbf{H}|} = \sqrt{\frac{\mu_0}{\varepsilon_0}}, \quad (4.12)$$

with μ_0 the magnetic permeability and ε_0 the electric constant, both in the free-space case. The impedance of a wave propagating in any material other than free space ($n, \varepsilon_r > 1$) is:

$$Z = \sqrt{\frac{j\omega\mu}{\sigma_m + j\omega\varepsilon}}, \quad (4.13)$$

with σ_m the conductivity of the material. In the case treated in this chapter a dielectric material is inspected—that is, an almost non-conductive material with $\sigma_m \rightarrow 0$. Therefore, the wave impedance in the material can be rewritten as:

$$Z = \sqrt{\frac{\mu}{\varepsilon}} = \sqrt{\frac{\mu_0}{\varepsilon_0\varepsilon_r}}, \quad (4.14)$$

with ε_r the relative permittivity of the material. The expression for Z can be related to Z_0 if we define the previous expression recalling (4.12):

$$Z = \frac{Z_0}{\sqrt{\varepsilon_r}}. \quad (4.15)$$

A composite made of multiple layers of different materials can be approximated as a multi-section transmission line, as depicted in Figure 4.11, with Z_0 the wave impedance in free air, and ρ_i the reflection coefficients, l_i the physical length of the section and Γ_i the reflection response of the i -th interface, respectively.

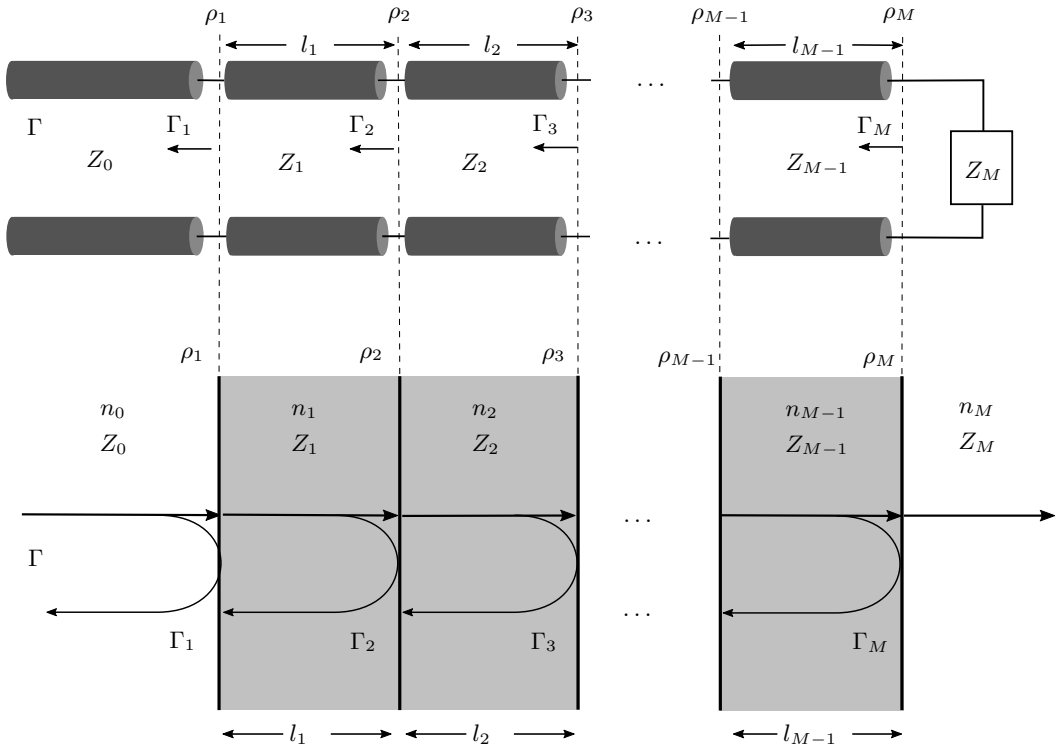


Figure 4.11: Equivalent circuit based on transmission lines theory for representing a multi-layered material and the interactions between interfaces and incident wavefronts.

At every transition or interface, and always under the condition that there is normal incidence $\theta_i = 0^\circ$, the impedance mismatch between transmission line sections creates a reflection coefficient which expresses the portion of energy reflected from the interface.

$$\rho_i = \frac{Z_i - Z_{i-1}}{Z_i + Z_{i-1}}, \text{ with } 0 \leq \rho \leq 1. \quad (4.16)$$

For the above-mentioned multi-section structure, the wave impedance of each i -th line can be derived from the general description of Z_0 in (4.15):

$$Z_i = \frac{Z_0}{\sqrt{\varepsilon_{r,i}}} = \frac{Z_0}{n_i}, \quad (4.17)$$

with $\varepsilon_{r,i}$ the relative permittivity of the i -th material in the section. The expression for the reflection coefficient in (4.16) can be modified by incorporating the definition of Z_i as in (4.17). After manipulation, we reach the following expression which only depends on the refractive indices of the materials and is frequency-dependent, although for the sake of simplicity this dependency is omitted:

$$\rho_i = \frac{n_i - n_{i-1}}{n_i + n_{i-1}}. \quad (4.18)$$

A recursive expression allows computing the partial and total reflection responses for all the interfaces [113]. Γ_i defines the reflection response of the i -th interface and all the following interfaces in a recursive way, starting from the last interface with $\Gamma_M = \rho_M$:

$$\Gamma_i = \frac{\rho_i + \Gamma_{i+1}e^{-2j\delta_i}}{1 + \rho_i\Gamma_{i+1}e^{-2j\delta_i}}, \quad (4.19)$$

from where it is obtained that $\Gamma = \Gamma_1$ is directly the global reflection response received back at the sensor. If a VNA is used, $\Gamma = S_{11}$. The parameter δ_i is the phase thickness for the i -th layer in the multi-layered material:

$$\delta_i = \frac{\omega}{c_i}l_i = \frac{2\pi fl_i}{c_o/n_i} = \frac{2\pi n_i l_i}{\lambda_0}, \quad (4.20)$$

with l_i the physical length of the i -th layer. f is the vector containing all the tested frequencies, therefore, Γ_i will also be a vector with all the reflection responses for every frequency in f . This formulation is typically used to characterize in an exact way [113] the response of a multi-layered material to an electromagnetic stimulus. In this case, an NDT measurement will exploit the reflected signals from each interface in the material.

4.4 Description of measurements

4.4.1 Sensor specifications

In order to test the medium interface reconstruction capabilities of CS applied to NDT, an artificial air gap simulating the effects of a delaminated two-layer composite was made of ABS

using a 3D printer. ABS was chosen due to its high transparency (a refractive index of $n \approx 1.5$ [114]) in the sub-THz band and its good thermal properties [115], required during the 3D printing process. In Figure 4.12, the two ABS blocks (M_1 and M_2) are placed with the axis of their widest dimension perpendicular to the beam propagation axis z at radius $r = 0$. This positioning guarantees that the beam spot is completely located on the samples. This distance is such that the samples are well within the Rayleigh length of the system and the focal point is located at the back side of M_1 , where the air gap is created. Block M_1 is placed on a fixed pedestal whereas block M_2 is on a moving platform which can be manually adjusted to create air gaps with a resolution of 0.1 mm.

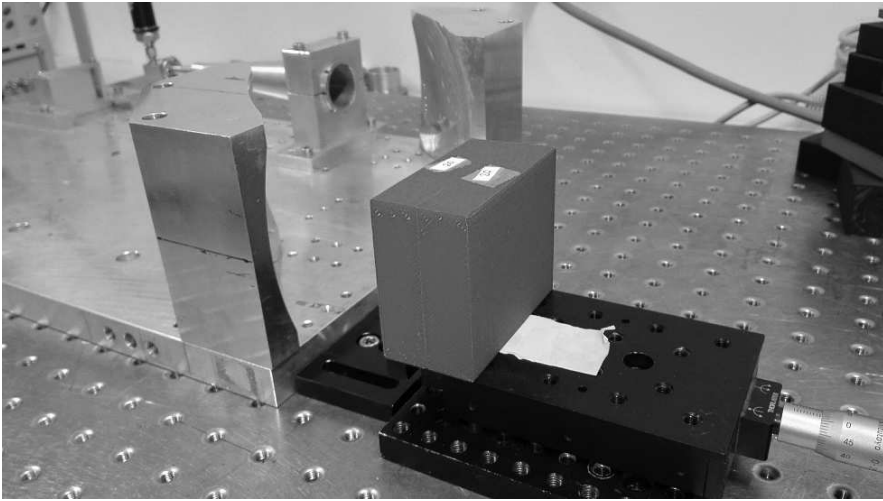


Figure 4.12: NDT measurement set-up in which two ABS blocks (foreground) replicate a delamination artifact. A set of reflectors and conic antenna (background) is used to collimate the beam into a focal point.

The sensor used for measuring the ABS sample is a VNA (shown in Figure 4.13) by AB Millimetre, model MVNA-8-350. It can perform measurements within the ranges 8-336 GHz and 660-1000 GHz [116, 117] and can collect complex valued S -parameters. The frequency range used for performing measurements was set between 45.834 GHz to 74.953 GHz since the band 44-45.843 GHz presented phase instability despite calibration. The operative bandwidth is therefore roughly 29 GHz, providing a range resolution of 5 mm in free space and 3.3 mm inside ABS. The dynamic range of the sensor for the exploited frequency band was approximately 120 dB [118].

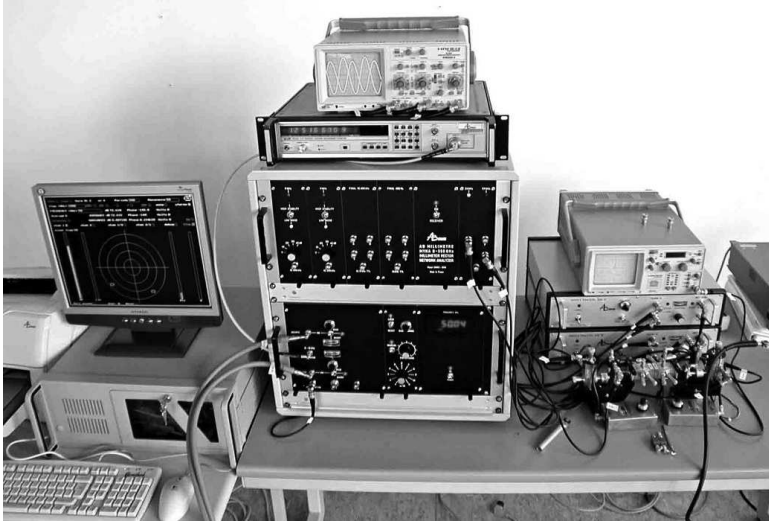


Figure 4.13: VNA model MVNA-8-350 by AB Millimetre with a visualization and data storage unit on the left side. Image obtained from [12].

A conical horn antenna as the one depicted in Figure 4.14 model SH-V-FB-10 with a gain of 24.58 dBi at 60 GHz is used in the 44-75 GHz band.



Figure 4.14: Conical horn antenna model AB Millimetre SH-V-FB-10. Image obtained from [13].

The top-down view in Figure 4.15 and the perspective view in Figure 4.16 show the same beam focusing configuration as in Figure 4.6, where the two concave mirrors focus the beam radiated by the antenna into the sample. The conical horn antenna, as well as the adjusting platform are also seen in both figures.

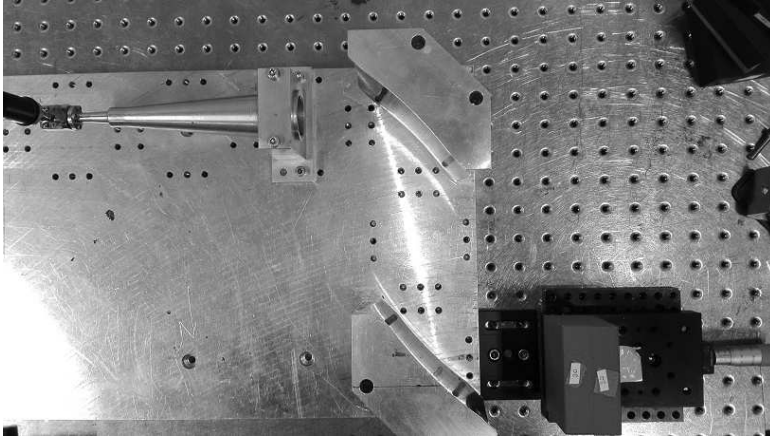


Figure 4.15: Top-down view of the measurement set-up. The antenna, two reflectors and D.U.T. follow the same arrangement as displayed in Figure 4.6.

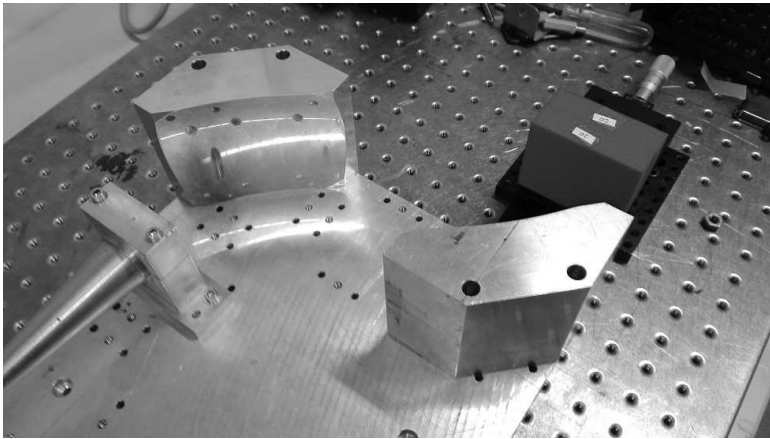


Figure 4.16: Close perspective view of the antenna, parabolic mirrors and the DUT.

4.4.2 Data simulation

In Figure 4.17, the arrangement of the two identical ABS blocks (both of thickness $l_1 = l_2 = l = 20$ mm) is shown, where multiple air gap conditions can be reproduced by manually adjusting their separation distance g , or air gap thickness. The equivalent multi-section transmission line schematic is also included which is used to derive the reflection responses of every interface.

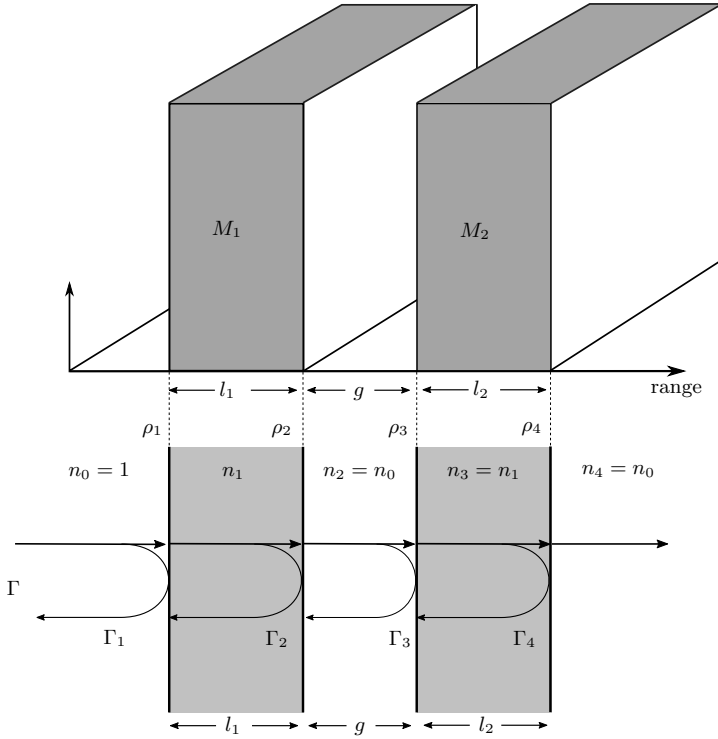


Figure 4.17: Schematic of the NDT set-up simulating an air gap between two delaminated layers of a composite polymer. Two identical ABS blocks (M_1 and M_2) with a width of $l = 20$ mm are used, whereas the air gap thickness g is manually adjustable.

The reflection coefficients for each interface assuming that $n_1 = n_3 = n$ and $n_0 = 1$ are calculated using (4.18) with the following results:

$$\begin{aligned}
 \rho_1 &= \frac{n_0 - n_1}{n_1 + n_0} = \frac{1 - n}{n + 1}, & \rho_2 &= \frac{n_1 - n_0}{n_1 + n_0} = \frac{n - 1}{n + 1}, \\
 \rho_3 &= \frac{n_0 - n_1}{n_1 + n_0} = \frac{1 - n}{n + 1}, & \rho_4 &= \frac{n_1 - n_0}{n_1 + n_0} = \frac{n - 1}{n + 1}.
 \end{aligned} \tag{4.21}$$

The phase thicknesses relative to the distance the wavefronts travel inside each of the three layers (material-air-material) are obtained using (4.20):

$$\begin{aligned}
\delta_1 &= \frac{2\pi n_1 l_1}{\lambda_0} = \frac{2\pi n l}{\lambda_0}, \\
\delta_2 &= \frac{2\pi n_2 l_2}{\lambda_0} = \frac{2\pi g}{\lambda_0}, \\
\delta_3 &= \frac{2\pi n_3 l_3}{\lambda_0} = \frac{2\pi n l}{\lambda_0}.
\end{aligned} \tag{4.22}$$

Finally, the reflection responses in frequency are recursively obtained for all interfaces using (4.19), and setting $\Gamma_4 = \rho_4$ as initial condition:

$$\begin{aligned}
\Gamma_4 &= \rho_4, \\
\Gamma_3 &= \frac{\rho_3 + \Gamma_4 e^{-4j\pi n l / \lambda_0}}{1 + \rho_3 \Gamma_4 e^{-4j\pi n l / \lambda_0}}, \\
\Gamma_2 &= \frac{\rho_2 + \Gamma_3 e^{-4j\pi g / \lambda_0}}{1 + \rho_2 \Gamma_3 e^{-4j\pi g / \lambda_0}}, \\
\Gamma &= \Gamma_1 = \frac{\rho_1 + \Gamma_2 e^{-4j\pi n l / \lambda_0}}{1 + \rho_1 \Gamma_2 e^{-4j\pi n l / \lambda_0}}.
\end{aligned} \tag{4.23}$$

4.4.3 Adapting NDT sensors to CS sampling

As described in Figure 4.18, a virtual instrumentation device is suggested for driving the VNA to perform reflection measurements following a given frequency vector $f = [f_1, f_2, \dots, f_N]$, where $f_n \in \{0, 1\}$ describes the M frequencies that will be interrogated (marked as 1) after selecting a given random frequency subsampling $k_f = M/N$ and those that will be skipped (marked as 0). The interspacing between selected frequencies is governed by a uniform random distribution which takes into account both minimum and maximum frequency interspacing values ($d_{f_{\min}}$ and $d_{f_{\max}}$, respectively), and must satisfy $1 \leq d_{f_{\min}} < d_{f_{\max}}$. Conventional VNA operation would directly interrogate all frequencies within the bandwidth B using a fixed frequency step size of Δf , as SFCW radars do as described in Subsection 2.3.3.

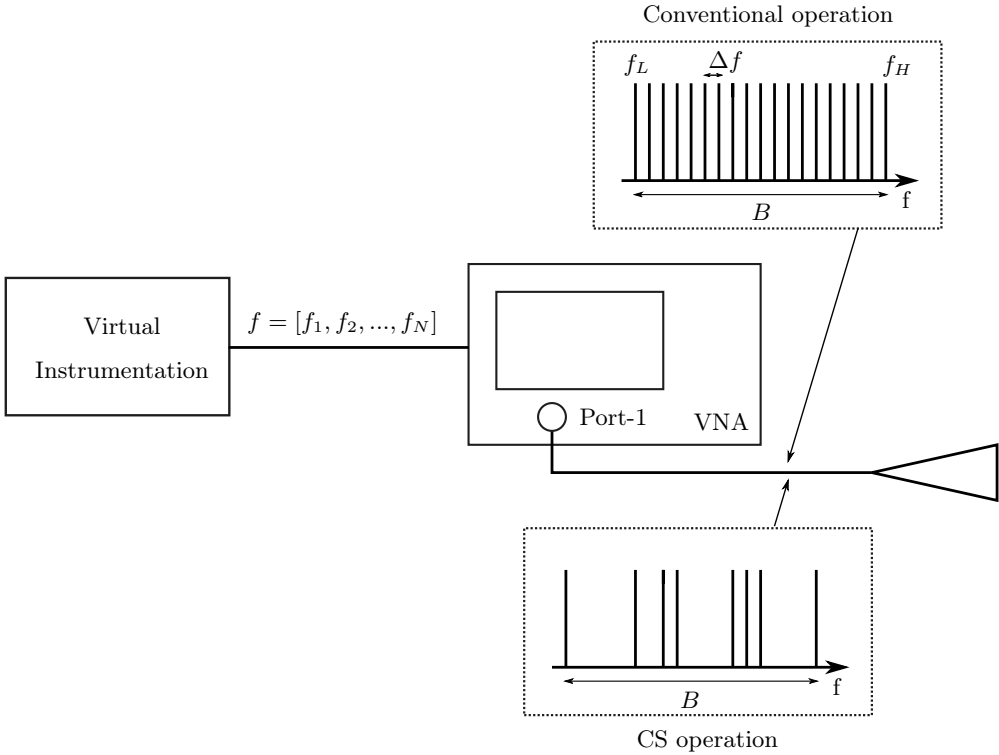


Figure 4.18: Generation of NDT measurements using a VNA could be governed by virtual instrumentation. The VNA needs to only interrogate those frequencies randomly selected as specified by f .

For the measurements presented in this chapter, the full S_{11} measurement is considered as the complete measurement vector x of length N . Table 4.2 summarizes all the parameters used in the measurement campaign.

VNA company	ABmm	Model	MVNA-8-350
Configuration	Focused beam	Mode	reflection only
Freq. band	44-74.953 GHz	Actual freq. band	45.834-74.953 GHz
Bandwidth	30.953 GHz	Actual bandwidth	29.119 GHz
Freq. samples N	6000	Actual N	5000
Freq. step	5.19 MHz	Dynamic range	≈ 120 dB
Free space resol.	5 mm	Resol. in ABS	3.3 mm
Antenna type	Conical horn	Antenna model	ABmm SH-V-FB-10
Aperture gain	24.6 dBi (60 GHz)	Horn size (LxD)	150 mm x 31 mm

Table 4.2: Main VNA and antenna parameters involved in the NDT measurement campaign discussed in this chapter.

For this experiment 6000 frequency points were swept for every S_{11} measurement, although the first 1000 frequencies are dropped due to phase instability introduced by the VNA (the size of vector x is therefore $N = 5000$).

4.4.4 Populating the dictionaries

An alternative to reconstructing the original Nyquist-rate signal x is reconstructing the so-called scene reflectivity function σ it by solving the minimization problem in (3.20). Vector σ is generally assumed to be sufficiently sparse thanks to the great sparsification capabilities of using a measurement-based transform or dictionary. This dictionary Ψ is populated with all possible or expected occurrences after conducting a measurement. In other applications like TWI or GPR, σ can be interpreted as the intensity level for each pixel or voxel describing a 2-D or 3-D scene, respectively. In this application, σ corresponds to the likelihood of a certain atom (column) in the dictionary Ψ to better represent the measured signal.

For the application hereby presented, each i -th column of Ψ , indicated as $(\psi)_i$, is populated with a synthetic or real reflectivity measurement of a given air gap thickness. In the case of synthetic measurements, all possible air gap values with an air gap step size are generated using a S_{11} -parameters simulator.

When using real measurements for populating Ψ it is advisable to include multiple realizations of the same measurement given the possible sensor fluctuations, noise and other spurious phenomena during the observation and which may be different from measurement to measurement. These repetitions may increase the possibility that an observation is described in Ψ , despite the above-mentioned phenomena.

4.5 Experimental results and CS reconstructions

4.5.1 CS reconstructions possibilities

The conceptual block diagram in Figure 4.19 shows the considered image reconstruction approaches in NDT and their respective steps to achieve scene reconstruction: The solid line is the path to perform a reconstruction \hat{x} of the unknown full measurement x and subsequent conventional image reconstruction (IFFT preconditioning for this application, as described in Section 3.5.1.1). The dashed line shows the two approaches for reflectivity function extraction based on the use of a dictionary (populated with either real measurements or synthetic data) describing all possible occurrences in the measurement.

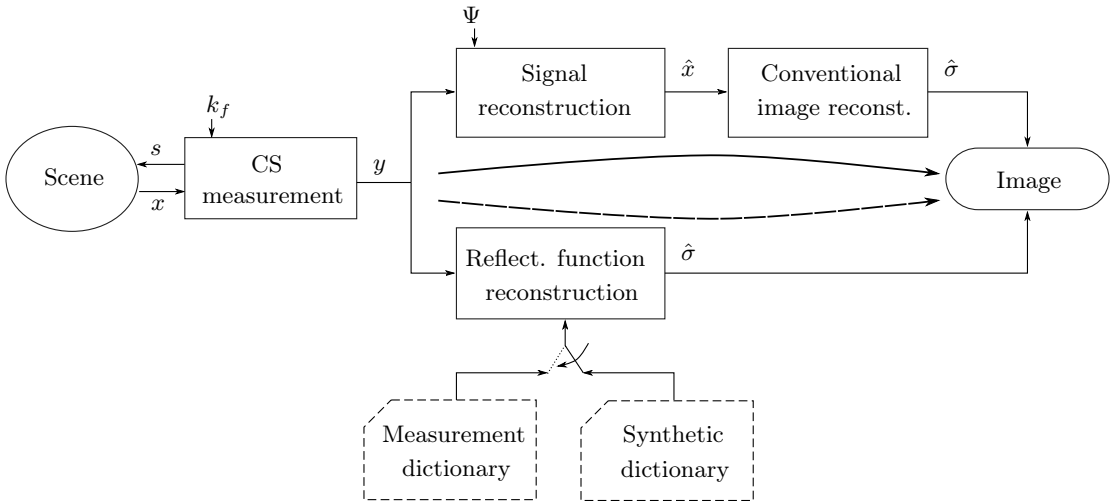


Figure 4.19: Image reconstruction possibilities: 1) the solid line shows the path using sparse signal reconstruction and farther conventional imagery; 2) the dashed line uses a measurement-based or synthetic dictionary to reconstruct the reflectivity function.

4.5.2 General simulation parameters

The assessment of the robustness is performed via Monte-Carlo simulations using real test measurements and dictionaries populated using synthetic or real measurement data. All frequency subsampling rates from 5% (high subsampling) to 50% (low subsampling) (10 rates). A range of additive Gaussian noise levels are injected in the test measurement, yielding SNR levels from -24 dB to $+15$ dB (20 levels). The OMP algorithm is used due to the very limited sparsity of the scene—it is assumed that a small number of bright coefficients corresponding to the medium interfaces will be recovered, whereas the rest will be close to zero thanks to the high transparency of ABS in the used frequency band. For every subsampling rate-SNR level combination, 500 realizations were run. The total amount of realizations was 100,000, lasting for 17 hours on a Intel Core i5-7200U processor running Matlab R2015b.

4.5.3 Reconstruction metrics

Based on the type of reconstruction performed, whether it is the determination of the interfaces or the gap class determination, two reconstruction metrics are used to generate robustness figures:

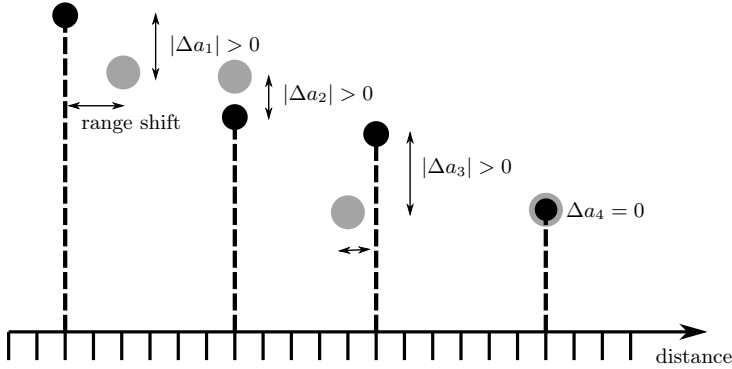


Figure 4.20: Schematic of the Metric A applied to signal reconstruction using CS. The amplitude and interface positioning differences are considered to compute a global reconstruction score.

- *Metric A* - Interface reconstruction: For every Monte-Carlo simulation, a clean test signal is kept containing only the $N_P = 4$ most prominent peaks corresponding to the interfaces echoes, as shows in Figure 4.20. These peaks, their amplitudes as well as their range locations are used as the ground truth. This type of ground truth is not CAD-based or physically obtained, but depends on the characteristics (e.g., range resolution) of the sensor. Two types of deviations are considered for this metric, which are expressed by the following equation describing the score J_A obtained with metric A:

$$J_A = \frac{1}{N_P} \sum_{j=1}^{N_P} [(1 - p_j)(1 - |\Delta a_j|)]^{1/p_E}. \quad (4.24)$$

First, the amplitude deviation Δa_j , which is the difference between the j -th expected amplitude in the ground truth and the reconstructed value. Perfect amplitude reconstruction implies that $\Delta a_j = 0, \forall i$. Secondly, the positioning deviation which translates into a given positioning tolerance to accommodate possible slight peak shifts in range due to limited range resolution or high reconstruction noise due to very low k_f values. In this NDT application, it is not of utmost importance to achieve a perfect gap thickness determination but to reveal its presence and approximate dimension. For the following results, a tolerance of one range bin is considered and a penalty $p_j = 0.5$ is applied in case a peak is shifted ± 1 range bin and $p_j = 1$ for any higher shift (total penalty). If a perfect match is obtained, a null penalty $p_j = 0$ is applied. An indulgence factor p_E is added to the expression to enable adapting the obtained scores based on the strictness requirements, which become less strict as p_E increases. For the experiments in this chapter, an intermediate $p_E = 2$ is chosen:

$$J_A = \frac{1}{N_P} \sum_{j=1}^{N_P} \sqrt{(1 - p_j)(1 - |\Delta a_j|)}. \quad (4.25)$$

The score J_A will vary between 1 for perfect interface amplitude and positioning reconstruction and 0 if any of the two deviations or both are unacceptable.

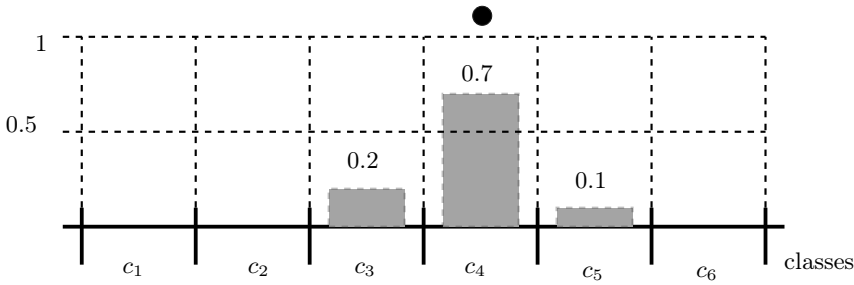


Figure 4.21: Schematic of the Metric B for which results are separated into classes and their respective likelihoods from which a final score is obtained for the winner class candidate. In the example, only 6 classes are considered.

- *Metric B* - Air gap thickness or class determination. In this case, for every Monte-Carlo realization the test measurement is assigned to a gap thickness class during reconstruction, as displayed in Figure 4.21. A perfect class determination is obtained if one class obtains a score of 1. Inversely, several classes may be given a likelihood score l_c which is normalized so that $\sum_{c=1}^C l_c = 1$. After CS reconstruction, the Metric B score J_B is obtained by selecting the decided gap thickness class with the highest normalized likelihood.

$$J_B = L_{c_{max}}(1 - p_{c_{max}}), \quad \text{with } c_{max} = \{c : \max_c(l_1, l_2, \dots, l_C)\}. \quad (4.26)$$

A class shift happens when a class is decided and does not correspond to the true class. The distance between the decision and the ground truth is called class shift. A penalty coefficient $p_c = 0.5$ substantiated on the same reasoning as in metric A and acting as a class tolerance is conceded if one of the classes adjacent to the true class is selected as the one with highest likelihood. The value of p_c is null if no penalty is to be applied, i.e. perfect class determination, and 1 if the class shift is 2 or more classes. In the event of using several measurements to build the training sets for each class, all the individual intra-class likelihoods obtained after CS reconstruction are summed in order to apply the Metric B normally.

4.5.4 Results: the signal reconstruction approach

For this reconstruction approach, a total of 100,000 Monte-Carlo simulations were run to achieve stable scores that accurately describe the approach performances. These scores are based on the metric A, which in this case will use a distance bin deviation tolerance of 1. The quality of the signal reconstruction will, as expected, vary based on the subsampling rate and the added Gaussian noise level of the observation.

Figure 4.22 shows a comparison of the obtained results using scores for the signal reconstruction and the IFFT transformation basis to sparsify data. Three frequency subsampling rates are plotted, 0.05, 0.25 and 0.5, along with the scores using the original fully-sampled measurement as a comparison against conventional imagery. For all cases, a reconstruction score of 90% is set to be the goal to reach so CS can be safely applied. For $k_f = 0.5$ and 0.25 the goal is reached for SNRs = +4 and +8 dB, respectively. A perfect target reconstruction (score 1) is achieved for both $k_f = 0.5$ and 0.25 at SNR = +12 dB, whereas this only happens at SNR = +22 dB for $k_f = 0.05$. The $k_f = 0.5$ scores curve overlaps that of the original imagery although the performance starts degrading rapidly for SNR values of 6 dB and lower. For this application, we make the assumption that any SNR level above +10 dB can be considered as favorable, near-laboratory condition measurements, as it is typically the case for short-distance NDT. For $k_f = 0.05$, however, the goal score is reached for an SNR of 16 dB and higher, which indicates that such a low subsampling rate would be discouraged. As a comparison, the conventional imagery method reached the goal score at SNR = -10 dB.

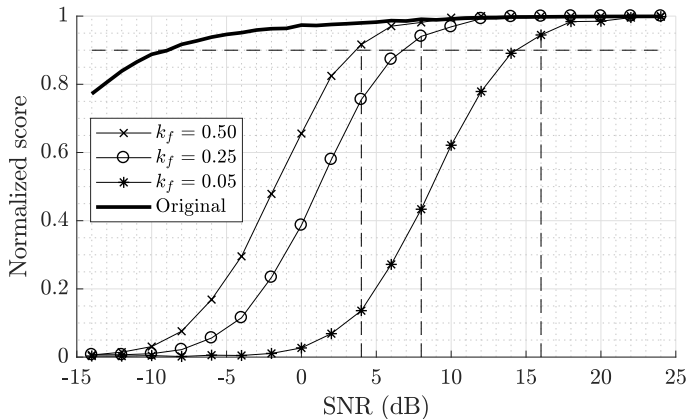


Figure 4.22: Reconstruction score vs. SNR using an IFFT transformation basis as sparsifying basis, OMP and 500 Monte-Carlo realizations.

The scores produced by all k_f and SNR combinations are shown in Figure 4.23 which, analogously to Figure 4.22, shows the region of k_f -SNR combinations where scores achieve the goal. The results show that a safe operation region for this sensor would be limited by the combinations satisfying SNR > 10 dB and $k_f > 0.2$.

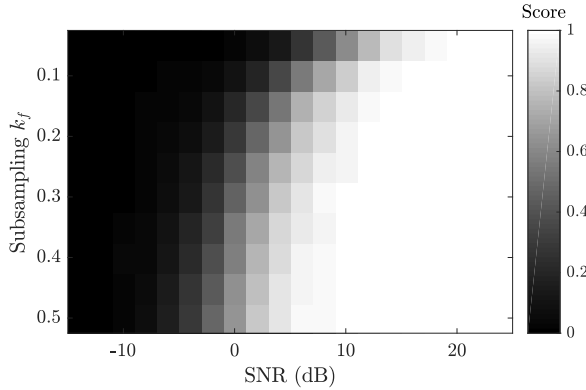


Figure 4.23: Matching scores for CS measurement reconstructions using an IFFT basis and OMP. A total of 500 Monte-Carlo simulations were run for each combination of subsampling rate (k_f) and SNR value.

4.5.5 Results: the reflectivity function reconstruction approach

Similarly to the presented results for the signal reconstruction approach, the air gap class determination likelihood scores (metric B) are presented in Figure 4.25. The dictionary matrix was populated using multiple repetitions of real measurements of air gap separations, that is, for every separation 4 real measurements were added to the dictionary, yielding a total of 36 (9x4) atoms for 9 possibilities. This is done to reduce the effects of spurious phenomena during a measurement that may reduce the reconstruction performance.

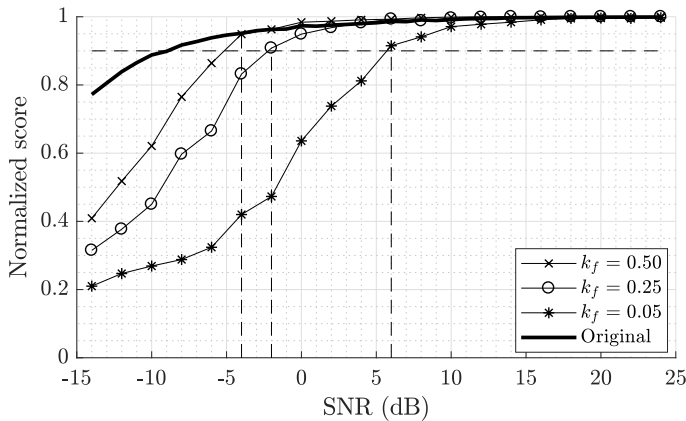


Figure 4.24: Reconstruction scores vs. SNR using real S_{11} measurements as sparsifying basis, OMP and 500 Monte-Carlo realizations.

The Monte-Carlo results in Figure 4.24 show that this method performs with very promising results, since the goal score is reached at SNRs -4 , -2 and $+6$ dB for the subsampling rates

$k_f = 0.5, 0.25$ and 0.05 , respectively. When compared to the scores obtained using the original imagery method, we can appreciate that the $k_f = 0.5$ curve overlaps the optimum results down to $\text{SNR} = -4$ dB, which suggests this method is highly robust against noise. Similarly, the conventional imagery only starts overperforming the $k_f = 0.25$ results for SNR levels of $+2$ dB or lower, which can be considered as very noisy under typical NDT measurement conditions.

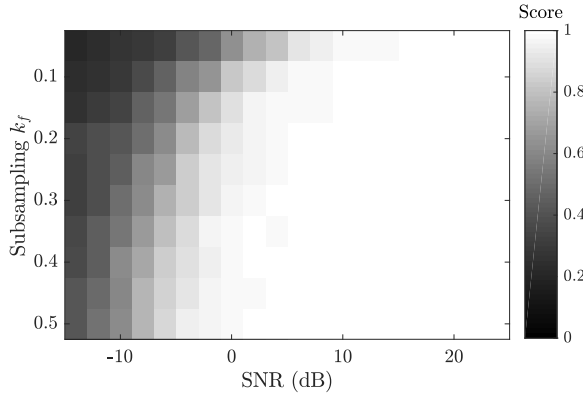


Figure 4.25: Matching scores for real-data dictionary and OMP. 500 Monte-Carlo simulations were run for each combination of subsampling rate (k_f) and SNR value.

In the third reconstruction approach, the dictionary was populated using synthetic measurements according to the S_{11} model, instead of real measurements. Scores are in this case also based on the metric B and are computed for the same number of hypotheses. The score of 0.9 is reached for subsampling rates $k_f = 0.5, 0.25, 0.05$ for SNR values of $+2, +6$ and $+14$ dB, respectively. The maximum score value for higher SNR values never reaches 1, in contrast to the previous experiments. The performances obtained using the third reconstruction approach are far from the original imagery results.

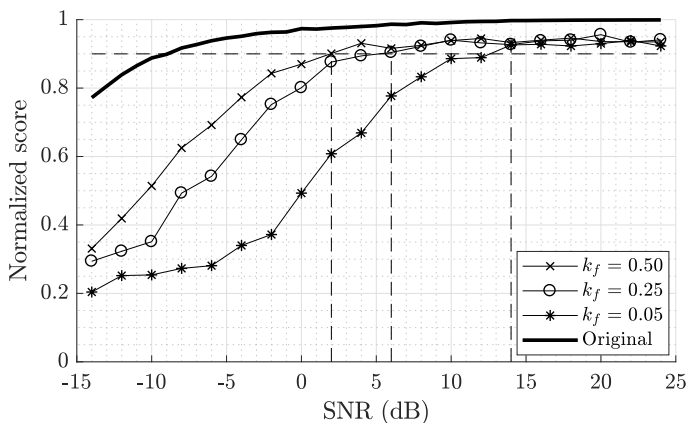


Figure 4.26: Reconstruction scores vs. SNR using synthetic S_{11} measurements as sparsifying basis, OMP and 500 Monte-Carlo realizations.

From Figure 4.27 we can see that none of the SNR- k_f combinations reaches the maximum score of 1, although a safe region above 0.9 can also be found for those operation points in $k_f > 0.15$ and SNR > 10 dB in all cases.

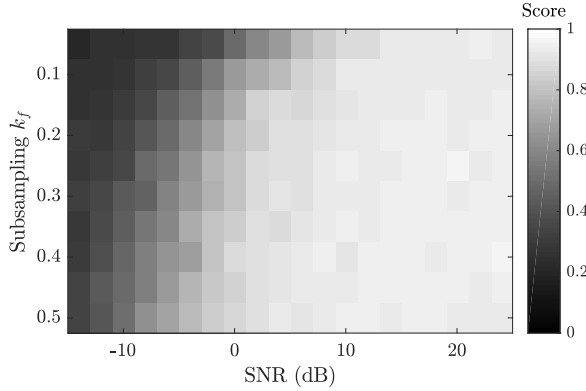


Figure 4.27: Matching scores for a synthetic-data dictionary and OMP. 500 Monte-Carlo simulations were run for each combination of subsampling rate (k_f) and SNR value.

The goal score is achieved for lower SNR values for the tested k_f although scores never reach perfect reconstruction levels and stay marginally above the goal score 0.9. This fact is shown to be true in Figure 4.27, where all k_f -SNR combinations indeed yield scores lower than in the previous experiments, most likely due to several effects which are not considered in the simple S_{11} model employed:

- Particular sensor behaviours not accounted for.
- Lack of model for the antenna radiation diagram.
- Mismatches produced by the quasi-optical focusing system (connectors, mirrors).
- Inaccurate estimation of ε_r for the tested samples.
- Wrong assumption of the location for the tested material.

4.5.6 Examples of the effects of subsampling and noise

Beyond the accurate performance evaluation of the presented NDT system combined with CS that the curves shown in the previous pages may provide, it is interesting to understand in a visual way how the different frequency subsampling rates k_f can affect the CS reconstruction, using as a reference a conventional, full sampling approach. Following that reasoning, next are displayed several examples which combine low and high subsampling rates k_f with low and high SNR levels, and this for every tested CS approach.

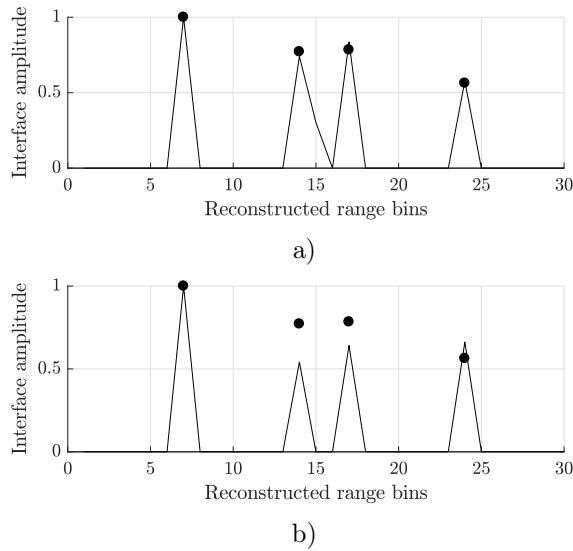


Figure 4.28: CS reconstruction of real NDT measurements using the signal reconstruction approach and OMP: a) $k_f = 0.50$ and $\text{SNR} = 16$ dB, b) $k_f = 0.50$ and $\text{SNR} = 0$ dB.

First, examples of the IFFT signal reconstruction approach are given. Figure 4.28-a) shows an almost perfect signal reconstruction using $k_f = 0.5$ and an $\text{SNR} = 16$ dB whereas in Figure 4.28-b) we can see a similar scenario but under a noisy observation with $\text{SNR} = 0$ dB. There are certain amplitude differences with respect to the ground truth but the interfaces positioning are perfectly reconstructed.

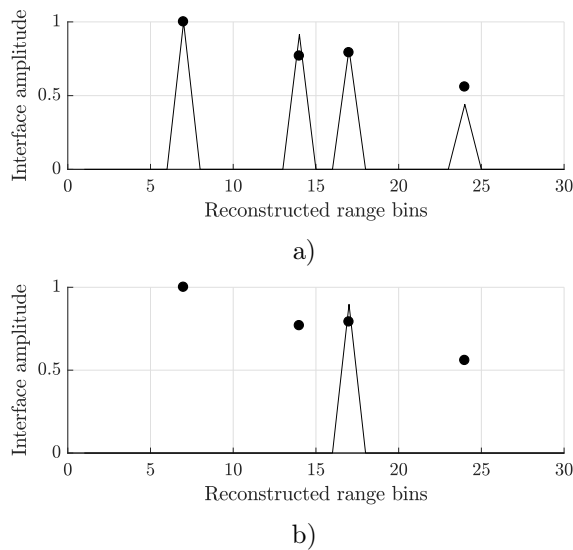


Figure 4.29: CS reconstruction of real NDT measurements using the signal reconstruction approach and OMP: a) $k_f = 0.05$ and $\text{SNR} = 16$ dB, b) $k_f = 0.05$ and $\text{SNR} = 0$ dB.

We can conclude that CS reconstructions using a subsampling factor as high as 50% are very much unaffected by noise, therefore visually validating the conclusions previously reached thanks to Figure 4.23.

Whenever the subsampling rate becomes much lower, the CS reconstruction quality is greatly affected. This is shown in Figures 4.29-a) and b). The former indicates that for SNR= 16 dB a more than acceptable reconstruction is obtained, despite the very low amount of data kept. As for the latter plot, only one of the interfaces was reconstructed, indicating that the low data collected and high noise levels produce a too high degree of uncertainty. In other realizations of the same experiment, one interface would be reconstructed although with a range shift or directly no interface would be reconstructed at all. As expected, low subsampling rates and noisy measurements are to be avoided.

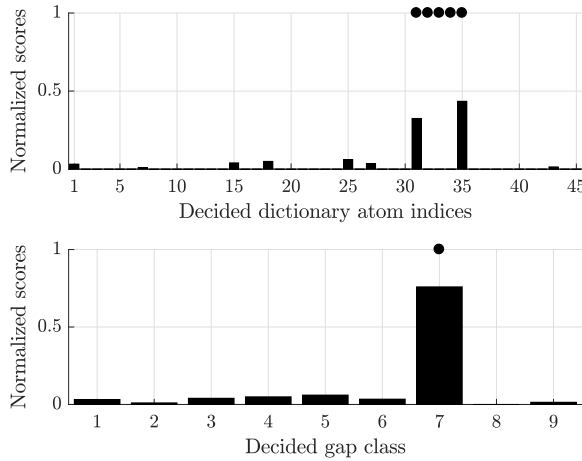


Figure 4.30: Decisions for an 11-mm air gap, SNR = 16 dB, and $k_f = 0.5$: Top, decided thickness atoms; bottom, decided thickness class. A dictionary built up using real measurements is used, along with OMP.

Second, examples of air gap thickness determination are given following the same procedure as above although using a dictionary populated with real measurements in its atoms. In Figure 4.30-top, all 45 training measurements or atom indices are numbered in the x axis of the plot. The normalized score for each atom is provided as well as, in circles, the atoms that must be decided upon to achieve a correct decision. In the following examples, a test vector from class 7 — corresponding to an air gap thickness of $g = 11$ mm— is used as test measurement. The circles indeed restrict the ground truth to indices 31-35, which are the five indices corresponding to class 7. The results shown in the top figure correspond to a high subsampling $k_f = 0.5$ and high SNR = 16 dB. It is apparent that one candidate from class 7 (index 34) has achieved the maximum score and, therefore, a correct decision. In Figure 4.30-bottom, the same results are displayed although stacked per class.

Figure 4.31 shows the scores for $k_f = 0.50$ and 0 dB of SNR. In this case, the likelihood of atom 35 is lower and we can also see that other candidates from adjacent classes 6 and 8 are obtaining non-zero scores. This gives the idea that, despite the high noise level, the tested observation will contain an air gap pertaining to classes 6, 7 or 8 (that is, thicknesses 9, 11 or 13 mm), with the most likely class being class 7, which is a correct assumption.

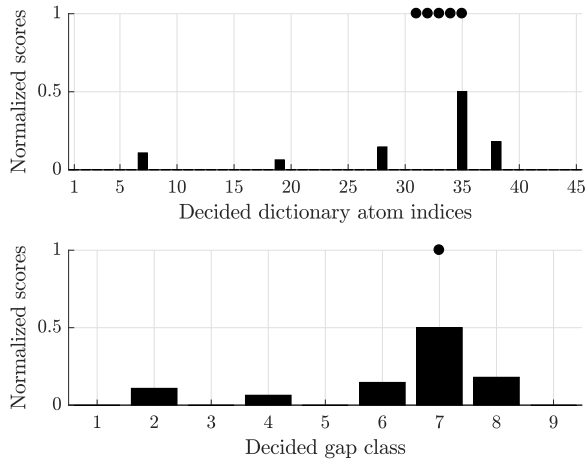


Figure 4.31: Decisions for an 11-mm air gap, SNR = 0 dB, and $k_f = 0.5$: Top, decided thickness atoms; bottom, decided thickness class. A dictionary built up using real measurements is used, along with OMP.

In the next figure, the very low subsampling rate $k_f = 0.05$ is tested. It is worth highlighting that, for such low k_f , best results were obtained by only keeping 3 candidate atoms instead of 9 in the previous examples. This is a known problem with CS algorithms such as OMP for which increasing the number of iterations during the greedy reconstruction typically leads to an uncontrolled degeneration of results. Figure 4.32 displays high scores for the correct class under an SNR of 16 dB, whereas in Figure 4.33, with SNR = 0 dB, class 7 is still selected although contributions from classes 2 and 5 also arise, increasing the uncertainty of evaluating the decision as correct.

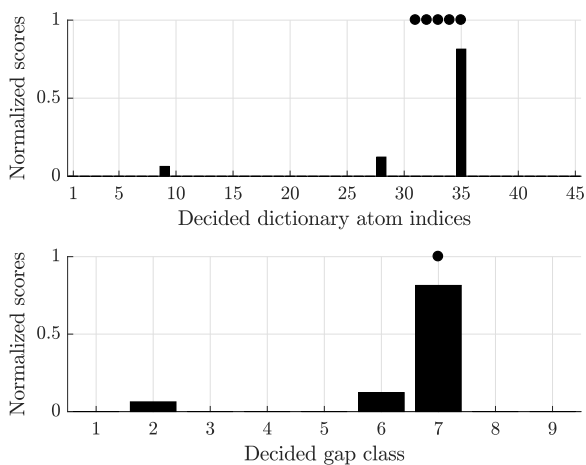


Figure 4.32: Decisions for an 11-mm air gap, $\text{SNR} = 16$ dB, and $k_f = 0.05$: Top, decided thickness atoms; bottom, decided thickness class. A dictionary built up using real measurements is used, along with OMP.

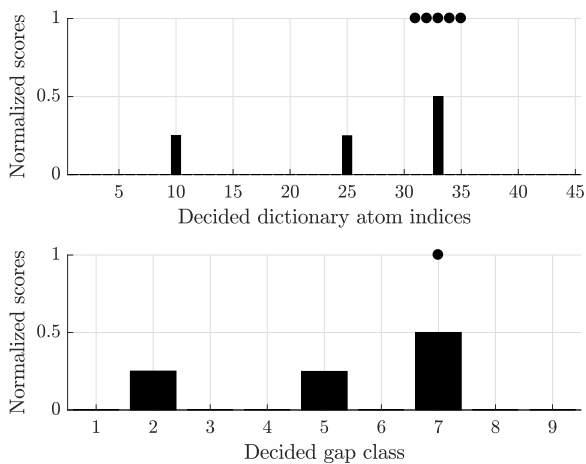


Figure 4.33: Decisions for an 11-mm air gap, $\text{SNR} = 0$ dB, and $k_f = 0.05$: Top, decided thickness atoms; bottom, decided thickness class. A dictionary built up using real measurements is used, along with OMP.

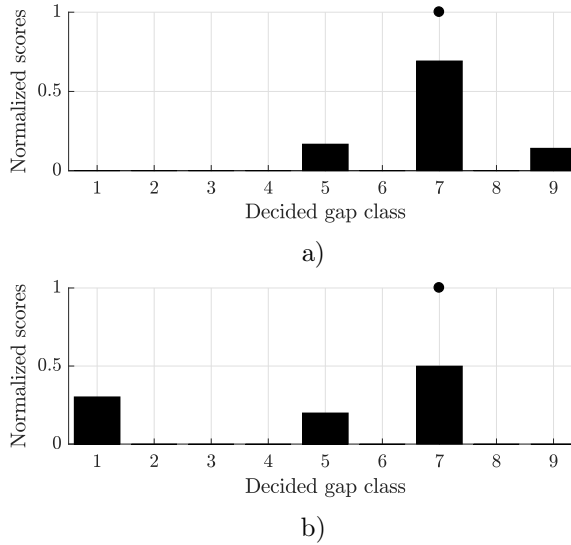


Figure 4.34: Gap class decisions for an 11-mm air gap, $k_f = 0.5$, and: a) SNR = 16 dB; b) SNR = 0 dB. A dictionary built up using simulated measurements is used, along with OMP.

Finally, the examples for the CS air gap determination based on a dictionary populated using synthetic measurements are presented. Figure 4.34-a), results obtained with $k_f = 0.5$ and SNR = 16 dB, shows clear although less blunt results indicating that the selected class is number 7 since. As for the case of having a noisier realization, Figure 4.34-b), class 7 is marginally selected with high uncertainty since class 1 presents a comparable score.

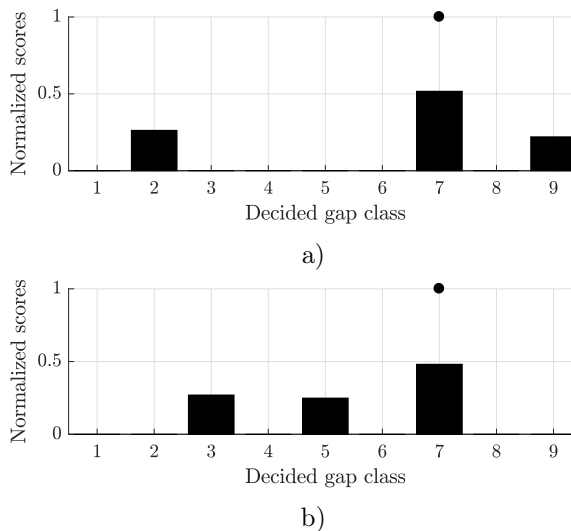


Figure 4.35: Gap class decisions for an 11-mm air gap, $k_f = 0.05$, and: a) SNR = 16 dB; b) SNR = 0 dB. A dictionary built up using simulated measurements is used, along with OMP.

The results for $k_f = 0.05$ are, as predicted by Figure 4.27, significantly more affected by high levels of noise and extreme frequency subsampling. Even in the case of $\text{SNR} = 16$ dB, class 7 is given a much lower score than when using real measured data for creating a training dictionary. This reconstruction approach indeed does not appear to be a solid candidate against the other two previous approaches, and this on the condition that an accurate enough model for the reflection responses is developed.

4.6 Conclusions and discussion

This chapter has explained how typical inspection of multilayered materials can benefit from CS. By a series of experiments on real NDT measurements simulating an ABS composite with defects (air gaps), and by creating a training database of all considered defects (varying air gap thicknesses), we have been capable of accurately extracting the positions of each layer in the fictive faulty sample, as well as identifying that an air gap is present while, at the same time, drastically reducing the amount of measurements required. The robustness of CS as a tool for NDT has been tested by corrupting the tested NDT observations with additive Gaussian noise which proved that CS can perform successfully even under very low SNR conditions. Low SNR levels are very unlikely to happen in this type of short-distance, quasi-ideal conditions, hence reinforcing the idea that the obtained CS performances are completely on the safe side and can be ready to be implemented in real NDT sensors.

The approach using real measurements to create a training dictionary yields the best performances since the similarity with the test observations is obviously maximum, provided that the sensors is always used on reproducible operation conditions. We can conclude that the idea of using modeled observations as an alternative to having to actually do the onerous task of measuring all possible expected occurrences is plausible although the model must be sufficiently well-matched to reality. If the available observation model yields poor results, the alternative of using the inverse Fourier transformation to form the dictionary may guarantee superior results. Moreover, the IFFT preconditioner is data independent and thus, whenever the measurement configuration is modified or a different sensor is used, it is unnecessary to readjust the CS problem solving part: the same dictionary is valid for all configurations.

All the key results obtained in this chapter are summarized in Table 4.3 to give a global idea of how NDT can perform under the effects of random subsampling and for every CS reconstruction approach tested.

Reconstruc. type	k_f	SNR at 90%	SNR at 100%	Exploitable
Signal reconst.	0.5	4 dB	12 dB	yes
	0.25	8 dB	12 dB	yes
	0.05	16 dB	22 dB	no
Meas. dict.	0.5	-4 dB	6 dB	yes
	0.25	-2 dB	6 dB	yes
	0.05	6 dB	18 dB	marginal
Synth dict.	0.5	2 dB	never	yes
	0.25	6 dB	never	yes
	0.05	14 dB	never	no

Table 4.3: Conclusions table providing concise guidelines on the exploitability of the three presented CS reconstruction approaches applied to NDT. The evaluations are given for three frequency subsampling rates: conservative (0.5), moderate (0.25) and extreme (0.05).

The interest of CS in this field is not only limited to data reduction but also enables reusing out-fashioned, typically low speed VNA's or similar systems for NDT imagery. Whereas a modern, cutting-edge VNA can perform a frequency sweep in the order of one second, older measurement systems may take minutes to fulfil one measurement. Given the achieved subsampling results, providing a subsampling rate $k_f = 0.2$, we can envisage a reduction by 5 in the scanning time which is a remarkable time reduction in moving scanners performing continuous imagery of large pieces or structures.

Chapter 5

Ground Penetrating Radar

This chapter will review the related GPR state of the art and introduce the theoretical background such as wave propagation and attenuation through the ground, as well as discuss how to adapt the NDT physical theory as described in Chapter 4 to GPR, especially the effects of media interfaces. Moreover, serious undesired target masking effects, produced by the very strong first reflection from the ground and the standing waves between the antenna and the ground, may completely disable the ability of the GPR to find suspicious targets buried close to the surface. Hence, a dedicated signal treatment based on intrinsic signal modeling is applied, which models the interactions between the antenna and the ground. The intrinsic signal modeling compensates for the often considerable depth mismatch due to the internal reflections inside the transmitting antenna. The same concept of SFCW radar with a VNA as the one used for NDT will operate the GPR system. Given the unfocused nature of GPRs and its movement along the ground during measurements, SAR will be used to create reference reconstructions, although CS and SAR-like measurements dictionary allows bypassing all SAR processing. Finally, there will be an explanation on how to perform frequency and spatial subsampling during measurements as prior knowledge to the final robustness analysis of CS reconstructions.

5.1 Introduction and applications

GPRs are radars used for producing imagery inside the ground, including substrates and any object that may be buried in it. Based on this generic description, many are the conceivable uses of GPR, whether they are established or state-of-the-art applications [119, 120]. The applications of GPR cover multiple fields, including the following:

- the detection of buried objects in military contexts (landmine detection [121] or wiring),
- the detection of road pavement or bridge maintenance [122], or pipe location and leakage, among many other civil engineering applications,

- the detection of utility [123] or clandestine man-made tunnels,
- multiple applications in agricultural and environmental engineering [124],
- the discovery and exploration of geological [125] and archaeological structures,
- the detection of animal [126] or human [127, 128] remains in forensics.

From a signal generation point of view, GPRs can be classified as time-domain, using short impulses and listening periods, just like pulsed radars; or frequency-domain GPRs, which use the SFCW type radar explained in Chapter 2. The flexibility of SFCW enables generating UWB signals that provide imagery showing the composition of the soil and any object with fine range resolutions. In this chapter, a GPR following the stepped-frequency approach is used to perform measurements. These SFCW GPR sensors were already employed in the UHF band [129] or lower bands [130] for detecting buried objects such as utility pipes since the 1980's. The L band (1-2 GHz) was used in [131, 132] for detecting buried mines with sufficient resolution thanks to the improved resolution provided by SAR measurements, while taking into account the limitations in ground penetration at that frequency band. GPR becomes common in the literature especially in the second half of 1990's, when the available technology was more and more affordable. Already in 1998, a research paper from the RMA [133], clearly mentions the need to use ultra-wideband GPRs and increase their maximum frequency to 3 GHz or above to improve the produced imagery. Many studies have appeared until today discussing several ways of improving the GPR results by combining data or modified processing techniques. It is not until the current decade that higher frequency GPRs became common, reaching 8 GHz [134] and covering the full L/S/C band for better resolution. Nevertheless, achieving higher frequencies may not be fruitful given the very high signal attenuation of soil-like materials at those frequencies.

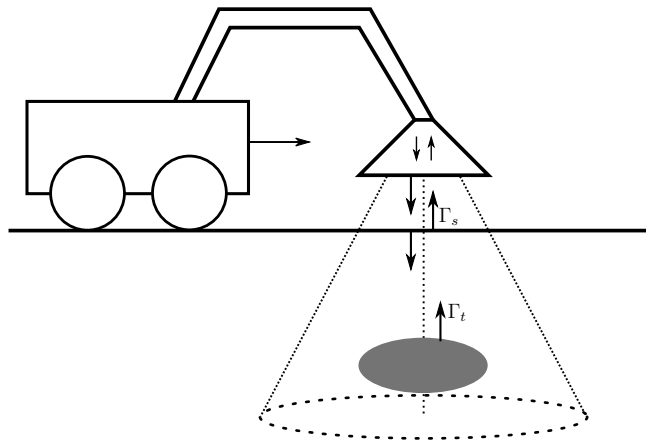


Figure 5.1: Example of a GPR measurement. A moving platform (e.g. remote rover or pushed cart) mounts a VNA used for signal generation, transmission and detection, while a wide-beam antenna illuminates an object buried deep into the ground.

As shown in Figure 5.1, GPRs can operate at short stand-off distances from the ground, making them minimally invasive and safer to operate under situations of high risk such as mine clearing

activities. Wide-beam antennas are used to speed up the scanning process of one area but require post-processing burden to focus the measurement into finer resolution imagery. This is typically done using SAR focusing algorithms.

5.2 Types of landmines

Landmines are relatively rudimentary devices containing a detonating charge which is activated by the action of a pressure plate or magnetic trigger. They were first used in the First World War and have rapidly developed thereafter and have been used in ulterior armed conflicts. Several hundreds of variations of landmines exist, adapting their design as necessary to achieve their damage goal. We can classify landmines into two broad categories:

- Anti-tank (AT): The simplest AT landmines are activated by applying a significant pressure on the pressure plate (see Figure 5.2) and only target tanks or vehicles of similar weight. In order to effectively damage armored vehicles, these landmines usually present large explosive charges and are buried so that most of the explosive effect is directed upwards to the surface at the point of contact with the tank. Due to their size, these mines are typically buried at a minimum of 20 cm and a maximum of 1 m. The structure of an AT landmine is generally made of metal although non-metal AT landmines exist, these are rare. The effects of AT mines on a tank aim at deactivating the unit and causing the crew as much harm as possible, whereas they become lethal on any other non-armored vehicle.

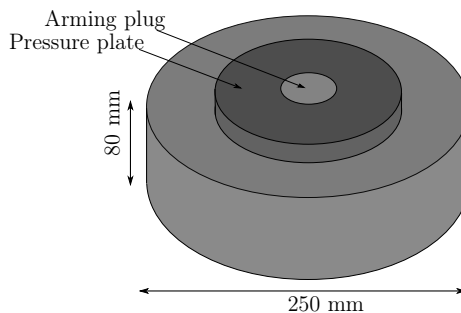


Figure 5.2: Schematic diagram of an anti-tank landmine.

- Anti-personnel (AP): Their size and explosive content are much smaller than the AT landmine, and are designed for impairing human activity in an indiscriminate way, whether it is civilian or military, since most of them are triggered with a pressure as little as 5 kilograms targeting children as well. Some of them even resemble colorful butterflies to attract civilian attention. They have a minimum metal content and, therefore, are difficult to detect using conventional mine detectors. AP landmines are also typically deployed in clusters surrounding AT landmines to prevent access of deminers to clear the area for armored vehicles. Figure 5.3 shows two of the most popular AP landmines, the PMN2 and the M14.

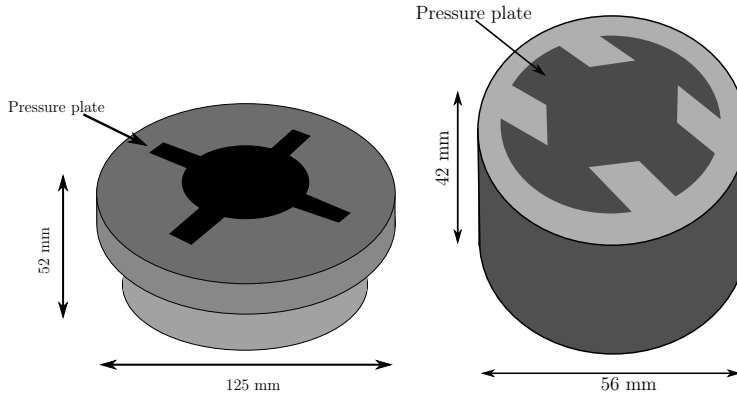


Figure 5.3: Commonly used AP landmines: Left, the PMN2; right, the M14. Both are mostly made of plastics and difficult to detect using standard mine detection techniques.

This chapter will discuss GPR measurements for landmine detection. In order to assess the performance of the proposed application, dummy reproductions of the three types of landmines presented (AT, PMN2 and M14) are used as buried test objects. The dimensions and metal contents of these landmines are listed in Table 5.1. Generally, most of the metal content is located in the structure and fuze although the majority of AP landmines are plastic-based.

Mine type	Metal content	∅ (mm)	H (mm)	D (mm)
AT	high	250	80	300
PMN2 (AP)	low	125	52	100
M14 (AP)	low	56	42	120

Table 5.1: Metal content, diameter, height and depth of the tested landmines.

5.3 Interactions with the ground

As any other electromagnetic radiation, GPR measurements are equally affected by the electrical characteristics of the media they propagate through. In contrast to NDT using radars where material attenuation is usually not a key factor since the materials are very transparent to the frequencies used, the soil attenuation must be studied in GPRs since it will be a very limiting factor in terms of maximum depth of inspection.

Assuming that an electric field is propagating through a lossy medium, its wave equation can be written as:

$$E(z) = E_o \exp(-\alpha_c z) \exp(-j\beta z), \quad (5.1)$$

where E_o is the initial amplitude of the electric field, α is the attenuation coefficient, β is the phase constant and z indicates the propagation direction of the wave. Soil substrates may present non-negligible conductivity levels σ_m , in contrast to dielectric composites as shown in Chapter 4, and these must be taken into account when calculating the attenuation and propagation velocity of the wave inside the medium. Assuming that the soil composition is homogeneous, the attenuation constant of the wave (with units Neper/m) is defined as:

$$\alpha_c = 2\pi f \sqrt{\frac{\mu\varepsilon}{2} \left(\sqrt{1 + \left(\frac{\sigma_m}{2\pi f\varepsilon}\right)^2} - 1 \right)}. \quad (5.2)$$

The phase constant, in turn, indicates the distortion of the transmitted signal in function of the frequency. Therefore, for an UWB transmission the phase will be affected differently by the material in a non-linear way, with a dependence on the frequency. This creates a distorted signal spectrum which worsens the longer the propagation path is. The expression for the phase constant is:

$$\beta_c = 2\pi f \sqrt{\frac{\mu\varepsilon}{2} \left(\sqrt{1 + \left(\frac{\sigma_m}{2\pi f\varepsilon}\right)^2} + 1 \right)}. \quad (5.3)$$

The two general equations in (5.2) and (5.3) can be simplified if the medium waves propagate through are considered to be ‘good dielectric’ if $(\sigma_m/2\pi f\varepsilon)^2 \ll 1$, or ‘good conductor’ if $(\sigma_m/2\pi f\varepsilon)^2 \gg 1$ [135]. In GPR, most of the situations are reduced to the ‘good dielectric’ case for which (5.2), after a Taylor expansion, is approximated to:

$$\alpha_c \approx \frac{\sigma_m}{2} \sqrt{\frac{\mu}{\varepsilon}}. \quad (5.4)$$

Likewise, the phase constant is simplified if the ‘good dielectric’ case holds:

$$\beta_c \approx 2\pi f \sqrt{\mu\varepsilon}. \quad (5.5)$$

Finally, the velocity of propagation of the wave in function of the frequency is expressed as:

$$v = \frac{2\pi f}{\beta_c}, \quad (5.6)$$

which, after using the approximation in (5.5), leads to the well-known expression:

$$v = \frac{1}{\sqrt{\mu\varepsilon}} = \frac{c_0}{\sqrt{\varepsilon_r}}. \quad (5.7)$$

5.4 Adapting common theory from NDT

The main principle behind GPR is similar to that of NDT: Electromagnetic waves are radiated by a radar which encounter an air-material (air-soil, in the GPR case) and continue to propagate inside the material until other changes of refractive indices are found due to the presence of objects (landmines for the application proposed). Each media interface radiates echoes back to the radar receiver which finally extracts depths and reflectivity information, as depicted in Figure 5.4.

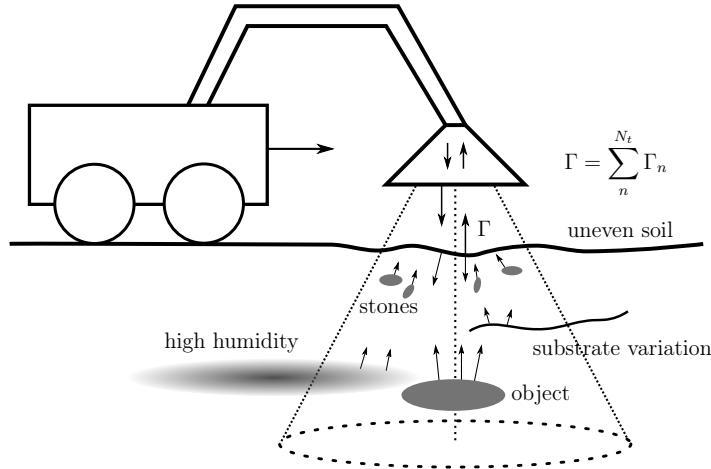


Figure 5.4: Example of a GPR measurement. A moving platform (e.g. remote rover or pushed cart) mounts a VNA used for signal generation, transmission and detection, while a wide-beam antenna illuminates an object buried deep into the ground.

However, this assumption is far from reality and the assumptions made in Chapter 4, using multi-section transmission lines no longer hold: Unlike NDT, where measurements usually take place under quasi-ideal conditions, in GPR the composition of the soil is often completely unknown or, optimistically, the composition can be roughly guessed from manual inspection. Several factors will affect the composition of the soil, altering the final GPR imagery:

- It may contain stones of unknown sizes, materials and distribution density,
- different types of sand with varying granularity distributed either in non-uniform layers or mixed,
- varying humidity levels,
- rocky substrates of unknown dimension and depth,
- any other uncontrolled aspect.

Such a heterogeneous environment is impossible to model and replicate and, therefore, the responses from a target cannot be modeled with high accuracy. Only complex approximations could take into account limited clutter scenarios, which makes modeling GPR measurements a cumbersome task with unclear benefits. There exist, though, post-processing imagery techniques to reduce the effects of clutter and detect objects of interest with higher probability rates, although those will not be used in this work for the sake of conciseness.

As a conclusion, and in contrast to the application of NDT for which expected scenes can be described in a simplified way, in GPR there is no simple approximation to what the response of a measurement would be without perfect knowledge of the soil composition, i.e. perfect knowledge of clutter and other undesired contributions to the scene, which seems far from attainable.

5.5 Intrinsic antenna modeling

The reflectivity of a landmine when exposed to radiation from a GPR will greatly depend on the size and metal content of the object. Since the structure of AT landmines is typically made of metal, they can be identified without further problems despite being buried deep. AP landmines, however, present almost no metal content and may be difficult to discern from stones or objects of similar size generating clutter. Moreover, and because AP landmines are buried shallowly (around 10 cm deep), physical wave reverberation phenomena happening between the GPR antenna aperture and the ground may mask these smaller landmines. The reflection of a transmitted wave into the surface is reflected back to the GPR with high intensity which is, once again, radiated back to the surface and so on and so forth. Internal reverberations inside the antenna aperture caused by the impedance mismatch in the different antenna parts are also possible. All these reverberation phenomena create echoes with propagation paths longer than the antenna-surface round-trip path, causing ghost echoes to appear in the final imagery. Low-reflectivity, shallow objects will be affected by this type of reverberations, leading to a lack of performance of GPRs in the case of AP landmines.

These reverberation phenomena inside the antenna aperture can be interpreted as a number of homogeneous fields, for each of which the transmitted and reflected waves are considered. An intrinsic model used in [136, 137] is expressed as a closed-form antenna equation, which has never been used before in combination with a CS-oriented imagery approach, and assumes that the interface with the ground is in the far-field region of the antenna [138]. Given that the same antenna is used for transmission and reception, the closed-form equation is simplified to [136]:

$$\Gamma'(f) = \frac{S_R(f)}{S_T(f)} = R_i(f) + \frac{T(f)G(f)}{1 - G(f)R_s(f)}, \quad (5.8)$$

where the following elements can be identified:

- $S_T(f)$: incident field into the antenna (stimuli),

- $S_R(f)$: the backscattered field out of the antenna (response),
- $R_i(f)$ is the global reflection coefficient of the antenna for fields incident from the radar reference plane onto the antenna phase center,
- $T(f) = T_i(f)T_s(f)$ the total transmission coefficient. $T_i(f)$ is the transmission coefficient for the incident waves from the reference plane into the aperture, whereas $T_s(f)$ is the equivalent case for those waves that are incident from the aperture onto the radar reference plane,
- $R_s(f)$ is the total reflection coefficient for waves incident from soil onto the antenna.
- $G(f)$ is the Green's function which can be derived using the recursion in (4.19) describing a multi-layered situation, as also discussed in [139].

The equation in (5.8) is schematically represented in Figure 5.5. The antenna-related coefficients in the equation ($R_i(f)$, $T(f)$ and $R_s(f)$) are extracted after an antenna calibration procedure for which several measurements are performed using a flat copper plate as reference plane at different stand-off distances from the antenna [136, 137].

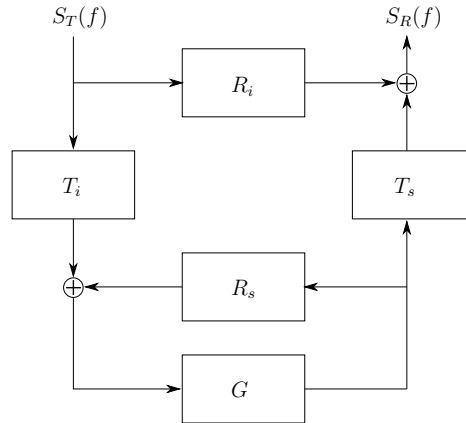


Figure 5.5: Block diagram describing the internal reverberations within the antenna aperture as well as the antenna-ground reflections.

After the antenna calibration and coefficients extraction are successful, the received signals can be filtered out, removing the totality of the internal antenna reverberations as well as the multiple reflections from the soil. The filtering of the frequency-domain data is performed as follows:

$$\Gamma(f) = \frac{\Gamma'(f) - R_i(f)}{T(f) + \Gamma'(f)R_s(f) - R_i(f)R_s(f)}. \quad (5.9)$$

In Figure 5.6 we can see a range-compressed GPR measurement including one AT and two AP landmines (PMN2 and M14), as described in subsection 5.2. The image at the top shows

the raw GPR data before filtering out the reverberation effects. Whereas the AT landmine is indeed visible since it is less or not affected at all by these internal and antenna-ground reverberations, the two AP landmines are fully affected. It would only be possible to identify these smaller landmines after close inspection of a trained operator. The image at the bottom shows the resulting range-compressed data (before any farther data processing) in which the AT mine presents a much higher contrast and the AP landmines are easier to identify, since only the first reflection from the air-ground interface is present. This filtering technique also obtains successful results in multilayered substrates [140] and can be applied both in far-of-near-field conditions [136, 141]. Moreover, after filtering, the correct depths for every mine are also compensated for since the reference plane is moved towards the antenna phase center.

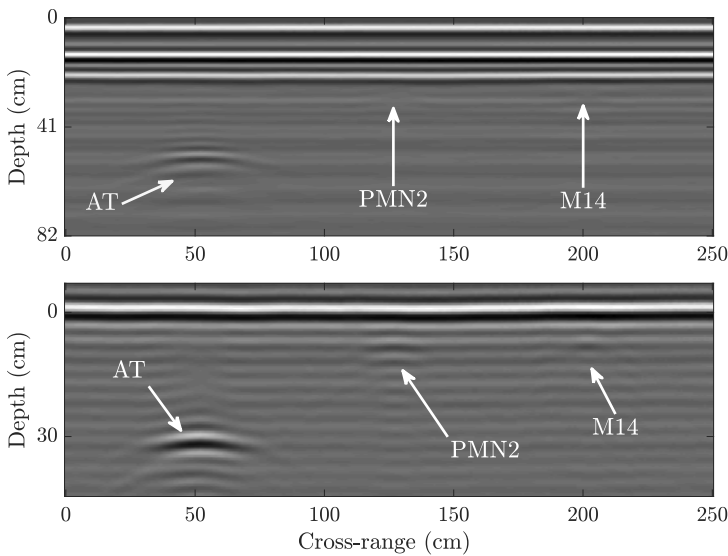


Figure 5.6: Echoes from a GPR range-compressed measurement not applying (top) and applying (bottom) the antenna-ground interaction modeling. The two AP mines are visible after modeling is applied and depths (time-of-flight) for all targets are corrected.

Figure 5.7 shows the superimposed depth profiles generated by the AT landmine. These profiles correspond to a single scan and show the results obtained after performing range compression on $\Gamma(f)$ using a Fourier transform correlator. The black curve shows the information obtained from the unfiltered measurements where we can see three strong reflections: The brightest one corresponds to the air-ground interface (1.9 ns) whereas the other two peaks (located at 0.6 and 2.7 ns) correspond to other reverberations phenomena. Another peak is visible at around 6.5 ns, which we assume it is caused by the AT landmine. The dashed curve displays a measurement for which no target is present. The thicker curve shows the depth profile after filtering. We can see that the only prominent peak left corresponds to the strong reflection from the ground whereas the peak produced by the AT landmine becomes more evident at 5.2 ns. Not only the energy of the AT landmine is more compacted, but also the depth has been corrected.

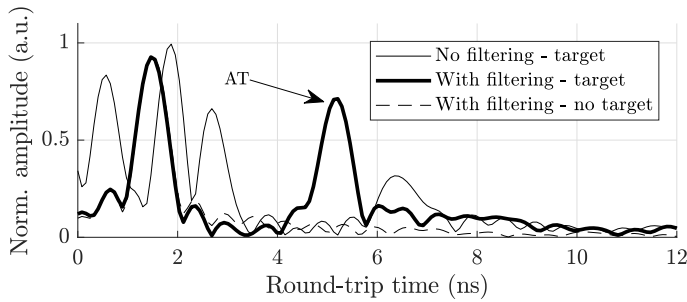


Figure 5.7: The depth profile after the Fourier correlator is shown for the AT landmines. The thin solid curve indicates raw, unfiltered data. The thicker curve shows the filtered profiles including a landmine, while the dashed curve does not include any target.

Figure 5.8 follows the same idea as 5.7, but in this case the profiles produced by the PMN2 landmine are shown. We can see that the landmine appearing in the thicker curve after filtering is virtually impossible to be identified in the unfiltered data curve. The slight difference between the thicker and dashed curves highlight the presence of the PMN2 landmine.

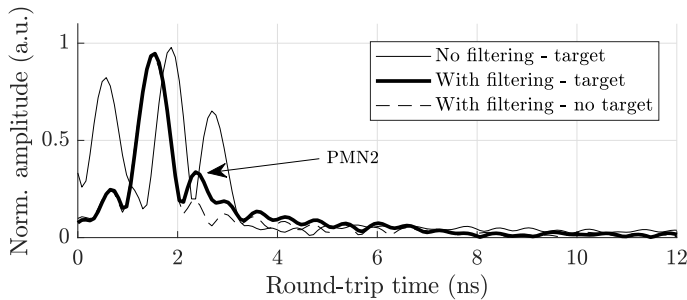


Figure 5.8: The depth profile after the Fourier correlator is shown for the PMN2 landmines. The thin solid curve indicates raw, unfiltered data. The thicker curve shows the filtered profiles including a landmine, while the dashed curve does not include any target.

For Figure 5.9, which shows the results for the even smaller and less bright M14 landmine, a similar analysis can be performed: The landmine would not be distinguished without the prior reverberation removal. The difference between the thicker and dashed curves is smaller than in the PMN2 case. A study of depth profiles adjacent in the cross-range dimension helps in visually isolating the target from the air-ground reflection and clutter.

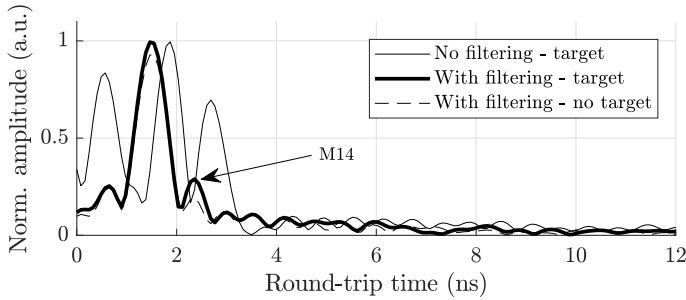


Figure 5.9: The depth profile after the Fourier correlator is shown for the M14 landmines. The thin solid curve indicates raw, unfiltered data. The thicker curve shows the filtered profiles including a landmine, while the dashed curve does not include any target.

We can safely assert that the intrinsic filtering is useful for all three cases, however its capability to reveal masked objects makes of it an extremely tool for detecting AP landmines.

5.6 Adapting GPR sensors to CS sampling

Based on the principle of SAR, where a moving radar illuminates the scene from multiple observation points, the data collection scheme is two-dimensional and data volume starts to become a burden to consider. Figure 5.10 shows a sensor receiving echoes from the ground at every measurement position which, after homodyne demodulation, are converted into reflection responses Γ .

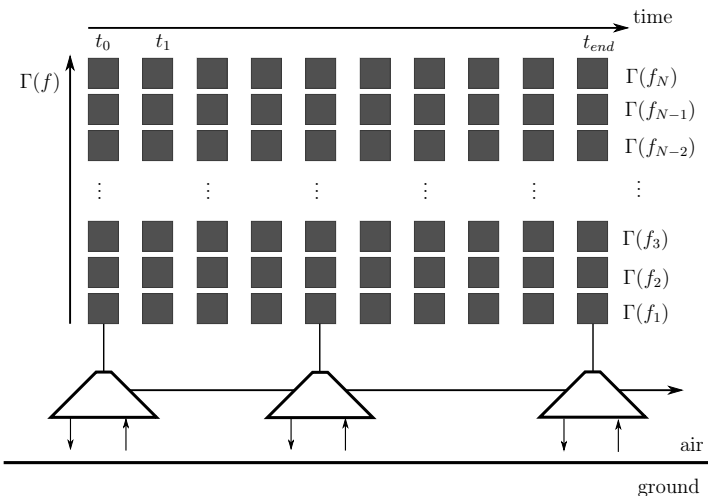


Figure 5.10: Conventional data acquisition in a SAR measurement. For every cross-range measurement position, N reflection responses are collected, each corresponding to a discrete frequency in the swept bandwidth.

Given the SFCW approach used in this chapter, the reflection responses will span the whole inspected bandwidth from f_1 to f_N . Therefore, assuming that during a full scan N_{xr} measurements are performed, the total amount of collected data will be $N_{xr} \times N$, which can be stored indistinctly in the form of a vector or matrix.

The hand-held VNA device used for these GPR measurements is installed on a platform driven by a 2-D scanner. The platform moves parallel to the ground with the antenna main lobe oriented normal to the path. For the whole path of the experiment, N_{xr} along-track or cross-range full-data measurements are performed in an stop-and-go fashion. This implies that the VNA must stop for a certain amount of time to perform the measurement and acquire the reflection responses Γ for N frequencies before proceeding to the next along-track position. In total, for a whole measurement, an array of length $(N_{xr} \times N)$ elements is created which is then subsampled in software emulating a CS radar that would effectively use $y = \Phi x$.

Similarly, an SFCW SAR simulator is used to populate the observations dictionary Ψ . Each atom of Ψ corresponds to a simulated replica—a vectorized matrix of size $(N_{xr} \times N)$ —of the reflection responses of a GPR measurement along the full scanning path for a point-target at a given position. The GPR imagery is reconstructed as shown in Figure 5.11, bypassing all the conventional SAR processing steps.

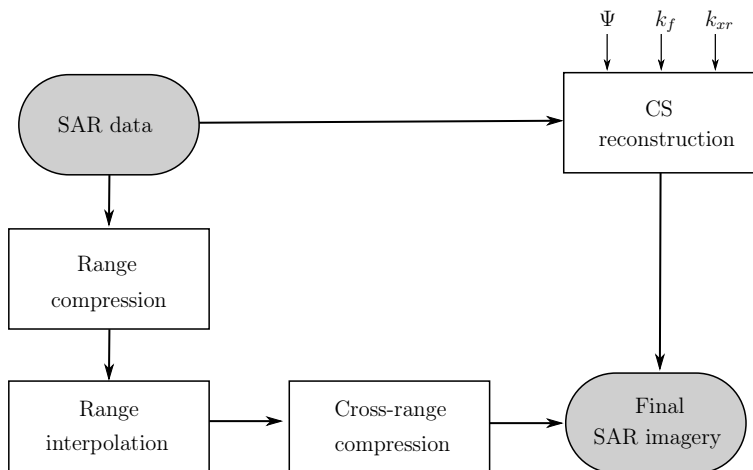


Figure 5.11: Conventional (range- and cross-range compression-based) and CS processing steps for generating SAR imagery.

Thanks to the simulator that models the scene, building up an observation dictionary is done in a fast and comprehensive fashion, covering all possible point-target positions in the scene. The atoms respect the following structure: A position in the scene is represented in Cartesian coordinates (q, r) with $q = 1, 2, \dots, N_{xr}$ the number of measurement positions and $r = 1, 2, \dots, N_d$ the number of depth positions. The atoms $\psi_{q,r}$ are arranged in the dictionary as follows:

$$\begin{aligned}
\mathbf{\Psi} &= [\psi_{1,1}, \psi_{1,2}, \dots, \psi_{1,N_d}, \psi_{2,1}, \psi_{2,2}, \dots, \psi_{N_{xr}, N_d}] \\
&= \begin{bmatrix} \Gamma_{1,1}^{\psi_{1,1}} & \Gamma_{1,1}^{\psi_{1,2}} & \dots & \Gamma_{1,1}^{\psi_{1,N_d}} & \Gamma_{1,1}^{\psi_{2,1}} & \Gamma_{1,1}^{\psi_{2,2}} & \dots & \Gamma_{1,1}^{\psi_{N_{xr}, N_d}} \\ \Gamma_{2,1}^{\psi_{1,1}} & \Gamma_{2,1}^{\psi_{1,2}} & \dots & \Gamma_{2,1}^{\psi_{1,N_d}} & \Gamma_{2,1}^{\psi_{2,1}} & \Gamma_{2,1}^{\psi_{2,2}} & \dots & \Gamma_{2,1}^{\psi_{N_{xr}, N_d}} \\ \vdots & \vdots & \ddots & \vdots & \vdots & \vdots & \ddots & \vdots \\ \Gamma_{N,1}^{\psi_{1,1}} & \Gamma_{N,1}^{\psi_{1,2}} & \dots & \Gamma_{N,1}^{\psi_{1,N_d}} & \Gamma_{N,1}^{\psi_{2,1}} & \Gamma_{N,1}^{\psi_{2,2}} & \dots & \Gamma_{N,1}^{\psi_{N_{xr}, N_d}} \\ \Gamma_{1,2}^{\psi_{1,1}} & \Gamma_{1,2}^{\psi_{1,2}} & \dots & \Gamma_{1,2}^{\psi_{1,N_d}} & \Gamma_{1,2}^{\psi_{2,1}} & \Gamma_{1,2}^{\psi_{2,2}} & \dots & \Gamma_{1,2}^{\psi_{N_{xr}, N_d}} \\ \Gamma_{2,2}^{\psi_{1,1}} & \Gamma_{2,2}^{\psi_{1,2}} & \dots & \Gamma_{2,2}^{\psi_{1,N_d}} & \Gamma_{2,2}^{\psi_{2,1}} & \Gamma_{2,2}^{\psi_{2,2}} & \dots & \Gamma_{2,2}^{\psi_{N_{xr}, N_d}} \\ \vdots & \vdots & \ddots & \vdots & \vdots & \vdots & \ddots & \vdots \\ \Gamma_{N, N_{xr}}^{\psi_{1,1}} & \Gamma_{N, N_{xr}}^{\psi_{1,2}} & \dots & \Gamma_{N, N_{xr}}^{\psi_{1,N_d}} & \Gamma_{N, N_{xr}}^{\psi_{2,1}} & \Gamma_{N, N_{xr}}^{\psi_{2,2}} & \dots & \Gamma_{N, N_{xr}}^{\psi_{N_{xr}, N_d}} \end{bmatrix}, \tag{5.10}
\end{aligned}$$

with $\Gamma_{n, n_{xr}}^{\psi_{q,r}}$ the reflection response for frequency n at the scanning position n_{xr} for a target in the scene located at position (q, r) . Hence, the dictionary matrix $\mathbf{\Psi}$ has $(N_{xr} \times N)$ rows and $(N_{xr} \times N_d)$ columns.

For the type of measurements presented, the reflectivity of the scene is described as every possible point target in a 2-D, $(N_{xr} \times N_d)$ scene image which is vectorized following the same order as the atoms of $\mathbf{\Psi}$:

$$\sigma = [\sigma_{1,1}, \sigma_{1,2}, \dots, \sigma_{1,N_d}, \sigma_{2,1}, \sigma_{2,2}, \dots, \sigma_{N_{xr}, N_d}]^T. \tag{5.11}$$

After CS reconstruction, the vector σ is reshaped into an $(N_{xr} \times N_d)$ -sized image. Each scene reflectivity coefficient $\sigma_{q,r}$ represents the reflectivity of the reconstructed target at position (q, r) and can be interpreted as a pixel of size $(\Delta_d \times \Delta_{xr})$. The size of the pixel in the depth and cross-range directions are described by Δ_d and Δ_{xr} , respectively. Therefore, the final size of the reconstructed image depends on the choice of the pixel size which, as a standard measure, was chosen to be similar to the range and spatial resolutions of the GPR, respectively. Using smaller pixel sizes will certainly increase the computational burden during the reconstruction and may not yield better quality images. Doing the opposite action, using larger pixels will simplify the reconstructed imagery and reduce the computational cost while obviously risking missing small targets with sizes in the order of the range and spatial resolutions. The goal of the GPR application will be decisive to select a pixel size.

5.6.1 Subsampling strategies

In GPR measurements, given the movement of the radar along the scene and the sequential interrogation of frequencies by the VNA, two subsampling strategies can be envisaged. The first

one aims at exploiting the wide-beam SAR measurements by selecting only random measurement positions in the scanning path. If the scanner uses a stop-and-go approach during measurements, that is, it cannot perform measurements on the go, there will be a measurement time reduction thanks to spatial subsampling and certainly a data reduction in all cases. A second option is, exactly as in NDT, only collecting a fraction of the interrogated frequencies by the VNA. Finally, a combination of both subsampling strategies may reduce data collection even farther although its effects on scene reconstruction quality must be considered.

The way the frequency or spatial subsampling is performed, as well as the visual interpretation follow next.

5.6.1.1 Frequency subsampling

Similarly to its definition for NDT measurements, the frequency subsampling factor is expressed as $k_f = M/N < 1$, with M discrete frequencies that are randomly selected following an interspacing governed by a uniform random distribution, or $d_n \in [d_{f_{min}}, d_{f_{max}}]$. Figure 5.12 depicts randomly selected frequency reflection responses in dark, whereas the $(N - M)$ discarded frequencies are in white. The minimum and maximum interspacing are defined as $d_{f_{min}}, d_{f_{max}} \in \mathbb{N}_{>0}$, respectively, satisfying $1 \leq d_{f_{min}} < d_{f_{max}}$. Eventually, the data volume produced after subsampling in frequency is directly k_f times the original volume, or $k_f \times N_{xr} \times N = N_{xr} \times M$.

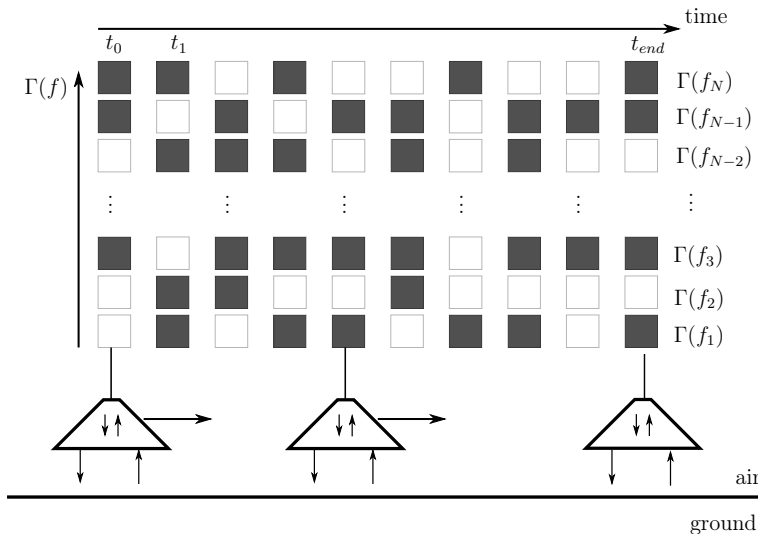


Figure 5.12: Frequency subsampling scheme in GPR. The VNA interrogates random frequencies following a subsampling rate k_f .

5.6.1.2 Spatial subsampling

Given the nature of wide-beam measurements, it is guaranteed that a same target will be illuminated from multiple scanning positions in the motion path. This creates unnecessary data from a sparsity-based point of view creating a data redundancy that be exploited. Gapped data can be generated by not performing all the measurements in the spatial dimension and still obtain successful results [142, 143].

The measurements along the measurement path that will be effectively performed are randomly selected as seen in Figure 5.13 according to $k_{xr} = M_{xr}/N_{xr} < 1$, the subsampling factor in cross-range, similarly as in frequency subsampling, with M_{xr} an integer representing the number of performed cross-range measurements. In this case, the data volume produced after subsampling in cross-range is k_{xr} times the original volume, or $k_{xr} \times N_{xr} \times N = M_{xr} \times N$.

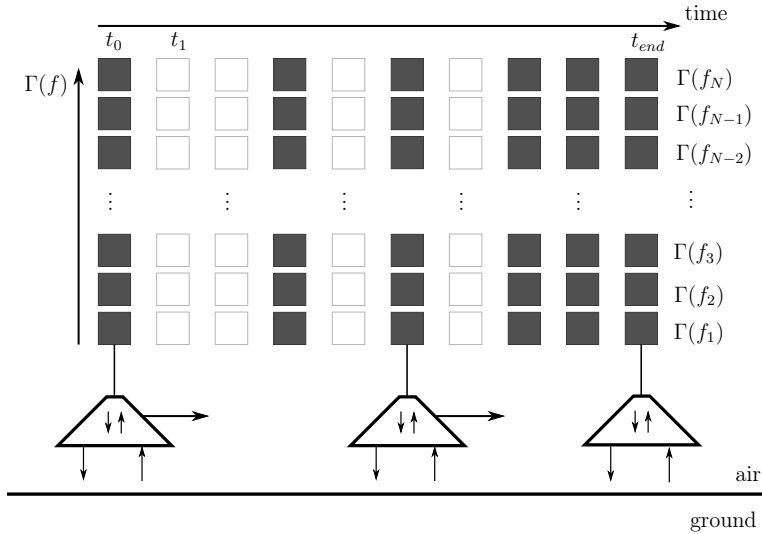


Figure 5.13: Cross-range positions subsampling scheme in GPR. The VNA only performs measurements collecting all Shannon-Nyquist frequencies at certain cross-range positions following a subsampling rate k_{xr} .

The maximum inter-spacing between the random cross-range positions is limited by the antenna footprint size in the cross-range dimension at a reference range. Figure 5.14 describes an example of an object not being illuminated, therefore not included in the final imagery, because the gap produced after random subsampling in the spatial dimension is too wide. This fact must be taken into consideration when choosing the distribution of the random sequence governing the selection of spatial measurements.

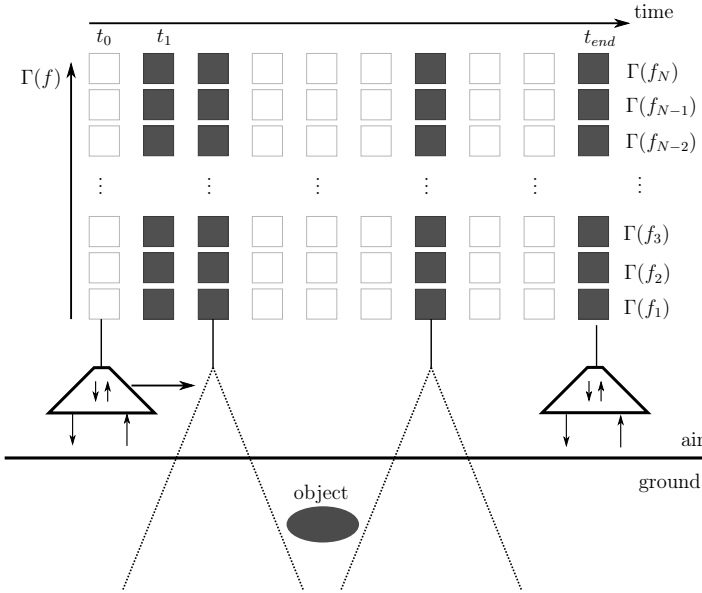


Figure 5.14: If the maximum intersampling between cross-range random measurements is too large, objects in the scene may be missed. The cross-range intersampling will depend on the antenna aperture and the depth of the object.

5.6.1.3 Combining subsampling strategies

Finally, the combination of the two previous strategies is shown in Figure 5.15, for which two random subsampling frequencies have been superimposed—in fact, those from Figures 5.12 and 5.13—yielding a total data volume reduction proportional to $k_{xr} \times k_f$, or $k_{xr} \times N_{xr} \times k_f \times N = M_{xr} \times M$.

This heavy data volume reduction may produce marginally exploitable results. Heavily subsampling in one dimension may limit the ability to subsample in the other dimension. Therefore, it is suggested that the limits of combined subsampling be explored before implementing it in a practical case.

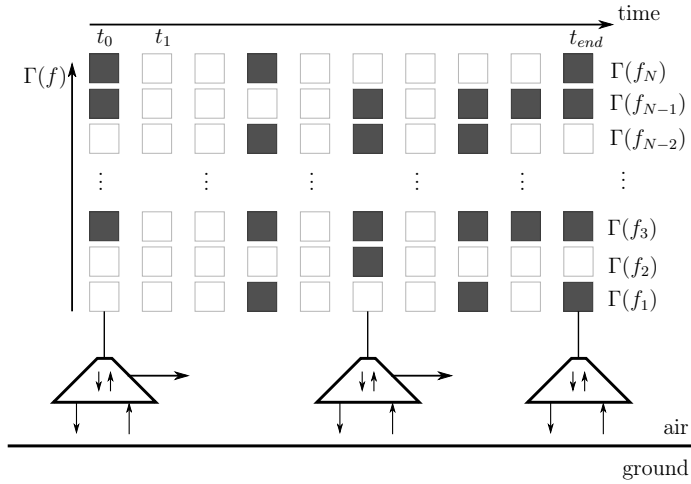


Figure 5.15: Frequency and cross-range positions are randomly subsampled in a GPR measurement. The VNA collects random frequencies at random cross-range positions following the subsampling rates k_f and k_{xr} , respectively.

5.7 Measurement campaign description and sensor specifications

The data used in this chapter were obtained during a measurement campaign under controlled laboratory conditions at The Netherlands Organization for Applied Scientific Research (TNO) (The Hague, The Netherlands) [144, 145] under the supervision of Prof. Sébastien Lambot.

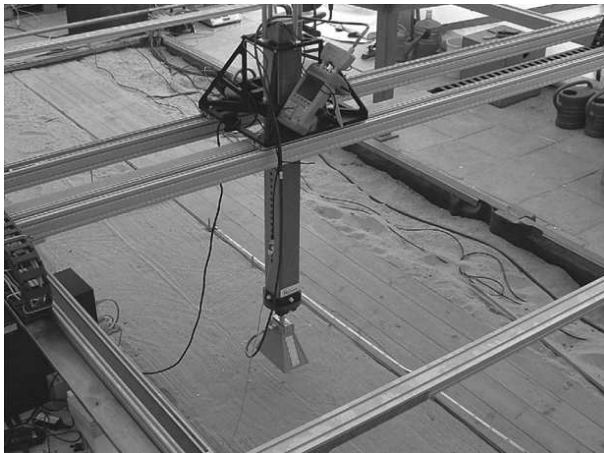


Figure 5.16: A sandbox hosted at TNO was used to obtain the presented GPR measurements. The scanner carries a portable VNA and horn antenna placed at a standoff distance of 200 mm from the ground.

A sandbox shown in Figure 5.16 of homogeneous sand presenting a low dielectric constant of $\epsilon_r = 2.8$ [144] with dimensions $10 \text{ m} \times 10 \text{ m}$ and 3 m deep was used to bury the test landmines described in Subsection 5.2. The choice of fine and as homogeneous sand as possible, with a constantly low humidity level (dry sand) moves the scenario away from real conditions since it provides lower attenuation and constant permittivity values, regardless of the depth or position over the motion path of the platform. This idealization was deemed necessary to obtain results as pristine as possible which could help understanding the effects of data subsampling purely, without any farther external influence.

As shown in Figure 5.17, the mines were buried at different depths based on their original purpose (affecting tanks or humans) and at a 750 mm separation from each other to avoid any type of interference or overlap. The AT mine was buried at 300 mm depth whereas the AP mines PMN2 and M14 were placed at 100 mm and 120 mm deep, respectively, which match with the typical bury depths.

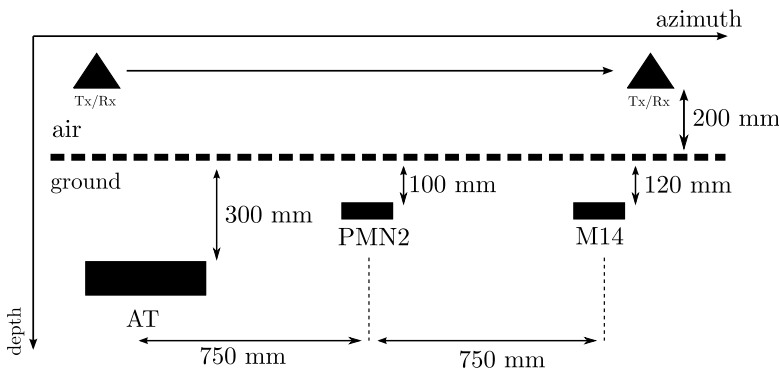


Figure 5.17: Three mines (AT, PMN2 and M14) were buried on a sandbox at different depths and separated by 75 cm of each other. The SFCW radar ran over a scanning path 2.5 m long at a distance of 20 cm from the ground.

The radar device employed for these GPR experiments is a hand-held VNA (Rohde & Schwarz FSH6) connected to a single doubled-ridge Schwarzbeck Mess-Elektronik BBHA 9120A horn antenna using a coaxial cable. This antenna presents relatively wide radiation patterns both in the E- and H-planes (those containing the electric and magnetic fields, respectively) allowing for 2-D and 3-D GPR measurements. The radar and antenna are mounted on a scanner with the antenna aperture being at a standoff distance of 20 cm from the ground.

VNA		Antenna	
Model	R&S FSH6	Model	BBHA 9120A
Freq. sweep	0.8–2.6 GHz	Aperture dimensions	142×245 mm
Number of freqs., N_f	301	Antenna length	220 mm
Freq. step, Δf	6 MHz	3-dB E/H (1 GHz)	45/30°
Used freq.	0.8–2.2 GHz	3-dB E/H (2 GHz)	27/22°
Bandwidth B	1.4 GHz	Antenna-to-ground	200 mm
Depth resolution Δ_d	64 mm	Spatial resolution Δ_{xr}	93 mm

Table 5.2: Configuration parameters used during the measurement campaign.

Initially, 301 discrete frequencies were interrogated covering the frequency range of 800-2600 MHz with a frequency step size of 6 MHz. The bandwidth portion from 2200 to 2600 MHz was not exploited due to low SNR produced by the surface roughness and less accurate antenna calibration within that frequency range, limiting the actual bandwidth to 800-2200 MHz [146] and 234 discrete frequencies. A summary of the configuration parameters used for this measurement campaign is found in Table 5.2.

5.8 CS reconstruction results and discussion

In order to study the effects of random subsampling in the frequency and spatial domains, whether individually or combined, Monte-Carlo realizations of CS reconstructions with BPDN are performed. Different subsampling rates k_f and k_{xr} are employed, where applicable, under different noise conditions. These realizations are run for several cases which include processing the raw radar data as they were directly collected from the measurement with and without intrinsic signal modeling, and transformed data for achieving higher performances thanks to the PCA-based preconditioning (see Chapter 3), also with and without antenna-to-ground reverberation effect removal.

P_d vs. SNR plots are generated to better understand the robustness of the CS reconstructions against noise, and this for each subsampling rate tested. To do so, the 2-D CA-CFAR detector presented in Chapter 2 is used for which the known position of each landmine is selected as the test cell, yielding P_d values out of the reconstructions for a not too restrictive $P_{fa} = 10^{-2}$. The additive white Gaussian noise with which the original GPR measurement is corrupted presents a varying SNR from -20 dB to +10 dB in 2-dB SNR steps. For every SNR-subsampling rate combination, 500 Monte-Carlo realizations are performed each of which has a completely different pseudo-random subsampling sequence to decorrelate as much as possible the recovery results from the random selection of samples. For each P_d vs. SNR plot, a total of 88,000 Monte-Carlo realizations were run. A total of 24 Intel Xeon E5649 2.53 GHz cores were used in parallel for circa. 8,000 core-hours, taking two weeks to complete all tasks using Matlab R2015b (64 bit).

Finally, for every type of landmine, the effects in the positioning of positive targets with respect to the ground truth for different SNR levels when using random subsampling are displayed as the percentage of times targets are reconstructed within the correct depth bin or one or two depth bins away from the ground truth. As a complementary metric to P_d , these tables give a global idea of how trustworthy target positioning is after CS reconstruction, in this case on PCA data sets only.

5.8.1 Example of CS reconstruction of a GPR scene

Figure 5.18 shows a full scene reconstruction as a demonstration where subsampling factors $k_f = 0.5$ and $k_{xr} = 0.5$ were used. The three targets, as depicted in Figure 5.17 are recovered in their correct positions. In this example, the real measurement was not corrupted with additional noise and only that from the measurement and scene clutter were considered. As it was expected, the depths of the landmines are rounded to the radar depth resolution inside the sandy soil which is around 64 mm.

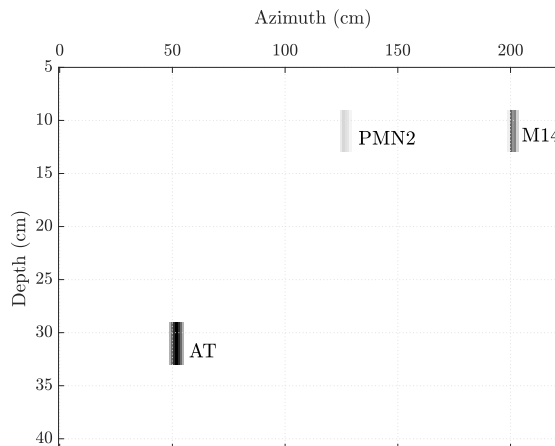


Figure 5.18: The three buried mines are correctly located with a dictionary-based CS recovery of a GPR scene and applying the antenna-ground modeling. Only 50% of the frequencies and scanning positions were used and no noise was added.

In the rest of the chapter, only a limited area around the tested target (whether it is an AT or AP landmine) will be reconstructed for the sake of computational complexity during the exhaustive Monte-Carlo simulations. For all the P_d vs. SNR plots, a thick curve represents the obtained performance results using a conventional SAR focusing algorithm [60] based on the MF and time-domain, coherent integration of the energy along the hyperbolic phase history $r(t)$. For obtaining these results, the fully sampled data and the intrinsic modeling are used, also corrupted by different noise levels. This comparison is used as a fair reference that makes criticism of the CS performance possible.

5.8.2 The AT landmine

The first studied scenario is the comparison in terms of P_d vs. SNR of the results obtained using raw radar data directly or PCA-transformed data for reconstructing the reflectivity function of the AT landmine. The results are displayed in Figures 5.19 and 5.20, which were generated using BPDN and after Monte-Carlo simulations applying several k_f cases. Finally, in those same figures the dashed lines show the results using the same methodology but without applying intrinsic filtering to the acquired signals. Interpretation of the results will lead to conclusions regarding whether using PCA as a preconditioner is interesting and how can be quantified the improvement due to applying intrinsic filtering.

For the raw-data case (Figure 5.19) it can be seen that for $k_f = 0.05$ and $k_f = 0.10$ a goal $P_d \geq 0.9$ is reached at SNR = 0 dB and SNR = -4 dB, respectively, for non-transformed data. In the PCA case (Figure 5.20), the same P_d goal is reached at SNR = -4 dB and SNR = -6 dB, respectively, for the PCA-transformed data. This clearly highlights that PCA outperforms the non-transformed data results. These SNR gains are less and less evident as k_f increases, although performances are still slightly better for PCA. This leads to first conclusion: the extra computational burden incurred by using PCA is no longer justified when high values of k_f are chosen but also when high quality, low-noise measurements are reconstructed.

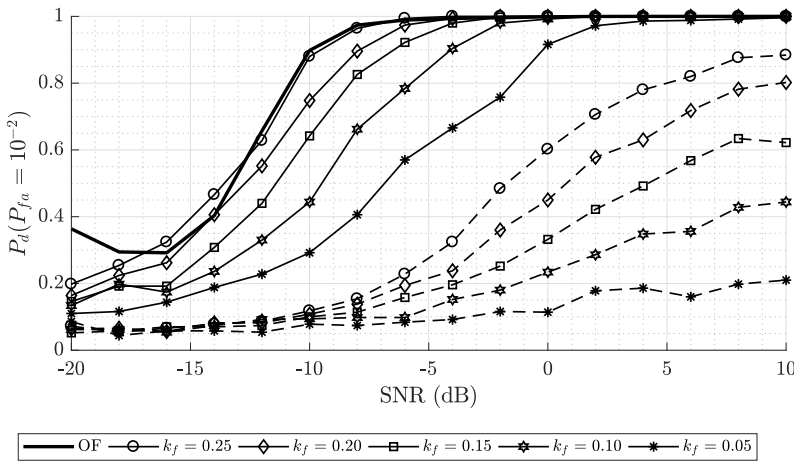


Figure 5.19: Robustness analysis of the CS reconstructions of the AT landmine using BPDN and raw data. The P_d vs. SNR curves are plotted for multiple k_f values. The solid line indicates intrinsic filtering is applied, whereas the dashed line indicates otherwise.

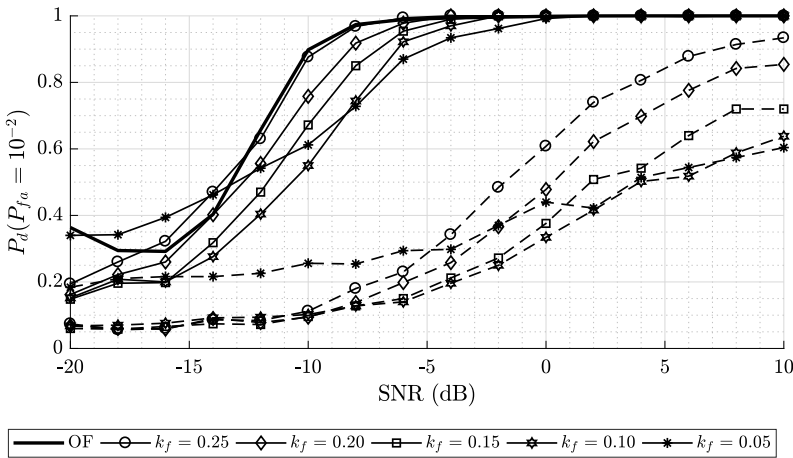


Figure 5.20: Robustness analysis of the CS reconstructions of the AT landmine using BPDN and PCA as data preconditioner. The P_d vs. SNR curves are plotted for multiple k_f values. The solid line indicates intrinsic filtering is applied, whereas the dashed line indicates otherwise.

Going more into detail regarding using intrinsic modeling, if it is not applied the P_d significantly increases when the PCA preconditioning is used although still performing substantially worse than with intrinsic modeling. This may be caused by the rejection of the noise subspace or non-signal related components produced by PCA when data dimensionality reduction is applied so that only the 5% strongest PCA components are kept. Per se, PCA is reducing the antenna-ground reverberation effects which are not removed when the intrinsic modeling is bypassed, and causing an increase in the P_d . This is visible in Figures 5.19 and 5.20 but also in the two following ones, although less noticeable, Figures 5.21 and 5.22, where cross-range subsampling is applied.

As for Figures 5.21 and 5.22, the performances shown are very similar, reaching a P_d well above 0.9 for $\text{SNR} \geq 0$ dB and $k_{xr} \geq 0.1$. The PCA-transformed data produce negligible P_d increases when the intrinsic filtering is used, whereas the increase is more noticeable if not used. Again, this is originated by the dimensionality reduction already discussed. In both cases, for $k_{xr} \geq 0.3$ and $\text{SNR} \leq -10$ dB the P_d curves appear to outperform the performances using the matched filter SAR processing. This is due to the very bright return from the AT landmine and the oversimplification of the reconstructed scene produced by the BPDN algorithm with respect to the MF-based results and to the fact that scene sparsity is forced: the cells used for noise learning and thresholding purposes happened to be less affected by the added Gaussian noise.

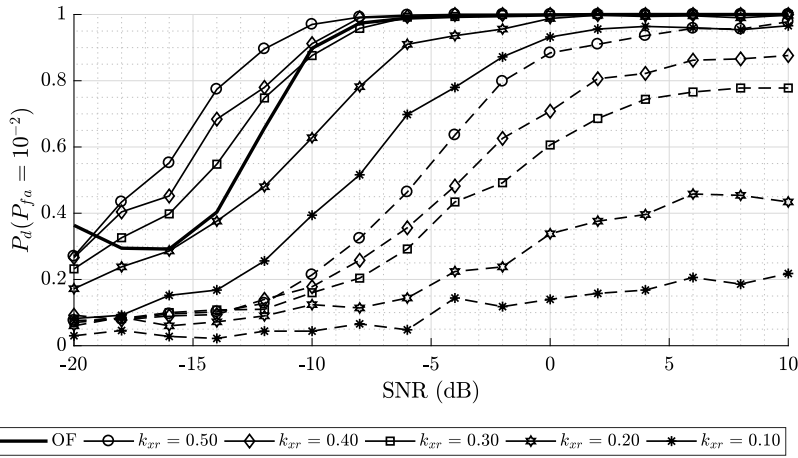


Figure 5.21: Robustness analysis of the CS reconstructions of the AT landmine using BPDN and raw data. The P_d vs. SNR curves are plotted for multiple k_{xr} values. The solid line indicates intrinsic filtering is applied, whereas the dashed line indicates otherwise.

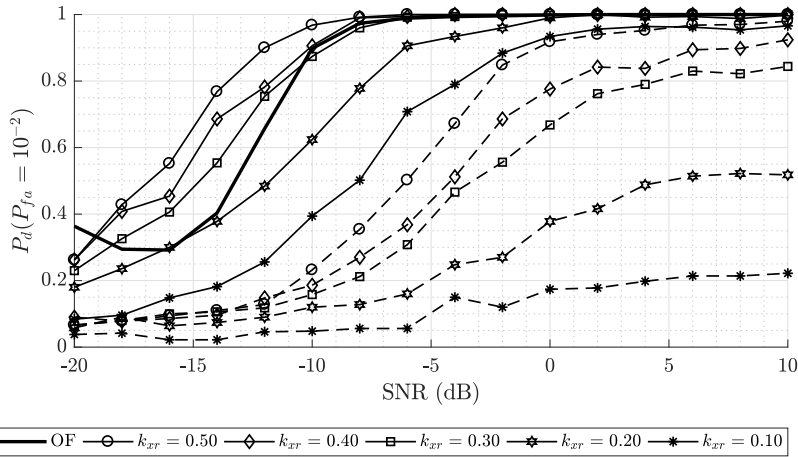


Figure 5.22: Robustness analysis of the CS reconstructions of the AT landmine using BPDN and PCA as data preconditioner. The P_d vs. SNR curves are plotted for multiple k_{xr} values. The solid line indicates intrinsic filtering is applied, whereas the dashed line indicates otherwise.

The different P_d values for the combined cross-range-frequency subsampling strategy are displayed in Figure 5.23 for the non-transformed data and in Figure 5.24 for PCA-transformed data. In both figures, the intrinsic filtering is applied to the data.

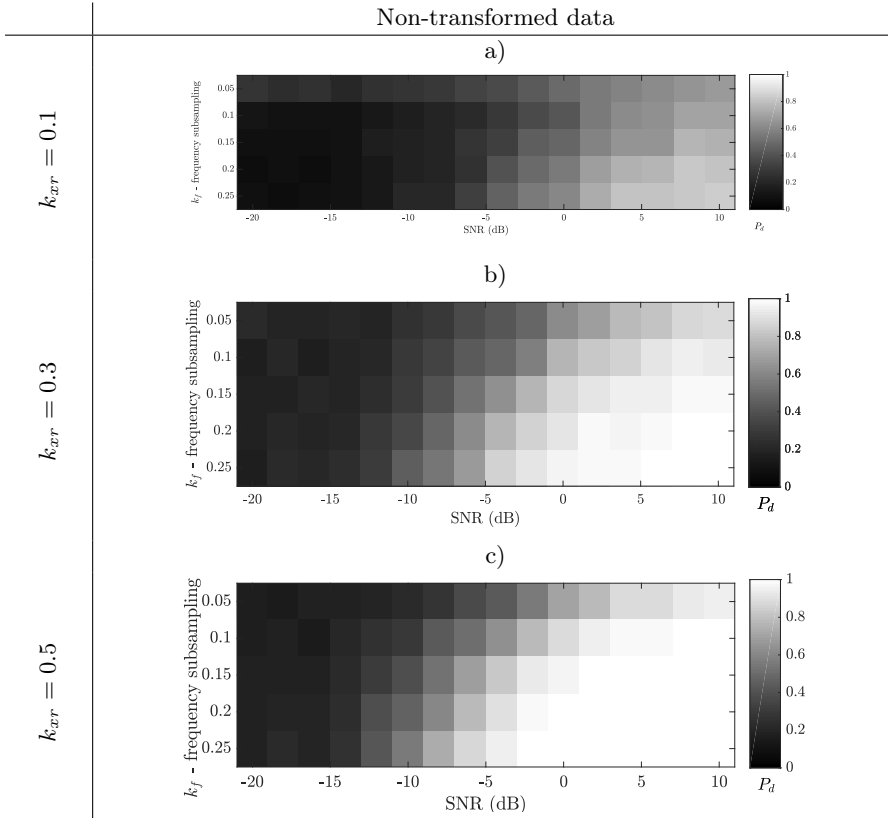


Figure 5.23: P_d vs. SNR for several subsampling rates $k_{xr} = 0.10, 0.3$ and 0.5 and $k_f = 0.05 - 0.25$ for the AT landmine and original non-transformed data. A probability of false alarm of 10^{-2} was chosen and 500 Monte-Carlo trials were run. A CA-CFAR detector was used to extract the P_d values.

Figure 5.23-a) —with a cross-range subsampling rate $k_{xr} = 0.1$ — presents low P_d values for any k_f -SNR combination, since the total amount of data is clearly insufficient even if high SNRs are considered. A maximum $P_d = 0.83$ is obtained for the combination $k_f = 0.25$ and SNR = 10 dB with non-transformed data. This implies that all the subsampling combinations $[k_{xr} = 0.1, k_f < 0.2]$ are producing low probabilities of detection $P_d \leq 0.75$, irrespective of the noise level. The results for subsampling $k_{xr} = 0.3$ in Figure 5.23-b) show that, indeed, the more conservative the cross-range subsampling is, the better the P_d is. Finally, Figure 5.23-c) shows that for $k_{xr} = 0.5$ the results are very robust with $P_d = 0.94$ even for low frequency subsampling $k_f = 0.1$ and a low SNR of 2 dB. Any k_f -SNR combination above this operation point will yield a $P_d = 1$, or perfect reconstruction.

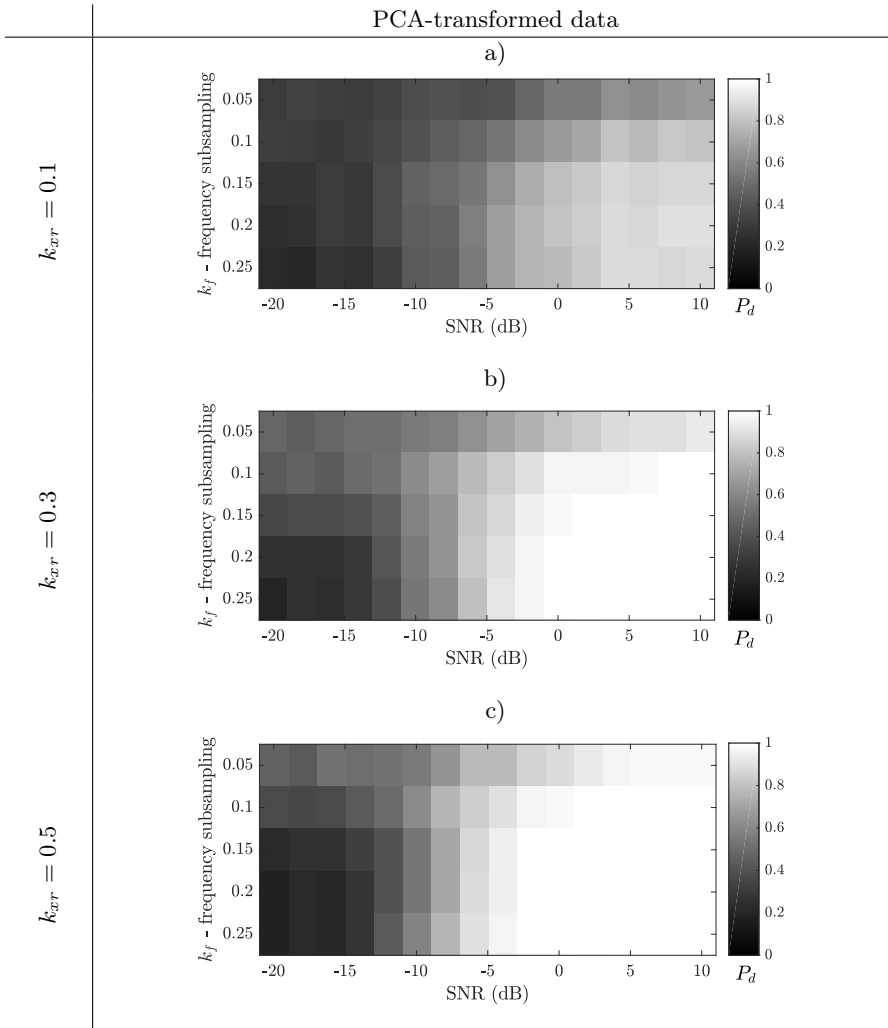


Figure 5.24: P_d vs. SNR for several subsampling rates $k_{xr} = 0.10, 0.3$ and 0.5 and $k_f = 0.05 - 0.25$ for the AT landmine and PCA-transformed data. A probability of false alarm of 10^{-2} was chosen and 500 Monte-Carlo trials were run. A CA-CFAR detector was used to extract the P_d values.

The performances shown in the graphs in Figure 5.24 show a general and remarkable improvement when using PCA as a preconditioning transform with respect to the non-transformed data performances. Although results for $k_{xr} = 0.1$ —see Figure 5.24-a)— are still far from those presented in Figure 5.24-b) and c), they constitute an interesting option for reducing data collection to a minimum while keeping P_d values above 0.8. That is the case for the combination [$k_{xr} = 0.1, k_f = 0.1$] and SNR = 10 dB.

The benefit of using PCA —thanks to its robustness against noise— is shown in Figures 5.23-c) and 5.24-c): The two figures show a similar behavior for the Monte-Carlo experiments using

$k_f = 0.25$. The P_d results for PCA are 0.02 – 0.03 higher than those of non-transformed data. As k_f decreases down to $k_f = 0.1$, it is clear that the P_d (Figure 5.24-c) remains above 0.95 for PCA and for SNR = -2 dB, whereas for non-transformed data (Figure 5.23-c) this only happens for $k_f \geq 0.2$. If more favorable conditions are assumed (SNR ≥ 10), $P_d > 0.9$ or $P_d = 1$ can be obtained just by keeping 1.5% of the original data with a combined subsampling strategy of [$k_{xr} = 0.3, k_f = 0.05$] or 2.5% with [$k_{xr} = 0.5, k_f = 0.05$] (Figures 5.24-b) and 5.24-c), respectively).

(a) Reconstruction position deviation for the AT landmine.

k_{xr}	0.1	0.3	0.5
SNR (dB)	-10 / 0 / 10		
P_d (%)	39.4 / 93.4 / 96.6	87.4 / 99.8 / 100	96.8 / 100 / 100
% at GT	47.6 / 85.4 / 94.6	78.3 / 96.9 / 99.5	93.1 / 100 / 100
% ± 1 bin	9.5 / 12.5 / 5	12.2 / 3.1 / 0.5	4.6 / 0 / 0
% ± 2 bins	2.4 / 0 / 0	6.1 / 0 / 0	0.8 / 0 / 0

(b) Reconstruction position deviation for the AT landmine.

k_f	0.05	0.15	0.25
SNR (dB)	-10 / 0 / 10		
P_d (%)	61.2 / 99.2 / 100	67.2 / 100 / 100	87.6 / 100 / 100
% at GT	32.9 / 84.8 / 94.9	52.7 / 100 / 100	77.3 / 100 / 100
% ± 1 bin	21.8 / 11.1 / 3.6	20.3 / 0 / 0	12.4 / 0 / 0
% ± 2 bins	21.8 / 1.2 / 1	16.2 / 0 / 0	3.1 / 0 / 0

Table 5.3: Reconstruction position deviation: Percentage of the reconstructions (using PCA and 500 trials) at the correct depth bin, or one or two depth bins away from the ground truth (GT). Several values for k_{xr} , k_f and SNR levels are used for each landmine type. The probabilities of detection for each case are also displayed.

From Table 5.3 it can be extracted that reconstruction location deviations stay minimal when cross-range subsampling is applied and under unfavorable noise conditions of SNR = 0 dB. In the worst subsampling case ($k_{xr} = 0.1$), the reconstructions in the ground truth depth bin reach 85.4% whereas 12.5% happen one bin away and the rest, three or more bins away. Keeping the same noise conditions, 96.9% of the reconstructions are in the ground truth for $k_{xr} = 0.3$ and 100% for $k_{xr} = 0.5$. Correct positioning of the reconstructions shows to be less affected by frequency subsampling and added noise, since $k_f = 0.15$ yields comparable results to $k_{xr} = 0.5$ in terms of P_d and positioning, both reaching 100% for SNR ≥ 0 dB.

5.8.3 The AP landmines

In general, for all the results presented, the performance curves appear to be less affected when subsampling in the cross-range dimension is applied. As an example, we compare separately the subsampling coefficients $k_f = k_{xr} = 0.2$, for which the final data volumes prior to the CS reconstruction are the same. In all cases, the obtained P_d figures show worse results for $k_f = 0.2$ than $k_{xr} = 0.2$.

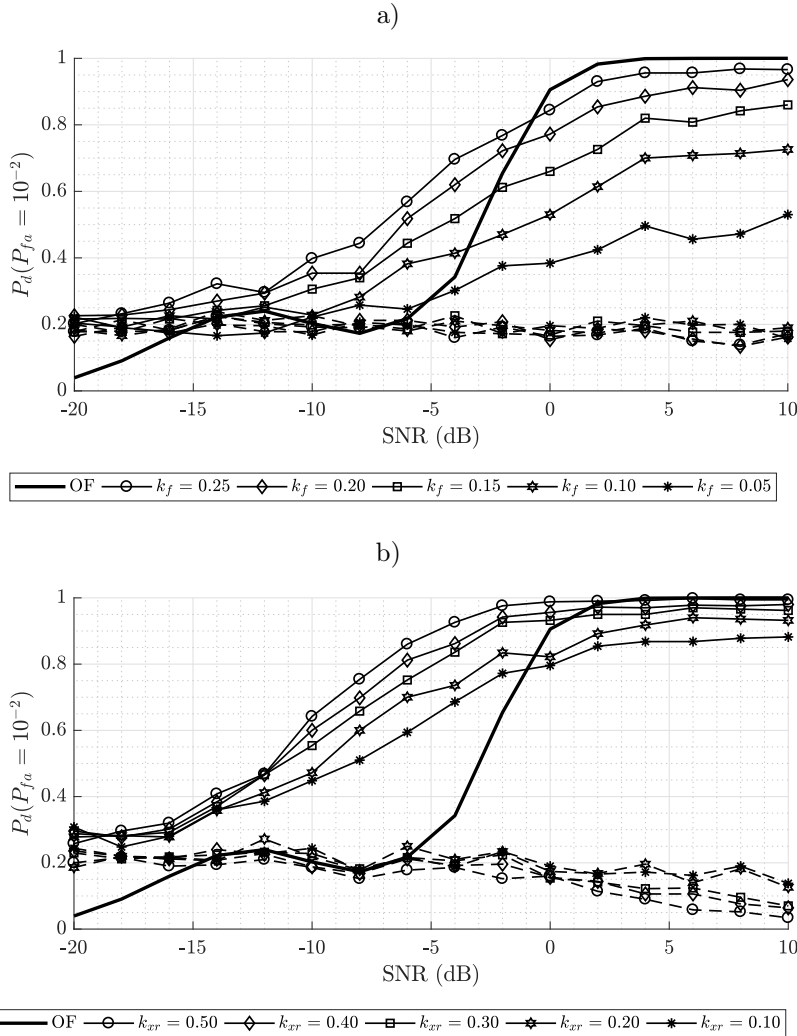


Figure 5.25: Robustness analysis of the CS reconstructions of the PMN2 AP landmine using BPDN and raw data. The P_d vs. SNR curves are plotted for multiple a) k_f and b) k_{xr} values. The solid line indicates intrinsic filtering is applied, whereas the dashed line indicates otherwise.

In the case of the PMN2 and raw data only, there is a 0.12 P_d difference when the P_d at SNR = -10 dB is assessed in Figure 5.25-a) and b). When the SNR is increased to 0 dB and +6 dB, the difference becomes 0.05 and only 0.02, respectively. From these results we can derive that these data are more robust to noise when subsampling is applied in the cross-range dimension.

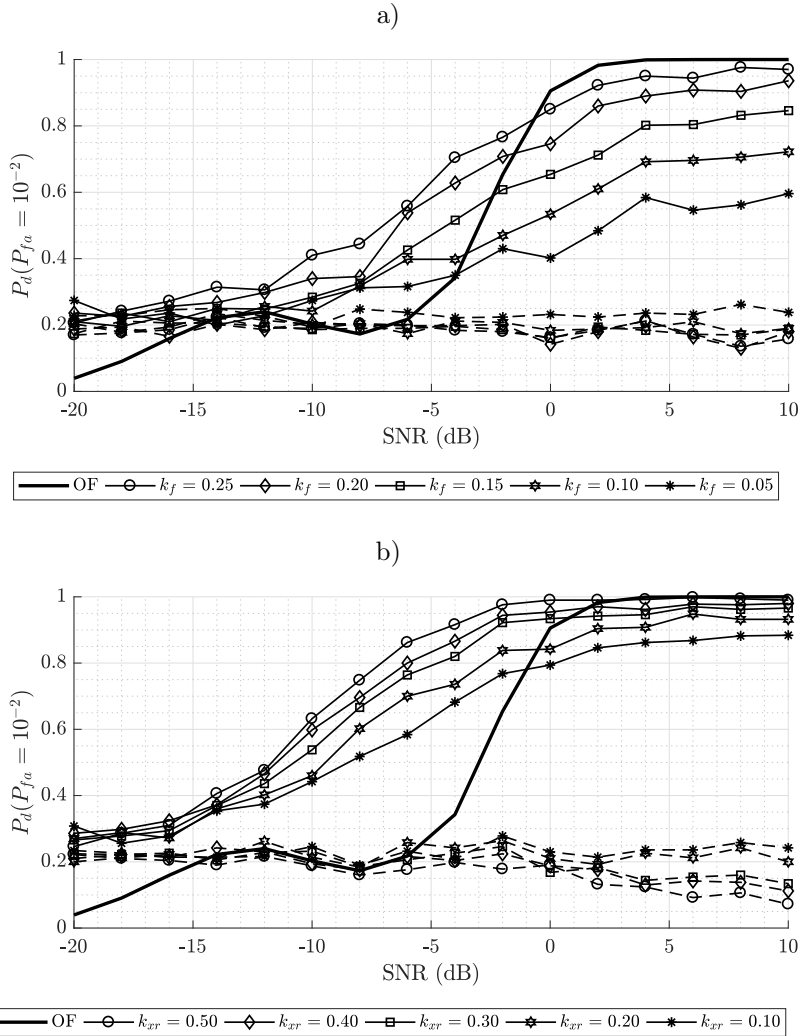


Figure 5.26: Robustness analysis of the CS reconstructions of the PMN2 AP landmine using BPDN and PCA data preconditioning. The P_d vs. SNR curves are plotted for multiple a) k_f and b) k_{xr} values. The solid line indicates intrinsic filtering is applied, whereas the dashed line indicates otherwise.

The same exercise can be done when using PCA-transformed data, as displayed in Figure 5.26. In this case, the P_d gain at -10 dB is 0.13, whereas it is reduced to 0.1 and 0.03 for SNR's of 0 and +6 dB, respectively. These results indicate that the P_d gains when comparing the

P_d obtained in $k_f = k_{xr} = 0.2$ are slightly improved when PCA-transformed data are used, which adds even more robustness to the cross-range subsampling strategy (especially under noisy conditions).

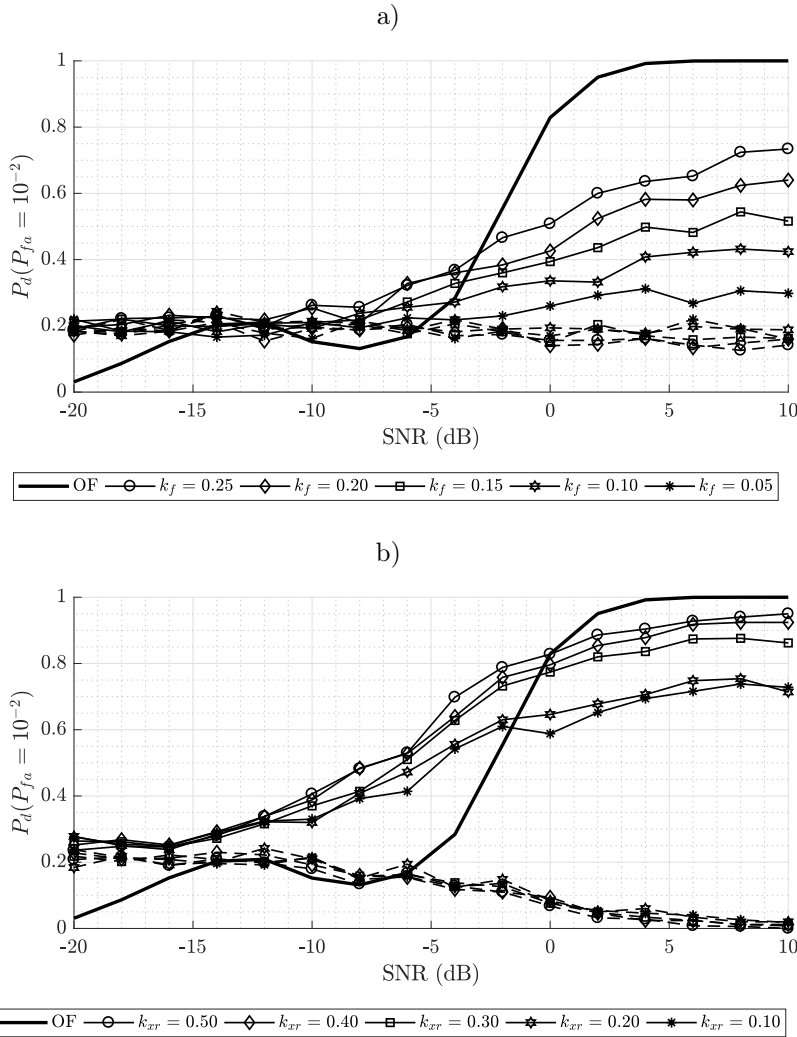


Figure 5.27: Robustness analysis of the CS reconstructions of the M14 AP landmine using BPDN and raw data. The P_d vs. SNR curves are plotted for multiple a) k_f and b) k_{xr} values. The solid line indicates intrinsic filtering is applied, whereas the dashed line indicates otherwise.

Finally, the P_d gains in the case of the M14 AP landmine (see Figure 5.27) yield different trends as the SNR increases. It is found that for SNR values of -10 , 0 and $+6$ dB, the P_d gain evolves as follows: 0.08 , 0.22 , and 0.17 . The smaller gain found for lower SNR values is due to the already very weak signal recovered from the M14 and the high added noise level, which obviously hinders

target detection. In Figure 5.27-a), a slight improvement in performance is appreciated for SNR levels of -5 dB and higher. From that level on, the weak target begins to stand out from noise, explaining that the P_d gain increases for at SNR = 0 dB, but latter decreases for higher SNR values, as it was expected in accordance to previous experiments.

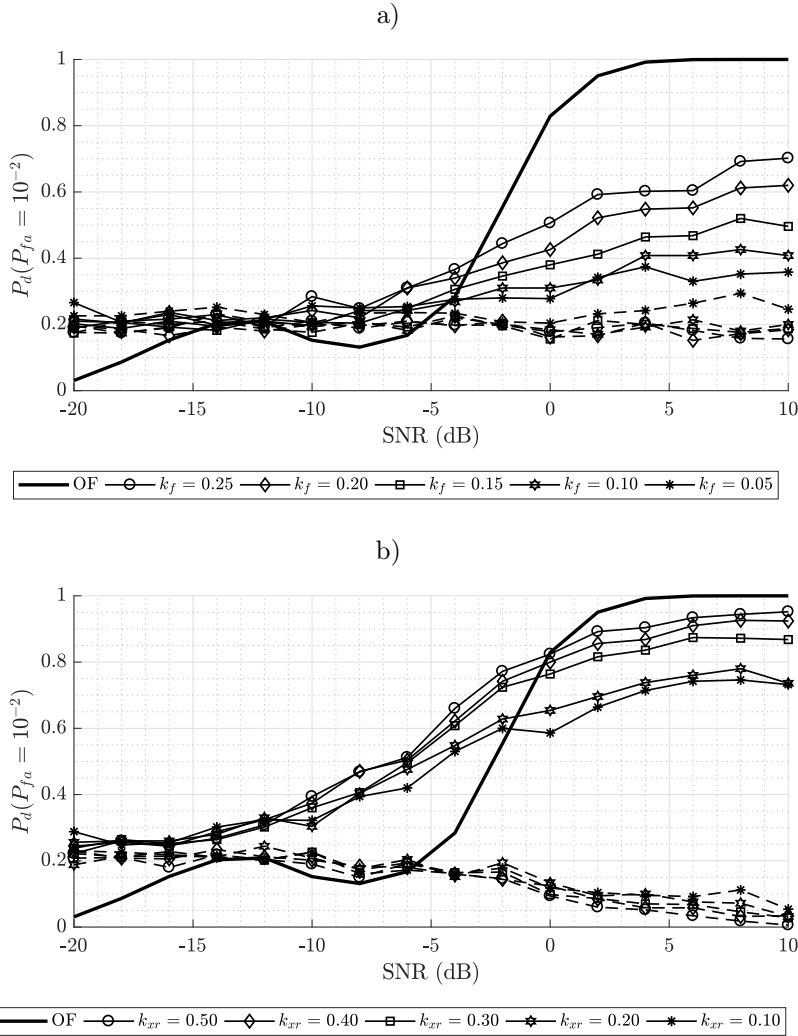


Figure 5.28: Robustness analysis of the CS reconstructions of the M14 AP landmine using BPDN and PCA-transformed data. The P_d vs. SNR curves are plotted for multiple a) k_f and b) k_{xr} values. The solid line indicates intrinsic filtering is applied, whereas the dashed line indicates otherwise.

For the PCA-transformed M14 data (see Figure 5.28) the P_d gains follow the expected trend: they vary from 0.05, to 0.23, and finally 0.21 (again for SNR values of -10, 0 and +6 dB, respectively). Again, once the M14 target can be distinguished from noise, the P_d gain achieves

slightly higher values than in the raw data case, confirming that PCA preconditioning is always positively affecting the P_d in reconstructions.

Although the results for $k_{xr} = 0.05$ are not displayed, it is also worth mentioning that tests using that subsampling rate showed that the P_d drastically dropped to unexploitable results since in most cases there were not enough cross-range measurements to adequately reconstruct the hyperbolic phase history of the target or directly there were no available measurements at all (several adjacent cross-range measurements may be skipped, creating a shadowing effect in the target region). From these results it is derived that the performance is more sensitive to subsampling in frequency than in cross-range although the worsening appears more gradually in the former, dropping faster to P_d values close to 0 for the latter.

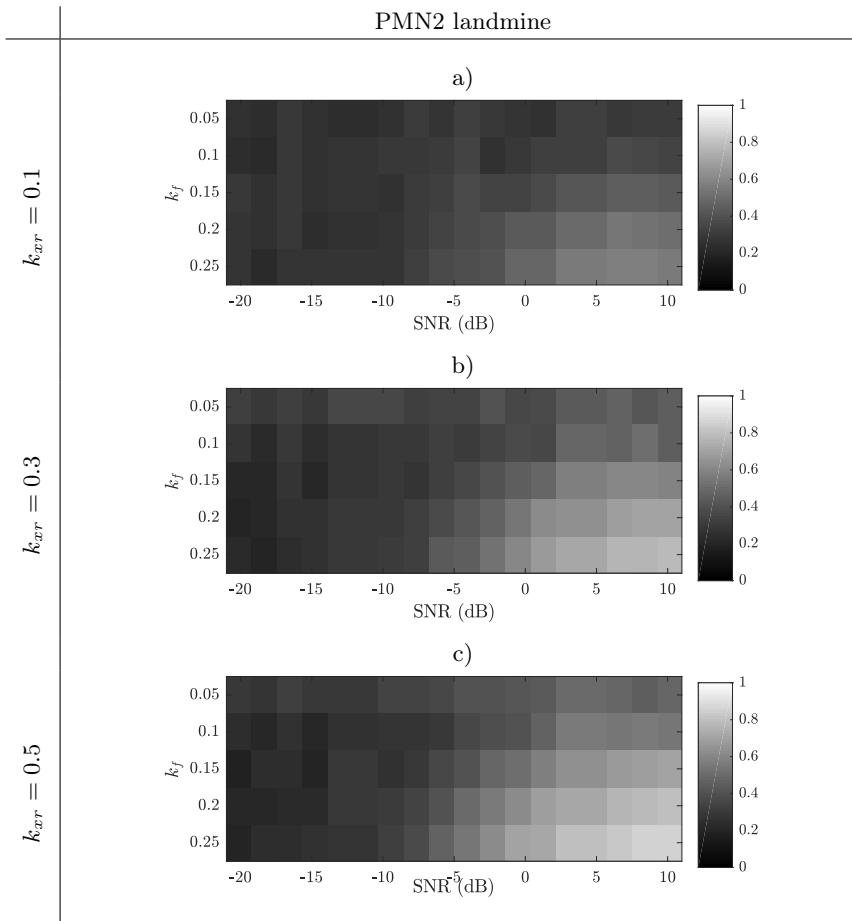


Figure 5.29: P_d vs. SNR for several subsampling rates $k_{xr} = 0.1 - 0.5$ and $k_f = 0.05 - 0.25$ for PCA-transformed data for the PMN2 landmine. A probability of false alarm of 1×10^{-2} was chosen and 500 Monte-Carlo trials were run. A CA-CFAR detector was used to extract the P_d values.

Regarding subsampling in both frequency and cross-range, and similarly to the AT case, we can derive from Figures 5.29 and 5.30 that for the PMN2 and M14 landmines the cross-range subsampling rate must be kept high in order to guarantee acceptable P_d values even for relatively high SNR levels. Due to the limited received energy back at the radar from these non-metal landmines, the detection ability is greatly reduced for heavily subsampled scenarios. This is especially noticeable for the M14, whose very small physical size makes it highly vulnerable to cross-range subsampling. Skipping some cross-range measurement positions may completely hinder the ability to retrieve exploitable information from this type of target (its hyperbolic phase history). Because of its slightly larger size, this is affecting less the PMN2 landmine, yielding P_d around 0.8 for the best-case scenario considered in these results. From these results we can infer that subsampling both in frequency and cross-range is not recommended for low-reflectivity, small-sized AP landmines.

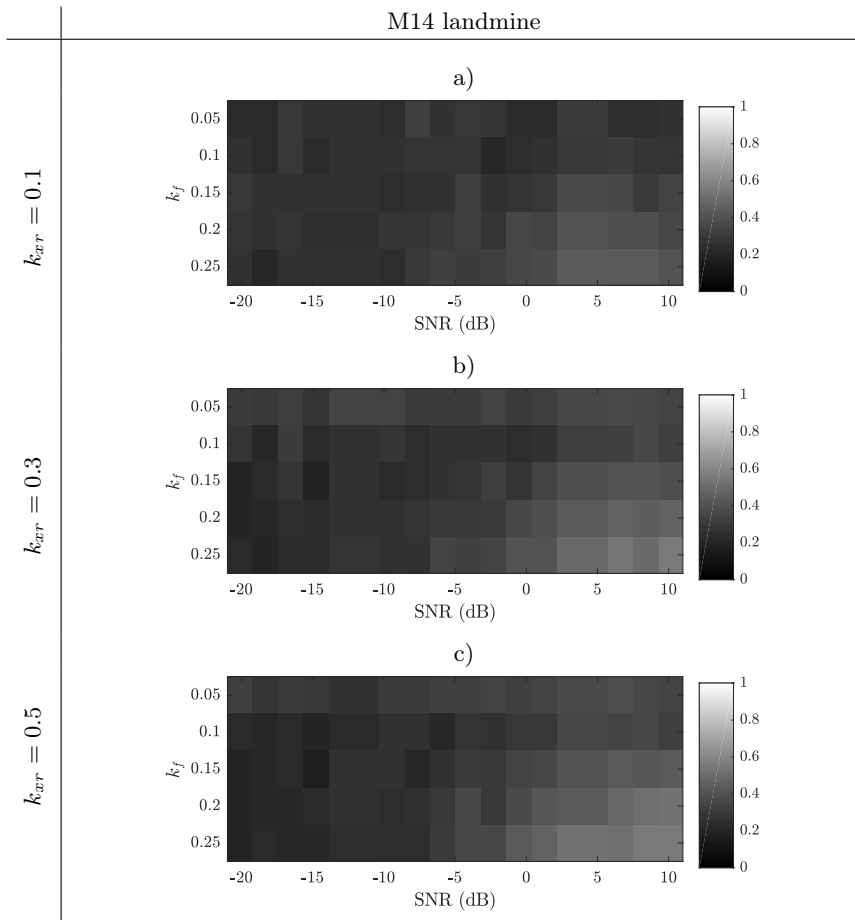


Figure 5.30: P_d vs. SNR for several subsampling rates $k_{xr} = 0.1 - 0.5$ and $k_f = 0.05 - 0.25$ for PCA-transformed data for the M14 landmine. A probability of false alarm of 1×10^{-2} was chosen and 500 Monte-Carlo trials were run. A CA-CFAR detector was used to extract the P_d values.

Regarding the PMN2 and M14 landmines, we reach the following conclusion: The effect of using PCA is less evident although it follows the same reasoning as in the AT landmine, helping increasing the P_d when frequency subsampling is applied (especially for lower k_f figures) but it is negligible when subsampling happens in the cross-range dimension (valid for all k_{xr} figures). Nevertheless, it is worth mentioning that the antenna-ground modeling employed for ground reflection removal enables unmasking and detection of these small landmines, which would remain undetectable otherwise ($P_d \lesssim 0.2$ for all cases studied).

Tables 5.5 and 5.6 show the same comparison for the PMN2 and M14 mines. In those cases, target positioning is significantly more affected as frequency subsampling and added noise become more severe, especially for the M14 which presents overall lower P_d figures than PMN2. Despite being close to the surface, the very low returns of these objects make them more vulnerable to mismatches with the training dictionary Θ , hence producing depth inaccuracies after target reconstruction and detection. Given the smaller size of these landmines, fewer cross-range positions are needed to describe their hyperbolic phase history than for the much larger AT landmine. This explains that PMN2 and M14 present similar positioning deviation to those of the AT landmine when cross-range subsampling is applied and under relatively benign noise conditions ($\text{SNR} \geq 0$).

(a) Reconstruction position deviation for the PMN2 landmine when applying cross-range subsampling.

k_{xr}	0.1	0.3	0.5
SNR (dB)	-10 / 0 / 10		
P_d (%)	44.2 / 79.4 / 88.4	53.8 / 93.4 / 96.6	63.2 / 99 / 99
% at GT	53.7 / 94 / 100	54.1 / 96.8 / 100	64.6 / 97.2 / 100
% ± 1 bin	24.8 / 4.7 / 0	20.2 / 3.2 / 0	17.8 / 2.8 / 0
% ± 2 bins	8.3 / 0.7 / 0	9.2 / 0 / 0	7.2 / 0 / 0

(b) Reconstruction position deviation for the PMN2 landmine when applying frequency subsampling.

k_f	0.05	0.15	0.25
SNR (dB)	-10 / 0 / 10		
P_d (%)	27.4 / 40.2 / 59.6	28.4 / 65.4 / 86.4	41 / 85 / 97
% at GT	28.6 / 36.7 / 56.2	43.2 / 72.5 / 81.1	40.6 / 94 / 100
% ± 1 bin	24.1 / 20 / 19.7	18.9 / 15.8 / 14.2	20.8 / 4.7 / 0
% ± 2 bins	22.3 / 14.2 / 7.3	11.6 / 5.8 / 2.8	9.4 / 0.7 / 0

Table 5.5: Reconstruction position deviation: Percentage of the reconstructions (using PCA and 500 trials) at the correct depth bin, or one or two depth bins away from the ground truth (GT). Several values for k_{xr} , k_f and SNR levels are used for each landmine type. The probabilities of detection for each case are also displayed.

(a) Reconstruction position deviation for the M14 landmine when applying cross-range subsampling.

k_{xr}	0.1	0.3	0.5
SNR (dB)	-10 / 0 / 10		
P_d (%)	32.2 / 58.6 / 73.2	36 / 76.4 / 86.8	39.4 / 82.4 / 95.2
% at GT	49.2 / 89.9 / 95.8	42.7 / 95.9 / 100	48.6 / 96.8 / 100
% ± 1 bin	23.3 / 5.8 / 3.6	18.2 / 2.5 / 0	18 / 2.4 / 0
% ± 2 bins	12.5 / 2.9 / 0.6	12.7 / 0.8 / 0	11.7 / 0.8 / 0

(b) Reconstruction position deviation for the M14 landmine when applying frequency subsampling.

k_f	0.05	0.15	0.25
SNR (dB)	-10 / 0 / 10		
P_d (%)	25.6 / 27.8 / 35.8	20.6 / 38 / 49.6	28.4 / 50.6 / 70.2
% at GT	27 / 30.4 / 46.6	38.8 / 53.8 / 72.4	37.1 / 72.6 / 94.7
% ± 1 bin	20.9 / 21.4 / 15.8	17.6 / 16 / 13.3	14.4 / 11.3 / 3.2
% ± 2 bins	20 / 19.6 / 12	15.6 / 13.4 / 5.7	16.5 / 6.6 / 2.1

Table 5.6: Reconstruction position deviation: Percentage of the reconstructions (using PCA and 500 trials) at the correct depth bin, or one or two depth bins away from the ground truth (GT). Several values for k_{xr} , k_f and SNR levels are used for each landmine type. The probabilities of detection for each case are also displayed.

5.9 Conclusions

In this chapter we have introduced the concept of GPR and highlighted some of the most common applications that are currently in use. The application covered in the chapter is landmine detection, hence three of the most well-known landmines have been presented as well. The physical interactions between the GPR and the ground are described, with special interest for the reverberations inside the GPR antenna and with the ground, which can completely disable the GPR if AP landmines are to be detected. To completely remove these undesired and potentially harmful effects, a model accurately describing them is presented and used to filter the measured data, for which explanatory examples are given.

Given the wide-beam antenna used in the measurements, SAR principles have been described. Although SAR is not a core subject in this work, the idea of using a GPR on a moving platform to generate SAR measurements enables the possibility of subsampling in the motion dimension. This chapter has also described how to adapt conventional GPR-SAR measurements to CS and the three subsampling strategies considered: in frequency, in scanning (cross-range) positions, or both.

Finally, the scene and radar used in the measurement campaign have been detailed. The measurements have been affected by multiple subsampling rates in frequency and cross-range, as

well as different SNR levels, so the robustness of the results that CS is offering for an application as GPR can be computed. In order to produce performance analysis in the form of probabilities of detection, the 2-D CA-CFAR detector as the one introduced in Chapter 3 has been used. We have found that using PCA as a data preconditioner helps in solving the CS minimization problem (in this case using BPDN), outperforming the standard results using raw data with no transformation applied. PCA also performs a dimensionality reduction which cancels out most of the noise subspace components, cleaning out the reconstructed signal. Most importantly, the intrinsic antenna modeling has made possible detecting low-reflectivity AP landmines which, in any other case, would remain undetectable to GPR and most metal-based mine detection techniques. Thanks to this model, the filtered measurements no longer contained reverberations masking the shallower landmines.

The following table summarizes the global conclusions reached for using subsampling and CS reconstruction on GPR measurements. The results displayed assume a far from ideal scenario of having a low SNR of 6 dB and intrinsic filtering. A subsampling rate of 0.2 is chosen for frequency or cross-range subsampling, both with and without PCA preconditioning.

Landmine	Transf.	P_d if $k_f = 0.2$	P_d if $k_{xr} = 0.2$	Exploitable
AT	Raw	1	1	yes
	PCA	1	1	yes
PMN2	Raw	0.9	0.94	yes
	PCA	0.9	0.98	yes
M14	Raw	0.58	0.75	no
	PCA	0.55	0.75	no

Table 5.9: Conclusions table providing concise guidelines on the exploitability of GPR and CS on the three types of landmines.

Results show very high P_d for the AT and PMN2 landmines (all above 0.9), which leads to concluding the proposed subsampling scheme is exploitable in real situations. Unfortunately, the already discussed limitations in backscattered energy from the M14 landmine makes it a difficult target scoring low P_d values in general. In that case, it is recommended to choose higher subsampling rates to improve the detection performance, although this would incur in higher data volumes and processing times.

Chapter 6

Passive Coherent Location

In this final application chapter, the concept of using illuminators of opportunity to detect targets is introduced and several examples are given based on the current state of the art. In this work, the DVB-T transmissions will be used as illuminators and, therefore, the main concepts behind them will be described, which includes the DVB-T signal structure and modeling. The range-Doppler imagery tool is defined and the type of imagery created is introduced to the reader. The typical resolution measurements in PCL are also mentioned, which will affect the choice of shorter or longer measurements based on the desired Doppler frequency resolution. Next, two methods to extract the reference signal and generate CS reconstructions of the airspace are proposed: One using a full measurement of the reference signal and another one applying CS to synthetically reconstruct the reference. Finally, the obtained results in terms of performance analysis are shown and discussed, followed by farther discussion on other sparsifying methods such as the re-weighted ℓ_1 minimization algorithm or using side information to include scene clutter information in the minimization problem.

6.1 Illuminators of opportunity

The inherent characteristic of bistatic or multistatic radars not requiring collocated Tx and Rx enables the possibility of exploiting other sources of radio illumination as transmitter. These are called opportunistic illuminators or illuminators of opportunity (IOP) because of their access, sometimes by chance or limited in time. An interesting IOP must present a sufficiently wide bandwidth although this is very application-dependent, and the possibility of direct access to a reference signal, that is to say, LOS between transmitters and receivers. Such illuminators should also provide a sufficiently ample coverage of the area or volume to survey and sufficiently high received echo powers. The undeniable positive aspects of using IOP include no direct access to transmitters is required and, therefore, there is no investment cost in transmitters which may include legal restrictions and greatly facilitates equipment deployment and minimizes radar detectability and interception by a foe since no energy needs to be emitted.

Some of the exiting bistatic/multistatic radars that employ IOP include third-party open transmission such as mobile communications (GSM [147] or LTE [148]), satellite remote sensing [149, 150, 151] or GPS systems, WiFi, or digital audio broadcast-terrestrial (DAB-T) [152] or digital video broadcast-terrestrial (DVB-T) [153, 154] transmissions, as it is the case in this chapter. The signals transmitted by most of these IOP were not designed specifically to be exploited by passive radars for target location and positioning and, consequently, their ambiguity function may not be optimal or even difficult to work with if high secondary lobes appear in the ambiguity function representation. Because of these reasons, and depending on the application, some IOP will be directly not exploitable.

In this chapter we will focus on the DVB-T transmissions given their vast availability in urban and sub-urban areas and their sufficiently broad channels in terms of bandwidth, which will be useful in target ranging.

6.2 OFDM fundamentals

The data transmission scheme used in DVB-T is sustained on orthogonal frequency-division multiplexing (OFDM). In contrast to other large bandwidth systems where the whole bandwidth is used as a block to transmit information, the OFDM modulation employs N_{sc} narrow-band, discrete frequency subcarriers within a limited bandwidth B , each of which has a bandwidth of $\Delta f_{sc} = B/N_{sc}$. In Figure 6.1 we can see an example of an OFDM transmission scheme with $N_{sc} = 7$ subcarriers. Thank to the design and inter-spacing of this modulation, the subcarriers are considered to be orthogonal between them (power peaks in one subcarrier correspond to nulls in all other subcarriers), hence minimizing the inter channel interference (ICI). This is not the case in conventional frequency-division multiplex (FDM) schemes, from which OFDM was derived, where frequency guards must be added between sub-channels to avoid ICI, reducing the spectral efficiency of the transmission.

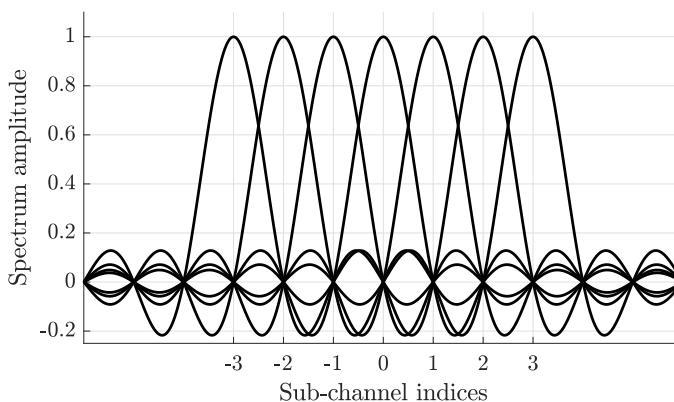


Figure 6.1: Seven orthogonal sub-channels cover the bandwidth of an OFDM signal.

This approach using multiple narrow-bandwidth subcarriers makes the transmitter and receiver parts simpler to implement. OFDM transmissions are more robust to narrow-band interfering signals [155], fast-fading multipath channels [156], frequency selective channels [157] or intentional jamming [158] since only a portion of the bandwidth is affected and may be recovered using error correction codes. Moreover, since subcarriers are narrow-band, it is easier to estimate the channel propagation conditions and perform signal equalization in reception [159]. This is usually done by adding pilots in the form of symbols or pilots subcarriers.

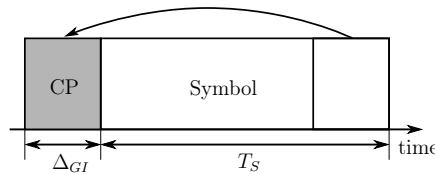


Figure 6.2: A CP of duration Δ_{GI} is added to the OFDM symbol to prevent ASI.

Multipath conditions in a channel can cause that delayed echoes of a symbol reach the receiver while the next symbol is being received, generating adjacent symbol interference (ASI). To avoid this, a guard interval or cyclic prefix (CP) of duration Δ_{GI} is also added to every symbol, hence reducing spectral efficiency to achieve no ASI. The CP is a copy of the last part of the transmitted symbol, as displayed in Figure 6.2. The CP duration Δ_{GI} will be 1/4, 1/8, 1/16 or 1/32 of T_S , and will depend on the expected maximum delay due to the multipath channel.

6.3 Structure and generation of DVB-T transmissions

The structure and the position evolution of subcarriers of the transmission parameters signaling (TPS), data and pilots used in DVB-T are described by the ETSI standard EN 300 744 [160].

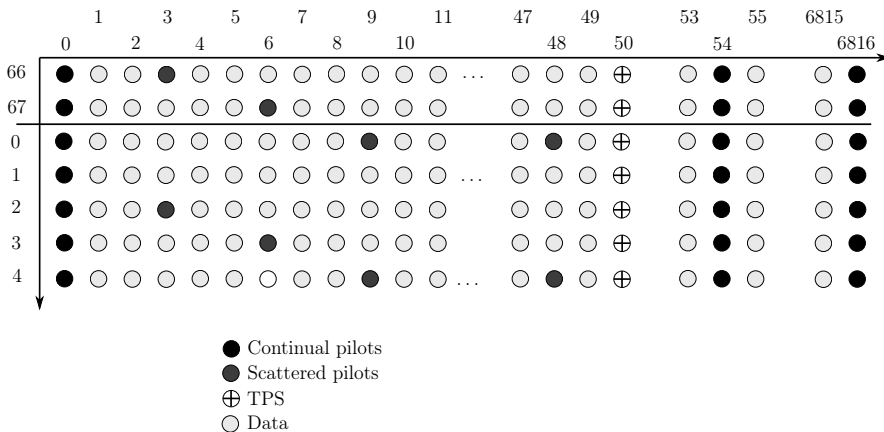


Figure 6.3: Subcarrier structure of a 8k DVB-T frame, which expands over 68 DVB-T symbols. The subcarriers are categorized as: continual or scattered pilots, TPS and data.

In Figure 6.3, the subcarrier structure of a generic DVB-T frame is shown for one channel. For each kind of subcarriers, a precise location pattern is followed, whereas the remaining subcarriers (in white) are left for carrying data inherent to the broadcast service.

DVB-T parameters	8K mode	2K mode
Number of subcarriers	6817	1705
Number of data subcarriers (N_{sc})	6048	1512
Number of pilot subcarriers	701	176
Of which, continual pilots	177	45
Number of TPS subcarriers	68	17
Symbol duration excluding CP	896 μ s	224 μ s
Subcarrier spacing	1116 Hz	4464 Hz
Signal bandwidth	7.61 MHz	7.61 MHz

Table 6.1: Main parameters of 8-MHz DVB-T channels for the transmissions modes 8K and 2K.

Every DVB-T frame has a total of 68 symbols with indices ranging from 0 to 67. The number of subcarriers varies depending on the selected transmission mode in the DVB-T standard, which are the 2K and 8K modes, as described in Table 6.1. For each mode, a list of subcarrier indices for continual or scattered as well as TPS is available and fixed by the DVB-T standard [160].

6.4 OFDM signal generation

Let us assume that a message of infinite length must be transmitted using an OFDM system. In DVB-T, the message bit stream is rearranged to fit a DVB-T symbol with a total length of N_{sc} data symbols, including the required pilots and TPS data according to the DVB-T structure described in Figure 6.3.

The data symbols are mapped using any of the modulation scheme's foreseen by the standard (16-QAM, 64-QAM or QPSK), which results in a stream of modulated data denoted as C , with $C_{(m,l,i)}$ the mapped data in the i -th subcarrier of the l -th DVB-T symbol in the m -th DVB-T frame. The signal model of the transmitted OFDM signal is:

$$s(t) = \text{Re} \left\{ e^{j2\pi f_c t} \cdot \sum_{m=0}^{\infty} \sum_{l=0}^{67} \sum_{i=0}^{N_{sc}} C_{(m,l,i)} \cdot \Omega_{(m,l,i)}(t) \right\}, \quad (6.1)$$

with f_c the central frequency of the channel and $\Omega_{(m,l,k)}(t)$ being defined as:

$$\Omega_{(m,l,i)}(t) = \begin{cases} e^{j2\pi \frac{i}{T_U} (t - \Delta_{GI} - lT_S - 68mT_s)} & t_1 \leq t \leq t_2 \\ 0 & \text{otherwise} \end{cases}, \quad (6.2)$$

where $i' = i - \frac{N_{sc}}{2}$ is the subcarrier index with respect to the channel's f_c , T_U is the symbol duration excluding the guard interval, Δ_{GI} is the guard interval duration, and T_S the symbol duration. Finally, $t_1 = (l + 68m)T_S$ and $t_2 = (l + 68m + 1)T_S$.

In Figure 6.4 we can see a typical OFDM block diagram for the transmission and reception parts. Binary data are mapped or modulated into QAM or QPSK symbols, which may also include forward error correction measures, before being parallelized into blocks of N_{sc} symbols, one for each subcarrier. At this point, pilots symbols are inserted following the pattern as described in Figure 6.3 above to allow channel estimation and equalization at reception.

From equations (6.1) and (6.2) we can identify the inverse Fourier transform (IFFT) of the modulated message C , which is a very efficient implementation of the OFDM modulation. The parallel transformed time-domain data are rearranged back into a serial stream and the CP is inserted before performing a digital-analog conversion and, if required, up-conversion to the selected frequency band.

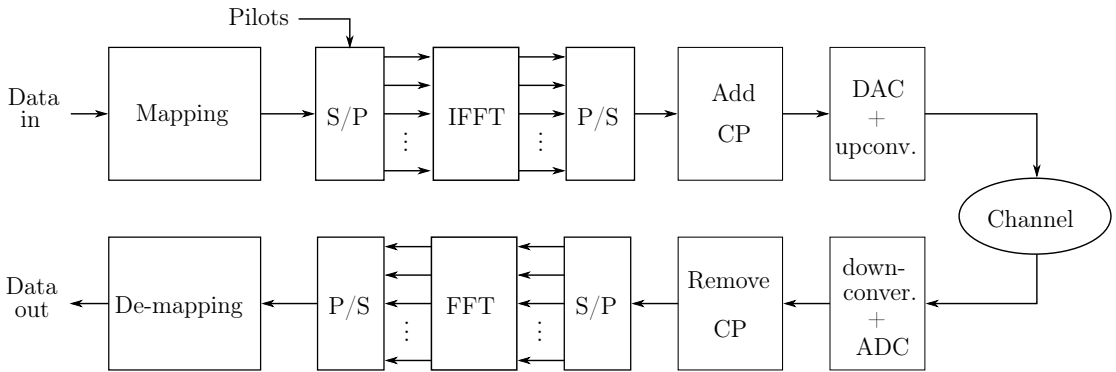


Figure 6.4: Block diagram of generic OFDM transmission and reception chains.

Inversely, in reception the CP is removed from the received signal, which is then demodulated using an OFDM scheme using an FFT block (after serial to parallel conversion) and a decoder. In this description we have omitted the use any error correction technique for simplicity.

Given the modulation schemes used for encoding the message, one can assume that a noise-like signal is transmitted in every subcarrier. In Figure 6.5-top we can see a time-domain representation of the signal amplitude (more precisely, the absolute value) which resembles noise.

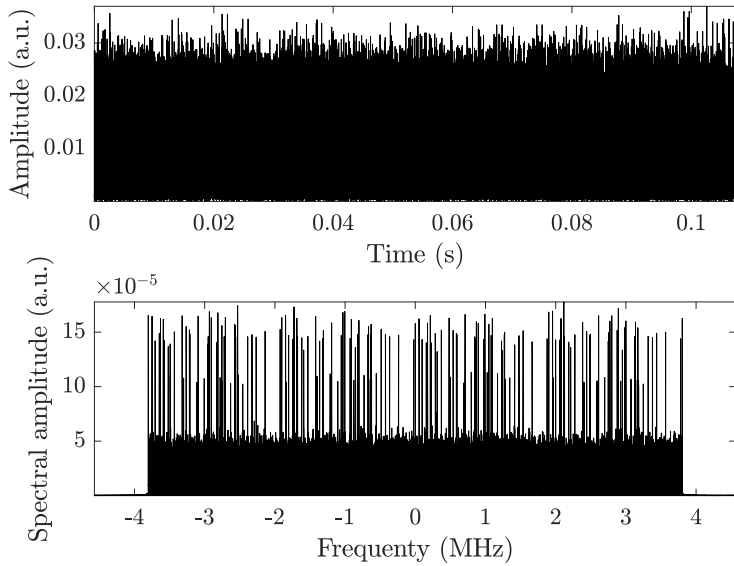


Figure 6.5: Time- (top) and frequency-domain (bottom) representations of a DVB-T signal.

Indeed, this OFDM signal is characterized by a normal distribution of zero mean and a given variance, as depicted in Figure 6.6, where the histograms for the real and imaginary values of an OFDM signal are displayed. This noise-like behavior is very interesting because it produces a very narrow, thumbtack-like ambiguity function close to the ideal Dirac delta $\delta(t)$.

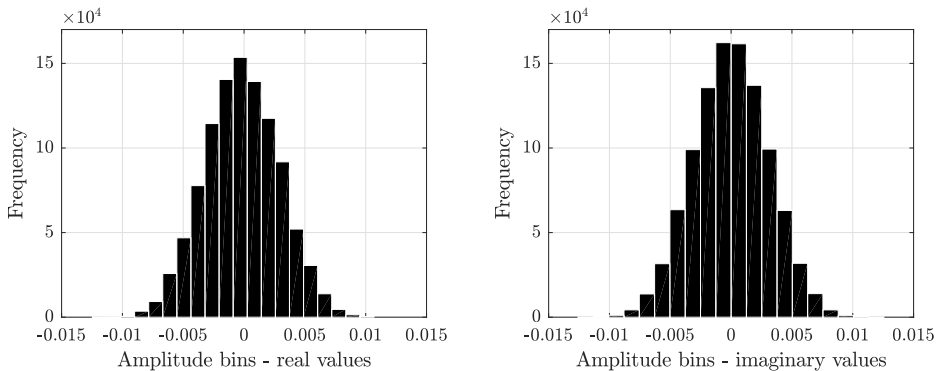


Figure 6.6: Histograms showing the noise-like distribution of DVB-T signals: Left, real values; right, imaginary values.

Nonetheless, as it will be explained in the next section, the continual and scattered pilots, as well as the TPS subcarriers added to the OFDM transmission —as defined by the DVB-T

standard—introduce a repetitive structure in the transmitted signals. This can be clearly seen in Figure 6.5-bottom, where the peaks in the frequency domain indicate the presence of constant signals—or at least non-noise-like signals.

6.5 The Doppler effect

Any radar measurement is affected by the configuration of the scene and the dynamics of the radar, the targets or both cases combined. Let us assume that a static object is transmitting a sinusoidal signal or tone with a frequency f which is received by a static observer, following a period $T = 1/f$. The highest points or crests of the transmitted signal are received by the observer every T seconds, or a distance equal to the wavelength λ_0 of the signal.

Let us now assume that the object is no longer static and starts moving toward the observer after transmitting one crest at a constant radial speed v_r . The next peak will be transmitted after T seconds, although now we must consider that, by then, the object will be $v_r T$ meters closer to the observer. This means that the wavelength seen by the observer λ'_0 , relative to the velocity of the object, is described as:

$$\lambda'_0 = \lambda_0 - v_r T. \quad (6.3)$$

Because the source is approaching the observer, the apparent frequency wavelength seen by the observer is smaller and, consequently, perceiving a higher frequency. This is known as the Doppler effect. Recalling the well-known expression of the frequency of a signal in function of its wavelength and the definition of λ'_0 , we can redefine the frequency seen by the observer as:

$$f' = \frac{c}{\lambda'_0} = \frac{c}{\lambda_0 - v_r T} = \frac{c}{\lambda_0} \left(\frac{1}{1 - v_r T / \lambda_0} \right) = \frac{c}{\lambda_0} \left(\frac{1}{1 - v_r / f_0 \lambda_0} \right), \quad (6.4)$$

and, since $c_0 = f \lambda_0$, the expression for f' becomes:

$$f' = f \left(\frac{c_0}{c_0 - v_r} \right). \quad (6.5)$$

Assuming now that the object may move away from the observer, the wavelengths the observer perceives become longer, therefore a lower observed frequency, as described by:

$$\lambda'_0 = \lambda_0 + v_r T, \quad (6.6)$$

which leads to the generalization of the Doppler effect, for a static observer and a moving source:

$$f' = f \left(\frac{c_0}{c_0 + v_r} \right). \quad (6.7)$$

where the velocity v is of negative sign when the source is approaching the observer and positive otherwise.

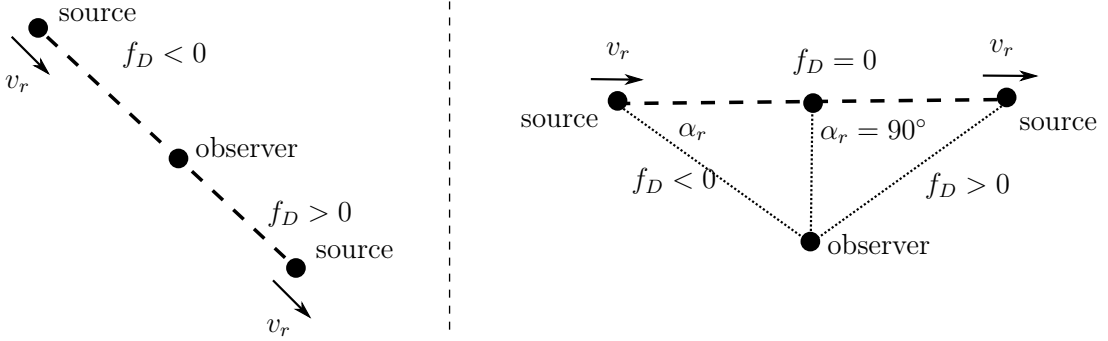


Figure 6.7: Description of possible Doppler shift situations: Left, the source moves at a constant speed towards the observer radially; right, the source moves at constant speed but its path will not intersect the observer's position.

The Doppler frequency shift produced by an object with radial velocity v_r with respect to a static receiver was already introduced in (2.23). If we now consider that the source is not moving radially but presents a certain radial velocity angle α_r as displayed in Figure 6.7-left, we can redefine the Doppler shift as:

$$f_D = \frac{2v_r}{\lambda_0} \cos(\alpha_r). \quad (6.8)$$

For the bistatic case, where a bistatic angle β is considered, equation (6.8) becomes:

$$f_D = \frac{2v_r}{\lambda_0} \cos(\alpha_r) \cos(\beta/2), \quad (6.9)$$

which corresponds to the case when the target is moving but the transmitter and receiver are static. In this chapter we will not consider the cases where the transmitter nor the receiver are moving. Therefore, and since the exact bistatic geometry is unknown, the Doppler frequency shift is computed in function of the variation of the range in function of time, that is, velocity. This is achieved by simply computing the first derivative of the bistatic range R_B :

$$f_D = \frac{1}{\lambda_0} \frac{dR_B}{dt} = \frac{1}{\lambda_0} \frac{d}{dt} (R_t + R_r). \quad (6.10)$$

6.6 Target detection using range-Doppler

The Doppler effect in a simple PCL scenario can be interpreted as the Doppler frequency shift by a moving source (e.g., an airplane) introduced to the back-scattered echo, which is received by a passive radar (observer) as seen in Figure 6.8. From this Doppler frequency, one can estimate the plane's radial speed but not the target's exact speed since, a priori, the exact target location and hence the scene geometry are not known (angles α_r and β). Therefore, we can only estimate the radial velocity using (2.23) and not (6.9). Should an approximate target location be available thanks to the interception of multiple hyperboloids, an accurate estimation of v_r using equation (6.9) would be possible.

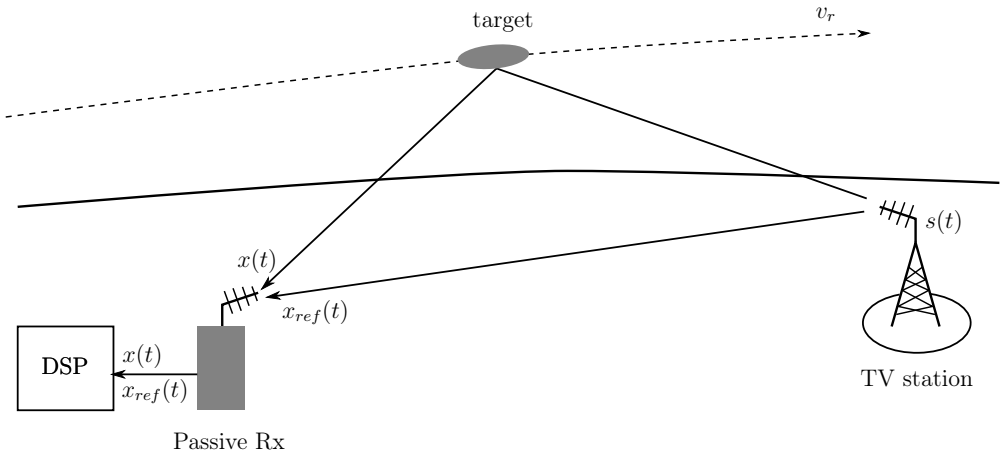


Figure 6.8: Schematic representation of a simplified PCL scenario: A passive Rx uses the broadcasts of a TV station to locate a target overflying the surveyed airspace. The Rx measures both the reflected $x(t)$ and LOS signals $x_{ref}(t)$. Finally, a DSP unit produces a rD image.

A very useful tool in PCL are range-Doppler diagrams which can visually show the bistatic range and measured Doppler frequency shift of one or multiple targets in the surveyed region by the passive receiver. The computation behind the range-Doppler diagram is based on the cross-correlation between the received signal $x(t)$ and the reference signal $x_{ref}(t)$. As in the expression of the ambiguity function already introduced in (2.61), the range-Doppler diagram also produces information in the frequency (or Doppler shift) domain. Hence, computing the range-Doppler diagram is done following the expression:

$$\gamma_{rD}(\tau, \nu) = \int_{-\infty}^{\infty} x(t)x_{ref}^*(t - \tau)e^{j2\pi\nu t} dt. \quad (6.11)$$

The range-Doppler diagram can be efficiently obtained using any implementation of the fast Fourier transform and a time delays for every inspected range, as displayed in Figure 6.9.

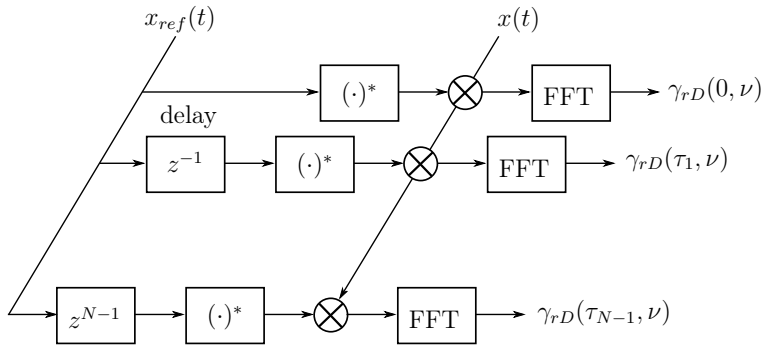


Figure 6.9: Conceptual block diagram of a r-D processor. The $x_{ref}(t)$ signal is delayed up to $N - 1$ time units and mixed with $x(t)$. The range-Doppler data are obtained after FFT of all the mixed signals.

Figure 6.10 shows an example of a range-Doppler diagram and the implications for a target depending on the region they appear. In this graph we can see that the range in the vertical axis obviously indicates the bistatic distance of the target from the receiver, the larger the range is, the farther the target is. Following the discussions derived in Section 6.5, the negative values in the horizontal axis show that the target is approaching the receiver, with increasing velocity as $|f_D|$ increases. Likewise, a positive Doppler frequency shift describes a target moving away from the receiver. Finally, the region around 0 Hz in the horizontal axis limits the regions where static clutter is found. This clutter is commonly received in PCL and is due to echoes of surrounding static targets (buildings, structures, large geological formations, or other contributions).

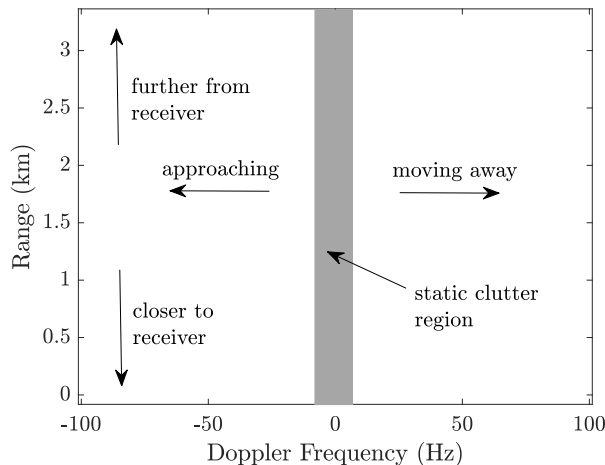


Figure 6.10: A, arbitrary range-Doppler diagram identifying the typical target appearances in this type of imagery.

If we use $x_{ref}(t)$ as sole input for the range-Doppler diagram γ_{rD} , we can directly obtain the autocorrelation or ambiguity function of a typical DVB-T signal. Figure 6.11 visually shows

that the ambiguity function of $x_{ref}(t)$ presents a prominent peak centered at $\gamma_{rD}(0, 0)$, dropping rapidly to value below -10 dB or lower. This decay can be observed as a function of the range in the zero-Doppler cut $\gamma_{rD}(\tau, 0)$ or as a function of the frequency in a zero-range cut $\gamma_{rD}(0, \nu)$, as shown in Figures 6.12-left and right, respectively.

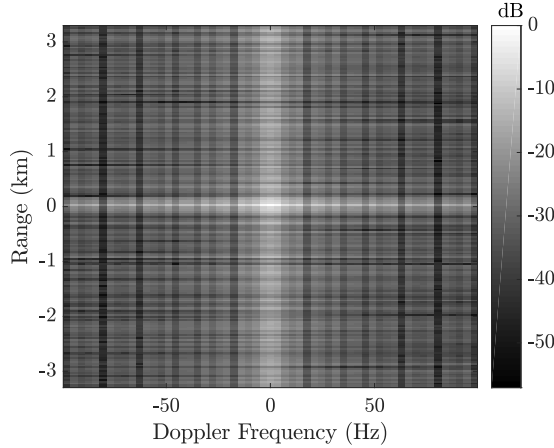


Figure 6.11: 2-D ambiguity function of a DVB-T signal. By inspecting range or frequency cuts of the the peak centered at $\tau = 0$ and $\nu = 0$, the PCL radar's Doppler frequency and range resolutions can be extracted, respectively.

From Figure 6.12-left we can extract that the range resolution (-3 dB ranges) is approximately 22 m (not far from the theoretically 18.75 m for an 8-MHz channel). Likewise, the Doppler shift resolution is inversely proportional to the observation or integration time T_{int} :

$$\Delta f_D = \frac{1}{T_{int}}. \quad (6.12)$$

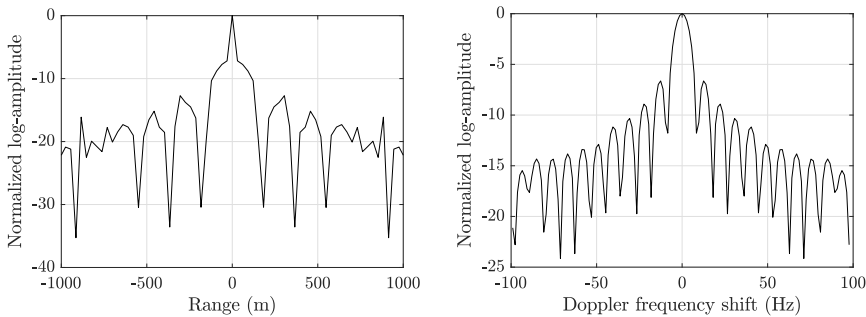


Figure 6.12: Two cuts of the DVB-T ambiguity function: Left) a zero-Doppler frequency cut $\gamma_{rD}(\tau, 0)$; right, a zero-range cut $\gamma_{rD}(0, \nu)$.

The normalized autocorrelation coefficients of x_{ref} (ambiguity function at zero Doppler) in Figure 6.13 shows a secondary peak at a time delay of $298.6 \mu s$, which implies having target ambiguities at a bistatic range of exactly 44.79 km. Likewise, other lower peaks appear at twice that delay or, what is equivalent, a bistatic range of 89.58 km. The amplitude decay shown by the peaks is due to the use of a linear convolution to generate the results.

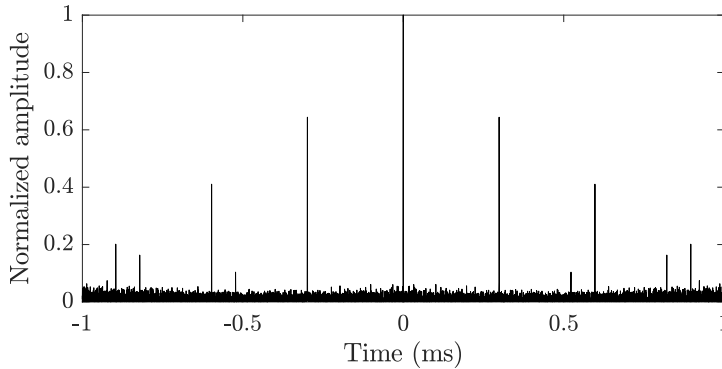


Figure 6.13: An extended zero-frequency cut of a DVB-T signal reveals two bright target ambiguities due to the signal's structure: one at $298.6 \mu s$ (or a bistatic range of 44.79 km), and a second one at exactly twice that distance (89.58 km).

Figure 6.14 shows an example of a simulated PCL case where a target is located at a bistatic range of 2.6 km and $f_D = 35$ Hz, which implies that the target is moving away from the receiver at an equivalent speed of 22 km/h, without any farther knowledge of the scene geometry.

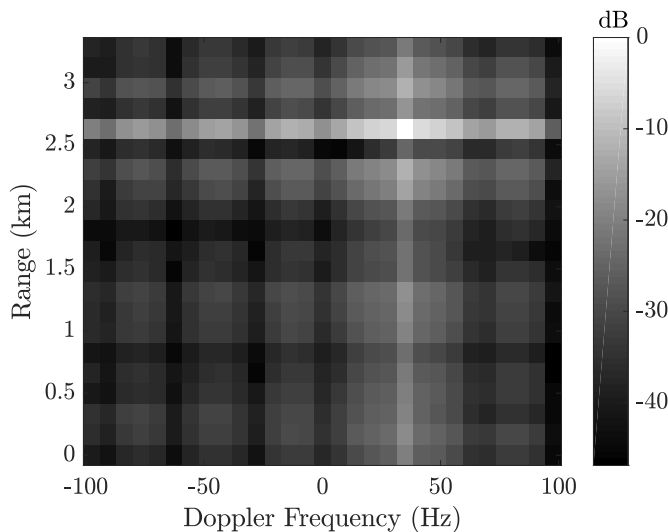


Figure 6.14: Example of a rD diagram obtained from simulated DVB-T data of a target located at a bistatic range of 2.6 km and $f_D = 35$ Hz (moving away at 22 km/h).

6.7 Adapting a PCL setup to CS

Given the lack of commercial or affordable radars or SDR reception modules able to perform random subsampling, we must apply the signal subsampling in an indirect way, that is, via post-processing of the fully sampled data at Nyquist rate. Although this consideration was not a limiting factor in the NDT and GPR applications, in PLC performing straightforward subsampling will not be possible in both the reference and surveillance signals due to the signal delay observed in PCL between them. In this section, this problem and possible solutions are explained and discussed.

6.7.1 Signal subsampling and reference signal recovery

Signal subsampling in PCL measurements is directly applied to the time-domain samples. In an initial setup we assume that both signals $x(t)$ and $x_{ref}(t)$ are received by one passive radar. Figure 6.15 depicts the problem of separating these two signals from each other, which be solved by using either:

- Two separate reception chains, physically isolated from each other to avoid presence of the reference signal in the surveillance signal.
- One single antenna and a signal filtering strategy such as the CLEAN algorithm or clutter rejection methods like the extensive cancellation algorithm (ECA).
- Spatial filtering by means of an antenna array and beamforming in post-processing.

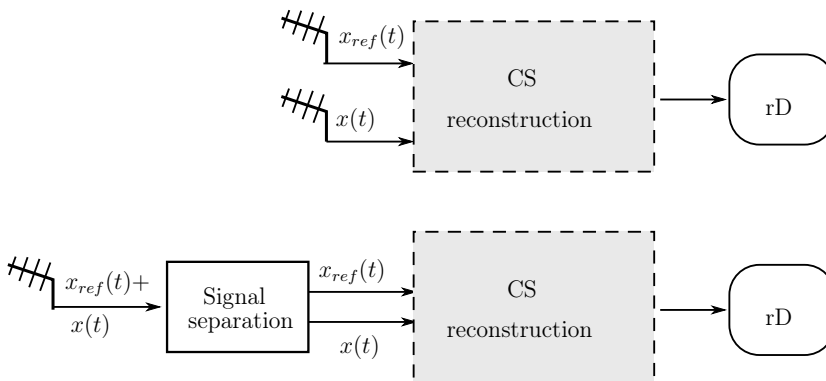


Figure 6.15: Two possible configurations for a passive radar to receive the reference and surveillance signals: Top, two physically separated receiving channels; bottom, one single reception chain is used for which signal separation of the two signals happens in software.

In this chapter, the data used for the presented experiments were collected using the second option: One single receiver and the ECA algorithm. This is the simplest and more efficient

solution, since the other two imply developing more complex hardware layouts —whether it is by using two reception chains duly isolated from each other or by using an array of large UHF antennas—, increasing production costs and making deployment and stealth operation more difficult.

Omitting farther discussion of the process behind signal separation, let us now consider that the two signals $x(t)$ and $x_{ref}(t)$ are available at the receiver and that there is no cross-contamination between them: They are ideally separated. Two options can be imagined to obtain range-Doppler imagery from randomly subsampled signals: randomly subsampling both signals, or simply the surveillance signal while the reference signal is fully sampled following the Nyquist sampling criterion.

The option of using random subsampling in both signals raises concerns while recovering the synchronization between two sets of incomplete data and populating the dictionary matrix Ψ with the reference signal. In Figure 6.16 we can see how an arbitrary PCL acquisition is started at time instant $t = 0$, where we assume that only the reference signal is received. After a time delay τ , the echo signal from a target is received and randomly sampled along with the reference signal, both simultaneously. Actually, in a real-world application, the IOP would have been continuously transmitting before the acquisition started and, therefore, the surveillance signal $x(t)$ would contain delayed versions of previous copies of $x_{ref}(t)$. In the proposed scenario as described by Figure 6.16, we assume that the IOP indeed started transmitting at $t = 0$.

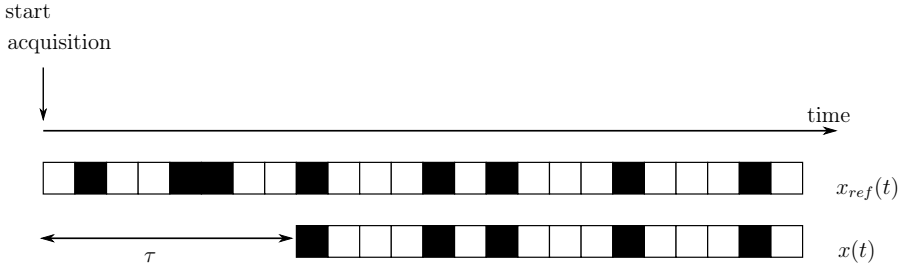


Figure 6.16: Two signals are received: The reference signal in direct LOS from the Tx and the surveillance signal from scene. Random subsampling (in black) in time domain is applied simultaneously in both signals.

Under this setup, there are several difficulties regarding the very probable lack of coincidence between the time samples from $x_{ref}(t)$ stored using an aggressive pseudo-random sequence (low k_f) and the samples kept from $x(t)$ but this time using a delayed pseudo-random sampling sequence. In order to solve this problem, a synthetic reference signal reconstruction from incomplete measurements is generated as schematically described in Figure 6.17.

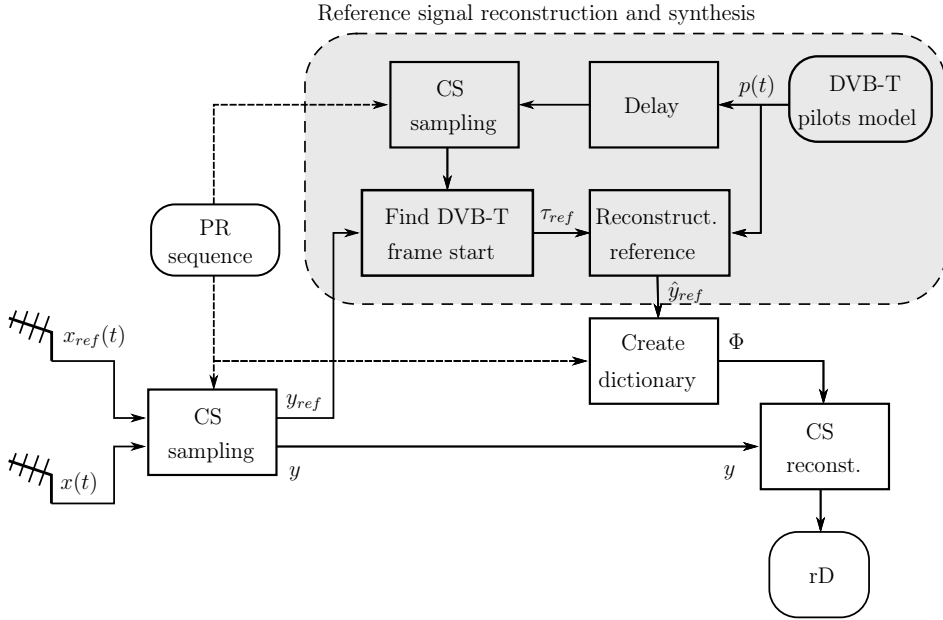


Figure 6.17: Obtaining a range-Doppler image using CS with a synthetically reconstructed reference signal from a subsampled, incomplete measurement.

The incomplete reference signal y_{ref} is fed to a module that locates the beginning of the first complete DVB-T symbol. This is done by generating delayed and subsampled copies of a synthetic DVB-T symbol using only pilots and no data. The pseudo-random (PR) sequence used for subsampling is identical to that used to subsample $x(t)$. These copies are used to find the maximum correlation with the y_{ref} signal, delay after delay. Once a maximum is found, the corresponding delay is assumed to be the reference delay τ_{ref} , which indicates that a DVB-T symbol starts at $t = \tau_{ref}$ in the recording. All processing will be referenced to that time instant, including the recording with the surveillance signal $x(t)$. Once known τ_{ref} , it is straightforward to build a synthetic-data-based dictionary using the same PR sequence and signal model. Finally, a CS minimization algorithm is used to generate the sparse range-Doppler diagram. The usability of this solution will depend on the similarity between the original reference signal and the synthetically reconstructed. This includes precise channel estimation, which will vary in time, and the lack of other emitting sources or jammers that may cause interference with the reference signal.

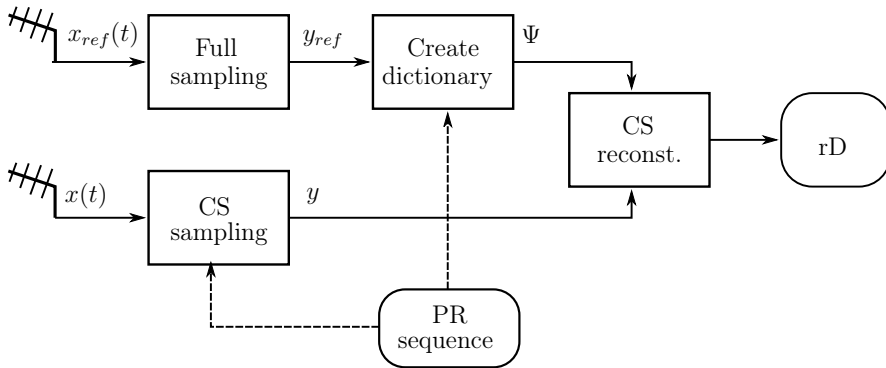


Figure 6.18: Obtaining a range-Doppler image using CS and full Nyquist sampling of the reference signal.

The second option described in Figure 6.18 presents a more conservative approach to the PCL application. The surveillance signal is subsampled using a CS sampler whereas the reference signal is fully sampled. Building up a dictionary Ψ from fully-sampled data is straightforward and leads directly to the usual CS reconstruction. For this set up, only one out of two channels are subsampled, therefore the gain of using CS is reduced by half in terms of lesser data collection and hardware complexity reduction. However, under a multistatic set up, multiple channels could be used for surveying different airspace regions, all of them randomly subsampled except for the reference signal, which would still need to be fully sampled. In this second case, the resulting dictionary is found to be the best candidate possible for the minimization problem, which does not mean ideal or optimal candidate. Channel estimation for the LOS signal is already implicit in the signal x_{ref} and, therefore, in Ψ although partially or even vaguely. The signal degradation produced during the LOS path may be closely related to that of the bistatic path if the two paths are similar ($\beta \rightarrow 180^\circ$); or completely dissimilar ($\beta \rightarrow 0^\circ$).

6.7.2 Sensor specifications and description of measurements

The equipment used for performing PCL with DVB-T signals was a USRP board Ettus Research B100 [161], driven by a laptop computer supporting the software radio toolkit GNU radio [162]. A USB connection was used to communicate between the laptop and the USRP and to store the received signals from the USRP registers. A Yagi-like antenna (Maxview MXR0012) used for reception of DVB-T broadcasts in the UHF band was employed to collect DVB-T echoes from flying targets. The antenna, presenting a gain of 11 dBi, was installed in a vertical polarization, matching the transmitter polarization. Figure 6.19 shows a picture of the setup during one measurement.

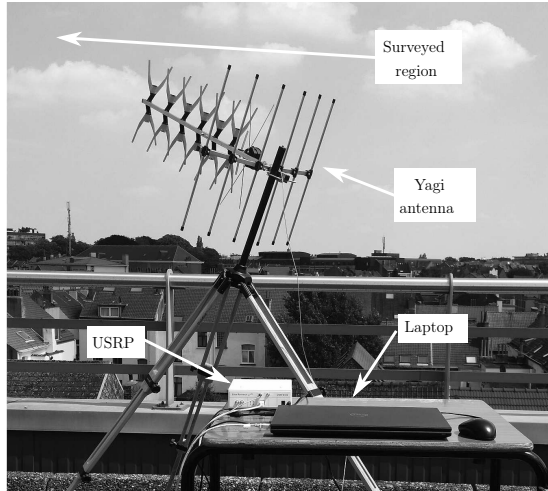


Figure 6.19: Photograph of the measurement setup used for PCL, located at the rooftop of the Royal Military Academy of Belgium.

The measuring equipment was set at the rooftop of building H of the Royal Military Academy of Belgium, Brussels (lat. 50.8443, long. 4.3929) and the antenna was directed NE, overlooking Hobbemastraat, in a privileged position to record the takeoff path of airplanes taking off from Brussels National Airport runways 25L or 25R (IATA code BRU), located at Zaventem (BE), 10 km NE of the Rx. The Tx was located at the Finance Tower, Kruidtuinlaan 50, in Brussel, 2.2 km NW from the Rx. The transmitter had an equivalent radiated power (ERP) of 10 kW for the 482 MHz channel. In Figure 6.20 the locations of the Tx and Rx are displayed over a map covering Brussels and the airport, as well as a typical takeoff and climb path from runway 25R in dashed. Extended details on the measurements and conventional PCL processing results can be found in [163].

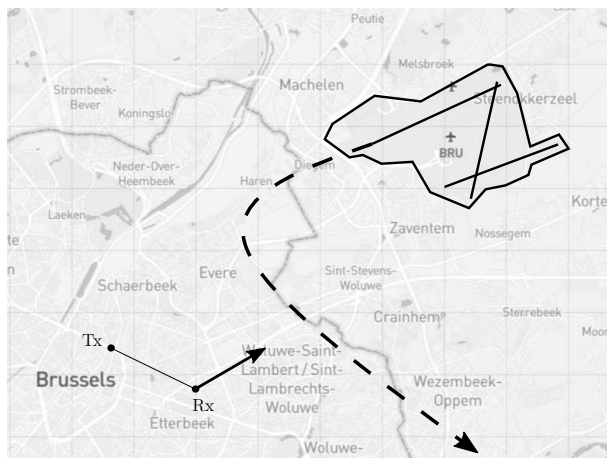


Figure 6.20: Map of Brussels (BE) and its NE suburbs showing the Tx, Rx, and a typical climb path of airplanes taking off from BRU airport.

6.7.3 PCL data transformation

As in the previous applications of NDT and GPR, we also address the possibility of applying a data transformation to the acquired signals. In Figure 6.21 are shown the sorted normalized amplitudes of the raw acquired data and their frequency-domain representation after a Fourier transform. The time and frequency domain representations of a DVB-T signal are far from being sparse in both domains, as was already shown in Figure 6.5.

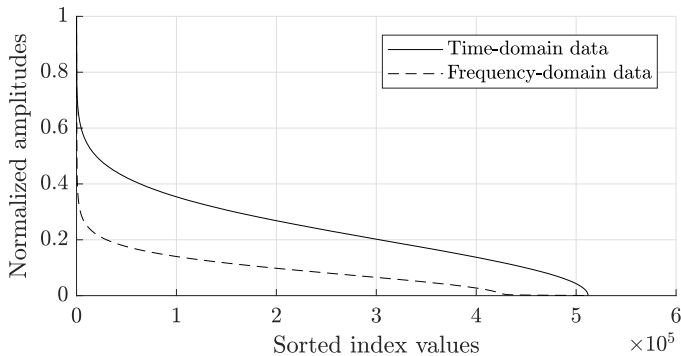


Figure 6.21: Normalized, sorted amplitudes of a DVB-T acquisition in the original time domain (solid line) and the frequency-domain transformed data (dashed line).

Thanks to the presented curves we can see that, although the Fourier-transformed data are slightly sparser than the raw data, the computational cost to transform the rather large data sets is not worth the effort. The increase in probability of detection obtained in early experiments ranged from none in most cases to +0.1% at best. Therefore, only time-domain data are used in all results presented in the following section.

6.8 Performance analysis

The performance analysis of the proposed approaches for PCL and CS (BPDN as the reconstruction algorithm of choice) are displayed in the following figures. P_d vs. SNR plots will compare the methods' performances based on different direct subsampling rates ($DS = 0.001, 0.005, 0.01,$ and 0.05) and two imposed probabilities of false alarm ($P_{fa} = 10^{-4}$ and 10^{-2}). Direct subsampling is performed when subsampling happens directly in the time-domain acquisition and no transformation is applied.

The length of the used DVB-T acquisitions can be 50 or 100 symbols in order to explore the effects in performance of choosing distinct acquisition lengths. Shorter acquisitions worsen the Doppler resolution as expressed in (6.12), but also reduce the amount of samples to integrate (thus degrading the performance in terms of SNR) and information available to the CS solver, increasing the uncertainty of the reconstruction. The P_d statistics for all the results presented

were obtained using a 2D CFAR detector centered at the expected target location and for 200 realizations per test. The surveillance data was contaminated with different noise levels ranging from $\text{SNR} = -20$ dB to 28 dB. A total of 24 Intel Xeon E5649 2.53 GHz cores and additional 8 comparable cores were used in parallel for circa. 16,000 core-hours for a total processing time of three weeks using Matlab R2015b (64 bit).

In Figure 6.22 the performance analysis generated for 50 DVB-T-symbol measurements is displayed for the four tested subsampling factors and the results for conventional range-Doppler imagery. The curves in Figure 6.22-a) show results when a fully sampled LOS signal is used as reference signal, whereas results in b) are obtained after synthetically reconstructing the reference signal. We can appreciate a significant degradation of the P_d vs. SNR curves when the synthetic reference signal is used for both $P_{fa} = 10^{-4}$ (left column) and $P_{fa} = 10^{-2}$ (right column). As it is expected, the lower the subsampling rate is, the poorer the P_d figures are.

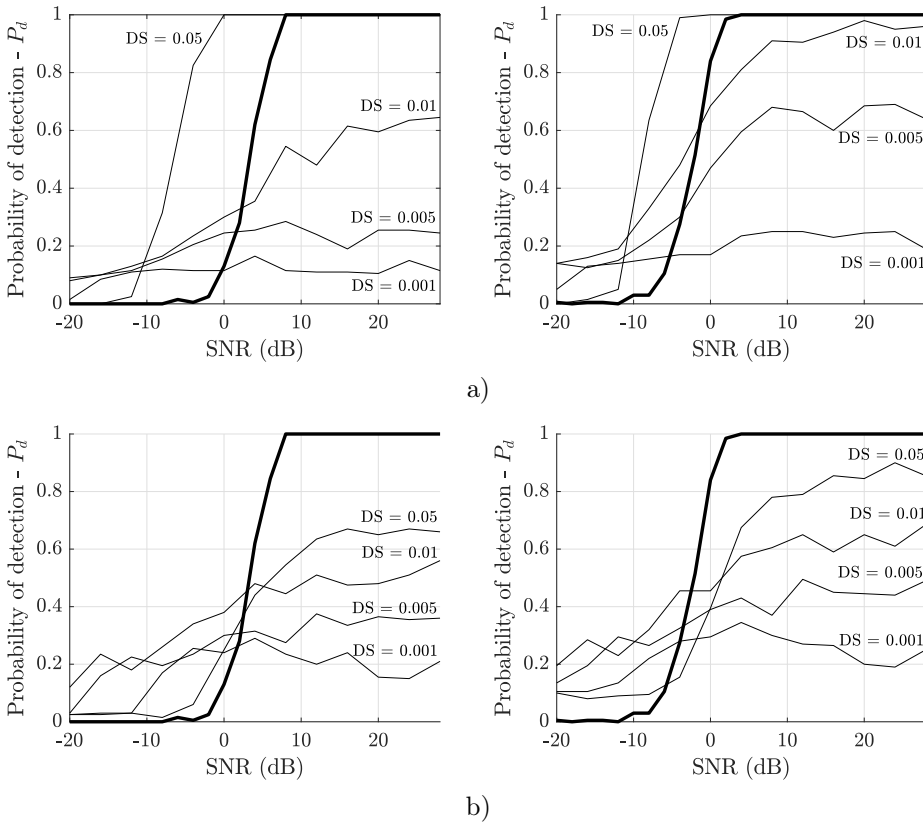


Figure 6.22: P_d vs. SNR curves for a 50-symbol DVB-T measurement and different DS rates. The dictionary matrix Ψ was populated using: a) measured reference signal; b) synthetically reconstructed reference signal. Left column, $P_{fa} = 10^{-4}$; right column, $P_{fa} = 10^{-2}$.

On the one hand, and although a subsampling rate of 0.05 for the synthetic reference signal approach could be exploitable when selecting $P_{fa} = 10^{-2} - P_d$ values roughly above 0.85—, the general impression is that the combination between having a synthetically reconstructed reference signal and using only 50 DVB-T symbols is not a safe option for PCL. On the other hand, when using a real reference signal, a subsampling rate of 0.05 is safe for $P_{fa} = 10^{-4}$ and 10^{-2} , reaching perfect reconstruction rates at SNR = 0 dB and -4 dB, respectively. Both results are outperforming the conventional range-Doppler imagery curves, which suggests that the scene simplification produced by CS at DS = 0.05 or DS = 0.01 is beneficial in terms of improving the P_d . The results obtained for the subsampling rate of 0.01 with a lax $P_{fa} = 10^{-2}$ is well above $P_d = 0.9$ for SNR ≥ 12 dB, which indicates that this choice of operation parameters can also be exploited in real-life applications. All the other remaining configurations must be discarded for safe operation of a PCL system integrating CS.

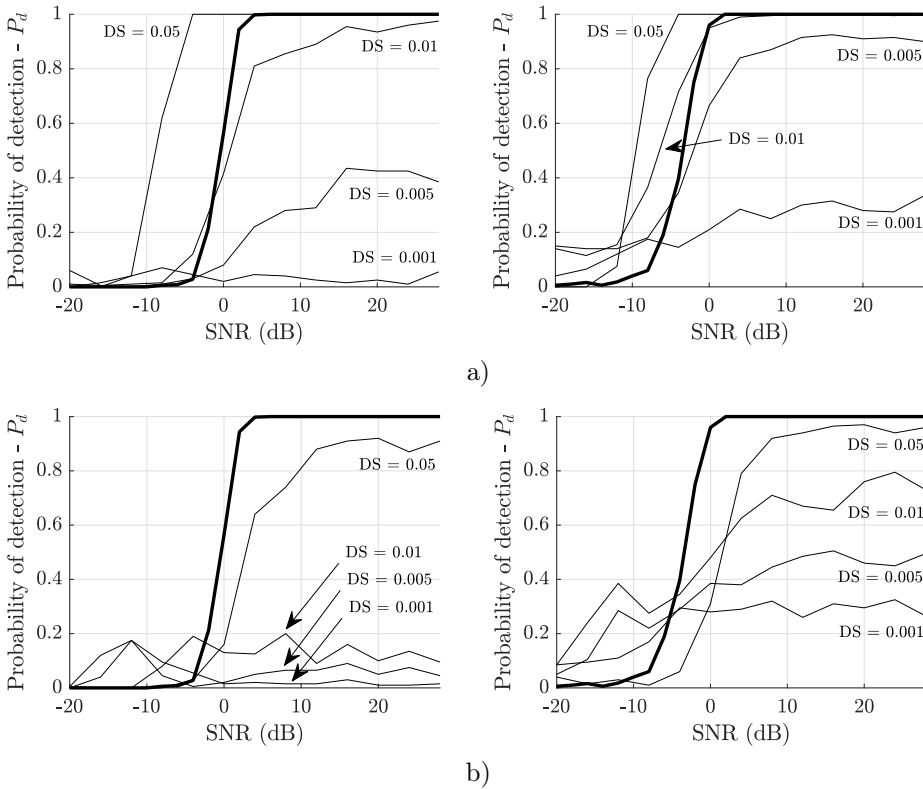


Figure 6.23: P_d vs. SNR curves for a 100-symbol DVB-T measurement and different DS rates. The dictionary matrix Ψ was populated using: a) measured reference signal; b) synthetically reconstructed reference signal. Left column, $P_{fa} = 10^{-4}$; right column, $P_{fa} = 10^{-2}$.

As for Figure 6.23, a similar exercise as with the previous figure can be done, this time using 100 DVB-T symbols. Starting with the real reference signal results in Figure 6.23-a), it can be observed that the results for $P_{fa} = 10^{-4}$ are improved for DS = 0.05 and 0.01. In the case

of $DS = 0.05$, the perfect reconstruction point is reached at $SNR = -4$ dB in contrast to 0-dB point for 50 DVB-T symbols. The $DS = 0.01$ results are also significantly improved for SNR above 10 dB, where the P_d is always at least 0.9. This same configuration was yielding $P_d \approx 0.6$ if only 50 DVB-T symbols were used. As per the results obtained if $P_{fa} = 10^{-2}$ is selected, we can see that the curve remains practically unchanged for $DS = 0.05$ but the performance is significantly improved for $DS = 0.01$ —now reaching perfect reconstructions at $SNR = 4$ dB. In the case of $DS = 0.005$, selecting a less strict P_{fa} enables using such a low DS factor which now produces results around $P_d = 0.9$ for $SNR \geq 12$ dB. This DS rate was completely unexploitable for $P_{fa} = 10^{-4}$. Again, these results using a real reference signal outperform the conventional range-Doppler results for both tested P_{fa} values.

The results for the synthetic reference signal and 100 DVB-T symbols—see Figure 6.23-b)—also present a performance improvement although less remarkable. For $P_{fa} = 10^{-4}$, the $DS = 0.05$ curve reaches P_d values around 0.9 for $SNR \geq 14$ dB, whereas when using 50 DVB-T symbols the performance never reached $P_d = 0.7$. We can conclude that, under this concrete setup, $DS = 0.05$ and synthetic reference signals can be safely used for PCL purposes. All other DS factors are reduced to P_d figures below 0.2 or close to 0. This is caused by the greater amount of data available when using 100 symbols, which maximizes the mismatch with the trained dictionary and reduces the uncertainty in the reconstruction. We can, therefore, assume that the curves for $DS = 0.01$ and lower obtained in Figure 6.22-b) for $P_{fa} = 10^{-4}$ are not reliable and mainly correspond to false positives due to very noisy, non-sparse reconstructions. As for the results using 100 symbols and $P_{fa} = 10^{-2}$, the P_d vs. SNR curves are slightly improved with respect to using 50 symbols, with the $DS = 0.05$ case being the most interesting one: from a marginally sufficient $P_d \approx 0.9$, the performance increased up to $P_d \approx 0.95$ and above, making this configuration also a candidate to be exploited in PCL.

6.9 The sparsifying effect of using the re-weighted ℓ_1 minimization

The re-weighted ℓ_1 minimization described in Section 3.5.3 is used to farther sparsify the obtained PCL rD imagery. The expected result is a equally prominent target and significantly lower background noise. Checking the ratio between target and background is done by using a maximum-to-median factor $Q_{MM} = \max\{|\sigma|^2\}/\text{median}\{|\sigma|^2\}$, with $Q_{MM}(dB) = 10 \log Q_{MM}$ its decibel equivalent.

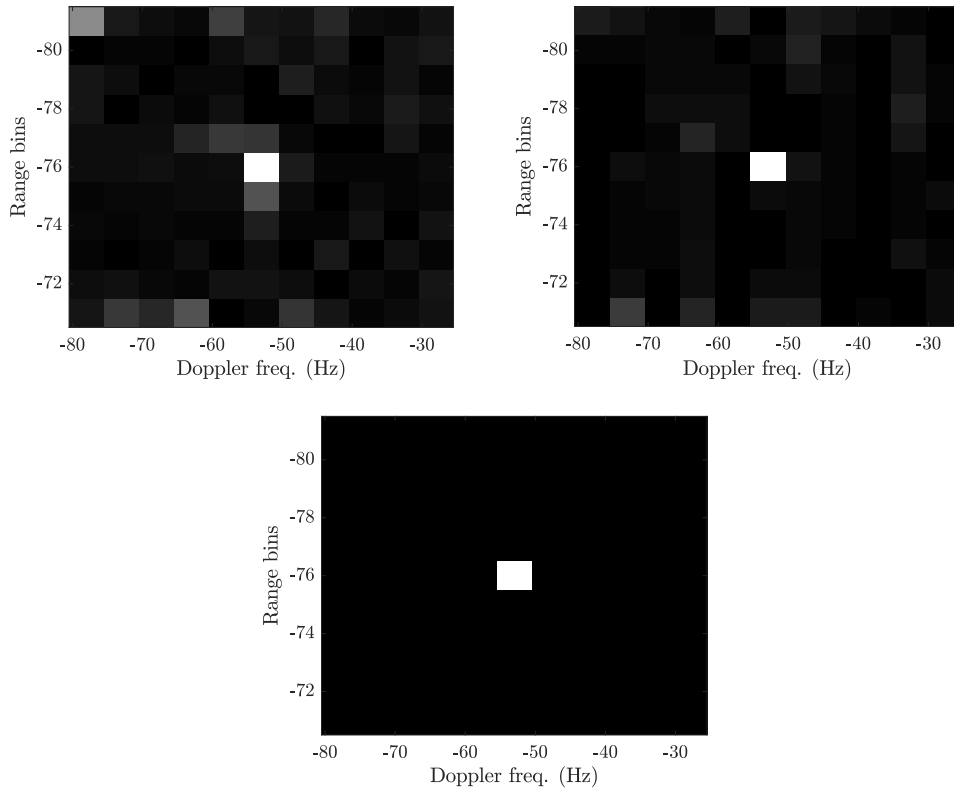


Figure 6.24: Initial (top left), intermediate (top right) and final (bottom) scene reconstructions using the re-weighted ℓ_1 minimization. A low-noise assumption (SNR = 24 dB) was used for this experiment, subsampling 0.01 and 100 DVB-T symbols.

Examples of scene reconstructions using the re-weighted ℓ_1 minimization are shown next. A real measurement is used with a target at 76 range bins away from Rx and a Doppler frequency of -53 Hz. A total of 100 DVB-T symbols are recorded, with a DS = 0.01. Figure 6.24 shows the three iterations required for the re-weighted algorithm to achieve a and a scene noise level of SNR = 24 dB (considered close to ideal). The first iteration shows a prominent target surrounded by reconstruction noise of varying amplitude without a certain distribution pattern, producing $Q_{MM} = 11.96$ dB. The second iteration shows slightly lower background noise while preserving the position of the detected target, with a $Q_{MM} = 15.75$ dB. Finally, the sparsest solution is reached after the third iteration, where the noise is greatly reduced and the target is yielding a $Q_{MM} = 51.35$ dB.

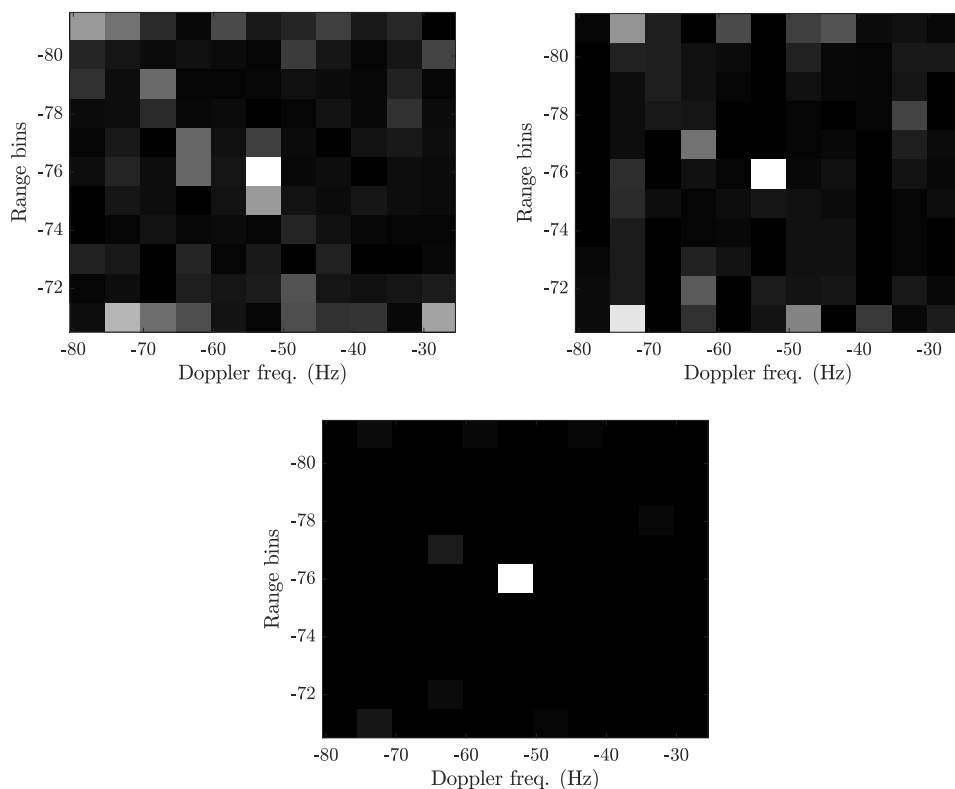


Figure 6.25: Initial (top left), intermediate (top right) and final (bottom) scene reconstructions using the re-weighted ℓ_1 minimization. A low-noise assumption (SNR = 0 dB) was used for this experiment, subsampling 0.01 and 100 DVB-T symbols.

The re-weighted ℓ_1 minimization is also tested against noisy measurements to validate the satisfactory sparsification results under normal noise conditions. In Figure 6.25, the original DVB-T signal is corrupted with noise. An SNR = 0 dB is chosen along with the same acquisition and subsampling conditions as in Figure 6.24. The initial reconstruction clearly shows a noisier reconstructed scene as expected, which is also reflected in a lower $Q_{MM} = 10.92$ dB. The second iteration produces a slightly sparser reconstruction with $Q_{MM} = 12.85$ dB, whereas the third and final iteration this time yields $Q_{MM} = 40.61$ dB. This sparsest reconstruction is marginally noisier than the low-noise case, which suggests that the added value of the re-weighted ℓ_1 method may be much more effective for noisy signals than clean ones.

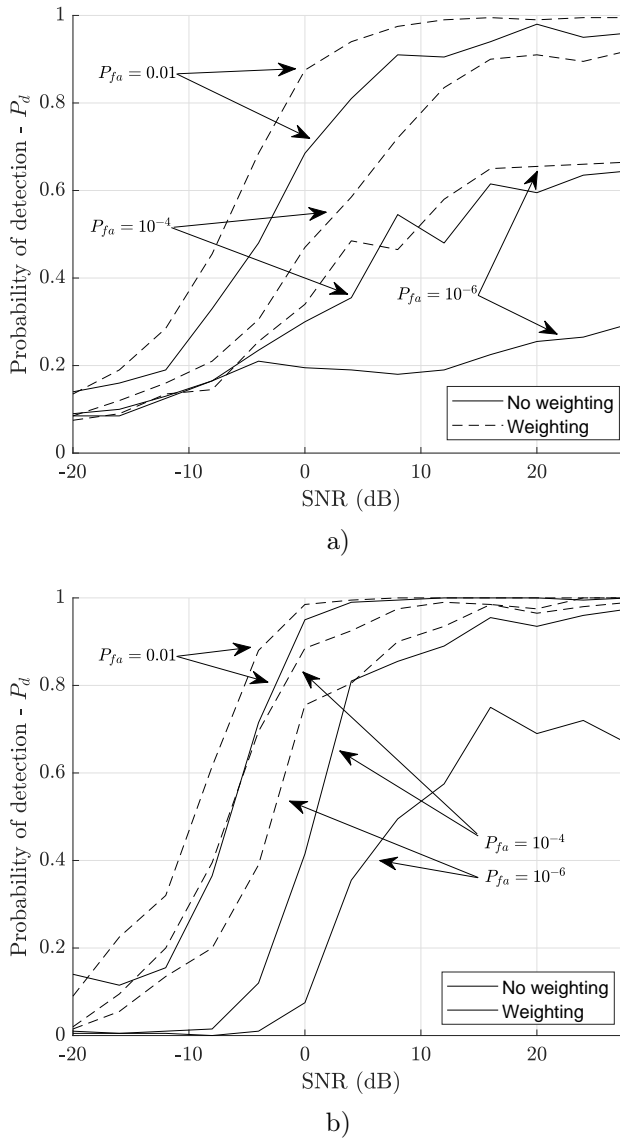


Figure 6.26: P_d vs. SNR results for the re-weighted ℓ_1 minimization: a) Number of symbols 50; b) number symbols 100.

According to the thresholding applied in 2D CA-CFAR detectors, it is assumed that this much sparser imagery will produce significantly higher P_d scores. To prove this, a series of Monte-Carlo simulations are run. Again, 200 realizations per test are performed using the real reference signal approach, with varying SNR levels from -20 to 28 dB. Figure 6.26 shows the P_d vs. SNR curves for a) 50, and b) 100 DVB-T symbols. The solid line shows the original results using the simply BPDN algorithm without re-weighting whereas the dashed line are the curves after re-weighting, which are also compared for several P_{fa} values.

Indeed, the P_d vs. SNR curves in Figure 6.26 show a general P_d improvement for all tested conditions when using the re-weighted ℓ_1 minimization (dashed curves). In Figure 6.26-a), which shows results for the 50 DVB-T-symbol measurement, we can already see that the P_d gain margins are higher compared to the 100 DVB-T-symbol measurement results. In general, the those solid curves with lower P_d scores will yield better improvements after applying the re-weighting method, as compared to those results already reaching P_d close to 1, which show an obvious smaller improvement. As an example of this fact, the $P_{fa} = 10^{-4}$ reaches a maximum P_d of 0.295 for BPDN measurements which, for the same SNR, increases up to 0.665 for the weighted approach. Although these results are promising, a $P_d = 0.67$ is not a satisfactory performance for airspace surveillance and, therefore, using a lower P_{fa} is required. For instance, the maximum P_d for a $P_{fa} = 10^{-4}$ are 0.65 and 0.92 for the method without and with re-weighting, respectively. In this case, the 0.27 P_d increase leads to exploitable performances even if just 50 DVB-T symbols are used. Finally, the P_d increase for $P_{fa} = 0.01$ is much smaller although re-weighted results reach almost perfect target reconstructions for $\text{SNR} \geq 10$ dB, which was not possible just by using BPDN alone.

The performance analysis for the 100 DVB-T-symbol measurements and re-weighting follows a similar trend. All performances are improved, even though for $P_{fa} = 0.01$ the P_d is already almost perfect for $\text{SNR} \geq 4$ dB. The effect of the re-weighting method is only visible in reaching $P_d \approx 1$ at $\text{SNR} = 0$ dB and improving P_d remarkably for all cases if $\text{SNR} \leq 0$ dB. In its turn, the improvement for $P_{fa} = 10^{-4}$ is much more evident for SNR figures between 0 and 16 dB where the BPDN was performing at P_d of 0.42 and 0.96, respectively, instead of 0.89 and 0.99 with the re-weighting applied. Finally, the most remarkable improvement happens for a strict $P_{fa} = 10^{-6}$: In this case, the BPDN results are mediocre, unstable (the curve cannot be approximated by a monotonically increasing trend— and unexploitable, reaching a maximum P_d of 0.75. In contrast to these poor results, when the re-weighted ℓ_1 minimization is applied on the same measurements the P_d rapidly increases from very low SNR levels such as -4 dB, for which a $P_d \approx 0$ was obtained by conventional BPDN and re-weighting increases that value up to 0.39. Although this P_d is still very low, one can already understand the benefits of the proposed iterative method. It is for SNR levels above 12 dB when the P_d gain is much more interesting: while conventional BPDN yields poor performances varying from 0.57 to 0.75, the re-weighted ℓ_1 results obtain performances from 0.94 up to 1, or perfect reconstruction.

It is, therefore, proven that the re-weighted ℓ_1 minimization is a very powerful tool to achieve sparser representations of already sparse reconstructions by decreasing the surrounding noise or clutter level to a minimum. Again, this is achieved thanks to the ability of having an additional degree of freedom—the weights matrix \mathbf{W} — to help the minimization problem absorbing the burden of diminishing such noise.

6.10 Side information: a-priori knowledge of the scene clutter

For this section, the simulated experiments like those presented in Section 6.8 are performed although this time including SI. Static clutter is expected to appear in every measurement given the chosen Rx location and always around $f_D = 0$ Hz: The echoes scattered towards the Rx from the surrounding urban area are surely received given the small height difference between the Rx position and the neighboring buildings and reflective objects, potentially acting as static clutter sources. To simplify the scene, we use the assumption that static clutter will not vary substantially from measurement to measurement, although smaller moving targets like cars may actually be present. It is assumed that, for a flying target crossing the $f_D = 0$ Hz region, clutter may mask the target's position or make hinder the ability to detect it.

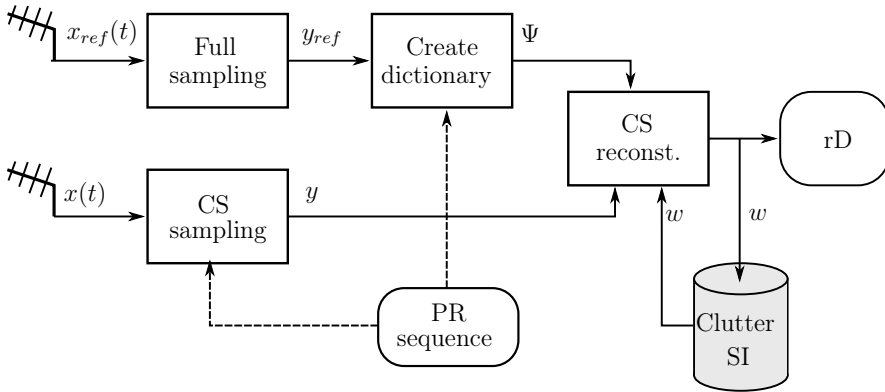


Figure 6.27: Schematic of the proposed method to integrate scene clutter SI into the CS reconstruction of PCL imagery.

In order to obtain a vector w including the reflectivity function of the scene clutter, a measurement of the urban area (see Figure 6.19) with no moving targets overflying it is reconstructed using CS. Therefore, a scene including only static clutter is simulated. In Figure 6.27 are described the steps followed: The reference signal is measured at full Nyquist rate, whereas the surveillance signal (clutter only) is subsampled. According to the results shown in the previous Section 6.8, this approach maximizes the reconstruction quality with respect to subsampling both measured signals. The clutter reflectivity is stored and is later fed to the CS solver which includes SI in the minimization problem, as described by (3.30) or (3.31). Next, a scene with one single target at an arbitrary range and $f_D = 0$ Hz is generated. This scene includes the same modeled static clutter contribution as the one used to generate the SI: indeed, the clutter is assumed to be invariant.

As a result, the obtained P_d vs. SNR curve comparison between CS target reconstruction with and without CS does not show any significant improvement in performance. Despite knowing previous information about the scene, static clutter, this does not help reaching a sparser solution

or minimizing the background reconstruction noise in this type of imagery —having lower noise levels in the images would make the CA-CFAR detector calculate lower thresholds leading to safely accepting more targets as detections.

The rather dense structure of static clutter — it is simulated as a narrow block around $f_D = 0$ Hz with varying (randomly) amplitudes along range— is far from the expected sparse scene required for CS to work properly. Although clutter reconstructions were obtained, the random nature of the measurement samples selection adds uncertainty for low sparsity scenes. The simulated granularity of the static clutter was reconstructed differently in every tested occasion and highly depended on the used PR sequence during subsampling, the subsampling rate and even the choice of ℓ_1 , ℓ_2 or the β factor in the SI problem statement.

Under adequate conditions and good SI, the ℓ_1 - ℓ_1 minimization produces lower reconstruction bounds with less samples being required [93]. One of the conditions for this to happen is that the elements in the sensing matrix Φ follow a Gaussian distribution. When a sensor like a radar is adapted from Nyquist-rate to random subsampling the sensing matrix Φ is far from being Gaussian distributed —actually, only one element per row will be set to 1, the rest to zero as described in (3.13). This fact combined with the uncontrolled variability in the amplitudes of the static clutter contributions due to their dense nature makes SI in this concrete application not exploitable. Farther investigations would be required to finally achieve high quality scene reconstructions with less samples than conventional CS.

6.11 Conclusions

In this last application chapter, the ideas behind PCL using an IOP such as DVB-T broadcasts have been presented, supported by the introductory section to bistatic radars (see Section 2.6). The expected targets for this application are mostly large, plane-like targets overflying areas with good DVB-T coverage, usually urban areas.

The main technical definitions concerning DVB-T broadcasts such as the OFDM structure and transmission and reception chains are explained. OFDM signal modeling is also described since its knowledge is required to be able to model DVB-T transmission to generate CS measurement dictionaries. The Doppler effect created by moving targets is mathematically introduced and is later intensively used in PCL imagery —i.e. range-Doppler diagrams.

PCL requires acquiring two signals: The reference and surveillance signals. This poses several questions regarding how to perform signal synchronization using the LOS signal, for which several options are proposed. Finally, a discussion on what type of reference signal should be used is provided with performance analysis: A fully sampled reference signal or a reconstructed, synthetic signal obtained from a subsampled LOS measurement. The obtained results suggest that it is always safer to use a full reference signal instead of a synthetically reconstructed one. The obtained performances reach perfect detection rates for subsampling rates of just 0.05 of the original sampled data (using 50 DVB-T symbols) or 0.05 and 0.01 if 100 symbols are recorded. For the synthetic reference approach, performance figures reach at most 0.9 for subsampling

rates of 0.05, for 50 and 100 symbols, which may suggest that this approach could be valid but not as safe as using the fully sampled reference signal.

As a last addition to this chapter, two attempts to farther sparsify the CS reconstructions are presented: First, the iterative re-weighting ℓ_1 algorithm using BPDN; and second, the inclusion of SI into the minimization problem, describing undesired clutter noise. The former improved the target's probability of detection in a remarkable way. Background noise —probably due to both measurement and reconstruction noise— was greatly reduced in most occasions while preserving the target's brightness and positioning. This method increases significantly the probability of detection, especially in those cases where the imposed probability of false alarm is too strict or in noisy measurements. In already high performance rates, it helps reaching perfect reconstruction rates and slightly increases robustness against noise. Finally, adding SI did not produce any improvement in terms of probability of detection for the reasons that have been explained in the previous section.

Finally, we can derive from the obtained results that the length of the DVB-T signal acquired will, as expected, play a key role in terms of performance: The more data are collected, the better the signal reconstruction will be. Two extreme cases are possible: On the one hand, strong signal subsampling will negatively influence the performance rates due to insufficient SNR in the data integration. On the other hand, longer acquisitions will increase the amount of data even under strong subsampling but may cause acquisitions to last for too long, possibly incurring in range and Doppler frequency walk in the obtained imagery. In order to avoid both extreme cases, a trade-off between subsampling and integration time must be found for each application.

Chapter 7

Conclusions and future work

This dissertation has introduced the relatively novel concept of CS, which is called to be the pillar to a new approach to signal sampling. It is expected that, after sufficient research and developing on implementing CS in hardware, these new sensors will be significantly more affordable and will create new opportunities: a fast and affordable proliferation of sensors —e.g. radars— for a countless list of completely diverse applications.

At the current moment of this work, using fully functional CS hardware is still far from being an option. Nevertheless, it is interesting to know which are the current technologies that may take advantage of CS, whether it is due to reduced exploitation costs, simplified imagery or both. During this thesis, three dual applications (interesting for both the military and civilian worlds) have been presented: NDT, GPR, and PCL. For each one of those applications, suggestions for possible joint exploitation along with CS and performance analyses have been provided.

After describing with the required detail each application, the summaries of the obtained results follow up next.

7.1 Summary of results for NDT

- The combination of NDT and CS —with the OMP algorithm as main choice— gives overall promising results for media interface reconstruction. Conservative (50% of the original data) and moderate (25%) subsampling rates can be safely applied in most situations, whereas extreme subsampling rates (just 5%) are exploitable in relatively noise-free measurements and for reconstruction scores above 90% but never reaching 100%, or perfect reconstructions.
- Signal reconstruction using an IFFT preconditioner yields the best reconstruction results, reaching reconstruction scores of 100% for relatively low SNR values. Bearing in mind that NDT measurements are usually high-quality measurements under sufficiently controlled

conditions, such results suggest that even under strict assumptions the application NDT on composites can be safely implemented and exploited.

- As an alternative, using dictionaries can be another useful approach: Instead of reconstructing media interfaces, the output is linked to measured or simulated air gaps. For dictionaries based on real measurements, results are very promising although being able to create a dictionary covering all possibilities for more complex situations may become cumbersome (several degrees of freedom can lead to thousands of conventional measurements required).
- For dictionaries based on simulated responses, results are also exploitable but reaching slightly lower reconstruction scores. These dictionaries can be generated in negligible times but may, most likely, require extensive modeling of all involved devices and components in the measurement, which may not be an option in every case. Theoretical responses provide satisfying results, although these are outperformed by the two previous approaches.
- Guidelines for applying CS: Given the typically favorable laboratory conditions found in NDT measurements, even the most extreme subsampling cases presented in this chapter are to be considered for an actual implementation of CS on NDT. In state-of-the-art VNAs it may be possible to use virtual instrumentation to directly perform a random frequency selection, that is, an uneven frequency subsampling. It is recommended that modeled responses be used to populate dictionaries if the complexity of the model is low. In any case, direct signal reconstruction using the IFFT will be an ideal candidate as the presented results were able to show.
- Future work: For more complex defects, generating sufficiently comprehensive dictionaries from real measurements can be a cumbersome, if not unfeasible, task. Therefore, other complex structures could be simulated and tested against real-life defects. Moreover, an accurate modeling of the sensor and material interactions could be developed to approximate as much as possible the synthetic realizations included in the dictionary to the actual measurements.

7.2 Summary of results for GPR

- Given the way the presented GPR measurements are performed —based on SAR theory, two random subsampling approaches are considered: in frequency and in cross-range. Additionally, a third approach derived from combining the first two can be foreseen.
- Whereas subsampling in frequency elements will reduce the amount of collected data and may not improve measurement speeds —this fact will depend on how the VNA operates, subsampling in the cross-range dimension will allow the VNA skipping several measurement positions.
- Given the nature of GPR measurements, it is common to find small targets buried superficially. Such targets can be masked by the strong first return from the air-soil interface.

GPR imagery in that case becomes unexploitable unless a model is incorporated to the imagery as it is presented in this work. The model must account for the air-soil interface as well as the internal antenna reverberations. Only then, can GPR imagery be fully exploitable regardless of the location of the target.

- Data preconditioning is also a way of slightly improving the system's probability of detection when using CS. The PCA preconditioner performs by itself a noise removal effect by isolating the signal subspace from the noise subspace. Despite its potentially cumbersome application in larger data sets, it is worth investigating its benefits based on a per-case analysis.
- For standard measurement conditions, CS provides satisfactory results for subsampling rates of around 20% both in frequency and cross-range. The only exception is the M14 AP landmine, which has a small size and presents very low metallic contents. In that case, performances drop down to 75% and, therefore, the application of CS for this type of landmines must be carefully assessed.
- Guidelines for applying CS: It is recommended that a thorough investigation of the detection performances is done before using GPR and CS given the limited results obtained for AP landmines. Although high detection rates are obtained for the PMN2 landmine, heavy subsampling is discouraged to keep operation of the GPR safe. Similarly, subsampling both in frequency and cross-range should only be done for large, mostly metallic AT landmines and should be avoided when inspecting AP landmines. If AT landmines are to be inspected, cross-range subsampling of 30% along with frequency subsampling of 15% will still safely produce perfect target detections, implying using as little as 5% of the conventional data volumes.
- Future work: An extension to 3-D measurements from the 2-D approach proposed in this work would require exploring the effects of subsampling in a third dimension (frequency, cross-range and along-range), and how this affects the subsampling rates in the other two dimensions.

7.3 Summary of results for PCL

- In PCL imagery, having access to a reference signal is a required condition. One can imagine acquiring a subsampled version of the reference and reconstructing the original signal. This approach has shown to yield lower performances than using directly a Nyquist-rate sampled reference signal, although it may be interesting if hardware complexity reduction is prioritized.
- The performance analysis showed that, in general, lower subsampling rates produce poorer results, as it was expected. By reducing the restrictions imposed by the selected probability of false alarm, the sensor can reach probabilities of detection close to 100%. However, it is desirable to achieve an increase of performance without affecting the false alarm rate.

This can only be obtained by increasing the amount of collected data and/or the length of the measurement to be processed.

- The re-weighted ℓ_1 minimization algorithm was able to farther sparsify the PCL reconstruction. This was especially noticeable for noisy measurements and low subsampling rates which, in some cases, made a operation configuration —subsampling rate and measurement length— change from discarded to exploitable. In other cases in which high performance figures were obtained, the final performance achieved perfect reconstructions or reached 100% reconstruction for lower SNR conditions, demonstrating the high robustness against noise of the re-weighted ℓ_1 iterative algorithm.
- Using SI of the scene clutter was not possible due to the relatively dense distribution of the clutter noise and low variability of its related reflectivity coefficients. Adding such information to the CS solver did not produce any improvement whatsoever.
- Guidelines for applying CS: Under favorable conditions including no interfering signals present in a rather sparse scene, heavy subsampling can be applied to PCL measurements yet obtaining high, almost perfect performance rates, always provided that the reference signal is acquired using a LOS measurement at full Nyquist rate. Extreme subsampling may cause a lack of available data for not long enough measurements. In order to correct this situation, longer measurements may be required although always bearing in mind that range and/or Doppler walk must be therefore expected to happen. A trade-off between subsampling and acquisition length must be found depending on the application's needs. It is recommended to use the re-weighted ℓ_1 minimization approach to increase the robustness against noise of the scene reconstructions as well as to obtain sparser imagery.
- Future work: Extending the current configuration from bistatic to multistatic. This would imply using several passive receivers to detect a target employing several bistatic ellipsoid, obtaining thus the approximate coordinates and altitude of the target. Other possible activity would be selecting multiple DVB-T channels or additional services with broader bandwidths (e.g. LTE) to improve the system's range resolution.

7.4 Closing remarks

In general terms, CS has been successfully used as a tool for reducing the data acquisition burden of the three explored applications and has, even under unfavorable conditions, simplified the complexity of the produced imagery while preserving the position and brightness of the tested targets.

For every application, suggestions of random subsampling lower bounds and subsampling strategies for future implementations have been given so that the resulting operation was above strict performance goals, always selected to be close to those performances yielded by well-established techniques. Imposing such high goals guarantees that the presented applications can be safely transitioned from conventional data acquisition towards CS with full confidence, both for civilian and military purposes.

Bibliography

- [1] E. Cristofani, F. Friederich, M. Vandewal, and J. Jonuscheit. Non destructive testing of aeronautics composite structures using UWB radars. In James D Taylor, editor, *Advanced Ultrawideband Radar. High Resolution Materials, Sensor Systems, and Practical Applications*, chapter 6, pages 237–270. Taylor & Francis Group, 6000 Broken Sound Parkway NW, Suite 300, Boca Raton, FL 33487-2742 CRC Press 2016, 2016.
- [2] E. Cristofani, M. Becquaert, S. Lambot, M. Vandewal, J. H. Stiens, and N. Deligiannis. Random subsampling and data preconditioning for ground penetrating radars. *IEEE Access*, 6:26866–26880, 2018.
- [3] M. Becquaert, E. Cristofani, H. Van Luong, M. Vandewal, J. Stiens, and N. Deligiannis. Compressed sensing mm-wave sar for non-destructive testing applications using multiple weighted side information. *Sensors*, 18(6):1761, May 2018.
- [4] M. Becquaert, E. Cristofani, B. Lauwens, M. Vandewal, J. Stiens, and N. Deligiannis. Online Sequential Compressed Sensing with Multiple Information for Through-the-Wall Radar Imaging. *Submitted to: IEEE Sensors*, 2018.
- [5] E. Cristofani, O. Mahfoudia, M. Becquaert, X. Neyt, F. Horlin, N. Deligiannis, J. Stiens, and M. Vandewal. Exploring side information for DVB-T-based passive radars. In *URSI Benelux Forum 2018*, pages 1–1. URSI, 1 2018.
- [6] M. Becquaert, E. Cristofani, M. Vandewal, J. Stiens, and N. Deligiannis. Online sequential compressed sensing with weighted multiple side information for through the wall imaging. In *URSI Benelux Forum 2018*, pages 1–5. URSI, 1 2018.
- [7] E. Cristofani, O. Mahfoudia, M. Becquaert, X. Neyt, F. Horlin, N. Deligiannis, J. Stiens, and M. Vandewal. Compressive Sensing and DVB-T-Based Passive Coherent Location. In *26th URSI Benelux Forum*, Brussels, Belgium, 2017. URSI.
- [8] M. Becquaert, E. Cristofani, J. Stiens, M. Vandewal, and N. Deligiannis. Compressed Sensing SAR Through-the-Wall Imaging with Side Information. In *26th URSI Benelux Forum*, Brussels, Belgium, 2017. URSI.
- [9] M. Becquaert, E. Cristofani, G. Pandey, M. Vandewal, J. Stiens, and N. Deligiannis. Compressed sensing mm-wave SAR for non-destructive testing applications using side

- information. In *2016 IEEE Radar Conference (RadarConf)*, number 2, pages 1–5. IEEE, may 2016.
- [10] E. Cristofani, M. Becquaert, G. Pandey, M. Vandewal, N. Deligiannis, and J. Stiens. Compressed Sensing And Defect-Based Dictionaries For Characteristics Extraction In Mm-Wave Non-Destructive Testing. In *Infrared, Millimeter, and Terahertz Waves (IRMMW-THz), 2016 41st International Conference on*, Copenhagen, Denmark, 2016.
- [11] E. Cristofani. Une nouvelle façon d’acquérir les signaux. *Belgisch Militair Tijdschrift - Revue Militaire Belge Nr. 14*, pages 121–127, june 2017.
- [12] AB Millimetre. MVNA-8-350 vector network analyzer, full installation, which can cover millimeter and submillimeter wave range at frequencies from 8 GHz to 1 THz, 2010. <http://www.abmillimetre.com/pictures/Picture1.htm>, accessed 2018-02-10.
- [13] AB Millimetre. Scalar horns for 44-170 GHz, 2010. <http://www.abmillimetre.com/pictures/Picture28.htm>, accessed 2018-02-10.
- [14] D. L. Donoho. Compressed sensing. *In Practice*, 52:1–34, 2004.
- [15] C. E. Shannon. A mathematical theory of communication. *The Bell Systems Technical Journal*, 27:379–423, 623–656, 1948.
- [16] John H. DeWitt. Technical and tactical features of radar. *Journal of the Franklin Institute*, 241(2):97 – 123, 1946.
- [17] H. Hertz and Joseph Francis Mulligan. *Heinrich Rudolf Hertz (1857-1894): A Collection of Articles and Addresses*. Garland reference library of the humanities. Garland Pub., 1994.
- [18] D. J. Cichon and W. Wiesbeck. The heinrich hertz wireless experiments at karlsruhe in the view of modern communication. In *Proceedings of the 1995 International Conference on 100 Years of Radio*, pages 1–6, Sep 1995.
- [19] J. C. Maxwell. A dynamical theory of the electromagnetic field. *Philosophical Transactions of the Royal Society of London*, 155:459–513, 1865.
- [20] D. R. Griffin. Echolocation by blind men, bats and radar. *Science*, 100(2609):589–590, 1944.
- [21] H. Hartridge. The avoidance of objects by bats in their flight. *The Journal of Physiology*, 54(1-2):54–57, 1920.
- [22] M. I. Skolnik. Radar applications. *New York, IEEE Press, 1988, 486 p.*, 1988.
- [23] M. I. Skolnik. *Radar Handbook, 2nd Edition*. McGraw Hill, New York, 3 edition, 2008.
- [24] C. G. Collier. *Applications of weather radar systems*. Wiley, 1989.

- [25] K. D. Ward, C. J. Baker, and S. Watts. Maritime surveillance radar. part 1: Radar scattering from the ocean surface. In *IEE Proceedings F (Radar and Signal Processing)*, volume 137, pages 51–62. IET, 1990.
- [26] R Westphal and A Kessler. 35-ghz-doppler radar for law enforcement agencies in europe. In *Microwave Symposium Digest, 1988., IEEE MTT-S International*, pages 1031–1033. IEEE, 1988.
- [27] M. E. Russell, A. Crain, A. Curran, R. A. Campbell, C. A. Drubin, and W. F. Miccioli. Millimeter-wave radar sensor for automotive intelligent cruise control (icc). *IEEE Transactions on microwave theory and techniques*, 45(12):2444–2453, 1997.
- [28] Y. Kim and H. Ling. Human activity classification based on micro-doppler signatures using a support vector machine. *IEEE Transactions on Geoscience and Remote Sensing*, 47(5):1328–1337, 2009.
- [29] F. M. Naderi, M. H. Freilich, and D. G. Long. Spaceborne radar measurement of wind velocity over the ocean-an overview of the nscat scatterometer system. *Proceedings of the IEEE*, 79(6):850–866, 1991.
- [30] C. Elachi. Spaceborne radar remote sensing: applications and techniques. *New York, IEEE Press, 1988, 285 p.*, 1988.
- [31] E. Rignot, J. L. Bamber, M. R. Van Den Broeke, C. Davis, Y. Li, W. J. Van De Berg, and E. Van Meijgaard. Recent antarctic ice mass loss from radar interferometry and regional climate modelling. *Nature geoscience*, 1(2):106, 2008.
- [32] P. C. Dubois, J. Van Zyl, and T. Engman. Measuring soil moisture with imaging radars. *IEEE Transactions on Geoscience and Remote Sensing*, 33(4):915–926, 1995.
- [33] K. Mostov, E. Liptsen, and R. Boutchko. Medical applications of shortwave fm radar: Remote monitoring of cardiac and respiratory motion. *Medical Physics*, 37(3):1332–1338, 2010.
- [34] L. Anishchenko, M. Alekhin, A. Tataraidze, S. Ivashov, A. S. Bugaev, and F. Soldovieri. Application of step-frequency radars in medicine. In *Radar Sensor Technology XVIII*, volume 9077, page 90771N. International Society for Optics and Photonics, 2014.
- [35] D. M. McCann and M. C. Forde. Review of ndt methods in the assessment of concrete and masonry structures. *Ndt & E International*, 34(2):71–84, 2001.
- [36] J. H. Bradford and J. C. Deeds. Ground-penetrating radar theory and application of thin-bed offset-dependent reflectivity. *GEOPHYSICS*, 71(3):K47–K57, 2006.
- [37] J. L. Davis and A. P. Annan. Ground-penetrating radar for high-resolution mapping of soil and rock stratigraphy 1. *Geophysical prospecting*, 37(5):531–551, 1989.
- [38] F. Ahmad, M. G. Amin, and G. Mandapati. Autofocusing of through-the-wall radar imagery under unknown wall characteristics. *IEEE transactions on image processing*, 16(7):1785–1795, 2007.

- [39] R. Zetik, S. Crabbe, J. Krajnak, P. Peyerl, J. Sachs, and R. Thomä. Detection and localization of persons behind obstacles using m-sequence through-the-wall radar. In *Sensors, and Command, Control, Communications, and Intelligence (C3I) Technologies for Homeland Security and Homeland Defense V*, volume 6201, page 62010I. International Society for Optics and Photonics, 2006.
- [40] M. I. Skolnik. *Introduction to Radar Systems /2nd Edition/*. McGraw Hill Book Co., New York, 2 edition, 1980.
- [41] A. G. Stove. Linear fmcw radar techniques. *IEE Proceedings F - Radar and Signal Processing*, 139(5):343–350, Oct 1992.
- [42] A. Meta and P. Hoogeboom. Signal processing algorithms for fmcw moving target indicator synthetic aperture radar. In *Geoscience and Remote Sensing Symposium, 2005. IGARSS'05. Proceedings. 2005 IEEE International*, volume 1, pages 4–pp. IEEE, 2005.
- [43] J. W. Taylor and G. Brunins. Design of a new airport surveillance radar (asr-9). *Proceedings of the IEEE*, 73(2):284–289, Feb 1985.
- [44] H. L. Van Trees. *Detection, estimation, and modulation theory*. Wiley, 1 edition, September 2001.
- [45] G. Turin. An introduction to matched filters. *IRE Transactions on Information Theory*, 6(3):311–329, June 1960.
- [46] J. Neyman and E. Pearson. On the problem of the most efficient tests of statistical hypotheses. *Philosophical Transactions of the Royal Society of London. Series A, Containing Papers of a Mathematical or Physical Character 231*, pages 289–337, 1933.
- [47] M. Abramowitz, I. A. Stegun, et al. *Handbook of mathematical functions: with formulas, graphs, and mathematical tables*, volume 55. Dover publications New York, 1972.
- [48] P. Stinco, M. Greco, F. Gini, and M. La Manna. Compressed spectrum sensing in cognitive radar systems. In *Acoustics, Speech and Signal Processing (ICASSP), 2014 IEEE International Conference on*, pages 81–85. IEEE, 2014.
- [49] L. M. Novak, G. J. Owirka, and C. M. Netishen. Radar target identification using spatial matched filters. *Pattern Recognition*, 27(4):607–617, 1994.
- [50] T. D. Ross, S. W. Worrell, V. J. Velten, J. C. Mossing, and M. L. Bryant. Standard SAR ATR evaluation experiments using the MSTAR public release data set. In *Algorithms for Synthetic Aperture Radar Imagery V*, volume 3370, pages 566–574. International Society for Optics and Photonics, 1998.
- [51] J. M. Steele. *The Cauchy-Schwarz Master Class: An Introduction to the Art of Mathematical Inequalities*. Cambridge University Press, New York, NY, USA, 2004.
- [52] M. Barkat, S. D. Himonas, and P. K. Varshney. CFAR detection for multiple target situations. *IEE Proceedings F - Radar and Signal Processing*, 136(5):193–209, Oct 1989.

- [53] M. A. Richards. *Fundamentals of Radar Signal Processing*. McGraw Hill Professional, 2005.
- [54] H. Rohling. Radar CFAR thresholding in clutter and multiple target situations. *IEEE Transactions on Aerospace and Electronic Systems*, AES-19(4):608–621, July 1983.
- [55] H. Rohling. Radar cfar thresholding in clutter and multiple target situations. *IEEE Transactions on Aerospace and Electronic Systems*, AES-19(4):608–621, July 1983.
- [56] P. P. Gandhi and S. A. Kassam. Analysis of cfar processors in nonhomogeneous background. *IEEE Transactions on Aerospace and Electronic Systems*, 24(4):427–445, July 1988.
- [57] V. G. Hansen and J. H. Sawyers. Detectability loss due to "greatest of" selection in a cell-averaging cfar. *IEEE Transactions on Aerospace and Electronic Systems*, AES-16(1):115–118, Jan 1980.
- [58] M. Weiss. Analysis of some modified cell-averaging cfar processors in multiple-target situations. *IEEE Transactions on Aerospace and Electronic Systems*, AES-18(1):102–114, Jan 1982.
- [59] D. T. Nagle and J. Saniie. Performance analysis of linearly combined order statistic cfar detectors. *IEEE Transactions on Aerospace and Electronic Systems*, 31(2):522–533, April 1995.
- [60] J. C. Curlander and Robert N. McDonough. *Synthetic Aperture Radar - Systems And Signal Processing*. John Wiley & Sons, Inc., 1991.
- [61] M. Schneider. Automotive radar—status and trends. In *German microwave conference*, pages 144–147, 2005.
- [62] N. Levanon. Multifrequency complementary phase-coded radar signal. *IEE Proceedings-Radar, Sonar and Navigation*, 147(6):276–284, 2000.
- [63] R. M. Narayanan, Y. Xu, P. D. Hoffmeyer, and J. O. Curtis. Design, performance, and applications of a coherent ultra-wideband random noise radar. *Optical Engineering*, 37(6):1855–1870, 1998.
- [64] M. Dawood and R. M. Narayanan. Ambiguity function of an ultrawideband random noise radar. In *Antennas and Propagation Society International Symposium, 2000. IEEE*, volume 4, pages 2142–2145. IEEE, 2000.
- [65] A. V. Oppenheim and R. W. Schaffer. *Discrete-Time Signal Processing*. Prentice Hall Press, Upper Saddle River, NJ, USA, 3rd edition, 2009.
- [66] M. Lustig, D. Donoho, and J. M. Pauly. Sparse mri: The application of compressed sensing for rapid mr imaging. *Magnetic Resonance in Medicine: An Official Journal of the International Society for Magnetic Resonance in Medicine*, 58(6):1182–1195, 2007.

- [67] J. F. Claerbout and F. Muir. Robust modeling with erratic data. *Geophysics*, 38(5):826–844, 1973.
- [68] T. J. Fitch, D. W. McCowan, and M. W. Shields. Estimation of the seismic moment tensor from teleseismic body wave data with applications to intraplate and mantle earthquakes. *Journal of Geophysical Research: Solid Earth*, 85(B7):3817–3828, 1980.
- [69] D. Donoho and Y. Tsaig. Extensions of compressed sensing. *preprint*, 2004.
- [70] E. J. Candès, J. Romberg, and T. Tao. Robust uncertainty principles: Exact signal reconstruction from highly incomplete frequency information. *IEEE Transactions on information theory*, 52(2):489–509, 2006.
- [71] D. L. Donoho. Compressed sensing. *IEEE Transactions on information theory*, 52(4):1289–1306, 2006.
- [72] I. Daubechies, M. Defrise, and C. De Mol. An iterative thresholding algorithm for linear inverse problems with a sparsity constraint. *Communications on Pure and Applied Mathematics: A Journal Issued by the Courant Institute of Mathematical Sciences*, 57(11):1413–1457, 2004.
- [73] E. J. Candès, J. K. Romberg, and T. Tao. Stable signal recovery from incomplete and inaccurate measurements. *Communications on Pure and Applied Mathematics*, 59(8):1207–1223, 2006.
- [74] B. K. Natarajan. Sparse approximate solutions to linear systems. *SIAM Journal on Computing*, 24(2):227–234, 1995.
- [75] S. Chen and D. Donoho. Basis pursuit. In *Proceedings of 1994 28th Asilomar Conference on Signals, Systems and Computers*, volume 1, pages 41–44 vol.1, Oct 1994.
- [76] S. S. Chen, D. L. Donoho, and M. A. Saunders. Atomic decomposition by basis pursuit. *SIAM review*, 43(1):129–159, 2001.
- [77] R. Tibshirani. Regression shrinkage and selection via the lasso. *Journal of the Royal Statistical Society. Series B (Methodological)*, pages 267–288, 1996.
- [78] G. Davis, S. Mallat, and M. Avellaneda. Adaptive greedy approximations. *Constructive Approximation*, 13(1):57–98, Mar 1997.
- [79] S. S. Chen, D. L. Donoho, and M. A. Saunders. Atomic decomposition by basis pursuit. *SIAM Review*, 43(1):129–159, 2001.
- [80] A. C. Gilbert, S. Muthukrishnan, and M. J. Strauss. Approximation of functions over redundant dictionaries using coherence. In *Proceedings of the Fourteenth Annual ACM-SIAM Symposium on Discrete Algorithms*, SODA '03, pages 243–252, Philadelphia, PA, USA, 2003. Society for Industrial and Applied Mathematics.

- [81] Y. C. Pati, R. Rezaifar, and P. S. Krishnaprasad. Orthogonal matching pursuit: Recursive function approximation with applications to wavelet decomposition. In *Signals, Systems and Computers, 1993. 1993 Conference Record of The Twenty-Seventh Asilomar Conference on*, pages 40–44. IEEE, 1993.
- [82] J. A. Tropp. Greed is good: Algorithmic results for sparse approximation. *IEEE Trans. Inf. Theor.*, 50(10):2231–2242, September 2006.
- [83] D. Needell and R. Vershynin. Uniform uncertainty principle and signal recovery via regularized orthogonal matching pursuit. *Foundations of computational mathematics*, 9(3):317–334, 2009.
- [84] W. Dai and O. Milenkovic. Subspace pursuit for compressive sensing signal reconstruction. *IEEE transactions on Information Theory*, 55(5):2230–2249, 2009.
- [85] J. A. Tropp, A. C. Gilbert, and M. J. Strauss. Algorithms for simultaneous sparse approximation. part i: Greedy pursuit. *Signal processing*, 86(3):572–588, 2006.
- [86] D. Needell and J. A. Tropp. Cosamp: Iterative signal recovery from incomplete and inaccurate samples. *Applied and computational harmonic analysis*, 26(3):301–321, 2009.
- [87] S. Mallat and Z. Zhang. Matching pursuit with time-frequency dictionaries. Technical report, Courant Institute of Mathematical Sciences New York United States, 1993.
- [88] T. Blumensath and M. E. Davies. On the difference between orthogonal matching pursuit and orthogonal least squares - technical report. 2007.
- [89] T. T. Cai and L. Wang. Orthogonal matching pursuit for sparse signal recovery with noise. *IEEE Transactions on Information theory*, 57(7):4680–4688, 2011.
- [90] R. O. Duda, P. E. Hart, and D. G. Stork. *Pattern Classification (2Nd Edition)*. Wiley-Interscience, 2000.
- [91] G. Darche. Iterative l1 deconvolution. *SEP Annual Report*, 61:281–301, 1989.
- [92] E. J Candes, M. B. Wakin, and S. P. Boyd. Enhancing sparsity by reweighted l1 minimization. *Journal of Fourier analysis and applications*, 14(5-6):877–905, 2008.
- [93] J. F. C. Mota, N. Deligiannis, and M. R. D. Rodrigues. Compressed sensing with side information: Geometrical interpretation and performance bounds. In *2014 IEEE Global Conference on Signal and Information Processing (GlobalSIP)*, pages 512–516, Dec 2014.
- [94] M. C. Grant and S. P. Boyd. The CVX users guide. CVX research. *Inc., Cambridge, UK*, 190, 2012.
- [95] A. P. Mouritz and A. G. Gibson. *Fire Properties of Polymer Composite Materials*. Solid Mechanics and Its Applications. Springer Netherlands, 2007.
- [96] F. Taillade, M. Quiertant, K. Benzarti, J. Dumoulin, and C. Aubagnac. *Nondestructive Evaluation of FRP Strengthening Systems Bonded on RC Structures Using Pulsed Stimulated Infrared Thermography*. 03 2012.

- [97] G. A. Matzkanin. Selecting a nondestructive testing method, part ii: Visual inspection. *The AMMTIAC Quarterly - Composites Affordability Initiative*, 1(3):7–10, 2007.
- [98] T. Hasiotis, E. Badogiannis, and N. Georgios Tsouvalis. Application of ultrasonic c-scan techniques for tracing defects in laminated composite materials. *Strojniski vestnik - Journal of Mechanical Engineering*, 57(3):192–203, 2011.
- [99] W. N. Reynolds. Nondestructive testing (ndt) of fibre-reinforced composite materials. *Materials & Design*, 5(6):256 – 270, 1984.
- [100] S. F. Hatfield, M. A. Hillstrom, D. N. Schultz, T. M. Werckmann, M. T. Ghasr, and K. M. Donnell. Uwb microwave imaging array for nondestructive testing applications. In *2013 IEEE International Instrumentation and Measurement Technology Conference (I2MTC)*, pages 1502–1506, May 2013.
- [101] B. B. Hu and M. C. Nuss. Imaging with terahertz waves. *Opt. Lett.*, 20(16):1716–1718, Aug 1995.
- [102] R. Pincu. Digital radiography and its advantages in field ndt inspections today. In *17 th World Conference on Non-Destructive Testing*, pages 25–28, 2008.
- [103] R. D. Owen. Portable linear accelerators for x-ray and electron-beam applications in civil engineering. *NDT & E International*, 31(6):401–409, 1998.
- [104] M. A. Abou-Khousa, A. Ryley, S. Kharkovsky, R. Zoughi, D. Daniels, N. Kreitingner, and G. Steffes. Comparison of X-Ray, Millimeter Wave, Shearography and Through-Transmission Ultrasonic Methods for Inspection of Honeycomb Composites. 894:999–1006, 03 2007.
- [105] A. J. Stamm F. F. P. Kollmann, E. W. Kuenzi. *Principles of Wood Science and Technology: II Wood Based Materials*. Springer-Verlag Berlin Heidelberg, 1 edition, 1975.
- [106] T. S. Lim, C. S. Lee, and D. G. Lee. Failure modes of foam core sandwich beams under static and impact loads. *Journal of Composite Materials*, 38(18):1639–1662, 2004.
- [107] J. R. Wright and L. J. Mathias. New lightweight materials: Balsa wood-polymer composites based on ethyl alpha-(hydroxymethyl)acrylate. *Journal of Applied Polymer Science*, 48(12):2241–2247, 1993.
- [108] D.J. Kozakoff. *Analysis of Radome-enclosed Antennas*. Number v. 1 in Analysis of Radome-enclosed Antennas. Artech House, 1997.
- [109] G. J. Dvorak, N. Laws, and M. Hejazi. Analysis of progressive matrix cracking in composite laminates I. thermoelastic properties of a ply with cracks. *Journal of Composite Materials*, 19(3):216–234, 1985.
- [110] L. Li. Comparison of cyclic hysteresis behavior between cross-ply C/SiC and SiC/SiC ceramic-matrix composites. *Materials (Basel, Switzerland)*, 9(1), January 2016.

- [111] A. Elhawil, L. Zhang, J. Stiens, C. De Tandt, N. A. Gotzen, G. V. Assche, and R. Vounckx. A quasi-optical free-space method for dielectric constant characterization of polymer materials in mm-wave band. In *Proceedings Symposium IEEE/LEOS Benelux Chapter*, volume 66, pages 187–190, 2007.
- [112] D. M. Pozar. *Microwave engineering; 3rd ed.* Wiley, Hoboken, NJ, 2005.
- [113] I. De Coster, E. Van Lil, and A. Van de Capelle. Comparison of design methods for binomial matching transformers. *Journal of Electromagnetic Waves and Applications*, 14(9):1229–1239, 2000.
- [114] H. Zain A. A. Hissen. *Spectral characterization of materials using terahertz time domain spectroscopy (THz-TDS)*. PhD thesis, Stellenbosch: Stellenbosch University, 2014.
- [115] K. S. Novoselov, A. K. Geim, S. V. Morozov, D. A. Jiang, Y. Zhang, S. V. Dubonos, I. V. Grigorieva, and A. A. Firsov. Electric field effect in atomically thin carbon films. *science*, 306(5696):666–669, 2004.
- [116] AB Millimetre. A quick overview of the MVNA-8-350 millimeter vector network analyzer produced by AB Millimetre, 2013. <http://www.abmillimetre.com/Introduction.htm>, accessed 2018-02-10.
- [117] T. Y. Wu. High dynamic range terahertz-wave transmission loss measurement at 330–500 GHz. *Measurement Science and Technology*, 23(8):085904, 2012.
- [118] AB Millimetre. Figure 16: The dynamic range.
- [119] S. Lambot, A. Giannopoulos, L. Pajewski, E. Slob, and M. Sato. Foreword to the special issue on advances in ground-penetrating radar research and applications. *IEEE Journal of Selected Topics in Applied Earth Observations and Remote Sensing*, 9(1):5–8, Jan 2016.
- [120] E. Slob, M. Sato, and G. Olhoeft. Surface and borehole ground-penetrating-radar developments. *GEOPHYSICS*, 75(5):75A103–75A120, 2010.
- [121] S. L. Earp, E. S. Hughes, T. J. Elkins, and R. Vickers. Ultra-wideband ground-penetrating radar for the detection of buried metallic mines. *IEEE Aerospace and Electronic Systems Magazine*, 11(9):30–39, Sep 1996.
- [122] U. Spagnolini and V. Rampa. Multitarget detection/tracking for monostatic ground penetrating radar: application to pavement profiling. *IEEE Transactions on Geoscience and Remote Sensing*, 37(1):383–394, Jan 1999.
- [123] T. Kikuta and H. Tanaka. Ground probing radar system. *IEEE Aerospace and Electronic Systems Magazine*, 5(6):23–26, June 1990.
- [124] J. Minet, P. Bogaert, M. Vanclooster, and S. Lambot. Validation of ground penetrating radar full-waveform inversion for field scale soil moisture mapping. *Journal of Hydrology*, 424-425:112–123, 2012.

- [125] V. Gundelach, N. Blindow, U. Buschmann, C. Salat, and Y. Krellmann. Exploration of geological structures with GPR from helicopter and on the ground in the Letzlinger Heide (Germany). In *Proceedings of the XIII International Conference on Ground Penetrating Radar*, pages 1–6, June 2010.
- [126] G. Grandjean, C. de Marliave, B. Buigues, D. Mol, and G. Ruffie. Searching out mammoth remains in permafrost (Taimyr, Siberia) using ground-penetrating radar. In *Proc. SPIE - Ninth International Conference on Ground Penetrating Radar*, volume 4758, pages 675–679, 2002.
- [127] R. S. Freeland, M. L. Miller, R. E. Yoder, and S. K. Koppenjan. Forensic application of fm-cw and pulse radar. *Journal of Environmental and Engineering Geophysics*, 8(2):97–103, 2003.
- [128] J. Hunter and M. Cox. *Forensic Archaeology: Advances in Theory and Practice*. Forensic science series. Routledge, 2005.
- [129] K. Iizuka and A. P. Freundorfer. Detection of nonmetallic buried objects by a step frequency radar. *Proceedings of the IEEE*, 71(2):276–279, Feb 1983.
- [130] T. Kikuta and H. Tanaka. Ground probing radar system. *IEEE Aerospace and Electronic Systems Magazine*, 5(6):23–26, June 1990.
- [131] P. Millot and A. Berges. Ground based sar imaging tool for the design of buried mine detectors. In *EUREL International Conference The Detection of Abandoned Land Mines: A Humanitarian Imperative Seeking a Technical Solution (Conf. Publ. No. 431)*, pages 157–159, Oct 1996.
- [132] K. Sturgess, L. Happ, J. Kurtz, and M. Collins. Results of a remote sensing experiment using a low frequency ultra-wideband sar to investigate the phenomenology of landmines. In *Geoscience and Remote Sensing Symposium, 1996. IGARSS '96. 'Remote Sensing for a Sustainable Future.'*, *International*, volume 4, pages 2027–2029 vol.4, May 1996.
- [133] B. Scheers, M. Piette, and A. Vander Vorst. The detection of ap mines using uwb gpr. In *1998 Second International Conference on the Detection of Abandoned Land Mines (IEE Conf. Publ. No. 458)*, pages 50–54, Oct 1998.
- [134] F. Parrini, F. Papi, and M. Pieraccini. An ultra high resolution stepped frequency gpr for civil engineering applications. In *2015 8th International Workshop on Advanced Ground Penetrating Radar (IWAGPR)*, pages 1–4, July 2015.
- [135] C. A. Balanis. *Advanced Engineering Electromagnetics*, 2nd Edition. *Wiley*, 2012.
- [136] S. Lambot, E. C. Slob, I. van den Bosch, B. Stockbroeckx, and M. Vanclooster. Modeling of ground-penetrating radar for accurate characterization of subsurface electric properties. *IEEE Transactions on Geoscience and Remote Sensing*, 42(11):2555–2568, 2004.
- [137] S. Lambot and F. Andre. Full-wave modeling of near-field radar data for planar layered media reconstruction. *IEEE Transactions on Geoscience and Remote Sensing*, 52(5):2295–2303, 2014.

- [138] A. P. Tran, F. Andre, C. Craeye, and S. Lambot. Near-field or far-field full-wave ground penetrating radar modeling as a function of the antenna height above a planar layered medium. *Progress in Electromagnetics Research-Pier*, 141:415–430, 2013.
- [139] E. C. Slob and J. Fokkema. Coupling effects of two electric dipoles on an interface. *Radio Science*, 37(5):1073, doi:10.1029/2001RS2529, 2002.
- [140] O. Lopera, E. C. Slob, N. Milisavljevic, and S. Lambot. Filtering soil surface and antenna effects from GPR data to enhance landmine detection. *IEEE Transactions on Geoscience and Remote Sensing*, 45(3):707–717, 2007.
- [141] A. De Coster and S. Lambot. Full-wave removal of internal antenna effects and antenna-medium coupling for improved ground-penetrating radar imaging. *IEEE Transactions on Geoscience and Remote Sensing*, x(x):x–x, 2017.
- [142] E. Cristofani, M. Becquaert, and M. Vandewal. Performance of 2D Compressive Sensing on Wide-Beam Through-the-Wall Imaging. *Journal of Electrical and Computer Engineering*, 2013(636972):1–11, 2013.
- [143] A. C. Gurbuz, J. H. McClellan, and W. R. Scott. A compressive sensing data acquisition and imaging method for stepped frequency GPRs. *IEEE Transactions on Signal Processing*, 57(7):2640–2650, July 2009.
- [144] O. Lopera, E. C. Slob, N. Milisavljevic, and S. Lambot. Filtering soil surface and antenna effects from GPR data to enhance landmine detection. *IEEE Transactions on Geoscience and Remote Sensing*, 45(3):707–717, March 2007.
- [145] S. Lambot, E. Slob, J. Rhebergen, O. Lopera, K.Z. Jadoon, and H. Vereecken. Remote estimation of the hydraulic properties of a sandy soil using full-waveform integrated hydrogeophysical inversion of time-lapse, off-ground GPR data. *Vadose Zone Journal*, 8(3):743–754, 2009.
- [146] F. Soldovieri, O. Lopera, and S. Lambot. Combination of Advanced Inversion Techniques for an Accurate Target Localization via GPR for Demining Applications. *IEEE Transactions on Geoscience and Remote Sensing*, 49(1):451–461, 2011.
- [147] P. Krysik, K. Kulpa, P. Samczynski, K. Szumski, and J. Misiurewicz. Moving target detection and imaging using gsm-based passive radar. In *IET International Conference on Radar Systems (Radar 2012)*, pages 1–4, Oct 2012.
- [148] S. Bartoletti, A. Conti, and M. Z. Win. Passive radar via LTE signals of opportunity. In *Communications Workshops (ICC), 2014 IEEE International Conference on*, pages 181–185. IEEE, 2014.
- [149] H.D. Griffiths, C.J. Baker, J. Baubert, N. Kitchen, and M. Treagust. Bistatic radar using satellite-borne illuminators. 2002.
- [150] P. Samczynski and K. Kulpa. Passive SAR imaging using a satellite pulsed radar as an illuminator of opportunity. In *Radar Symposium (IRS), 2012 13th International*, pages 157–161. IEEE, 2012.

- [151] E. Cristofani, V. Kubica, and X. Neyt. A multibeam opportunistic sar system. In *Radar Conference (RADAR), 2011 IEEE*, pages 778–783. IEEE, 2011.
- [152] M. Malanowski and K. Kulpa. Analysis of bistatic tracking accuracy in passive radar. In *Radar Conference, 2009 IEEE*, pages 1–6. IEEE, 2009.
- [153] D. Olivadese, M. Martorella, E. Giusti, D. Petri, and F. Berizzi. Passive isar with dvb-t signal. In *EUSAR 2012; 9th European Conference on Synthetic Aperture Radar*, pages 287–290, April 2012.
- [154] J. E. Palmer, H. A. Harms, S. J. Searle, and L. Davis. Dvb-t passive radar signal processing. *IEEE transactions on Signal Processing*, 61(8):2116–2126, 2013.
- [155] L. Cimini. Analysis and simulation of a digital mobile channel using orthogonal frequency division multiplexing. *IEEE transactions on communications*, 33(7):665–675, 1985.
- [156] M. Wetz, I. Periša, W. G. Teich, and J. Lindner. Robust transmission over fast fading channels on the basis of ofdm-mfsk. *Wireless Personal Communications*, 47(1):113–123, 2008.
- [157] T. M. Schmidl and D. C. Cox. Robust frequency and timing synchronization for ofdm. *IEEE transactions on communications*, 45(12):1613–1621, 1997.
- [158] L. Jun, J. H. Andrian, and C. Zhou. Bit error rate analysis of jamming for ofdm systems. In *Wireless Telecommunications Symposium, 2007. WTS 2007*, pages 1–8. IEEE, 2007.
- [159] M. K. Ozdemir and H. Arslan. Channel estimation for wireless ofdm systems. *IEEE Communications Surveys & Tutorials*, 9(2):18–48, 2007.
- [160] ETSI Standard. En 300 744 v1. 5.1. *Digital video broadcasting (DVB)*, 2001.
- [161] Ettus Research. USRP B100 bus series, 2012. https://www.ettus.com/content/files/07495_Ettus_B100_DS_Flyer_HR.pdf, accessed 2018-02-10.
- [162] GNU Radio. GNU Radio, 2018. <https://www.gnuradio.org/news/gnu-radio-v3-7-13-4-release>, accessed 2018-07-22.
- [163] O. Mahfoudia. *Optimum reference signal reconstructon for DVB-T passive radars*. PhD thesis, Royal Military Academy and Université libre de Bruxelles, Brussels, 2017.